Research and Development of a Segmented GEM Readout Detector

Christoph Jagfeld

München 2023

Research and Development of a Segmented GEM Readout Detector

Christoph Jagfeld

Dissertation
an der Physik
der Ludwig–Maximilians–Universität
München

vorgelegt von
Christoph Jagfeld
aus München

München, den 10.03.2023

Erstgutachter: Prof. Dr. Otmar Biebel
Zweitgutachter: Prof. Dr. Wolfgang Dünnweber
Tag der mündlichen Prüfung: 16.05.2023

Zusammenfassung

Microstrukurierte Gasdetektoren sind hochleistungsfähige Teilchendetektoren. Sie weisen eine ausgezeichnete räumliche und zeitliche Auflösung auf. Zwei Typen von ihnen, GEM (Gas Electron Multiplier) und Micromegas (MIcro-MEsh GAseous Structure) Detektoren, sind in HEP-Experimenten weit verbreitet.
Diese Arbeit kombiniert beide Detektortypen zum neuartigen Segmented GEM Readout (SGR) Detektor. Der SGR-Detektor verwendet eine 2D-Micromegas-Streifenauslesestruktur und eine GEM-Folie, deren Kupferbeschichtung auf einer oder beiden Seiten in Streifen unterteilt ist. Diese GEM-Folie ersetzt das Mikrogitter des Micromegas-Detektors. Mit dieser neuen Technologie werden dem Detektor bis zu zwei neue Auslesestreifenlagen hinzugefügt, so dass er insgesamt bis zu vier Auslesestreifenlagen hat.

Der SGR-Detektor hat zwei wesentliche Vorteile gegenüber dem herkömmlichen Micromegas-Detektor:
Erstens wird aufgrund der Geometrie der Detektorauslese eine Koordinate des einfallenden Teilchens genauer bestimmt als die andere. Das Signal der GEM-Streifen wird genutzt, um dies zu kompensieren.
Zweitens ist eine eindeutige 2D-Teilchenpositionsrekonstruktion nur möglich, wenn der Detektor nur von einem Teilchen gleichzeitig getroffen wird. Wenn mehrere Teilchen gleichzeitig eintreffen wird eine eindeutige X-Y-Zuordnung stark erschwert. Dies kann durch GEM-Streifen vermieden werden, die um 45° zu den Micromegas-Streifen gedreht sind. Simulationen haben gezeigt, dass die Ambiguitäten bei der Mehrteilchenrekonstruktion durch eine Drehung der GEM-Streifen um 45° zu den Micromegas-Streifen stark reduziert werden. So wird der Detektor an der GEM-Folie entlang einer zusätzlichen Koordinate (U-Koordinate) ausgelesen, während die X- und Y-Koordinate durch die Micromegas-Auslesestreifenlagen bestimmt werden. Es wird erwartet, dass der SGR-Detektor sehr gut geeignet ist um die eindeutige 2D-Position mehrerer Teilchen gleichzeitig zu bestimmen.

Der für diese Arbeit entwickelte und gebaute SGR-Prototyp verwendet GEM-Streifen, die senkrecht zu den oberen Micromegas-Auslesestreifen verlaufen. Bei senkrechtem Einfall bietet der SGR-Detektor eine hervorragende Energie- ($\Delta E/E \approx 10\,\%$) und Positionsauflösung (besser als $80\,\mu m$). Selbst bei einem großen Einfallswinkel von 20° bleibt die Auflösung besser als $155\,\mu m$. In beiden Fällen liegt die 2D-Positionsrekonstruktionseffizienz deutlich über 90 %.

Darüber hinaus liefert diese Arbeit durch umfangreiche ANSYS und Garfield++ Simulationen eine umfassende Beschreibung der experimentell beobachteten Signalformen. Die Ergebnisse zeigen signifikante Unterschiede in den Signalformen zwischen den verschiedenen aktiven Detektorschichten. Bipolare Signale werden sowohl auf den Micromegas-Ausleselagen als auch auf den GEM-Streifen beobachtet, wenn die Segmentierung der Anode zugewandt ist. Wenn die segmentierte Seite in die andere Richtung zeigt, ist das Signal auf dieser Seite unipolar. Der starke Einfluss der Elektronenbewegung auf der hochohmigen Anode auf die Eigenschaften und Signalformen der Micromegas-Ausleseslagen wurde im Detail untersucht. Die unterschiedliche Genauigkeit der beiden Micromegas-Auslesestreifenlagen wurden verstanden. Darauf aufbauend werden Vorschläge für Optimierungen gegeben.

Diese Arbeit zeigt, dass das Prinzip eines SGR-Detektors erfolgreich umgesetzt werden kann und das dahinterstehende Funktionsprinzip verstanden wird. Basierend auf dieser Arbeit ist der Bau eines X, Y, U SGR-Detektors erfolgversprechend.

Abstract

Micro-Pattern Gaseous detectors are high-rate capable particle detectors. They show an excellent spatial and temporal resolution. Two types of them, GEM (Gas Electron Multiplier) and Micromegas (Micro-MEsh GAseous Structure) detectors are widely used in HEP experiments.
This work combines both detector types to the novel Segmented GEM Readout (SGR) detector. The SGR detector uses a 2D Micromegas strip readout structure and a GEM foil whose copper coating on one or both sides is segmented into strips. This GEM foil replaces the micro-mesh of the Micromegas detector. Based on this new technology, up to two new readout strip layers are added to the detector, so that it has up to four readout strip layers in total.

The SGR detector has two main advantages over the conventional Micromegas detector:
Firstly, due to the geometry of the detector readout, one coordinate of the incident particle is determined more accurately than the other one. The signal of the GEM strips is used to compensate for this.
Secondly, a unique 2D particle position reconstruction is only possible if the detector is hit by only one particle at the same time. If multiple particles arrive simultaneously a unique X–Y assignment is strongly aggravated. This can be compensated by GEM strips rotated 45° to the Micromegas strips. Simulations have shown a large reduction in ambiguities in the multi-particle reconstruction by turning the GEM strips by 45° to the Micromegas strips. Thus, the detector is read out at the GEM foil along an additional coordinate (U-coordinate), while the X and Y-coordinate are obtained by the Micromegas readout strip layers. The SGR detector is expected to be very well suited to determine the unambiguous 2D position of several particles simultaneously.

The SGR prototype developed and built for this work uses GEM strips that are perpendicular to the strips of the upper Micromegas readout layer. At perpendicular incidence, the SGR detector provides an excellent energy ($\Delta E/E \approx 10\,\%$) and position resolution (better than $80\,\mu m$). Even at a large incidence angle of 20° the resolution remains better than $155\,\mu m$. In both cases, the 2D position reconstruction efficiency is well above 90 %.

Additionally, this work provides a comprehensive description of the signal shapes observed in experiments, through extensive simulations using ANSYS and Garfield++. The results reveal significant differences in signal shapes among the various active detector layers. Bipolar signals are observed in both Micromegas readout coordinates and on the GEM strips when the segmentation faces the anode. If the segmented side faces toward the other direction, the signal on this layer is unipolar. The strong influence of electron motion on the highly resistive anode onto the properties and signal shapes of the Micromegas readout layers was elaborated in detail. The different accuracies of the two Micromegas readout strip layers were understood. Based on that suggestions for optimizations are provided.

This work shows that the principle of an SGR detector works very well and the working principle is understood. Based on this work, the construction of an X, Y, U SGR detector is possible.

Contents

Chapter 1

Micro Pattern Gaseous Detectors

Micro Pattern Gasseous Detectors (MPGD) are used in high energy and nuclear physics as well as in medical imaging for the detection of charged particles and photons. They are high rate capable and show a good position and timing resolution [Pinto, 2010].
The main components of MPGDs are produced by lithographic methods as used for Printed Circuit Board (PCB) production. Therefore they are easy and cheap to produce. Production of large scale ($\mathcal{O}(\mathrm{A}) = \mathrm{m}^2$) MPGDs is possible up to several square meters in size [Herrmann, 2019].
Two of the most prominent MPGD technologies, Gas Electron Multiplier (GEM) and MICRO MEsh GAseous Structure (Micromegas) detectors are newly used in the end cap region of the muon spectrometer at Compact Muon Solenoid (CMS) and A Toroidal LHC ApparatuS (ATLAS) experiment at CERN [Colaleo et al., 2015] [Kawamoto et al., 2013]. These detectors cover an area of several tens of square meters.
MPGDs can also be used for muon tomography experiments. For example, Micromegas detectors were used to discover hidden chambers in the Khufu's Pyramid in Giza [Morishima et al., 2017].
Research is also going on in the medical application of MPGDs. Micromegas detectors are used for ion transmission radiography. Imaging during tumor treatment by monitoring the ion beam in front of and behind the patient is necessary for this. Due to their low material budget and the thus resulting low multiple scattering in the detector, Micromegas detectors are well suited for this purpose [Bortfeldt et al., 2017].

The working principle is similar for all types of MPGDs. As the name suggests, MPGDs are gas-filled detectors. The interaction of incident particles with the detector takes place in the gas volume. MPGDs are divided into regions with different levels of electric fields. Incoming radiation ionizes the gas inside the detector volume. A low electric field separates the gas ions and electrons. Electron avalanches in detector regions with a high electric field multiply the number of electrons so that they can be detected [Pinto, 2010]. Mostly the high electric field is chosen such that the charge collected on the anode is proportional to the number of primary ionized electrons. In most MPGDs the electrons are collected on readout strips.
The working principle is explained in detail in Chapter 2.

The goal of this work is to improve the strip readout of the Micromegas detector. The newly developed Segmented Gem Readout (SGR) detector (see Chapter 2.3) combines the GEM (see Chapter 2.2) and Micromegas detector (see Chapter 2.1). It splits the amplification process into two parts, a pre-amplification process, and a main amplification process. The electric fields necessary can be chosen lower in each step. Discharges become more unlikely.

The SGR detector reads out the signal at the position where the ions drift to as well as at the position the electrons drift to. This adds another readout strip layer to the detector.

1.1 Physics Background

For a complete understanding of MPGDs, the underlying physical processes have to be considered first. In the following, the interaction of particles with matter (see Chapter 1.1.1) as well as the charge transport (see Chapter 1.1.3) and the charge amplification (see Chapter 1.1.2) in the detector gas are described.

1.1.1 Particle Interaction with Matter

Particles need to interact with the detector volume to be detected. The interaction processes differ for neutral and charged particles.
Charged particles are detected directly via electromagnetic interaction.
Neutral particles must interact with the detector volume first to produce charged particles. These then interact electromagnetically and can be detected in the same way as charged particles [Kleinknecht, 2005].
For this thesis, the detectors are investigated using 120 GeV muons, and 5.9 keV photons. Therefore, the following focuses on the interaction of heavily charged particles with matter and photons with matter.

Heavy Charged Particles

If a charged particle traverses a medium, it interacts with the medium through electromagnetic interaction. It can emit Cherenkov light or transition radiation. The most important interaction process for MPGDs is the ionization of the medium along the particle path [Kleinknecht, 2005].
The mean energy loss of a heavy charged particle with $0.1 \lesssim \beta\gamma \lesssim 1000$ in a medium is described by the Bethe Bloch equation [Workman and Others, 2022]:

$$\frac{dE}{dx} = 4\pi N_A r_e^2 m_e c^2 \rho \frac{Z}{A}\frac{z^2}{\beta^2}\left[\frac{1}{2}\ln\left(\frac{2m_e c^2\beta^2\gamma^2 W_{max}}{I^2}\right) - \beta^2 - \frac{\delta(\beta\gamma)}{2}\right] \tag{1.1}$$

with N_A: Avogadro's number, r_e: classical electron radius, m_e: electron mass, c: speed of light in vacuum, ρ: density, Z: atomic number of absorber, A: atomic mass of absorber, z: charge number of incident particle, v: speed of the incident particle, $\beta = \frac{v}{c}$, $\gamma = 1/\sqrt{1-\beta^2}$, I: mean excitation energy, $W_{\max}$: energy transfer to an electron in a single collision and δ: density effect correction to ionization energy loss.

The Bethe-Bloch equation has its minimum at $\beta\gamma \approx 4$ (see Figure 1.1). For all media, except Hydrogen, the mean energy loss at this value is $2-3\,\mathrm{MeVcm^2/g}$ [Kleinknecht, 2005].
For particle momenta lower than the minimum the energy loss is proportional to β^2. The more a non-relativistic particle is decelerated, the larger its energy loss becomes. At $\beta\gamma \lesssim 0.1$ the particle momentum is in the same range as the momentum of the bound electrons of the medium and Equation 1.1 loses its validity [Frauenfelder and Henley, 1979].
For energies higher than the minimum energy the energy loss increases slowly until for $\beta\gamma \gtrsim 1000$ radiative losses start to become important. Equation 1.1 loses its validity here as well. At the muon critical energy, $E_{\mu c}$ the radiative loss due to ionization and radiative losses

are equal. For muons in Argon this value is at $E_{\mu c} \approx 450\,GeV$ [Kleinknecht, 2005].
For this thesis measurements are performed with 120 GeV muons, which are at $\beta\gamma \approx 1000$.
In thin media such as gases, the distribution of energy transferred from charged particles to the detector gas is not Gaussian. It shows an excess towards high values caused by δ – electrons [Kleinknecht, 2005].

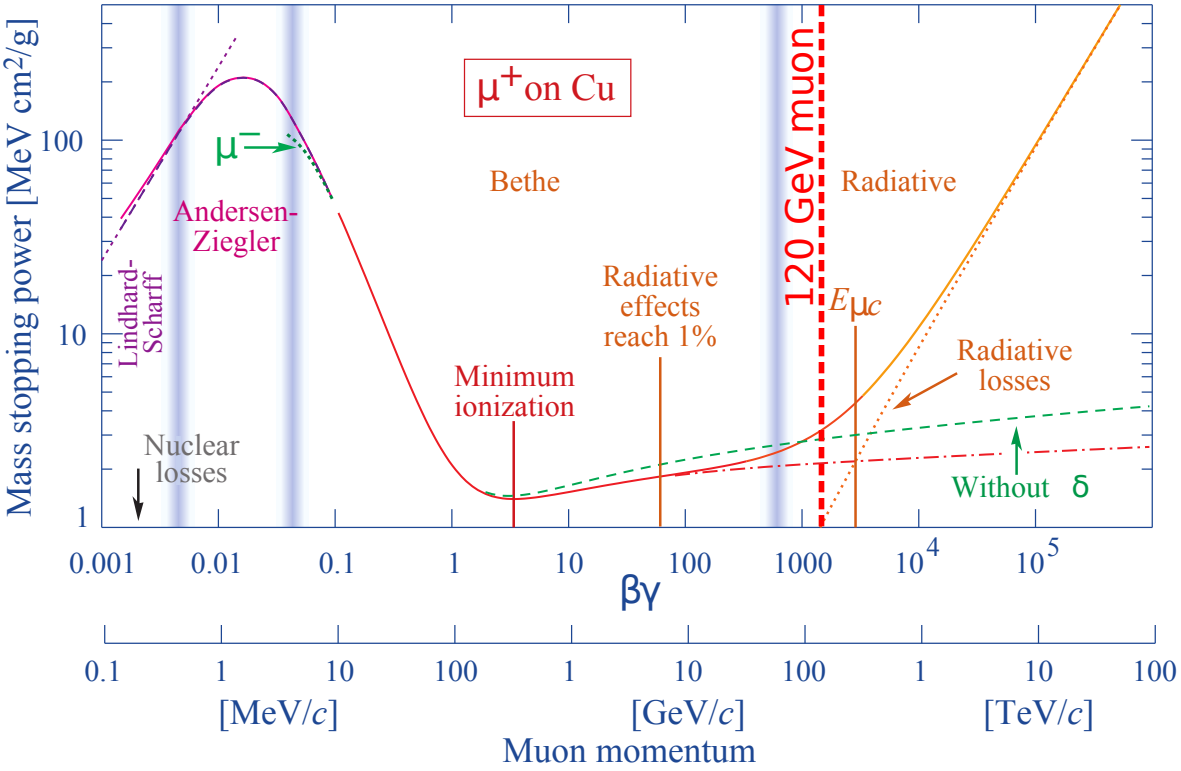

Figure 1.1: Mass stopping power ($dE/d(\rho x)$) for a positively charged muon in copper depending on the muon momentum. Figure adapted from [Workman and Others, 2022].
120 GeV muons used for the presented measurements are marked in this figure.

Photons

Photons are massless neutral particles. Therefore they do not interact with the medium as described in Chapter 1.1.1.
The intensity $I(x)$ of a photon beam with an initial intensity I_0 decreases by traversing a medium with an attenuation coefficient μ and density ρ. It is given by [Kleinknecht, 2005]:

$$I(x) = I_0 e^{-\mu x/\rho} \tag{1.2}$$

The mass attenuation coefficient μ/ρ for Argon is shown in Figure 1.2. Depending on the photon energy E_γ different interaction processes dominate (see Figure 1.2).
For $E_\gamma < 100\,keV$ the dominant process is the photoelectric effect. The photon gets absorbed by an electron in the medium. The energy is used to free an electron from its shell. The kinetic energy T of the photoelectron ionized by a photon with the energy $E_\gamma = h\nu$ is [Einstein, 1905]:

$$T = E_\gamma - W \tag{1.3}$$

with W being the minimum energy needed to remove the electron from the bound state.
For $100\,keV < E_\gamma < 2\,MeV$ the Compton effect dominates. The photon gets scattered inelastically on an electron of the medium. The transferred energy ionizes an atom. Depending

on the photon scattering angle Θ the kinetic energy T_e of the electron varies. For $\Theta = 0$ the transferred energy of the photoelectron is $T_e = 0$. It increases continuously until the maximum energy transfer is reached at the Compton edge for $\Theta = \pi$ [Kleinknecht, 2005].
If $E_\gamma > 2m_e c^2$ the photon can decay in an electron-positron pair. For momentum conservation, this process can only occur in the presence of a coulomb field of an atom. Pair production in the coulomb field of an electron is also possible but suppressed.
Pair production dominates for $E_\gamma > 2\,\mathrm{MeV}$ [Frauenfelder and Henley, 1979].

For this thesis measurements are performed using ^{55}Fe as a γ source. The photon energy of ^{55}Fe is $E_\gamma = 5.9\,\mathrm{keV}$. Therefore the dominant interaction process is the photoelectric effect (see Figure 1.2).

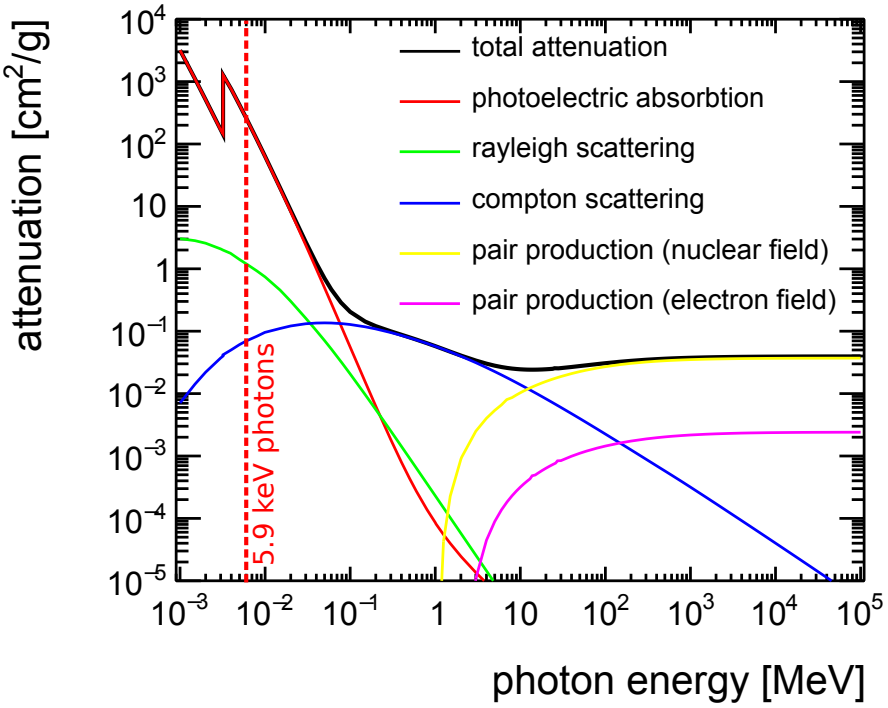

Figure 1.2: Attenuation coefficient for photons in Argon depending on the photon energy and its underlying processes.
5.9 keV photons used for the presented measurements are marked in this figure.
Data are taken from [The National Institute of Standards and Technology]

1.1.2 Gas amplification

To efficiently detect the charges created as described in Chapter 1.1.1 the number of charges needs to be multiplied. In MPGDs this process takes place in the detector. It is achieved by gas amplification.
In a high electric field $\mathcal{O}\left(|\vec{\mathrm{E}}|\right) = 10^4 - 10^5\,\mathrm{V/cm}$, an electron is accelerated between two collisions with gas molecules so much that the gained kinetic energy is higher than the ionization energy of the gas molecules. At each collision the number of electrons increases. The newly released electrons are also accelerated in addition to those already present. This leads to an electron avalanche process [Kleinknecht, 2005].
The number of electrons N in dependence of the drift distance x is described by the following differential equation [Townsend, 1910]:

$$dN(x) = \alpha\left(|\vec{E}\,(x)\,|\right) N(x) dx \tag{1.4}$$

with α being the first Townsend coefficient.

Solving Equation 1.4 gives the total number of electrons $N\,(x)$:

$$\begin{aligned} N\,(x) &= N_0 e^{\int \alpha(x) dx} \\ N\,(x) &= N_0 G \end{aligned} \tag{1.5}$$

with N_0 being the initial number of electrons.

The first Townsend coefficient α can be calculated knowing the mean free path λ:

$$\alpha\left(|\vec{E}|\right) = \frac{1}{\lambda\left(|\vec{E}|\right)} \tag{1.6}$$

As described in [Korff, 1946] it can be rewritten using two gas and detector dependent constants A, B, the pressure p, and the temperature T:

$$\alpha\left(|\vec{E}|\right) = \frac{Ap}{T} \exp\left(-\frac{Bp}{\left(|\vec{E}|\right) T}\right) \tag{1.7}$$

For a Micromegas detector the constants A and B are determined in [Lippert, 2012].

Using Equation 1.5 and Equation 1.7 the gain calculates as:

$$G = \exp\left[A \frac{p}{T} \exp\left(-\frac{Bp}{|\vec{E}|T}\right) x\right] \tag{1.8}$$

The gain increases exponentially with increasing drift distance x and increasing electric field $\vec{E}$ (see Equation 1.8).
If the Raether limit [Raether, 1964] which is at $\alpha x > 20$ is exceeded, a conducting plasma is created between the electrodes. The number of electrons in the avalanche is no longer proportional to the number of primary electrons. This is usually not desired in MPGDs and can harm the detector and readout electronics.

1.1.3 Drift of Charged Particles

Since ions are much heavier than electrons, they are not accelerated strongly enough by the electric fields used for the amplification process in the gas. The same applies to electrons at lower electric fields ($\mathcal{O}\left(|\vec{E}|\right) \ll 10^4 - 10^5\,\mathrm{V/cm}$). In these cases, the charged particles only drift along the electric field.

Electron Drift

For electric fields lower than needed for gas amplification (see Chapter 1.1.2) the electrons move along the electric field lines. Since the mean free path of electrons is larger than for ions, they can gain more energy between two collisions [Kleinknecht, 2005].
Figure 1.3 shows the drift velocity $|\vec{v}_{\mathrm{drift}}|$ of electrons in a mixture of $\mathrm{Ar} : \mathrm{CO_2}$. Higher $|\vec{v}_{\mathrm{drift}}|$ are possible with increasing $\mathrm{CO_2}$ content.
Measurements in this thesis are done with a gas mixture $\mathrm{Ar} : \mathrm{CO_2}$ 93 : 7 Vol. %. The drift field $|\vec{E}_{\mathrm{drift}}|$ is chosen such that v_{drift} becomes maximum. For $\mathrm{Ar} : \mathrm{CO_2}$ 93 : 7 Vol. % this is fulfilled at $|\vec{E}_{\mathrm{drift}}| \approx 600\,\mathrm{V/cm}$.
Additionally, the electrons diffuse in the longitudinal and transverse directions, while they drift. The diffusion depends on the electric field [Kleinknecht, 2005].

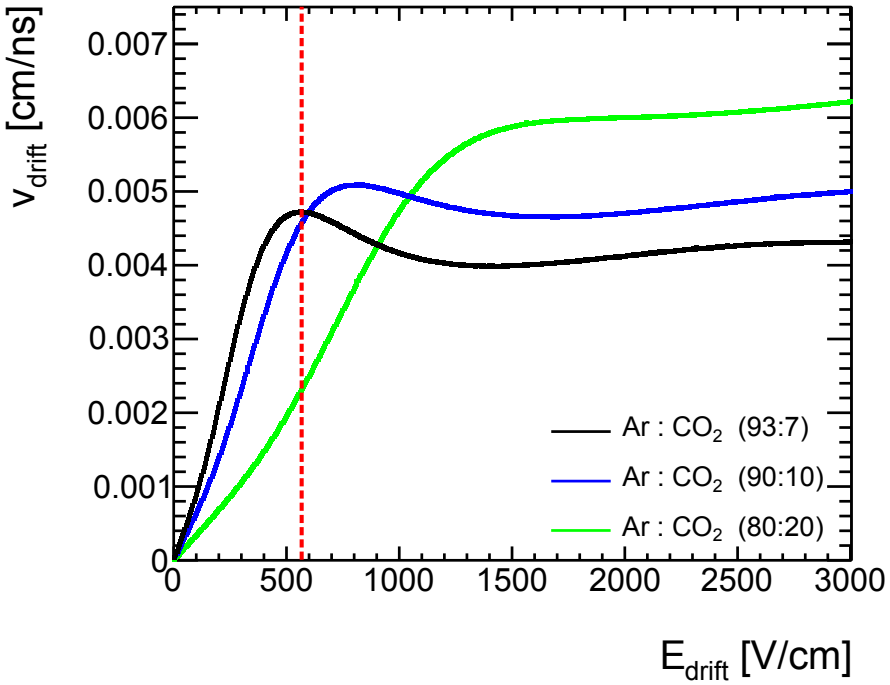

Figure 1.3: Electron drift velocity for different compositions of $\mathrm{Ar} : \mathrm{CO_2}$ depending on the drift field $\vec{E}_{\mathrm{drift}}$.
For $\mathrm{Ar} : \mathrm{CO_2}$ 93 : 7 Vol. % the maximum of $|\vec{v}_{\mathrm{drift}}|$ is at $|\vec{E}_{\mathrm{drift}}| \approx 600\,\mathrm{V/cm}$.
The values shown are simulated with MAGBOLTZ [Biagi, 2021].

Ion Drift

In the electron avalanche process as described in Chapter 1.1.2 an equal number of ions and electrons are created. The ions perceive the same electric field as the electrons. But the mobility of ions μ_{ion} is $10^2 - 10^3$ times smaller as for electrons [Kleinknecht, 2005]. Due to their much larger mass, they get accelerated much slower. At collisions with other gas atoms, they lose less energy than an electron at a collision with an ion [Rolandi et al., 2008]. The drift velocity $|\vec{v}_{\text{ion}}|$ of the ions is given in [Kleinknecht, 2005] as:

$$\vec{v}_{ion} = \mu_{ion} E \frac{p_0}{p} \tag{1.9}$$

with the normal pressure $p_0 = 760\,Torr$ and the gas pressure p. For a mixture of multiple gases the ion mobility μ_i of the ion belonging to the i$^{\text{th}}$ gas component is given by:

$$\frac{1}{\mu_i} = \sum_{k=1}^{n} \frac{c_k}{\mu_{ik}} \tag{1.10}$$

with c_{k} being the volume share of the gas k and μ_{ik} being the mobility of ion i in the gas k as it is described in [Kleinknecht, 2005].
For a gas mixture of $\text{Ar} : \text{CO}_2$ 90 : 10 Vol. % the mobility is measured to be approximately $\mu_{\text{ion}} \approx 1.72\,cm^2/V$ [Deisting et al., 2018]. It decreases with an increasing fraction of CO_2 (see Table 1.1).
The ion mobility is constant with increasing $|\vec{\text{E}}_{\text{drift}}|$ as long as the energy gained is much smaller than the thermal energy. For higher energies it decreases as $\mu_{\text{i}} \propto 1/\sqrt{|\vec{E}_{\text{drift}}|}$ [Deisting et al., 2018].
Like electrons, ions also diffuse while they drift. Since the diffusion becomes smaller with increasing particle mass, it is lower for ions than for electrons [Kleinknecht, 2005].

$\text{Ar} : \text{CO}_2$	$\mu_{\text{ion}} \left[\frac{\text{cm}^2}{\text{Vs}}\right]$
90:10	1.72
80:20	1.54
70:30	1.45
60:40	1.33
50:50	1.23

Table 1.1: Ion mobility for different compositions of $\text{Ar} : \text{CO}_2$. Data are taken from [Deisting et al., 2018].

Chapter 2

Types of Micro Pattern Gaseous Detectors

Discussing all types of micro-pattern gaseous detectors exceeds the scope of this thesis. Only the detector types relevant for this thesis, Micromegas, resistive Micromegas, and GEM detectors are explained.

The captions in the following chapters are very detailed, providing a comprehensive understanding of the essential information presented in the figures. Therefore, there may be overlaps between the captions and the body text.

2.1 Micro-MEsh GAseous Structure (Micromegas) Detectors

One of the most prominent MPGDs is the high-rate capable Micromegas detector. It was invented by Giomataris et al. [1996].

2.1.1 Working Principle of the Micromegas Detector

A schematic of a Micromegas detector is shown in Figure 2.1. The detector is filled with gas. For the present work a gas mixture of $Ar : CO_2$ 93 : 7 Vol. % is used.
A metal micro-mesh divides the detector into two electric field regions.
In the drift region, the gas gets ionized by incoming radiation (see Chapter 1.1.1). The height of the drift region is several millimeters and a low electric field $\mathcal{O}\left(|\vec{E}_{\text{drift}}|\right) = 100 - 1000\,\text{V/cm}$ between the cathode and the micro-mesh separates the electrons and ions. Whereas the ions are guided to the cathode, the electrons are drifting to the micro-mesh (see Chapter 1.1.3). Due to the field configuration close to the mesh, more than 90 % of the electrons are guided through the micro-mesh openings to the amplification region [Lösel, 2017].
The amplification region is formed from the micro-mesh and the anode. The constant height ($\mathcal{O}\left(h_{\text{ampl}}\right) = 120\,\mu\text{m}$) of the amplification region is given by insulating pillars. A high electric field ($\mathcal{O}\left(|\vec{E}_{\text{ampl}}|\right) = 50\,\text{kV/cm}$) is applied between the micro-mesh and the anode. Electron avalanches (see Chapter 1.1.2) multiply the signal of the primary electrons. To ensure a uniform electric field and thus a uniform gain over the entire area h_{ampl} needs to be kept as uniform as possible.
The electron avalanche is collected on the anode and read out via the readout strips below. Depending on the type of Micromegas detector the anode structure differs. The different readout structures are explained in the following (see Chapter 2.1.2).

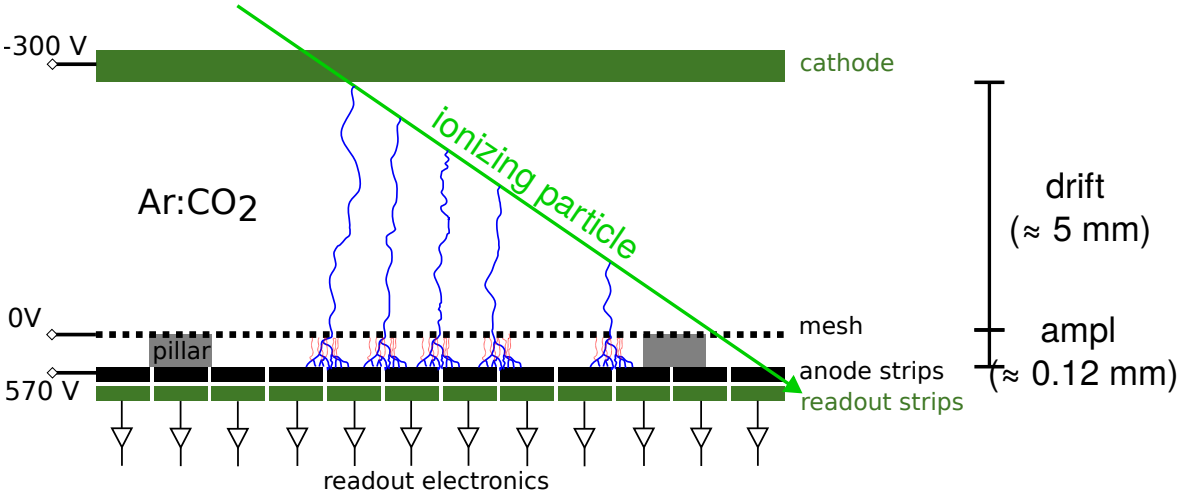

Figure 2.1: Working principle of a Micromegas detector.
A charged particle traversing the detector ionizes the gas along its path. The electrons are guided to the micro-mesh due to an electric field between the micro-mesh and the cathode ($|\vec{E}_{\text{drift}}| \approx 600\,\text{V/cm}$). Due to a high electric field ($\vec{E}_{\text{ampl}} \approx 40 - 60\,\text{kV/cm}$) between the micro-mesh and the anode, the electron transparency of the micro-mesh is over 90 %, and the number of electrons is multiplied then by Townsend avalanches (see Chapter 1.1.2).
The electrons are collected at the anode. Depending on the Micromegas type (see Chapter 2.1.2), the signal is either read out directly at a segmented copper anode or coupled to readout strips below the anode as in the case of resistive anodes.

2.1.2 Types of Micromegas Detectors

The different types of Micromegas detectors are given by different anode and readout structures.

Standard Micromegas Detector

The original Micromegas detector as it was introduced by Giomataris et al. [1996] is called standard or original Micromegas detector.
The anode is segmented into copper strips. These anode strips also act as readout strips. They are grounded via the readout electronics, whereas the micro-mesh and the cathode are set on high voltage.
In the amplification region of the detector, a high electric field below the Raether limit [Raether, 1964] is applied. This limit can be exceeded locally, e.g. if the detector is set to detect minimally ionizing muons, but strongly ionizing background particles interact with the detector. The consequence is a discharge between the micro-mesh and the anode, which strongly reduces the potential of the micro-mesh. The micro-mesh needs to be recharged. This leads to a dead time for the detector and can damage the readout electronics. Even small defects on the anode or the micro-mesh can cause local electric field peaks. Thus the Raether limit might be exceeded locally as well.
Further developments of the Micromegas detector towards floating strip or resistive type Micromegas detectors solved the discharge problem.

Floating Strip Micromegas Detector

Floating strip Micromegas detectors were introduced by the Compass experiment and optimized by Bortfeldt [2014]. Floating strip Micromegas detectors use copper strips as an anode. Separate readout strips are positioned underneath the anode strips. Both strip layers are insulated from each other. The positive high voltage is applied to the individual anode strips via large resistors R = 30 MΩ. The individual anode strips are therefore only weakly connected to each other. The micro-mesh is set to ground potential. When a local discharge occurs, only the voltage of the readout strips at the discharge position equalizes to the voltage of the mesh. The rest of the detector remains unaffected. The few discharged readout strips are recharged within 1.5 ms, which is much faster than the recharge time of a standard Micromegas detector (75 ms) [Bortfeldt, 2014].
With a floating strip Micromegas detector, it is also possible to add a second layer of readout strips to the readout structure, rotated by 90° to obtain a 2D position [Klitzner, 2019]. Klitzner [2019] understood the complicated signal formation on the lower readout strip layer and succeeded in achieving an equal pulse height and spatial resolution on both readout strip layers by strongly optimized strip shapes.

Resistive Type Micromegas Detectors

Another approach to suppress discharge effects in Micromegas detectors is the use of a resistive anode. The design with anode strips of resistive material (MΩ/cm) without any copper (see Figure 2.2), reduces the discharge-related dead time even further. The detector becomes insensitive to discharges. The readout strips are insulated and located below the resistive anode [Alexopoulos et al., 2011].
Local discharges quench quickly because the charges on the resistive anode do not flow fast enough to the discharge point. The voltage of the micro-mesh and the anode equalizes only locally. The remaining detector regions are not being affected.
With a resistive Micromegas detector, it is also possible to add a second layer of readout strips to the readout structure, rotated by 90° to obtain a 2D position.
On top of the readout strips a thin layer of insulation material like Kapton [Kap, 2023] is located. On top of this insulator, resistive strips can be screen-printed using a resistive paste. The resistive strips need to match the pattern of the readout strips [Alexopoulos et al., 2011]. For a 2D resistive strip Micromegas detector as it is used for measurements in this thesis the resistive strips are aligned with the bottom layer of readout strips as it is shown in Figure 2.2. For the Micromegas detectors recently installed at ATLAS resistive strip Micromegas are used [Kawamoto et al., 2013].

The latest development of resistive Micromegas detectors uses a continuous 10 - 100 nm thick Diamond Like Carbon (DLC) layer as the anode. The DLC is coated on an insulating Kapton[Kap, 2023] foil, which is glued on top of the readout strips (see Figure 2.3). The sheet resistance of the DLC anode for the used detector is $R_{\square} = 10\,M\Omega/\square$. The DLC layer does not need to be aligned perfectly with the resistive strips anymore.

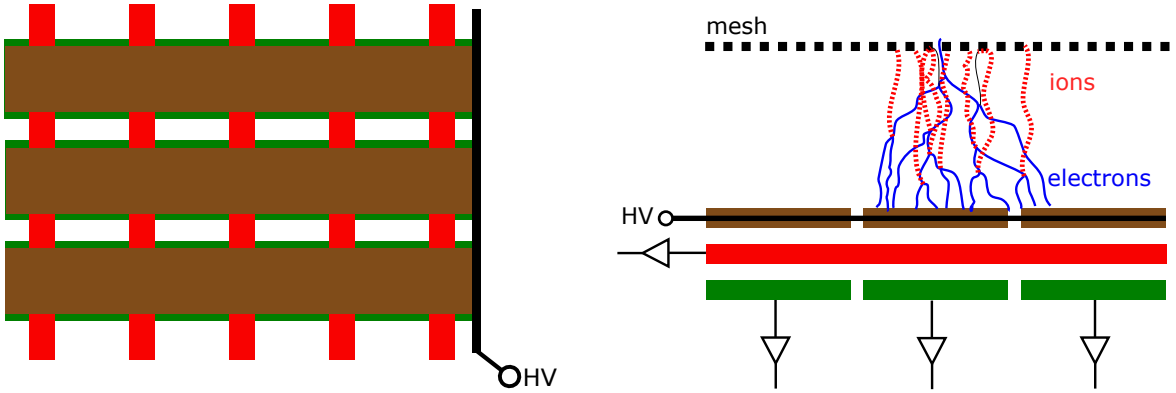

(a) View from the top. **(b)** View from the side.

Figure 2.2: Sketch of a 2D resistive strip Micromegas anode and readout structure.
The resistive strips (brown) are connected to high voltage and thus act as the anode for the detector.
Two layers of readout strips are located below the resistive strips.
The top layer of readout strips (red) is perpendicular to the resistive strips, whereas the bottom layer (green) is parallel to the resistive strips.
To prevent shielding of the signal from the bottom strip layer, the strips on the top layer have a larger gap between each other (smaller strip width at same pitch).

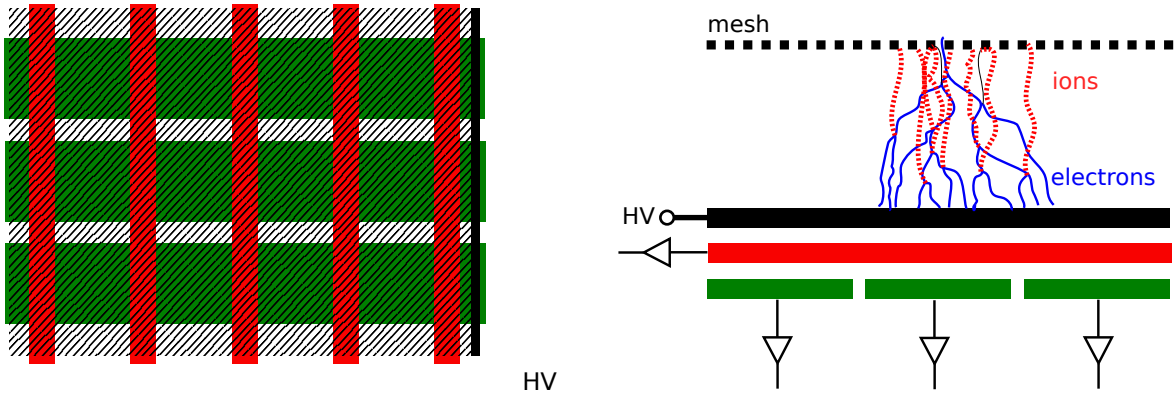

(a) View from the top. **(b)** View from the side.

Figure 2.3: Sketch of a 2D resistive DLC layer Micromegas anode and readout structure.
The resistive DLC layer (black shaded) is connected to high voltage and thus acts as the anode for the detector.
Two layers of readout strips are located below the DLC layer. Both layers of readout strips are perpendicular to each other with a typical pitch of 0.4 mm.
As for the resistive strip Micromegas detector (see Figure 2.2) the gap between the top strips is larger to prevent shielding of the signal for the bottom strip layer.

2.2 Gas Electron Multiplier (GEM) Detector

The GEM detector was introduced by Sauli [1997]. It is also a high rate capable MPGD. Internally it can be divided into three different regions (see Figure 2.4):

- A drift region, like in a Micromegas detector, where the gas is ionized by incoming radiation and the charges are separated by a low electric field $|\vec{E}_{drift}| \approx 600\,V/cm$.
- An amplification region (several GEM foils), where the number of electrons is multiplied by electron avalanches in a strong electric field $\mathcal{O}\left(|\vec{E}_{ampl}|\right) = 50\,kV/cm$ (see Chapter 1.1.2).
- An induction region between the amplification region and the anode, where the charge movement due to a low electric field E_{induct} induces a signal on the readout strips. The readout strips act as an anode as well.

The key component of the GEM detector is the GEM foil, in which the amplification process takes place. A GEM foil is a thin polymer foil metalized on both sides. Small holes $\mathcal{O}\left(r_{hole}\right) = 25 - 50\,\mu m$ are etched via a lithographic production process into the foil. The holes are arranged in a regular pattern (see Figure 2.5). The foil is glued to a thin frame to stiffen its structure.
Between the top and the bottom side of the GEM foil a high voltage ($\mathcal{O}\left(U_{GEM}\right) = 300\,V$) is applied causing a high electric field ($\mathcal{O}\left(\vec{E}_{GEM}\right) = 60\,kV/cm$). Due to the funnel-shaped electric field configuration above the holes towards the drift region (see Figure 2.6) the electrons are guided from the drift region into the GEM holes. Inside the holes, the electrons are multiplied by electron avalanches (see Chapter 1.1.2) typically by a factor of 20. The avalanche electrons are exiting the GEM foil into the induction region $\mathcal{O}\left(h_{induct}\right) = mm$, where a low electric field ($\mathcal{O}\left(\vec{E}_{induct}\right) = kV/cm$) causes the electrons to drift to the readout strips. While the electrons are drifting toward the anode they induce a signal on the readout strips.
To avoid discharges inside the GEM foil, a stack of typically three GEM foils alternating with drift regions is used. Each GEM foil can be operated at relatively low voltages. The total gain, which reaches values up to 10,000, can thus be increased compared to a single GEM detector [Sauli, 2016].

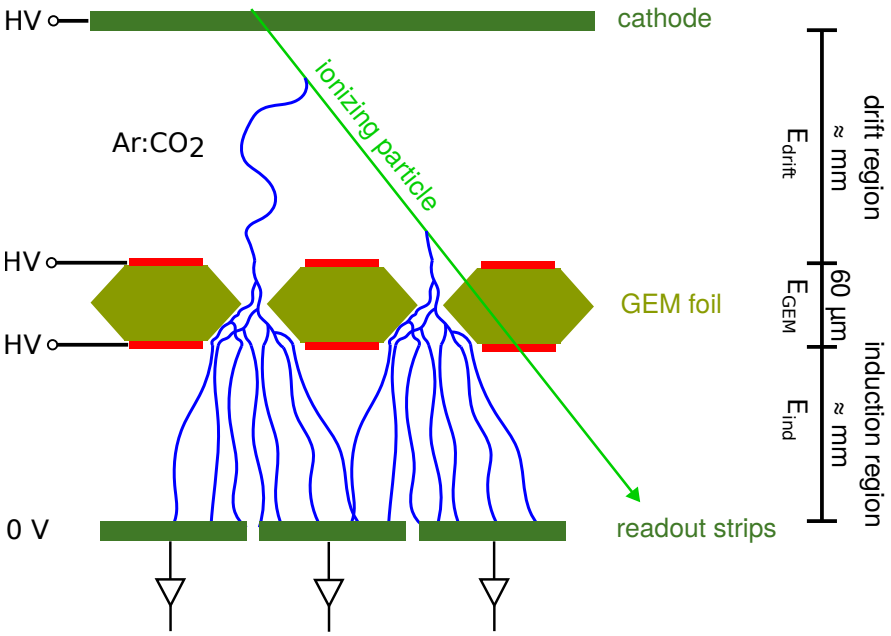

Figure 2.4: Schematic working principle of a GEM detector.
A charged particle traversing the detector ionizes the gas along its path. The electrons are guided due to the electric field between the top side of the GEM foil and the cathode ($|\vec{E}_{\text{drift}}| \approx 600\,\text{V/cm}$) towards the GEM foil. Similar to a Micromegas detector, the field lines bend near the holes and form a funnel that guides the electrons through the holes (see Figure 2.6).
Due to a high electric field ($\mathcal{O}\left(|\vec{E}_{\text{GEM}}|\right) = 60\,\text{kV/cm}$) between the top and bottom side of the GEM foil, the number of electrons is multiplied in the holes of the GEM foil by avalanches (see Chapter 1.1.2). Usually, multiple GEM foils are stacked with a distance of a few millimeters, to obtain a high enough gain without applying too high fields to a single GEM foil [Sauli, 2016].
An electric field $\vec{E}$ guides the electrons from the last GEM foil to the readout strips. Due to the charge movement, a signal is induced on the readout strips which are read out by the readout electronics.

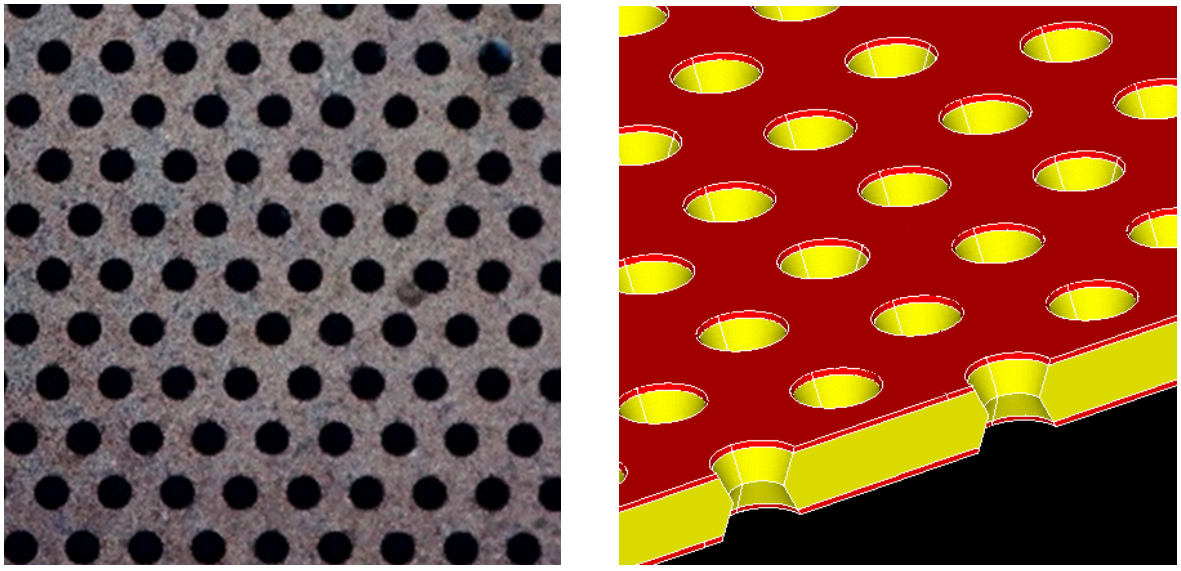

(a) Photograph of a GEM foil (viewed from the top).

(b) Schematic picture of a GEM foil.

Figure 2.5: A GEM foil are two layers of 5 µm copper (red) isolated by 50 µm Kapton (yellow). The holes have a distance of 140 µm. The holes are double cone-shaped. The outer diameter of the holes is 70 µm. At the narrow, the cone diameter is reduced to 50 µm. The electron avalanches are created inside the holes due to an electric field between both copper layers.

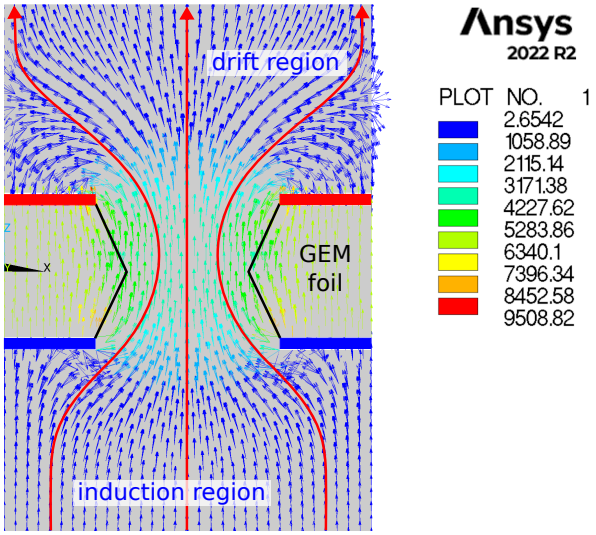

Figure 2.6: Electric field configuration of a GEM foil.
For visualization reasons, some field lines are sketched in this figure (red). The magnitude of the electric field is not proportional to the field line vector density. It is given by the color coding of the vectors [V/mm].
Inside the GEM holes the electric field is much higher than in the drift region or the induction region. Funnel-shaped field lines guide the electrons through the GEM holes.
$|\vec{E}_{induct}| = 3\,kV/cm$, $U_{GEM} = 300\,V$, $|\vec{E}_{drift}| = 600\,V/cm$.

2.3 Segmented GEM Readout Detector (SGR)

The SGR detector is a hybrid of a pre-amplifying GEM foil and a resistive DLC layer Micromegas detector. The goal of the SGR detector is to achieve more than two position information by reading out the signal of the Micromegas detector at the position of the micro-mesh as well. The signal at the micro-mesh position is expected to have approximately the same pulse height as the top readout strip layer signal.

2.3.1 Working Principle of the SGR detector

A segmentation is needed to read out a position-sensitive signal at the position of the micro-mesh. Since a segmented micro-mesh is difficult to realize it is replaced by a GEM foil. A GEM foil is produced lithographically. Therefore it is possible to include a segmentation in the copper of the GEM foil (see Chapter 2.3.2).
A sketch of a SGR detector is shown in Figure 2.7. Instead of the micro-mesh the GEM foil directly lies on the pillars of the Micromegas readout structure.
The new detector has two amplification steps that merge into each other.
The first amplification step takes place inside the GEM foil (see Chapter 2.2). The number of electrons is multiplied there by a factor up to 20.
The second step takes place in the Micromegas amplification region between the bottom side of the GEM foil and the DLC anode. Most of the charges are created in this second amplification step. Therefore almost the same number of electrons is reaching the DLC anode as ions are reaching the bottom side of the GEM foil.
The configuration of the electric field can be chosen such that either most of the ions end on the bottom side of the GEM foil or its top side. This will be shown in the next chapters.
The use of the pre-amplifying GEM foil allows operating the detector at relatively low GEM voltages (U_{GEM}) and relatively low anode voltages (U_{ampl}) and thus at safe operating conditions.

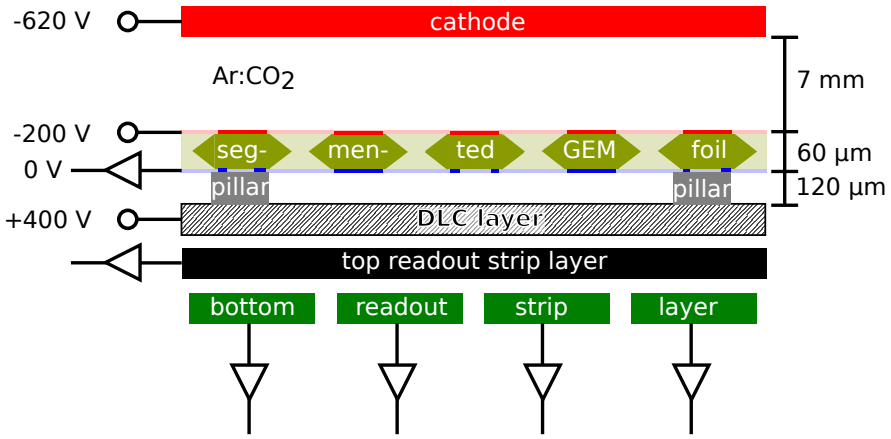

Figure 2.7: Schematic picture of the SGR detector.
The micro-mesh of a Micromegas detector (see figure 2.1) is replaced by a GEM foil (see Chapter 2.2). The GEM foil lies directly on top of the pillars. One side (or both sides) of the GEM foil is segmented into strips. These strips are read out by the same readout electronics as the Micromegas readout strips (see Chapter 2.3.2).

2.3.2 Segmented GEM Foil

The segmented GEM foil (SGR foil) is the key component of the SGR detector. It is a standard GEM foil with the typical dimensions as explained in Figure 2.5. The difference is that the copper on one side of the foil is segmented into strips (see Figure 2.8). The Kapton and the other metal side remain unaffected by the segmentation. In this work foils with a segmentation on the top or the bottom side are investigated.
The latest measurements have also investigated a SGR foil that is segmented on both sides. The periodicity of the GEM strips (pitch) is four GEM holes respectively 484 µm. The spacing between the strips is snakelike so that all holes are surrounded by copper on all sides. The spacing between the strips has a width of 20 - 40 µm. The GEM holes are located in the active area only.
The strips are routed from the active area to the outside of the gas volume. Each strip is soldered to a pin of a connector[1], where the readout electronics is plugged in.
To ensure that the foil lies directly on the pillars of the anode, the stretched foil is glued to a 4 mm thick frame on one side only.
In each corner of the frame, the SGR foil is screwed onto the anode structure.

[1] Panasonic AXK6SA3677YG

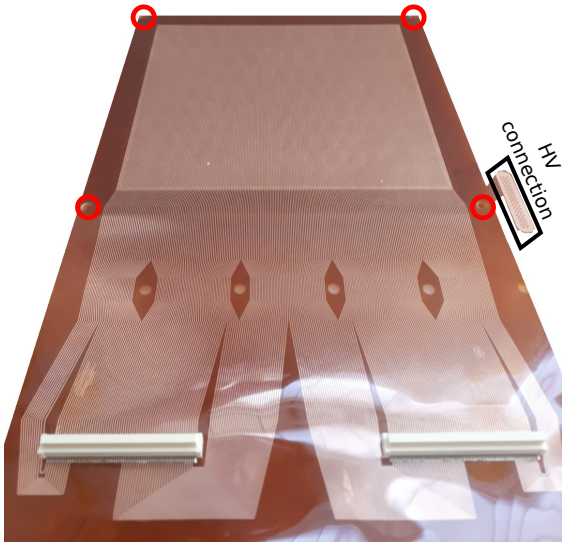

(a) Photograph of a segmented GEM foil.
At the marked positions, holes are located to mount the foil on the Micromegas anode.

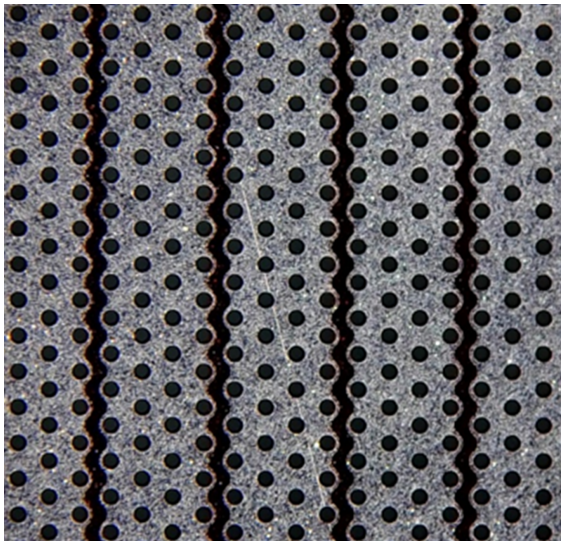

(b) Photograph of a segmented GEM foil, taken with a Microscope.
The Segmentation of the copper layer is visible.

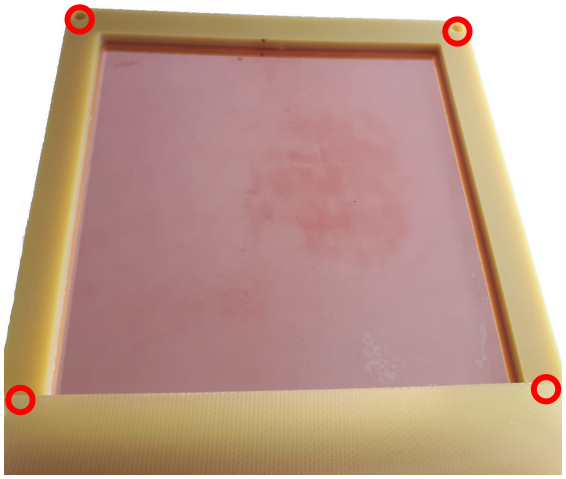

(c) Photograph of the non-segmented side of a segmented GEM foil.
This side is glued to the supporting frame.
At the marked positions, holes are located to mount the foil on the Micromegas anode.

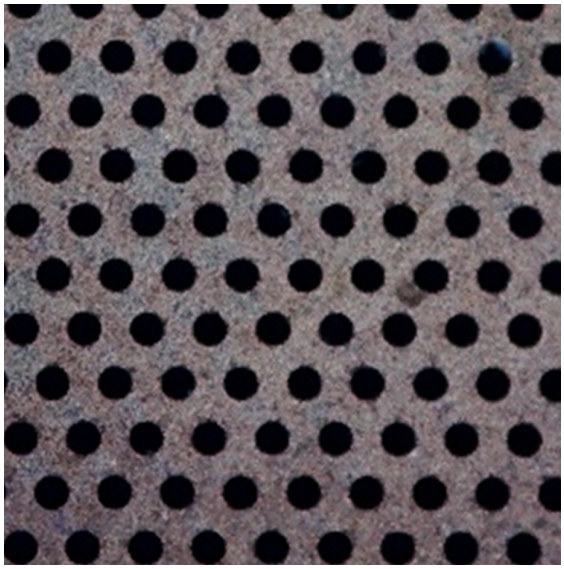

(d) Photograph of the non-segmented side of a segmented GEM foil, taken with a Microscope.

Figure 2.8: Pictures of the segmented GEM foil (only one side is segmented).
One side of the foil is segmented in strips, which are guided to connectors for the readout electronics (figures 2.8a and 2.8b).
The other side looks like a standard GEM foil (figures 2.8c and 2.8d).
To stretch the foil a 4 mm thick frame is glued on the top side of the GEM foil (in this case the not segmented side). No frame is mounted on the bottom side of the foil.

2.3.3 Construction of the SGR Detector

In all four corners of the frame (see Figure 2.8) the SGR foil is screwed onto the anode and readout structure. The side without the frame faces towards the anode (see Figure 2.9). The SGR foil lies along its frame on the coverlay, of the anode structure. The coverlay is an insulating layer outside the active area of the Micromegas anode. It is made of the same material as the pillars and shows the same height as them.
In the area where the foil is glued to the frame a slightly uneven surface is observed. To ensure the same height everywhere in the amplification gap of the Micromegas an additional press frame is pressing the foil onto the coverlay of the Micromegas readout structure. A layer of rubber is attached to the bottom side of the press frame to compensate for the unevenness of the press frame. This ensures that the GEM foil lies uniformly on top of the pillars.
The Kapton foil with the readout strips is guided out of the gas frame on an FR4[2] sheet. With a distance of 7 mm to the GEM foil, the cathode is mounted.

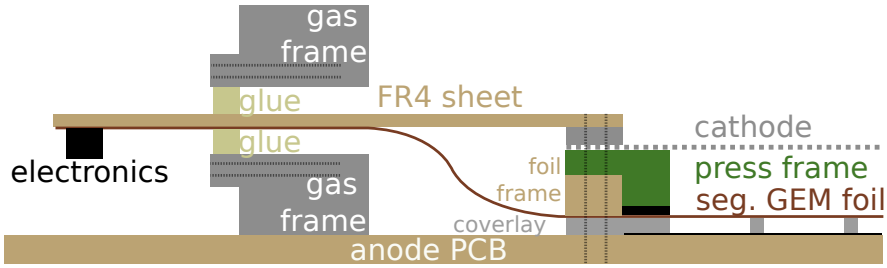

(a) Schematic picture of the mounted SGR foil.

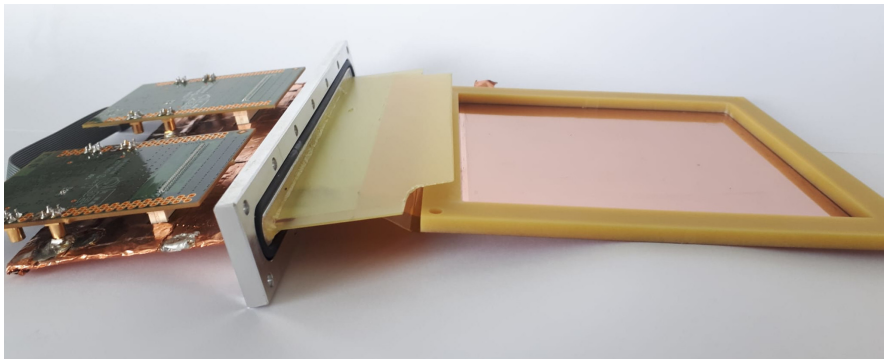

(b) Photograph of the mounted SGR foil (Micromegas anode and gas frame are not shown).

Figure 2.9: Mounted SGR foil.
The foil is guided out of the gas frame through a 4 mm high slit. To support the foil, it is glued onto a 0.5 mm thick FR4 sheet. The foil and the supporting FR4 are glued into a flange which is screwed onto the gas frame. An O-ring (not drawn) between the flange and the gas frame ensures gas tightness.
On the four corners of the frame, the GEM foil is pressed by screws to the anode structure. The cathode is also mounted by the same screws with a distance of 7 mm to the GEM foil.

[2]FR4 is a glass-reinforced epoxy laminate material, which is commonly used as PCB material.

2.3.4 Motivation for the Development of the SGR Detector

In MPGDs the signal is most commonly read out via readout strips. With one layer of readout strips, it is easily possible to determine a one-dimensional hit position of a traversing particle (see Chapter 3.6). By adding a second layer of readout strips below the top layer (see Figure 2.10), the signal couples on both readout strip layers. Usually, both readout strip layers are separated from each other by an insulating layer, i.e. Kapton [Kap, 2023]. Two one-dimensional positions are reconstructed, one on each readout strip layer. Combining both 1D positions gives a unique 2D position for single particles traversing the detector.

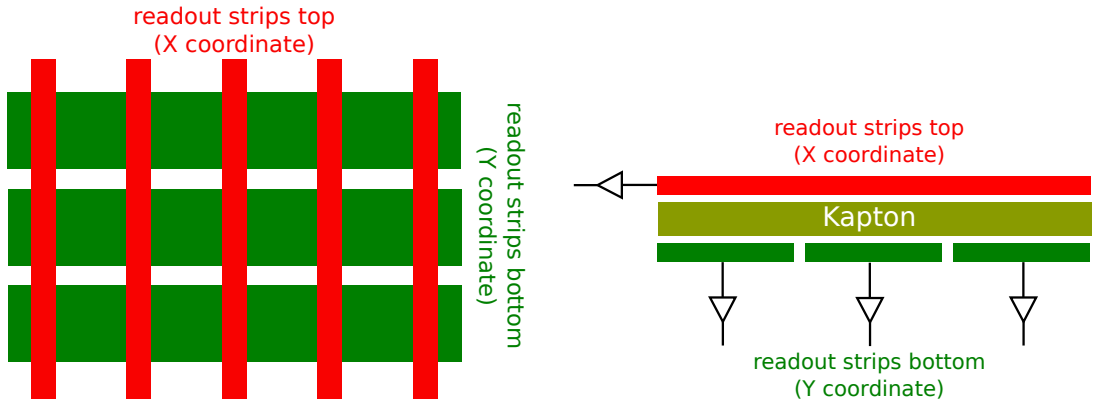

(a) View from the top.
The insulating Kapton layer between both readout strip layers is not shown.

(b) View from the side.
Both readout strip layers are insulated from each other by a layer of Kapton

Figure 2.10: Sketch of the readout structure of a 2D strip readout.
The X strips are located above the Y strips. Kapton [Kap, 2023] between the layers is used for insulation.

Multi Particle Reconstruction

If multiple particles are detected at the same time it is not possible to reconstruct a unique 2D position with one single 2D strip detector. It is not clear which X-position should be assigned to which Y-position (see Figure 2.11a).
If, for instance like in Figure 2.11a, four particles induce a signal in the detector at the same time, four particle positions are reconstructed by each individual readout strip layer. This results in 16 possible hit position combinations.
Using a telescope consisting of multiple detectors one can reconstruct unique 2D positions using iterative reconstruction algorithms like a Kalman-filter-based track reconstruction as described in [Klitzner, 2019].
For events with multiple hits, e.g., when multiple photons occur in only a single detector, this reconstruction algorithm does not work. Low energy photons interact via the photoelectric effect (see Figure 1.2). They cannot be detected by multiple detectors in coincidence.
This is the case in a Cherenkov Ring Imaging MPGD detector [Rinnagel, 2022]. In this detector, Cherenkov photons are emitted in a LiF crystal, which is located above the cathode. A CsI photocathode is evaporated onto the radiator, which also acts as a cathode for the MPGD. In the photocathode, the Cherenkov photons release electrons by the photoelectric effect. These electrons are entering the active volume of the detector. They correspond to the primary charges in the detector, which are otherwise generated due to the ionization of the gas.
The goal of this detector is to simultaneously measure the momentum and position of travers-

ing cosmic muons. The Cherenkov angle depends on the particle momentum. To determine the Cherenkov angle (and so the momentum of the incoming muon) the 2D position of almost all photoelectrons needs to be reconstructed.
One way to achieve this is to use a pixelated readout structure. This leads to a huge demand for readout channels. For example, at least 1200 pixels with a size of 1 mm × 1 mm are needed to resolve a Cherenkov cone with radius r = 2 cm.
Another approach is to use a third (and fourth) layer of readout strips which is turned by 45° to the other two readout strip layers [Jagfeld et al., 2023]. A particle creates a signal on all three (or four) readout strip layers. For each particle, exactly one 2D position is reconstructed where the signals on all three (or four) readout strips overlap (see Figure 2.11b).
For each readout strip layer 40 strips with a periodicity of 250 µm are needed to resolve a Cherenkov cone with radius r = 2 cm.

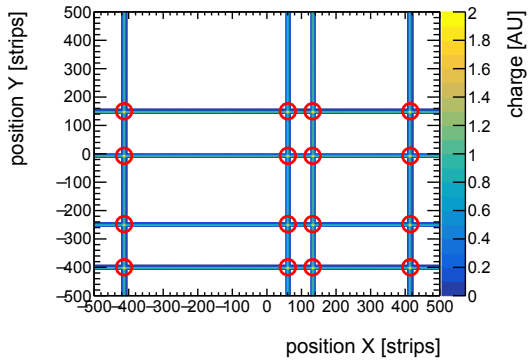

(a) Hit of 4 particles at the same time on an X, Y detector.
The reconstruction of a 2D position is not clearly possible. 16 different positions are possible to be reconstructed.

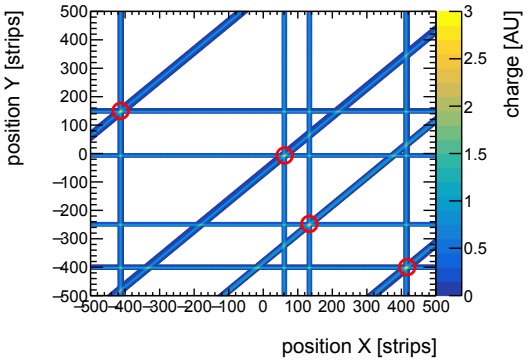

(b) Hit of 4 particles at the same time on an X, Y, U detector.
The reconstruction of a 2D position is clearly possible. Only at four positions, a hit is observed in all readout strip layers.

Figure 2.11: Simulation of an event with four particles hitting the detector simultaneously. All signals show the same pulse height for this simulation.

The number of ambiguities decreases with an increasing number of readout strip layers (see the simulation in Figure 2.12). With X and Y readout strips only 10 % of 14 incident particles are reconstructed correctly. This fraction increases to 40 % for using X, Y, and U strips. With four readout strip layers (X, Y, U, V), more than 90 % of 14 incident particles are reconstructed correctly. Using other parameters like the exact pulse height of each signal and the exact timing improves this factor.
Due to the big variation of the pulse height for the different readout layers (see Chapter 6.6.2) it is not possible to add the rotated readout strip layers below the bottom readout strip layer in a single readout structure. The newly added readout strip layer would only detect signals of very low pulse height.
In a SGR detector one or two readout strip layers are added at the position of the micro-mesh of a standard resistive type Micromegas detector. As it is very difficult to segment a micro-mesh, the micro-mesh is replaced by a segmented GEM foil (see Chapter 2.3). The new layers of readout strips can also be rotated by any desired angle. The production of an X, Y, U, V SGR detector is possible.
A prototype of such a SGR detector was built with the third readout layer being parallel to the top strip layer on the readout structure.

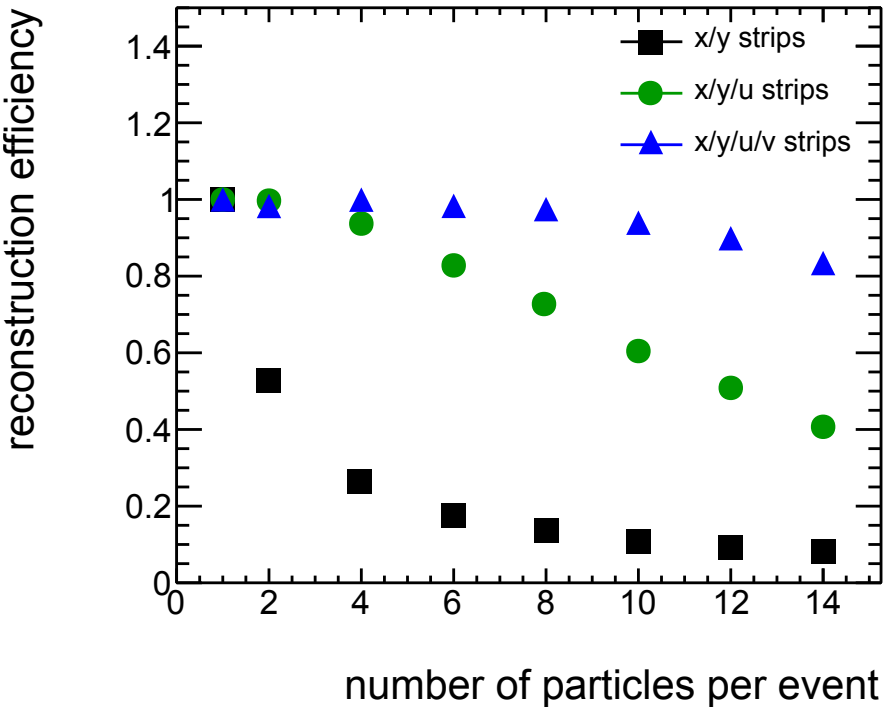

Figure 2.12: Fraction of correct reconstructed 2D events in dependence of the number of particles per event for different readout strip setups (simulation).
In this simulation, it is assumed that all particles arrive at exactly the same time and that the induced pulse height of all particles is identical. The used periodicity of the X and Y strips is 250 µm. For the U and V strips, it is 500 µm. A signal width of 1.5 mm (6 X / Y strips) is assumed. Each readout strip layer is assumed to be 100 % efficient

Pulse Height on the Different Readout Strip Layers

For a readout structure as shown in Figure 2.10 with two layers of readout strips on top of each other the pulse height on both readout strip layers differs if the width of the strips is not exactly adapted (see Chapter 6.6.2). A large difference in pulse height is problematic for the readout electronics. The readout electronic is only sensitive in a certain pulse height range. If both readout strip layers do not have a pulse height in the sensitive range of the readout electronics, the efficiency and accuracy of the reconstruction of 2D positions decrease.
For the SGR detector, the pulse height of the newly added GEM readout strips is approximately identical to the top layer of readout strips in a readout structure as shown in Figure 2.3 (see Chapter 7.5.2).
The 2D position reconstruction improves thus by obtaining one coordinate from the newly added readout strip layer, and the other one from the top strip layer of the standard readout structure.

2.4 Overview of the Detectors used in this Thesis

In this section, the MPGDs used in this thesis are summarized. Schematics of the detectors used are shown in Figure 2.13.
The various detectors differ only in nuances. However, the signal shape varies significantly.
The signals of the top and bottom Micromegas readout strips are strongly dependent on the choice of the anode structure (compare Figure 2.14a and Figure 2.14b).
The signals of GEM strips differ strongly depending on whether the GEM foil is segmented on the bottom side or top side (compare Figure 2.14c and Figure 2.14d).
Besides the amplitude, the signal shapes of the detector layers differ significantly. Therefore, capacitive coupling between the individual readout strip layers plays only a minor role in the signal creation[3]. The signal creation process differs for the individual readout strip layers.
In Chapter 5 a detailed simulation of all processes relevant to signal generation is presented. The simulated results are successfully compared with measurement data.
An energy resolution of up to 10 % is achieved with the DLC layer Micromegas detector (see Chapter 6) and with the SGR detector (see Chapter 7).
A spatial resolution better than 80 µm for perpendicularly traversing 120 GeV muons is presented in Chapter 9. The angle of muons passing through the detector at an angle of $\Theta = 20°$ is reconstructed with an accuracy of $\Delta\Theta = ^{-2°}_{+3°}$. The corresponding spatial resolution is approximately 155 µm.

[3] If capacitive couplings were predominant, the signal shapes would be the same on all readout strip layers.

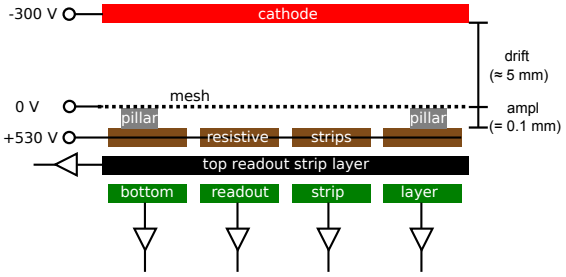

(a) Resistive strip Micromegas detector (see chapter 2.1.2).

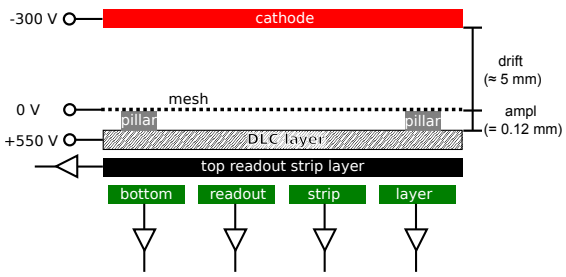

(b) DLC layer Micromegas detector (see chapter 2.1.2).

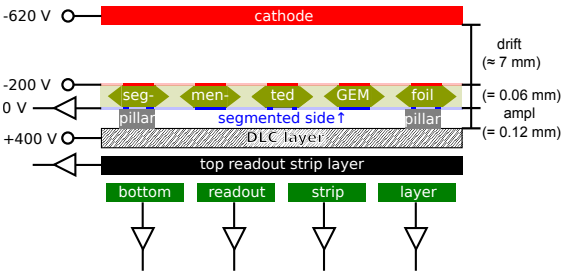

(c) SGR detector with the segmentation on the bottom side of the segmented GEM foil (see chapter 2.3).

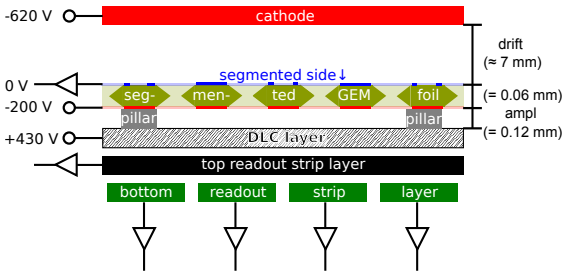

(d) SGR detector with the segmentation on the top side of the segmented GEM foil (see chapter 2.3).

Figure 2.13: Detector structures used in this thesis.

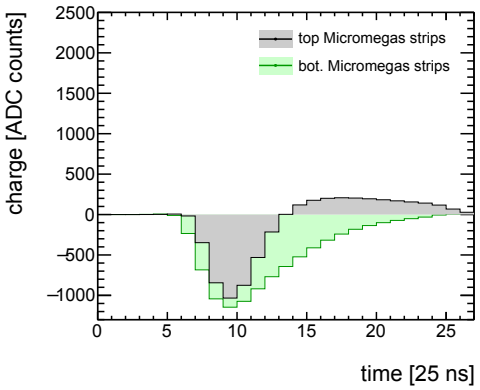

(a) Signal of the resistive strip Micromegas detector (see Figure 2.13a).

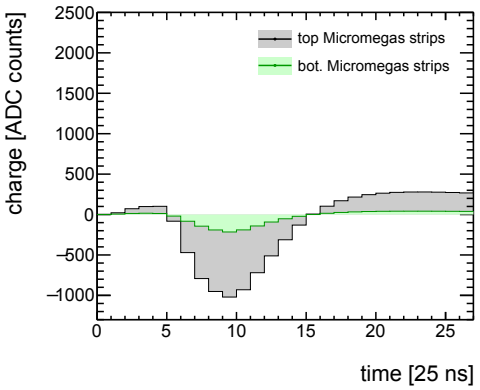

(b) Signal of the DLC layer Micromegas detector (see Figure 2.13b).

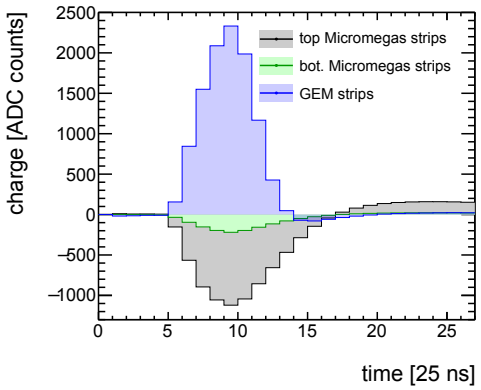

(c) Signal of the SGR detector with the segmentation on the bottom side of the segmented GEM foil (see Figure 2.13c).

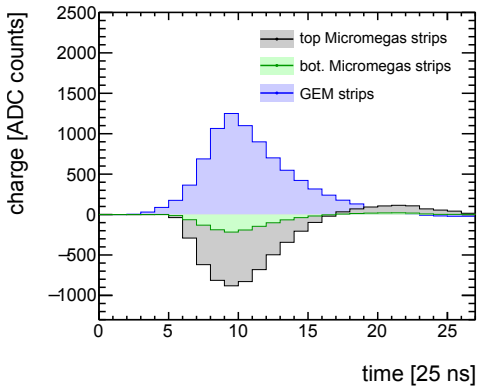

(d) Signal of the SGR detector with the segmentation on the top side of the segmented GEM foil (see Figure 2.13d).

Figure 2.14: Signal shapes of the detector structures used in this thesis. The voltage combinations used are the same as shown in Figure 2.13.

Chapter 3

Tools and Methods for the Measurement of the Detector

In this chapter, the components of a typical measurement setup are explained as well as the general techniques of the analysis of the measured data.

3.1 Used Detector Structures

In this work, all the detector structures used are based on the Micromegas principle. All of them use resistive type Micromegas anode and readout structures[1].
The SGR detector is investigated with up to four resistive strip Micromegas detectors used to determine a reference track.
In addition, the SGR detector is compared to a Micromegas detector that uses the same readout structure as the SGR detector.
The typical layout of all anode structures used is shown in Figure 3.1. The readout structures are lithographically produced PCBs. The resistive anode and pillars are subsequently added to the PCB.
All investigated readout structures provide a 2D readout. Each readout strip layer consists of 360 readout strips (see Table 3.1) connected to three 130-pin connectors[2] each.
Both readout strip layers have the same pitch. The width of the strips is smaller for the top readout strip layer. The size of the active area is $A_{active} = 9\,cm \times 9\,cm$. It is given by the number of readout strips.

Measurements are mostly performed using a resistive DLC layer anode structure (see Figure 3.1). The DLC layer anode structure used is a floating mesh structure, meaning there is no micro-mesh integrated on top of the pillars. The mesh, or as in our case the SGR foil, is mounted on a separate holding frame and can be removed.
The pillars are arranged in a periodic triangular pattern with a periodicity of p = 7 mm. The

readout strip layer	number of strips	pitch	strip width	strip gap
top readout strip layer	360	250 µm	100 µm	150 µm
bottom readout strip layer	360	250 µm	220 µm	30 µm
SGR foil	212	484 µm	444 - 464 µm	20 - 40 µm

Table 3.1: Parameters of the different readout strip layers.

[1] In the following, this is referred to as either anode or readout structure.
[2] Panasonic AXK6SA3677YG

pillars have a size of 1.2 mm × 0.2 mm. The height of the pillars is h_{ampl} = 120 µm. It defines the height of the gain gap.
The SGR foil has an active area of A_{active} = 10 cm × 10 cm. Since this is larger than the active area of the readout structure, the outermost strips of the foil lie on the insulating coverlay. As described in chapter 2.3.3 the SGR foil is pressed in this region to the coverlay.

The four reference tracking detectors are standard resistive strip Micromegas detectors. The readout structure of these detectors is a bulk structure, which means the micro-mesh is laminated into the pillars [Giomataris et al., 2006]. The pillars are arranged in a square pattern with a periodicity of p ≈ 2.5 mm. They are cylindrically shaped with a diameter of ≈ 300 µm. Since the micro-mesh is laminated into the pillars at a distance h_{ampl} = 100 µm from the anode it can not be replaced.
The properties of the detectors used differ as shown in Table 3.2.

	SGR	DLC layer MM	resistive strip MM (tracking detectors)
anode structure	DLC layer	DLC layer	resistive strips
readout strip layers	bot. MM strips (Y) top MM strips (X) GEM strips (Y) (GEM strips 2^{nd})	bot. MM strips (Y) top MM strips (X)	bot. MM strips (Y) top MM strips (X)
mesh/SGR foil	SGR foil	micro-mesh	micro-mesh
height of the drift region	7 mm	5 mm	5 mm
applied $\lvert\vec{E}_{drift}\rvert$ applied U_{drift}	600 V/cm 420 V	600 V/cm 300 V	600 V/cm 300 V
height of the amplification region	60 µm (SGR foil) + 120 µm (MM ampl.)	120 µm	100 µm
amplification steps	SGR foil MM amplification	MM amplification	MM amplification
adjustable voltages	U_{ampl} U_{GEM} U_{drift}	U_{ampl} U_{drift}	U_{ampl} U_{drift}

Table 3.2: Differences between the different detectors used.
The parameters of the readout strip layers are shown in Table 3.1.

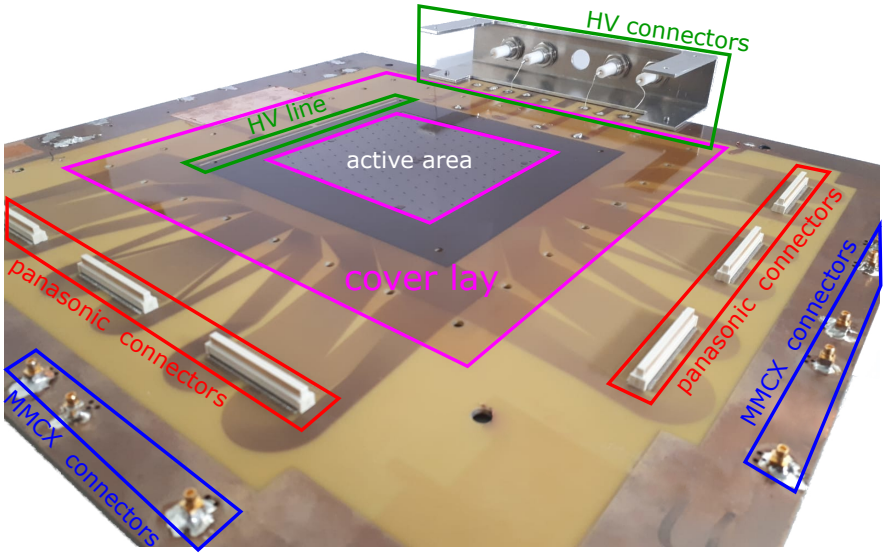

Figure 3.1: Photo of the used DLC layer Micromegas readout structure.
The front-end readout electronics can be connected to the readout strips via the Panasonic connectors. The ground potential for the front-end readout electronics is provided via MMCX connectors. HV is provided to the resistive layer/strips via an HV line which is connected to the HV connectors.
The gas housing, mesh/GEM foil, and cathode are not shown.

3.2 Readout Electronics

For the measurements performed in this thesis, the detectors are read out by a Scalable Readout System (SRS) using APV25 chips on hybrid boards (see Figure 3.2). The SRS system is split into multiple parts as explained in [Baek et al., 2012]:

- The front-end hybrid board carrying the APV25 Application Specific Integrated Circuit (ASIC)
- The Analog to Digital Converter (ADC) adapter card
- The Front End Concentrator (FEC) card
- The Scalable Readout Unit (SRU)
- A Data AcQuisition (DAQ) PC

Besides discharge protections and power regulators, the front-end hybrid board is carrying the APV25 readout ASIC. The APV25 readout chip is an analog 128 channel ASIC which was originally designed for the CMS silicon tracker. It shapes and pre-amplifies the detector signal [Jones et al., 1999]. With the APV25 readout chip, the signal shape is sampled in 27-time bins, each 25 ns wide. The pulse height recorded by an APV25 channel saturates at approximately 1500-1800 ADC counts (see Figure 6.13). The hybrid board is connected to the detector via a 130-pin Panasonic connector[3]. The readout strips are connected to the ground potential via the APV25 hybrid boards. Two APV25 hybrid boards can be connected in a master-slave configuration.
Each master-slave pair is connected via one HDMI cable to the ADC card. In the ADC card the analog signal is digitized. A maximum of eight HDMI cables or 16 APV25 hybrid boards can be connected to one ADC card.

[3]Panasonic AXK5SA3277YG

The ADC card is connected via PCIe connectors to the FEC card. "It carries out all operations required for the control of the front-end and data acquisition." [Baek et al., 2012]
The FEC card is connected to the DAQ PC via an Ethernet cable. If multiple FEC cards are used, an SRU module is used to synchronize all FEC cards.

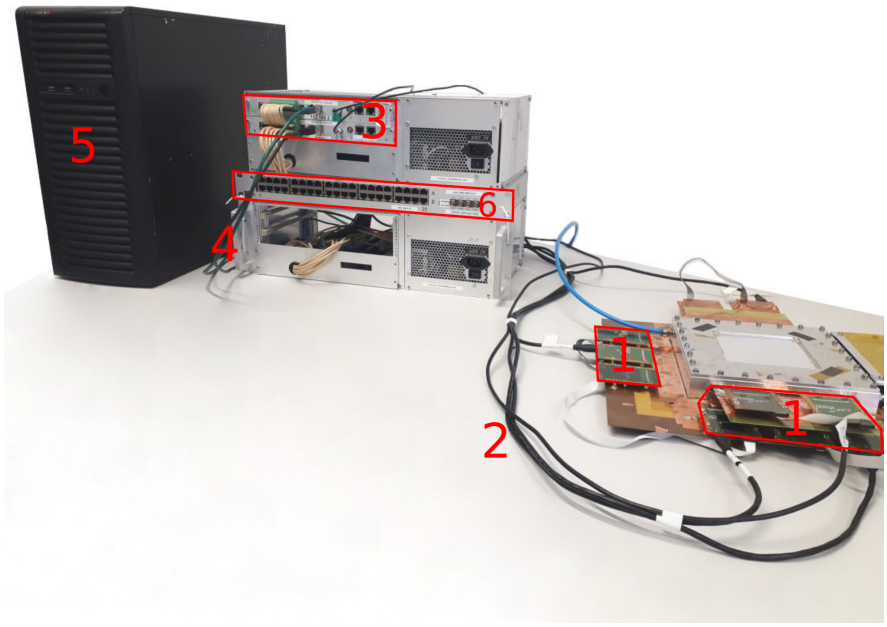

Figure 3.2: Photo of the SRS system used for a SGR detector.
The marked components of the SRS are: 1. APV25 hybrid boards, 2. HDMI cables connecting the APV25 hybrid boards with the ADC card, 3. ADC and FEC mounted in a mini crate (power supply), 4. Ethernet cables connecting the FEC card with the DAQ PC (5), 6. SRU

3.3 Adapter Board for Noise Reduction

When the detector is tested using radioactive nuclides, the pre-amplified micro-mesh signal or the signal of the non-segmented side of the SGR foil is usually used as the trigger signal. If the readout electronics receive a trigger signal the detector is read out. This procedure works fine for Micromegas and GEM detectors. The setup for such measurements is explained in chapter 6.1.
No trigger signals are expected if no source irradiates the detector. This holds for the SGR detector if the readout electronics is switched off (see Table 3.3). When the readout electronics are turned on and configured, a fake trigger rate of $f_{noise} \approx 1\,kHz$ is observed. This is only observed when the SGR foil is connected to the readout electronics.

		without adapter board	with adapter board
FEC off	no source	0	0
	source	1121.9 ± 0.5	936.2 ± 0.8
FEC on	no source	4201.4 ± 2.2	32.3 ± 0.3
	source	4739.0 ± 1.8	922.7 ± 1.1

Table 3.3: Trigger rates at same trigger threshold using a Fe55 γ – source. All values are shown in Hz.
The noise/wrong trigger originates from the SRS. When the SRS is switched off no noise is detected at the selected trigger level, when the SRS is switched on a few kHz of noise is detected. Using the adapter board the noise is reduced.
$U_{drift} = 420\,V$, $U_{GEM} = 200\,V$, $U_{ampl} = 420\,V$.

The fraction of noise coupled to the trigger signal is depending on the capacitance between the trigger layer and the nearest readout layer (see Table 3.4). Assuming the detector can be regarded as a plate capacitor, the C is given by:

$$C = \epsilon_0 \epsilon_r \frac{A}{d} \tag{3.1}$$

with the electric field constant ϵ_0, and the relative permittivity $\epsilon_r \approx 1$ for gas and $\epsilon_r \approx 3.5$ for Kapton. A is the area and d the distance between both areas.

As shown in Table 3.4 the capacitance between the trigger layer and the closest readout layer is ≈ 8 times higher for the SGR detector as for the Micromegas detector. More disturbing signals couple from the readout chip to the trigger layer.

detector	trigger layer	nearest ro-strip layer	capacitance
SGR	top side of the SGR foil	bottom side of the SGR foil (all strips)	6 nf
Micromegas	micro-mesh	top readout strips (all strips)	0.74 nf

Table 3.4: Calculated capacitances between the trigger layers and the closest readout layers.
The capacitances are calculated assuming the detector can be approximated as a plate capacitor (see Equation 3.1). The calculated capacitances are multiplied by $(1 - \textit{optical transparency})$ to obtain the capacitance of the micro-mesh and SGR foil, respectively.

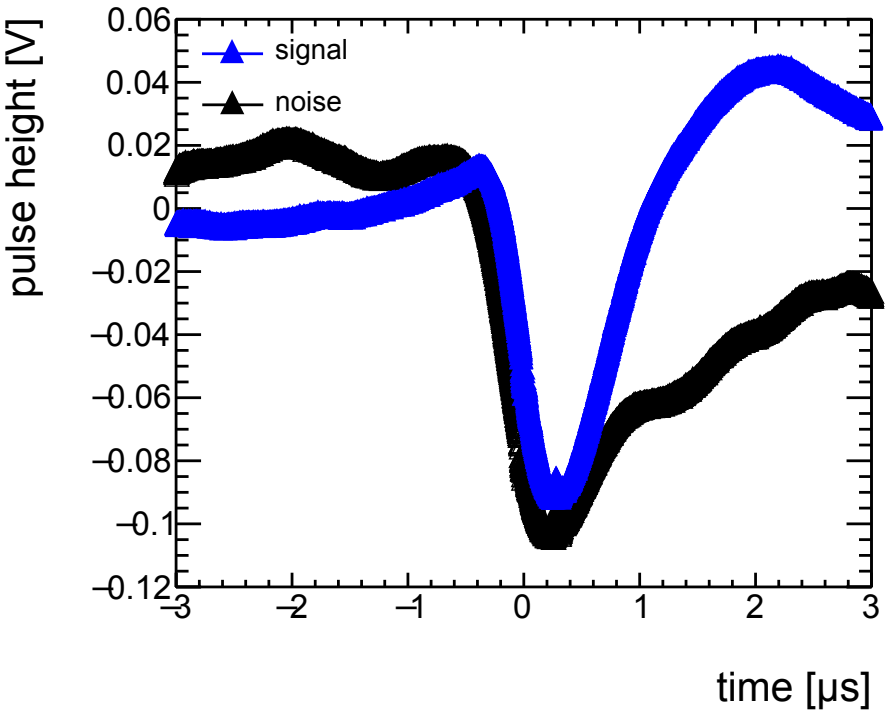

Figure 3.3: Pre-amplified trigger signal and pre-amplified noise recorded with an oscilloscope. The falling edge of the signal is used to trigger. It has the same shape as the noise.

For a reasonable gain in the SGR detector, the amplitude of the noise is in the same range as the amplitude of the signal (see Figure 3.3). It is not possible to trigger only on signal and not on noise.

If an external trigger signal is used, e.g. a scintillator signal of a traversing muon, data can be recorded without any impact from noise. The noise level recorded with the SRS (see Figure 3.7) is very low at 15-20 ADC counts and significantly lower than the recorded heights of the individual strip signals (several hundred ADC counts).
Therefore, it can be assumed that the observed noise is only a disturbing signal that couples from the readout electronics to the trigger signal. The signals of the SGR detector measured with the SRS are not affected by this noise more than the signals of a typical Micromegas detector.
A method has to be found to ensure that a trigger signal is obtained which is not influenced by noise.
Since the shape of the trigger signal and the noise are very similar (see Figure 3.3), it is not possible to construct a frequency filter for the trigger signal to distinguish between noise and signal.

The coupling of noise to the trigger signal must be prevented. To do so an adapter board with a high pass filter between each APV25 channel and each readout strip is constructed (see Figure 3.4). It prevents noise from the chip from coupling to the readout strips. In return, the pulse height of the read-out strip signal is reduced (see Figure 3.6).

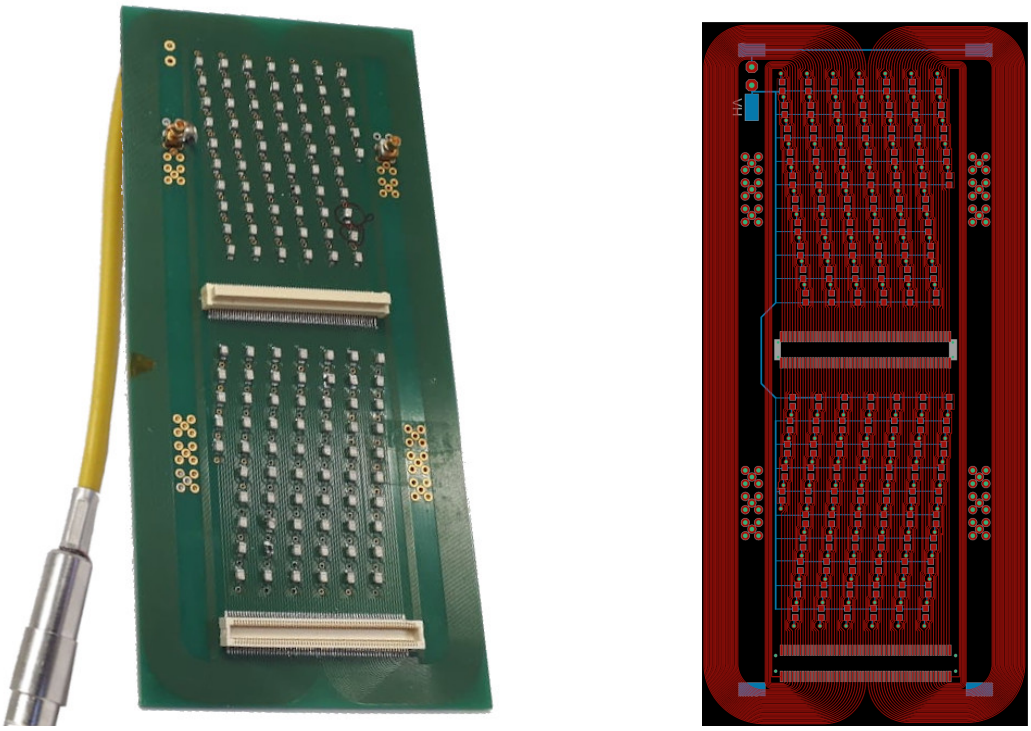

(a) Photo (left) and Gerber file (right) of the adapter board looking on the top side, where the capacitors of the high pass filter are located. The resistors are placed on the bottom side of the board (not shown). The APV25 hybrid board and the detector can be connected via two connectors (Panasonic AXK5SA3277YG and Panasonic AXK6SA3677YG). Either ground potential or high voltage can be applied through the adapter board to the readout strips by a cable.

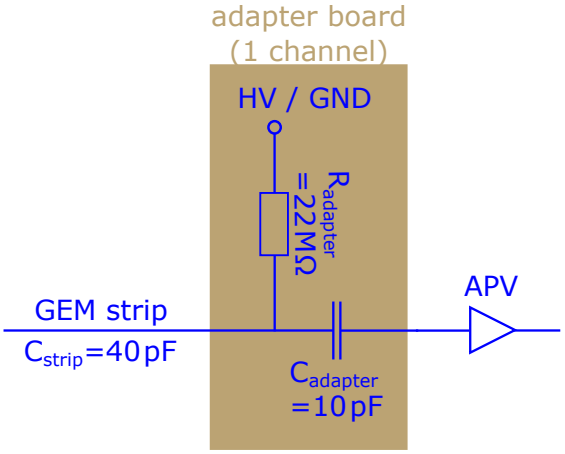

(b) Sketch of one channel of the adapter board. The adapter board acts as a high pass filter.

Figure 3.4: Adapter board for noise reduction.
With this adapter board, the back coupling of signals from the APV25 hybrid board is more suppressed than the coupling from signals to the APV25.
Since this adapter board is a high pass filter for every channel, it is possible to set the readout strips on HV without damaging the readout electronics.

With $C_{\text{adapter}} = 10\,pF$ and $R_{\text{adapter}} = 22\,M\Omega$ the cut-off frequency of that filter is at:

$$f_{cut} = \frac{1}{2\pi R_{adapter} C_{adapter}} = 723\,Hz \tag{3.2}$$

This is far off the frequency of the signal $\mathcal{O}\left(\text{f}_{\text{signal}}\right) = \text{MHz}$. Therefore, the current signal is reduced by capacitive coupling only.

A fraction ($frac_{\text{adapter}}$) of the total induced signal (Q_{tot}) is capacitively coupled from a readout strip to the adapter board with capacitance C_{adapter}. The rest of the signal (Q_{strip}) capacitively couples to all electrodes in the detector, including ground (see Figure 3.5a). The summed capacity between the strip and all electrodes, including ground is C_{strip}. $frac_{\text{adapter}}$ calculates as following:

$$frac_{adapter} = \frac{Q_{adapter}}{Q_{tot}} \tag{3.3}$$

using $Q_{\text{tot}} = Q_{\text{strip}} + Q_{\text{adapter}}$ and $\frac{Q_{\text{strip}}}{C_{\text{strip}}} = \frac{Q_{\text{adapter}}}{C_{adapter}}$ one obtains:

$$\begin{aligned} frac_{adapter} &= \frac{Q_{adapter}}{Q_{adapter} + Q_{strip}} \\ frac_{adapter} &= \frac{C_{adapter}}{C_{adapter} + C_{strip}} \end{aligned} \tag{3.4}$$

For the bottom GEM strips the capacity of one strip is $C_{\text{strip}} \approx 40\,pF$ (see Table A.1). The fraction of the signal intruded to the adapter board is $frac_{\text{adapter}} \approx 20\,\%$.
The same procedure applies to calculate the fraction of the signal that is coupled from the adapter board to the APV with a capacitance $C_{\text{APV}} = 100\,pF$ ($frac_{\text{APV}}$). The fraction $frac_{\text{tot}}$

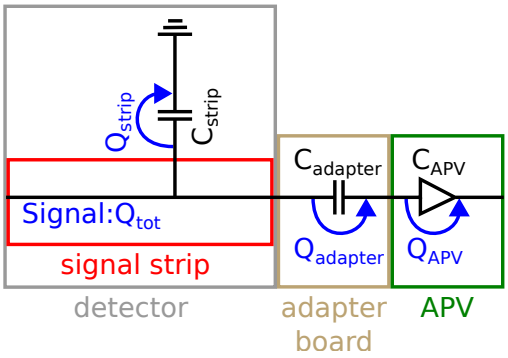

(a) Coupling of the signal from the readout strip.
A Signal Q_{tot} is induced on the readout strip. A part of the signal $Q_{\text{strip}} < Q_{\text{tot}}$ is coupling to all other electrodes in the detector (incl. ground). The remaining charges Q_{adapter} are coupled to the adapter board. From there a part Q_{APV} is coupled to the readout electronics. The rest is coupled to a virtual ground (not drawn).

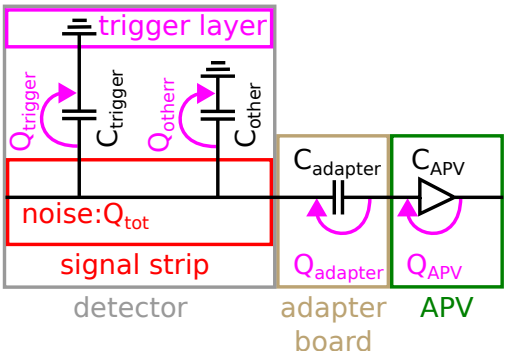

(b) Coupling of noise from the APV25 to the trigger layer.
Noise (Q_{APV}) couples from the APV25 to the adapter board. A part of the noise Q_{adapter} is coupled via the adapter board to the readout strip. The rest is coupled to a virtual ground (not drawn). Q_{tot} is the absolute value of noise coupled from the APV25 to one readout strip. From the readout strip the noise either couples to the trigger layer Q_{trigger} or to the other electrodes Q_{other}.

Figure 3.5: Coupling of the signal to the APV (left) and coupling of the noise to the trigger signal (right).

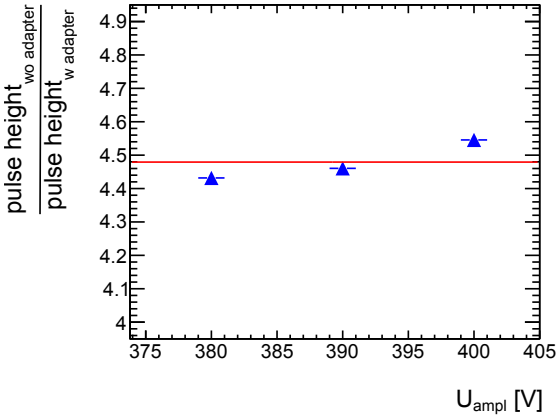

Figure 3.6: Ratio between pulse height of the highest strip in the cluster without and with adapter board (GEM strips).
The pulse height decreases by a factor of approximately 4.5 by using the adapter board. As a trigger, the signal of the non-segmented side of the SGR foil is used. The measurement without an adapter board was only possible with more than 90 % of the triggers being noisy. The noise is successfully discarded in the analysis afterward.
To obtain a reliable result only voltages are shown where no strips are saturated.
U_{GEM} = 200 V, U_{drift} = 420 V

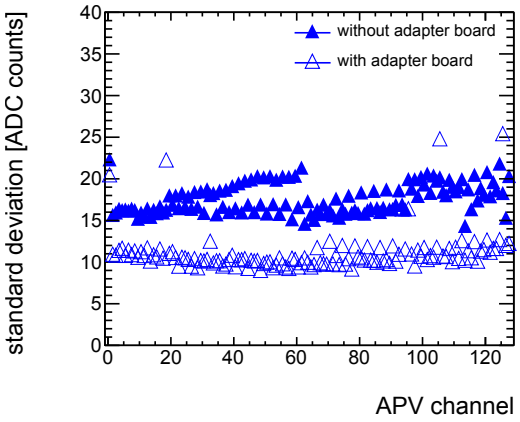

Figure 3.7: Standard deviation of the pedestal of the signal height for each channel, when no particle traversed the detector. The standard deviation is a measure of the measured noise. Even though the noise level without the adapter board is quite low (15 ADC counts), it decreases by using the adapter board (10 ADC counts).
U_{ampl} = 420 V, U_{GEM} = 200 V, U_{drift} = 420 V

of the total signal Q_{tot} that is read out by the APV at the end is:

$$frac_{apv} = \frac{Q_{APV}}{Q_{tot}}$$
$$frac_{apv} = frac_{adapter} \times frac_{APV} \approx 18\% \tag{3.5}$$

This fraction is approximately four times smaller than for the directly extracted signal[4]. This is in good agreement with the measured value of $frac_{\text{APV measured}} \approx 4.5$ (see Figure 3.6).

The same procedure is used in the reverse way to calculate the fraction of noise coupling from the APV25 to the readout strip (see Figure 3.5b). Using the adapter board this fraction is $frac_{\text{noise}} \approx 7\%$. This is also about four times smaller than if no adapter board is used.
Even though the noise level in the measurement data of the strips read out with APVs was already very low, it was further reduced using the adapter board (see Figure 3.7).

Since each readout strip is separated from the APV25 readout chip via a high-pass filter, it is possible to set the readout strips to high voltage via the adapter board. The readout strips behind the high pass filter remain at ground potential so that the APV25 frontend boards can be connected to them.

[4]The calculation for the directly coupled signal is analogous, but without taking the adapter board into account.

3.4 Signal Reconstruction

A typical event of a 120 GeV muon traversing the SGR detector is shown in Figure 3.8[5]. With the APV25 readout electronics, a time-dependent pulse height distribution is obtained for each strip. The duration of the signal is a few hundred nanoseconds. Due to the transverse diffusion of the charges in the amplification process, the signal is detected on multiple strips. From the signal shown in Figure 3.8 a position is reconstructed with an accuracy better than the pitch. For this purpose, an exact pulse height and time information is needed for each strip.
The signal rise of each strip is fit using an inverse Fermi function (see Equation 3.6 and Figure 3.9) to obtain a precise pulse height and time information better than the 25 ns sampling of the APV25.

$$q(t) = \frac{q_0}{1 + exp\left(\frac{t_0 - t}{\Delta t_{rise}}\right)} + q_{offset} \tag{3.6}$$

As strip pulse height q_0 is used. The point of inflection t_0 is used as strip time information. Δt_{rise} is the rise time of the signal.

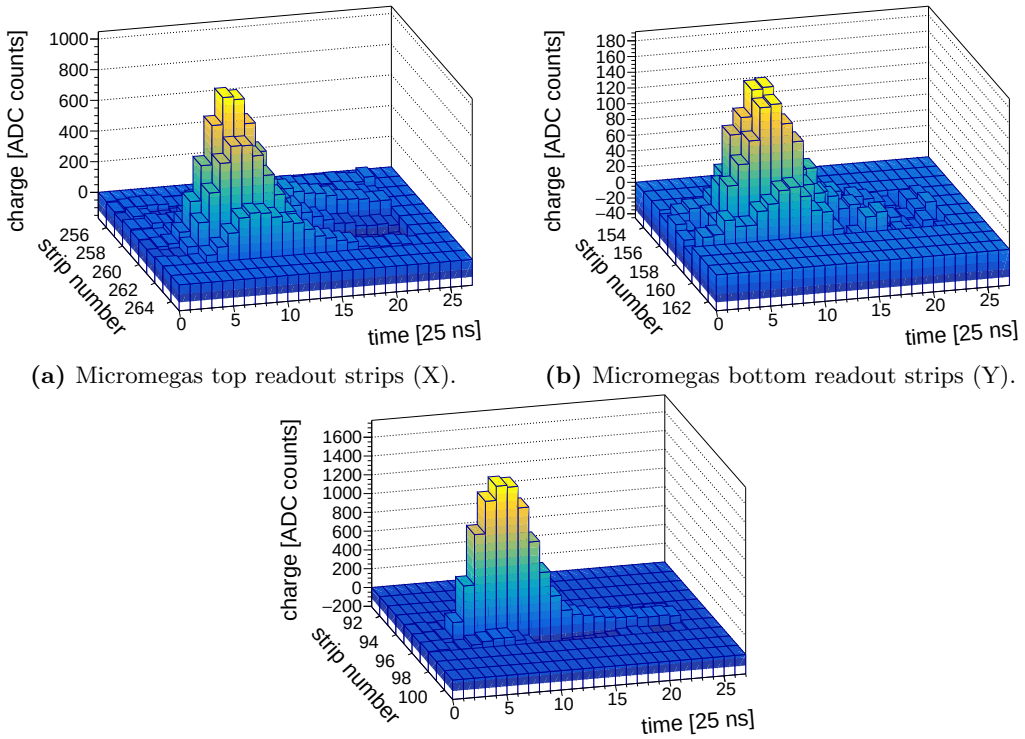

(a) Micromegas top readout strips (X).

(b) Micromegas bottom readout strips (Y).

(c) GEM readout strips, segmentation on the bottom side (Y).

Figure 3.8: Raw signals for a 120 GeV muon perpendicularly traversing the detector.
Due to transverse diffusion during the gas amplification, the signal is detected on multiple strips. Furthermore, on both Micromegas readout strip layers, the charge signal spreading on the DLC layer anode is resolved, leading to additional hit strips (see chapter 6.3).
Due to the larger pitch of the GEM readout strips compared to the Micromegas strips and the non-resolved signal spread, fewer GEM strips than Micromegas strips are hit.
Due to the design of the readout structure, the pulse height of the bottom Micromegas readout strip layer is significantly lower than that of the other layers (see Chapter 6.6.2)
U_{GEM} = 200 V, U_{drift} = 420 V, U_{ampl} = 440 V.

[5]The signals of a Micromegas detector look very similar

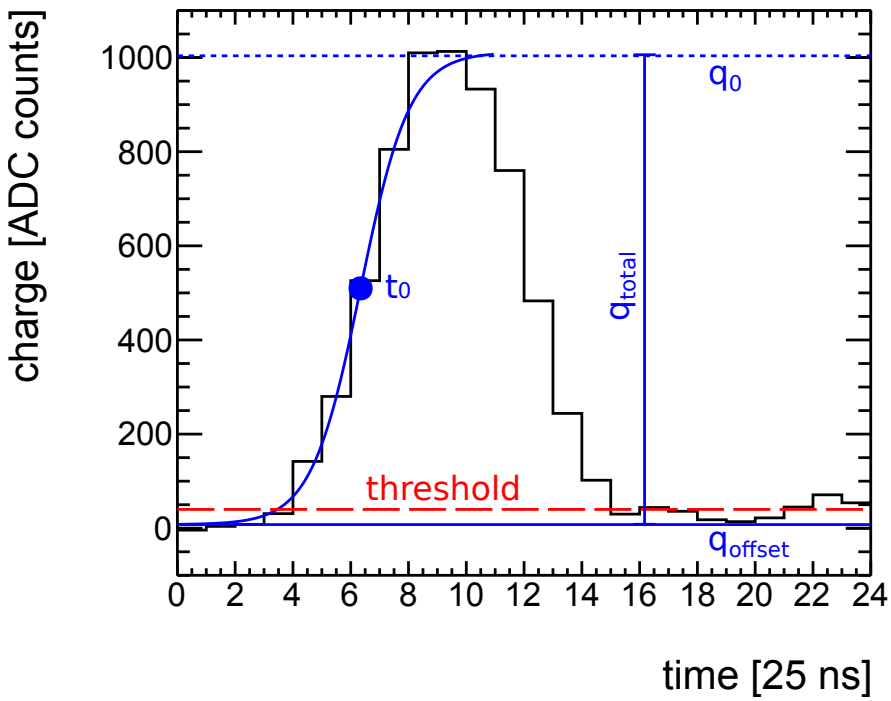

Figure 3.9: Typical APV25 signal of a single GEM readout strip.
The signal was created by a 120 GeV muon. The APV25 chip samples the signal in 25 ns steps. The maximal size of the time window is 27 time-bins, but only 24 of them are shown.
When the signal exceeds a threshold (here: 40 ADC counts), an inverse Fermi fit is performed (equation 3.6), to determine the signal time t_0 and the signal height q_{total}.
If the signal does not exceed the threshold, it is discarded as noise.
U_{drift} = 420 V, U_{GEM} = 200 V, U_{ampl} = 440 V.

3.5 Event Selection

With the SRS using APV25 readout chips every strip is read out if the readout electronics obtains a trigger signal. Strips that detected a particle signal need to be identified. All other strips will be discarded.
The baseline of the signal is subtracted for each time bin and readout channel. Then it is checked whether the pulse height of the strip is a multiple higher than the noise level of the respective strip[6]. As noise level, the standard deviation of the strip pulse height when no signal is detected is used (see Figure 3.7). This process is executed on the DAQ PC during data taking. It is explained in detail in [Flierl, 2018].
Further event selection is based on the parameters resulting from the signal fit explained in chapter 3.4:

- Strips where the average charge of the highest and its neighboring time bins does not exceed a threshold are discarded as not hit: $q_0 > 40$ (see Figure 3.10a).
- Strips with a nonphysical rise times Δt_{rise} are discarded: $0.1 < \Delta t_{\text{rise}} < 4$ (see Figure 3.10b).
- The signal of all hit strips must be within a certain time range. The limits t_{min} and t_{max} differ for different trigger setups. $t_{\text{max}} - t_{\text{min}}$ is chosen to be approximately 200 ns (see Figure 3.10c).
- The Standard deviation of the time-dependent strip signal (see Figure 3.9) normalized by the strip pulse height needs to be in a certain range (see Figure 3.10d).

As a last step strips are discarded if they are not assigned to a cluster (see chapter 3.6).

[6] For this thesis this is usually 1.7 × standard deviation of the baseline fluctuation.

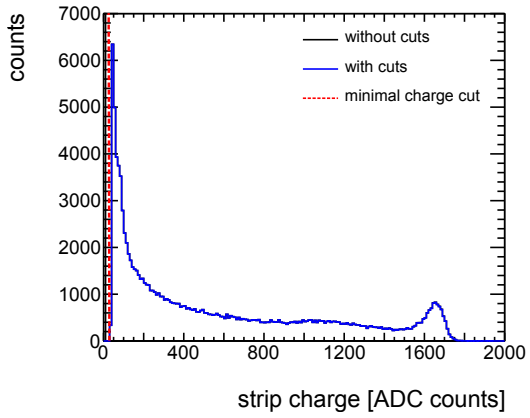

(a) Strip charge q_0 from Equation 3.6.
Too low signals (q_0 < 40 ADC counts) are discarded as noise.
The peak at 1650 ADC counts is created by saturation of the APV readout channel.

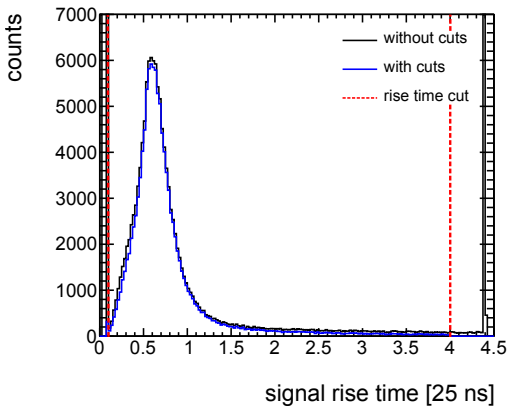

(b) Signal rise time Δt_{rise} from Equation 3.6.
A cut is applied at too fast (2.5 ns) and too slow (100 ns) signal rise times.
In the distribution with cuts, the charge cut of Figure 3.10a is applied in addition to the rise time cut.

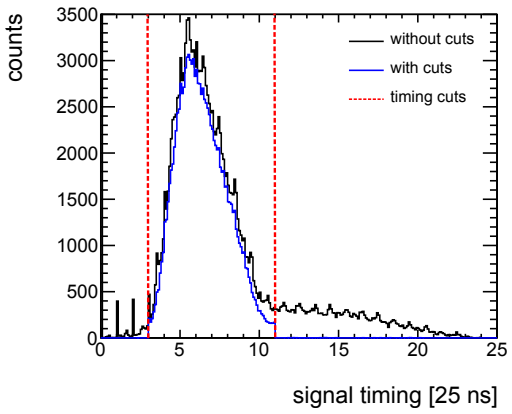

(c) Signal time t_0 from Equation 3.6.
A cut is applied at too-early (75 ns) and too-late (275 ns) signals.
In the distribution with cuts, the cuts of Figure 3.10a and Figure 3.10b are applied in addition.

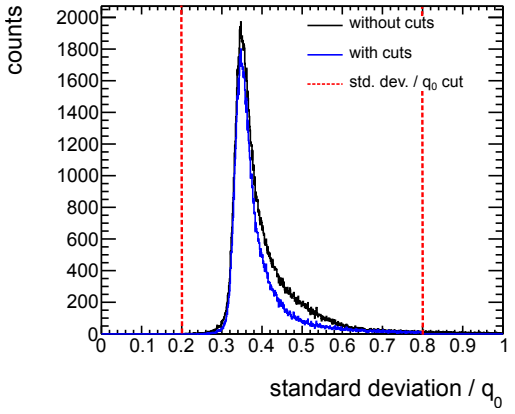

(d) Standard deviation of the time-dependent strip signal (see Figure 3.9) normalized by q_0 from Equation 3.6.
Signals kept having $0.2 < std\,dev./q_0 < 0.8$.
In the distribution with cuts, all cuts from the other figures are applied in addition.

Figure 3.10: Signal parameters obtained by an inverse Fermi fit (Equation 3.6) to the signal detected by a readout strip. These parameters were used to distinguish between noise and signal. Approximately 51000 events of 120 GeV muons traversing the detector are shown.
U_{GEM} = 200 V, U_{ampl} = 440 V.

3.6 Cluster Reconstruction

A group of neighbored responding strips is called a cluster. In general, depending on the pitch size, multiple strips are expected to detect a signal from a traversing particle (see Figure 3.8). The number of strips in a cluster, possibly also multiplied by the strip pitch, is called the cluster size.
The charge originating from a perpendicular incident particle is Gaussian distributed (see Figure 3.11a). The inhomogeneous ionization along the trajectory of the traversing particle is resolved only for inclined tracks (see Figure 3.11b). In the following, pulse height refers to the sum of all strip pulse heights assigned to a cluster:

$$q_{cluster} = \sum_{i=0}^{strips\ in\ cluster} q_i \tag{3.7}$$

with q_i being the strip pulse height for the i^{th} strip in a cluster.
The position and the incident angle of a particle are reconstructed at the cluster level.

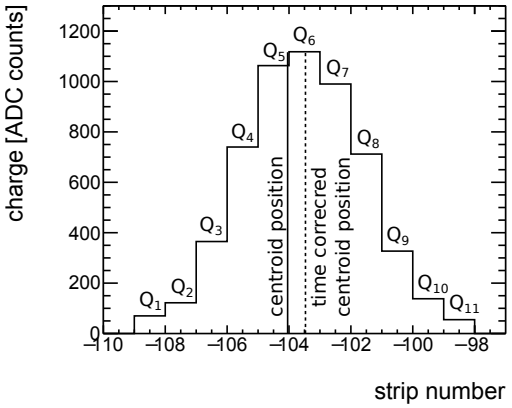

(a) 120 GeV muon perpendicularly traversing the detector.
The positions reconstructed with the centroid method (Equation 3.8; solid line) and the time-corrected centroid method (Equation 3.9; dashed line) are shown.
The inhomogeneous ionization along the particle trajectory is not resolved. The signal is Gaussian distributed.
U_{drift} = 420 V, U_{GEM} = 200 V, U_{ampl} = 440 V.

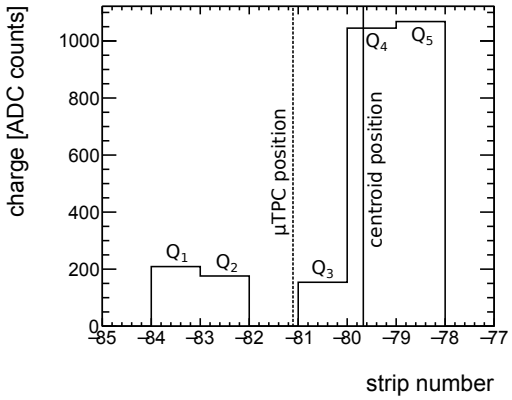

(b) 120 GeV muon traversing the detector at an angle of $\Theta = 20°$.
The positions reconstructed with the centroid method (Equation 3.8; solid line) and the µTPC method (chapter 3.6.2; dashed line) are shown.
The inhomogeneous ionization along the particle trajectory plays now a role. Therefore the signal is no longer Gaussian distributed.
U_{drift} = 420 V, U_{GEM} = 200 V, U_{ampl} = 440 V.

Figure 3.11: Strip pulse height in dependence of the strip position for one single event.

3.6.1 Centroid Method

The charge-weighted mean (centroid) of a charge distribution as shown in Figure 3.11a is used as particle position. It refers to the position of the particle in the middle of the strip gap. It is calculated with Equation 3.8:

$$x_{centroid} = \frac{\sum_{i=0}^{strips\ in\ cluster} q_i \times x_i}{\sum_{i=0}^{strips\ in\ cluster} q_i} \tag{3.8}$$

with x_i being the position and q_i the strip pulse height of the ith strip in a cluster.

On resistive anode readout structures, the charges spread with a finite velocity on the resistive layer or resistive strips after they are collected by the anode. This charge movement induces a signal which is resolved by the readout electronics[7]. At the DLC layer detector, signals created by the charge movement follow the immediate signal with a reciprocal velocity of approximately 200-250 ns/mm[8]. A V-shape is observed when the strip time (t_0 from Equation 3.6) is plotted against the strip number (see Figure 3.12). The reciprocal velocity is determined by an event-wise V-fit to this V-shape.

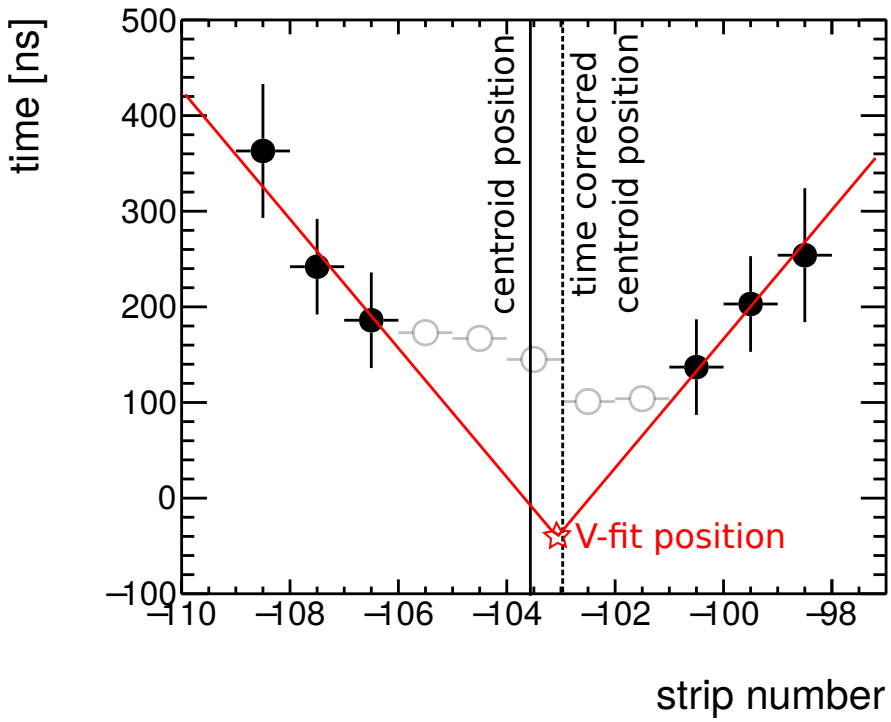

Figure 3.12: Timing information for the top Micromegas readout strips (120 GeV muon perpendicularly traversing the detector).
The V-shape of the signal due to the radial electron diffusion on the DLC layer is resolved by the outer readout strips of the signal cluster. By fitting the timing information of these strips with a V-shape function, a position is reconstructed. In this event the slope of the V-legs is approximately 250 ns/mm.
In the center of the cluster, the signal induced directly by the avalanche dominates (non-filled markers). These points are neglected for the V-fit.
Weighting each strip by t_0^{-2} in addition to the charge weight, the immediate signal is weighted stronger (see Equation 3.9).
DLC layer Micromegas detector, U_{GEM} = 200 V, U_{ampl} = 440 V.

[7] This is described in detail in chapter 5.3.
[8] This V-shape is analyzed in detail in 6.3.1.

Due to their low pulse height and slightly different shape signals induced due to the charge diffusion are often discarded as noise. To obtain a position information that is independent of the electron spread, every strip in the cluster is weighted by the square of the inverse signal time t_i^2. t_i is the signal time of the ith strip[9]. Late-arriving signals are weighted less than the immediate signals induced directly by the avalanche. The time-corrected charge weighted mean position is calculated with Equation 3.9:

$$x_{cor} = \frac{\sum_{i=0}^{strips\,in\,cluster} \frac{q_i}{t_i^2} \times x_i}{\sum_{i=0}^{strips\,in\,cluster} \frac{q_i}{t_i^2}} \tag{3.9}$$

The time-corrected charge-weighted mean position slightly differs from the charge-weighted mean position (see Figure 3.12).
Another approach to reconstructing the particle position is to use only the strip time information of the signals induced by the electron diffusion (V-shape). By extrapolation of the V-legs, an intersection of both V-legs can be determined and used as a position, referred to as V-fit position (see Figure 3.11a).
All the position reconstruction methods listed here are compared in chapter 9.4.3.

3.6.2 μTPC Method

For inclined tracks, the inhomogeneous ionization along the particle trajectory dominates the position resolution. The strip pulse height is no longer Gaussian distributed over the strip position (see Figure 3.11b). The charge-weighted mean of the signal (see Equation 3.8) is affected by this. This worsens the resolution using the charge-weighted mean method for inclined tracks (see chapter 9.4.2). However, it is possible to additionally use the time information for the position determination.
With MPGDs it is possible to reconstruct the trajectory of an inclined incident particle with only one detector layer. This is done with the so-called μTPC method. This is similar to the reconstruction algorithms in a Time Projection Chamber (TPC) [Iakovidis, 2014].
An electron created closer to the cathode has a longer drift time to the amplification region than a particle created closer to the micro-mesh (see Figure 3.13). For inclined tracks, this time dependency is strip-wise resolved by the APV25 ASICs. Using Equation 3.10 the angle of inclination Θ_{measured} is reconstructed.

$$\begin{aligned} \Theta_{measured} &= 90^\circ - atan\left(\frac{\Delta t \times v_{drift}}{\Delta strips \times p}\right) \\ &= 90^\circ - atan\left(\frac{v_{drift}}{slope \times p}\right) \end{aligned} \tag{3.10}$$

with the electron velocity in the drift region v_{drift}, the strip pitch p and the track *slope*.
v_{drift} is obtained by simulation (see Figure 1.3) or from the drift time distribution $t_{\text{last}} - t_{\text{first}}$

The slope is obtained for each event by a linear fit as shown in Figure 3.13. The quality of the fit is strongly depending on the chosen uncertainties of the time information.
By default the following uncertainties are chosen: $\Delta x = p/2$ and $\Delta t = 12.5\,ns$. Reconstructed track points that lie outside the dimensions of the drift area are ignored. When the strip pulse height is saturated (see chapter 3.2), the uncertainty is doubled. In addition, a Hough transformation (see Appendix A) is used to determine the error more precisely. A Hough

[9] Also weighting each strip by t_i^{-1} and t_i^{-3} were tested, but slightly better results were obtained by using t_i^{-2} as weight.

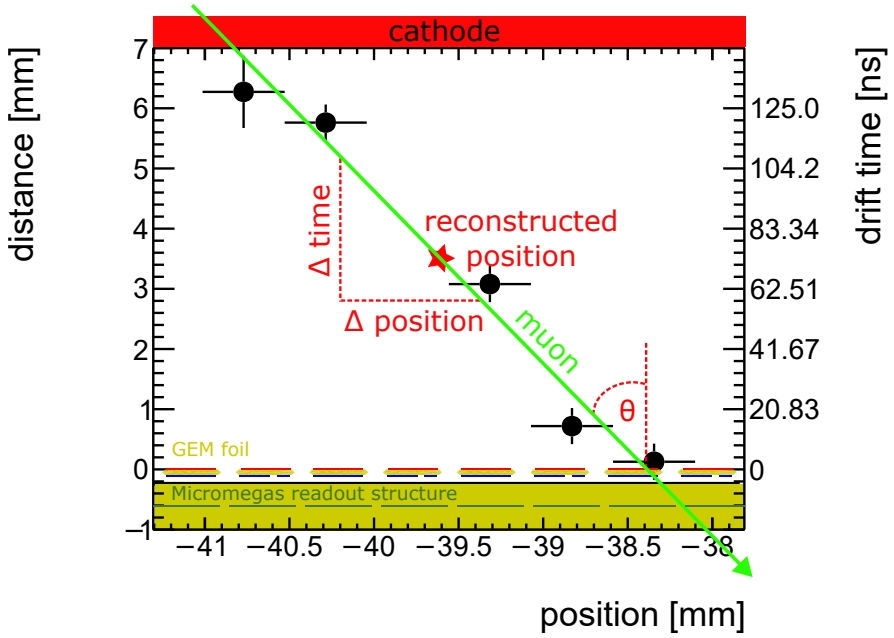

Figure 3.13: Track reconstruction for inclined particle tracks using the μTPC method.
The signal time of the hit strip is depending on the location, where the primary electron is created. Electrons created closer to the cathode show a longer drift time than electrons created closer to the GEM foil. For inclined tracks, this time dependency can be used for position determination. Knowing the electron velocity for the applied drift field, a particle track is reconstructed via a linear fit.
$\Theta = 20°$, $U_{drift} = 420\,V$, $U_{GEM} = 200\,V$, $U_{ampl} = 440\,V$.

transformation identifies points lying on a straight line. With an increasing distance to that line, the error of the track points is increased.
The track position corresponding to the middle of the drift gap is used as μTPC position $x_{\mu TPC}$.

The timing information is extracted from the time-dependent charge signal of the APV25 (see Figure 3.9). This is influenced by capacitive coupling between adjacent strips. Thus the μTPC method is influenced thereby as well. The charge-weighted mean position (see chapter 3.6.1) remains unaffected due to the symmetry of the capacitive coupling.
To improve the μTPC reconstruction a correction for the capacitive coupling between readout strips is needed. It can be deduced from [Lösel, 2017] that for a readout strip length of $l = 10\,cm$ a fraction $r = 23\%$ of the strip pulse height couples to the neighboring strips.
As proposed in [Lösel, 2017] the capacitive coupling can be corrected for the i^{th} strip by subtracting the coupled charge from the neighboring strips ($i \pm 1$) and adding it to the i^{th} strip:

$$\begin{aligned} (q_i)_{corrected}(t) &= q_i(t) + 2rq_i(t) \\ (q_{i\pm1})_{corrected}(t) &= q_{i\pm1}(t) - 2rq_i(t) \end{aligned} \tag{3.11}$$

This correction is applied time-bin-wise for all inclined tracks. The inverse fermi function fit (see chapter 3.4) is applied afterward.

3.7 Track Reconstruction

To determine the resolution of the SGR detector, a precise reference track is needed. This is obtained by using a detector hodoscope, which consists of several tracking detectors. The hit position in the tracking detectors is determined using the centroid method (see chapter 3.6.1). The hit positions in the tracking detectors and the location of the detectors along the beam axis are used to determine a linear reference track. The track reconstruction using the χ^2 Minimization method is done as explained in [Klitzner, 2019].
The accuracy of a track determined by n reference detectors is calculated as [Horvat, 2005]:

$$\sigma^2_{track}(z) = \frac{\Lambda_{22} - 2z\Lambda_{12} + z^2\Lambda_{11}}{\Lambda_{11}\Lambda_{22} - \Lambda^2_{12}} \tag{3.12}$$

Λ_{ij} is calculated with Equation 3.13 using the position z and resolution σ of the tracking detector.

$$(\Lambda_{11}, \Lambda_{12}, \Lambda_{22}) = \sum_{i=1}^{n} \frac{\left(1, z_i, z_i^2\right)}{\sigma_i^2} \tag{3.13}$$

The resolution of the reference detectors is determined via the geometric mean method [Carnegie et al., 2005]. The resolution of the detector is determined as it is described in chapter 3.9.1. It is determined twice: first with the detector included in the track fit σ_{in} and second with the detector excluded from the track fit σ_{ex}. If all the detectors used have a similar spatial resolution, the following applies to the geometric mean spatial resolution of the detector [Carnegie et al., 2005]:

$$\sigma = \sqrt{\sigma_{in}\sigma_{out}} \tag{3.14}$$

Between the reference detectors, the resolution of the reference tracks is better than the resolution of the individual reference detectors (see chapter 9.2).
The track is reconstructed for each detector coordinate separately.
Only tracks where all reference detectors are hit and the extrapolated track passes through the active area of the detectors under investigation are used for analysis. If the track passes through problematic or inefficient areas in the reference detectors the track is discarded as well.

3.8 Detector Alignment

The track reconstruction (see chapter 3.7) only works if all detectors are well aligned. Detector hodoscopes can usually only be mechanically aligned with an accuracy of up to millimeters. The exact alignment to micrometer accuracy is done in the analysis. The software alignment process is explained in this chapter.
The detector alignment is an iterative process. First, all the reference tracking detectors are aligned. For this purpose, one of the reference detectors is excluded from the track finding. This detector is aligned to the track using the methods explained in the following sections. Afterward, this detector is used again for track finding and another reference detector is excluded from the track fit. This process is repeated iteratively for all reference detectors until all of them are aligned.
As soon as all detectors are perfectly aligned with each other, the detectors under investigation are aligned using the reference track.

3.8.1 3D Point construction

For each detector a 3D point is constructed:

$$\vec{P}_{hit} = \begin{bmatrix} X \\ Y \\ Z \end{bmatrix} \tag{3.15}$$

with X and Y being the coordinates measured by the detector and Z the position along the beam axis. This point is corrected for each detector by the alignment steps described in the following.

3.8.2 Alignment of the Detector Position

To correct for a shift of the detector with respect to the reference track a constant offset $\Delta\vec{P}_{\text{hit}}$ is added to the 3D point from Equation 3.15:

$$\Delta\vec{P}_{alligned} = \vec{P}_{hit} + \Delta\vec{P}_{hit} \tag{3.16}$$

with:

$$\Delta\vec{P}_{hit} = \begin{bmatrix} \Delta x \\ \Delta y \\ \Delta z \end{bmatrix} \tag{3.17}$$

A non-vanishing intercept is accounted for by a correction of the X respectively Y position as explained above.

X and Y Position

In the sensitive coordinates of the detector Δx and Δy are observed in the residual distribution (see Figure 3.14). The residual is the distance between the hit position in the detector and the reference track (see Equation 3.25). A residual distribution for a miss-aligned detector is shown in Figure 3.14a. After the shift is corrected the residual is centered around zero (see Figure 3.18).

Z Position

If the detector is shifted along the Z-axis a linear correlation between the residual Δy (respectively the residual Δx) and the slope of the particle track is observed (see Figure 3.15). This broadens the residual distribution. To determine the displacement along the beam axis ΔZ, a linear fit (Equation 3.18) is applied to the correlation between residual and track slope:

$$\Delta y = slope \times track\ slope + intercept \tag{3.18}$$

ΔZ corresponds to the slope of Equation 3.18:

$$slope = \frac{\Delta y}{track\ slope} = \frac{\Delta y}{\frac{\Delta y}{\Delta Z}} = \Delta Z \tag{3.19}$$

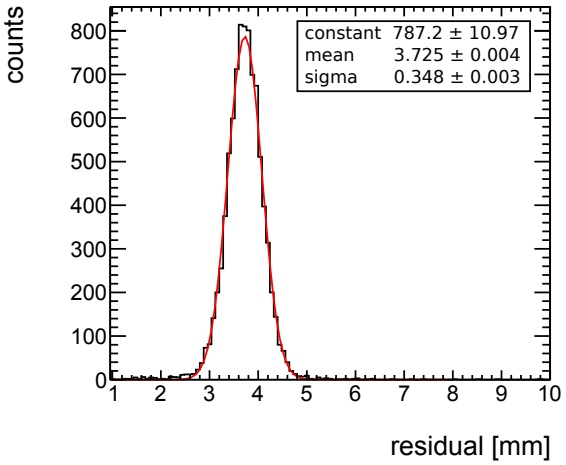

(a) Residual Y distribution.
A systematic shift of the measurement values is observed. The detector is shifted along the Y-axis by the mean of the residual distribution (Δy).
U_{drift} = 420 V, U_{GEM} = 450 V, U_{ampl} = 450 V, Θ = 20°

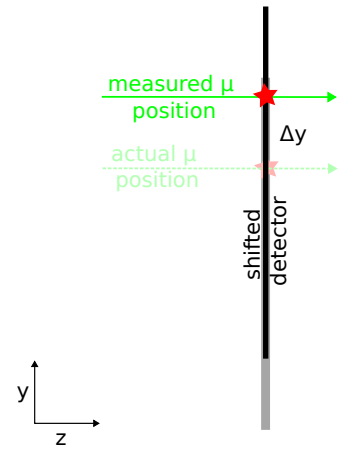

(b) Schematic picture of the shifted detector along the Y-axis.
If the detector is shifted by a distance Δy along the Y-axis a mean residual Δy to the actual track position Y is observed.

Figure 3.14: Shift along the Y-axis.
From the distribution of the residual in Y the shift along the Y-axis can be derived. Knowing Δy the position can be corrected for. The same applies to the X coordinate.

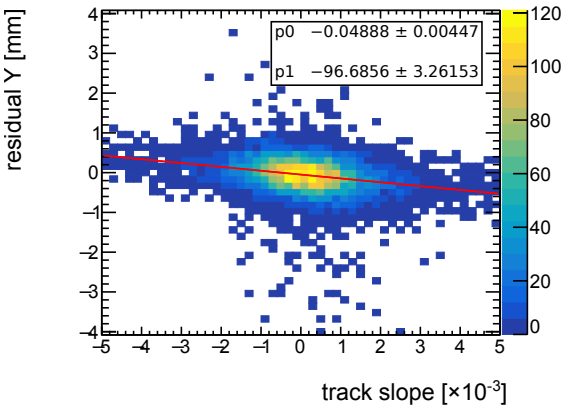

(a) Residual Y plotted against the track slope.
An observed linear correlation is an indication of a shift along the Z-axis. The distribution is fit with a linear polynomial (see Equation 3.22). The slope of this fit is equal to ΔZ. For the shown case the shift is ΔZ = 96 *mm*
U_{drift} = 420 V, U_{GEM} = 450 V, U_{ampl} = 450 V, Θ = 20°.

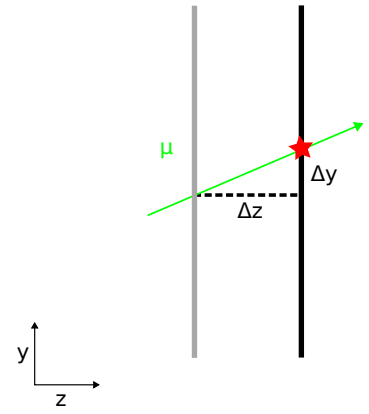

(b) Schematic picture of the detector shifted along the Z-axis.
If the detector is shifted by a distance −ΔZ along the Z-axis a residual Δy to the actual track position Y is observed. Δy correlates with the track slope.

Figure 3.15: Shift along the Z-axis.
From the distribution of the residual in Y, plotted against the track slope, the shift along the Z-axis can be derived. Knowing ΔZ the position can be corrected for.

3.8.3 Alignment of the Detector Rotation

After the displacement of the detectors along the coordinate axes is corrected, the rotation of the detectors to each other is corrected. This is done by multiplying the aligned hit position (Equation 3.16) with the rotation matrices (Equation 3.20):

$$
\begin{aligned}
R_x &= \begin{bmatrix} 1 & 0 & 0 \\ 0 & cos(\Theta) & -sin(\Theta) \\ 0 & sin(\Theta) & cos(\Theta) \end{bmatrix} \\
R_y &= \begin{bmatrix} cos(\Theta) & 0 & sin(\Theta) \\ 0 & 1 & 0 \\ -sin(\Theta) & 0 & cos(\Theta) \end{bmatrix} \\
R_z &= \begin{bmatrix} cos(\Theta) & -sin(\Theta) & 0 \\ sin(\Theta) & cos(\Theta) & 0 \\ 0 & 0 & 1 \end{bmatrix}
\end{aligned}
\tag{3.20}
$$

$$
\Delta\vec{P}_{rotated} = R_{x/y/z} \times \vec{P}_{aligned} \tag{3.21}
$$

The rotation is done for each coordinate separately. The angles of rotation are determined as explained in the following.

Rotation around the X- and Y-Axis

If the detector is rotated around the X-axis a linear correlation between the residual Δy and the hit position in Y is observed (see Figure 3.16). For the rotation around the Y-axis, this applies analogously to the X-axis residual plotted against X. With a linear fit

$$
\Delta y = slope \times Y + intercept \tag{3.22}
$$

to this distribution the angle of rotation Θ is calculated using Equation 3.23.

$$
cos\,(\Theta) = \frac{y}{y + \Delta y} = \frac{1}{1 + slope} \tag{3.23}
$$

Rotation around the Z-Axis

If the detector is rotated around the Z-axis a linear correlation between the residual Δy (Δx respectively) and the hit position in X (Y respectively) is observed (see Figure 3.17). With a fit of a linear polynomial to this distribution the angle of rotation Θ is calculated using Equation 3.24.

$$
tan\,(\Theta) = slope = \frac{\Delta y}{X} \tag{3.24}
$$

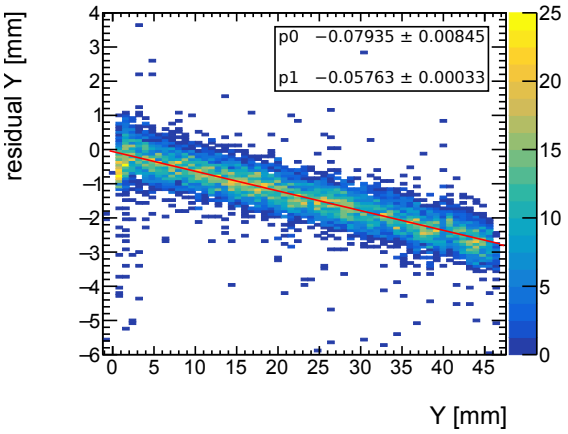

(a) Residual Y plotted against the Y-position. An observed linear correlation is an indication of a rotation of the detector around the X-axis. The distribution is fit with a linear polynomial (see Equation 3.22).
U_{drift} = 420 V, U_{GEM} = 450 V, U_{ampl} = 450 V, $\Theta = 20°$

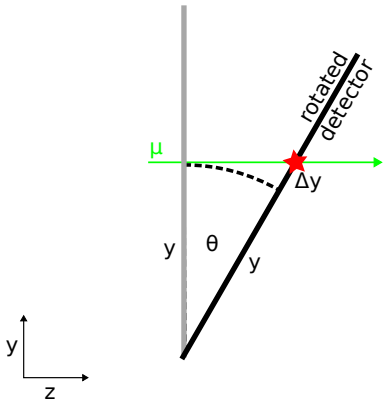

(b) Schematic picture of the rotated detector. If the detector is rotated by an angle Θ around the X-axis a residual Δy to the actual track position Y is observed. Δy is depending on Y.

Figure 3.16: Rotation around the X-axis.
From the distribution of the residuum in Y, plotted against the position in Y, the angle of rotation Θ around the X-axis is obtained. Knowing this angle the position can be corrected using Equation 3.21.
For the rotation around the Y-axis, this applies analogously.

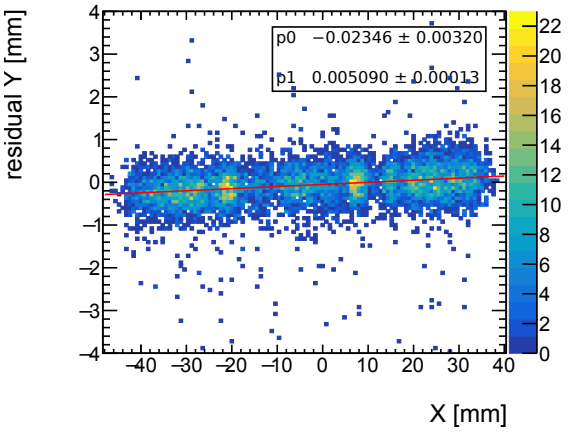

(a) Residual Y plotted against the X-position. An observed linear correlation is an indication of a rotation of the detector around the Z-axis. The distribution is fit with a linear polynomial.
The inhomogeneity of this distribution originates from problematic sections in the reference detectors. These areas are excluded from the analysis.
U_{drift} = 420 V, U_{GEM} = 450 V, U_{ampl} = 450 V, $\Theta = 20°$

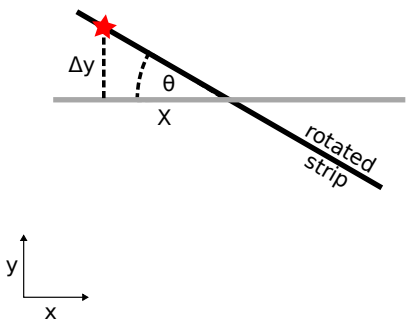

(b) Schematic picture of a readout strip rotated around the Z-axis.
If the detector is rotated by an angle Θ around the Z-axis a shift in Y by a factor Δy is observed. Δy is depending on X.

Figure 3.17: Rotation around the Z-axis.
From the distribution of the residuum in Y, plotted against position X, the angle of rotation Θ around the Z-axis is obtained. Knowing this angle the position can be corrected.

3.9 Determination of the Resolution

With an aligned detector hodoscope, the resolution of the detectors under investigation is determined. Incorrect alignment of both the reference detectors and the detectors under investigation leads to a broader distribution of the residuals and thus to a deterioration of the residuals.

3.9.1 Spatial Resolution and Efficiency

The reference track is interpolated to the position of the detector under investigation. The residual is determined as the deviation of the measured position x_{hit} from the reference position x_{ref}:

$$\Delta x = x_{ref} - x_{hit} \tag{3.25}$$

For a well aligned setup the residual is centered around $\Delta x = 0\,mm$ (see Figure 3.18).
The width of the residual distribution is used to determine the spatial resolution of the detector. The residual distribution is fit with a double Gaussian function :

$$\begin{aligned} f(x) &= gauss_{core}(x) + gauss_{tail}(x) \\ f(x) &= A_{core} \exp\left(\frac{(x-\Delta x_{core})^2}{2\sigma_{core}^2}\right) + A_{tail} \exp\left(\frac{(x-\Delta x_{tail})^2}{2\sigma_{tail}^2}\right) \end{aligned} \tag{3.26}$$

The width of the core Gaussian function σ_{core} refers to the resolution of an ideal detector. The rather broad Gaussian distribution of the tails is created by delta electrons or multiple scattering of the traversing particle. Delta electrons leave a track itself and thus influence the spatial resolution (σ_{tail}) .
To get a combined width σ_{combined} each sigma is weighted by the integral of its Gaussian distribution:

$$\sigma_{combined} = \frac{\sigma_{core} \int gauss_{core} + \sigma_{tail} \int gauss_{tail}}{\int gauss_{core} + \int gauss_{tail}} \tag{3.27}$$

For a tracking accuracy better than the resolution of the detector the tracking accuracy σ_{track} (see Equation 3.12) is subtracted quadratically from σ_{combined} to obtain the bare resolution of the detector:

$$\sigma = \sqrt{\sigma_{combined}^2 - \sigma_{track}^2} \tag{3.28}$$

Using the residual distribution the position reconstruction efficiency can be determined:

$$\varepsilon = \frac{N_{hits,\ |\Delta x<1\,mm|}}{N_{track,\ ref}} \tag{3.29}$$

with $N_{hits,\ |\Delta x<1\,mm|}$ being the number of hits with a residual smaller than 1 mm and $N_{track,\ ref}$ being the total number of reconstructed reference tracks.

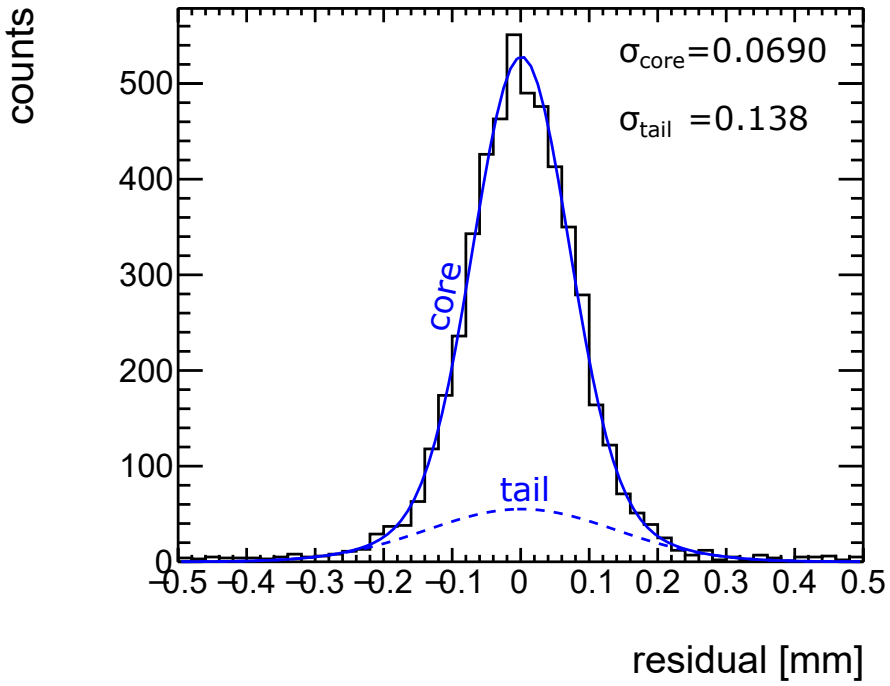

Figure 3.18: Residual distribution fit using a double Gaussian function.
A combined sigma is obtained by weighting each gaussian width with the integral of the corresponding Gaussian function. The resolution is obtained by quadratically subtracting the track resolution from the total width.
The combined resolution is $\sigma = 0.0768\,\text{mm}$.
The residual distribution is shown for the GEM strips on the bottom side.
$U_{drift} = 420\,V$, $U_{GEM} = 200\,V$, $U_{ampl} = 440\,V$

3.9.2 Angular Resolution

For inclined tracks, the incident angle is reconstructed using the μTPC method (see chapter 3.6.2). To avoid systematic errors induced due to the nonlinearity of Equation 3.10 a variable bin width is used for the angular distribution (see Figure 3.19) [Bortfeldt, 2014]. The obtained distribution is asymmetric. The tail towards larger angles is due to not fully corrected capacitive coupling [Klitzner, 2019]. To get the most probable reconstructed angle Θ_{MPV} and the angular resolution the distribution is fit piece-wise with two Gaussian functions one towards smaller angles and one towards larger angles:

$$\begin{aligned} f_<(\Theta) &= A \exp\left(0.5\left(\frac{\Theta - \Theta_{MPV}}{\sigma_<}\right)^2\right) \qquad \forall|\Theta| < |\Theta_{MPV}| \\ f_>(\Theta) &= A \exp\left(0.5\left(\frac{\Theta - \Theta_{MPV}}{\sigma_>}\right)^2\right) \qquad \forall|\Theta| \geqslant |\Theta_{MPV}| \end{aligned} \tag{3.30}$$

The widths ($\sigma_>$ and $\sigma_>$) of both Gaussian functions are a measure for the angular resolution.

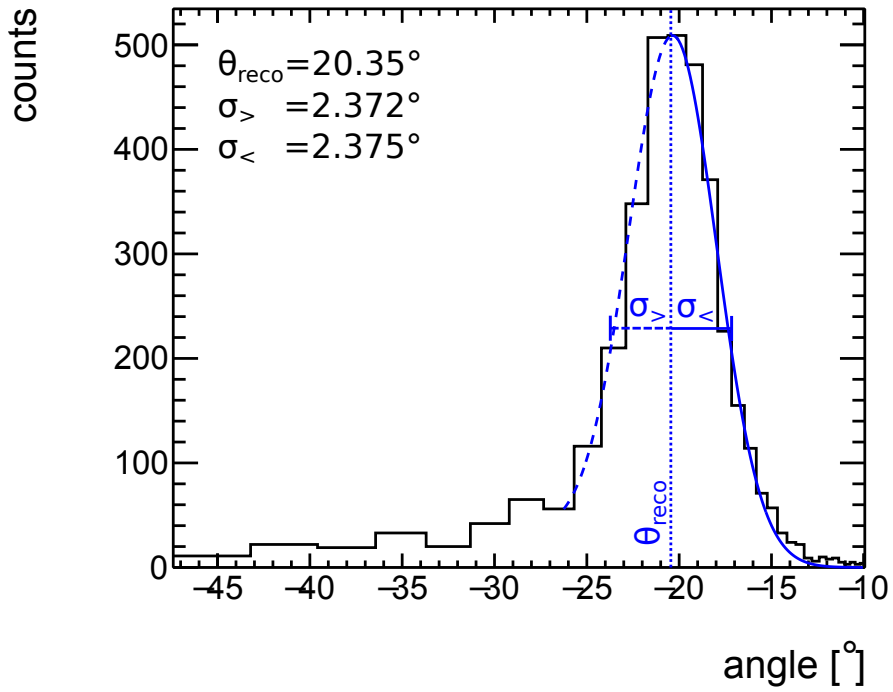

Figure 3.19: Distribution of the reconstructed angle using variable binning.
The distribution is fit with two Gaussian functions. Two σ are obtained as a measure for the angular resolution.
The angle distribution is shown for the GEM strips on the bottom side.
$\Theta_{\mathrm{set}} = -20.5 \pm 1°$, $U_{\mathrm{GEM}} = 200\,\mathrm{V}$, $U_{\mathrm{ampl}} = 430\,\mathrm{V}$

Chapter 4

Tools and Methods for the Simulation of the SGR Detector

To understand the processes mentioned in Chapter 2.4 that take place in the detector simulations are carried out. In this chapter, the simulation software used is briefly explained.

4.1 ANSYS

ANalysis SYStem (ANSYS) [ANS, 2022] is a finite element software. With the finite element technique complex physical processes are solved numerically.
In ANSYS a three-dimensional model of the SGR detector is built. Electrical properties are assigned to the different components of the detector. An electric potential is set to all electrodes. ANSYS calculates the electric field and voltage configuration of the detector (see Figure 5.2).

4.2 MAGBOLTZ

With MAGBOLTZ [Biagi, 2021] the electron transport properties in gas mixtures are simulated [Schindler, 2022]. Besides the drift velocity (see Figure 1.3), the longitudinal and transversal diffusion of electrons, the first Townsend coefficient (see Equation 1.6), and the Lorentz angle are simulated with MAGBOLTZ for different electric and magnetic fields.

4.3 Heed

The particle interaction of ionizing radiation is done with Heed [Smirnov, 2007]. It is an "implementation of the photo absorption ionization model" [Schindler, 2022]. It is written to simulate ionization by fast-charged particles in gases, but it can also simulate X-ray absorption.

4.4 Garfield++

Garfield++ is a simulation package for detailed simulations of gaseous and semiconductor detectors [Alsamak et al., 2022]. For simple geometries, the electric field configuration of the

detector can be calculated by Garfield++ itself. The electric field of more complex geometries can be imported.
For the simulation of the SGR detector the geometry and electric field configuration simulated with ANSYS (see Chapter 4.1) is imported.
After the electric field configuration is loaded an event created by an ionizing particle can be simulated by Garfield++.
The primary ionization is simulated using an interface to Heed (see Chapter 4.3).

Using the gas properties simulated with MAGBOLTZ (see Chapter 4.2) Garfield++ simulates the electron and ion drift (see Chapter 1.1.3), as well as the electron avalanches (see Chapter 1.1.2).
To simulate the ion drift with Garfield++ the ion mobility for different electric fields must be loaded. Ion mobility files are provided in the Garfield++ package only for pure argon and pure CO_2 but not for a mixture $Ar : CO_2$ 93 : 7 Vol. % at atmospheric pressure. Therefore, a new mobility file is generated. Since the values shown in Table 1.1 are only valid for lower electric fields, the new file is created using Equation 1.10 and the existing mobility files.
However, the mobilities determined in this way resulted in too long ion drift times. The duration of the measured signal was significantly shorter than that of the simulated signal. A 1.3 times higher ion mobility than previously determined is used for the following simulations to avoid this. The reason for this remains to be investigated. Impurities in the gas and unknown environmental conditions are among the possible reasons.

A simulated event of a muon traversing the SGR detector is shown in Figure 4.1.
The signal induced on the readout strips is calculated using the Shockley [1938]-Ramo [1939] theorem (see Chapter 4.4.1). The readout electronics is adapted to the simulated signal as described in Chapter 4.4.2.

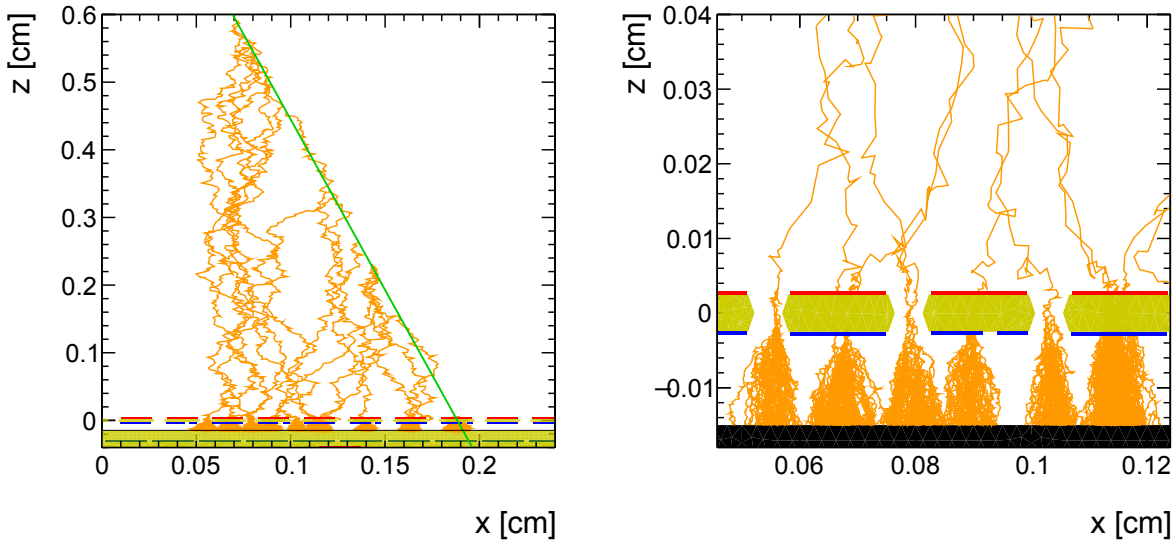

(a) Full detector view.

(b) Enlarged view at the amplification steps.

Figure 4.1: Simulation of a muon traversing the SGR detector using Garfield++ [Alsamak et al., 2022], MAGBOLTZ [Biagi, 2021], Heed [Smirnov, 2007] and ANSYS [ANS, 2022].
The gas is ionized along the muon path. The created electrons drift toward the GEM holes. Inside the GEM holes, the first amplification step takes place. Directly after the GEM foil, the second amplification step takes place inside the Micromegas amplification gap.
For visualization reasons, only electrons are shown.

4.4.1 Weighting Field Technique

The weighting field technique was introduced by Shockley [1938] and Ramo [1939]. It is a method for calculating the current on electrodes induced by moving charges. This method does not consider the capacitive coupling between the readout strips.
A signal is induced on the readout strips of a detector even if no charges terminate directly on the readout strips. This is the case, for example, in a resistive Micromegas detector. The charges end on the anode, which is insulated from the readout strips. These are located below the anode (see Chapter 2.1.2).
Applying the weighting field method, the current I induced on an electrode by a charge q moving with the velocity $\vec{v} = d\vec{x}/dt$ is given by:

$$I(t) = -q\vec{E}_{weight}\left[\vec{x}(t)\right]\frac{d\vec{x}(t)}{dt} \tag{4.1}$$

$\vec{E}_{\text{weight}}$ is the weighting field. It is the simulated electric field at the position of the moving charge for a configuration where:

- all charges are removed, including the moving charge.
- all electrodes are set to 0 V
- the electrode of interest is set to 1 V

For each readout strip/electrode where the signal needs to be simulated, the weighting field configuration must be simulated. In the present simulation this is done using ANSYS.

4.4.2 Simulation of the Readout Electronics

To compare the simulation with the measurements, the readout electronics (see Chapter 3.2), in particular, the processes in the APV25 [Jones et al., 1999], must also be taken into account. This is done as explained in [Klitzner, 2019] based on [Rolandi et al., 2008].
The pulse shape is mainly characterized by the linear amplifying and shaping stage of the APV25. The transfer function can be approximated as:

$$h(t) = \frac{t}{\tau_f \tau_p} exp\left(\frac{-t}{\tau_p}\right) \tag{4.2}$$

with $\tau_p \approx 50\,ns$ being the time constant of the amplification and shaping stage and $\tau_f \gg \tau_p$ being the time constant of the pre-amplifier.

Convoluting the induced current signal $I(t)$ with the transfer function (Equation 4.2) gives the response $O(t)$ of the APV25:

$$O(t) = \int_{\infty}^{\infty} h\left(t - t'\right) I\left(t'\right) dt' \tag{4.3}$$

However, the entire signal induced on a strip is not coupled to the readout chip. This is due to the capacitance of the detector strips and the non-negligible input impedance of the readout chips.
If this is also considered in the transfer function (see Equation 4.2), the transfer function changes according to [Klitzner, 2019]:

$$h(t) = \frac{A}{\tau_f \tau_p} \left(\tau_1 \frac{e^{-t/\tau_1} - a^{-t/\tau_p}}{(\tau_1/\tau_p - 1)^2} + t \frac{e^{-t/\tau_p}}{1 - \tau_1/\tau_p} \right) \tag{4.4}$$

with τ_1 being $\tau_1 = R_{\text{in}} C_{\text{det}}$, R_{in} being the input resistance of the readout electronics and C_{det} being the strip capacitance. In [Klitzner, 2019], good agreement is shown between the measured and calculated APV25 response of a delta-peaked signal.

Chapter 5

Signal Creation in the SGR Detector

In this chapter, the signal-creation processes in the detector are investigated.
Since, in very simplified terms, GEM strips collect ions and Micromegas strips collect electrons, the GEM strip signal is positive and Micromegas strip signal is negative (see Figure 5.1). All signals become bipolar after a certain time. Only the bipolar shape of the signal on the GEM strips can be explained solely by the charge movement in the amplification regions (see chapter 5.3.1).
The signals of the Micromegas readout strip layers become bipolar due to electron movement on the DLC anode layer after the electron avalanche is collected there. In the following, this electron movement is called electron spread.
The signal creation due to the electron spread is investigated in Chapter 5.3.2.

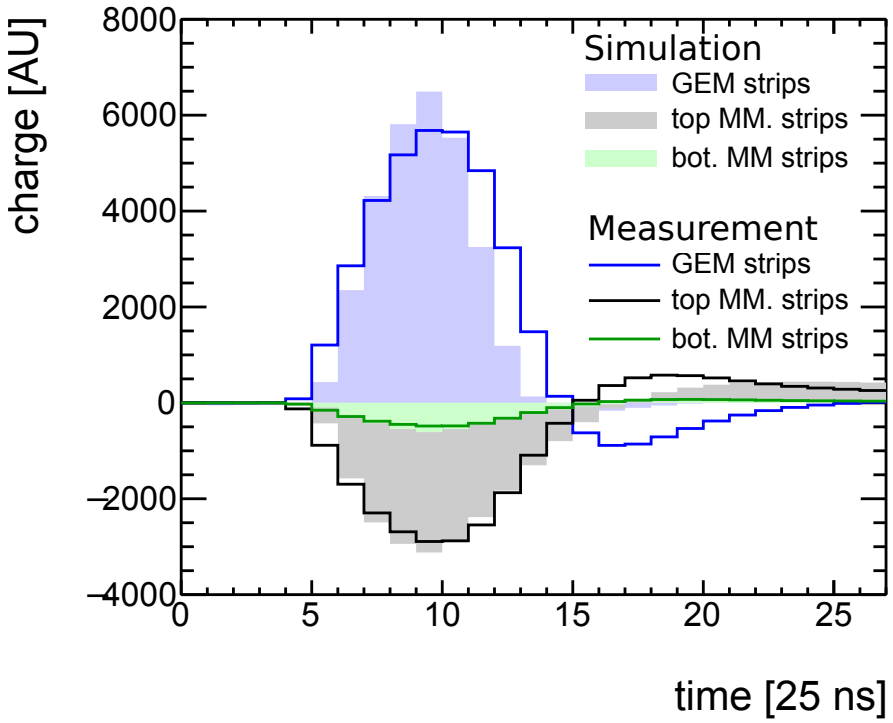

Figure 5.1: Signal of the SGR detector (segmentation on the bottom side of the SGR foil). The highest strip in the signal cluster is shown for each readout strip layer.
U_{drift} = 420 V, U_{GEM} = 200 V, U_{ampl} = 400 V

This chapter is mainly based on simulations done with Garfield++ and ANSYS (see Chapter 4). The simulation allows the investigation of processes in the detector that cannot be resolved with the existing readout electronics. All processes important to obtain a signal as measured are described here. The simulation described in this chapter is also used to understand measurement results in the following chapters.
5.9 keV photons are used for this simulation as ionizing radiation.
If not stated differently the following refers to a SGR detector with the segmentation on the bottom side.

5.1 Simulation of the Electric Field Configuration using ANSYS

The electric field configuration and geometry of a SGR detector are simulated for different combinations of U_{ampl} and U_{GEM} using ANSYS (see Chapter 4.1). Both setups of SGR detectors, one with the segmentation on the top and the other one with the segmentation on the bottom side of the SGR foil are simulated. An exemplary field configuration for U_{ampl} = 400 V, U_{GEM} = 200 V, U_{drift} = 420 V is shown in Figure 5.2 for a SGR detector with the segmentation on the bottom side. The typical properties of the electric field of a MPGD are clearly visible. These are namely a low electric field in the drift region and a high electric field in the amplification regions.
At some distance from the GEM holes, the electric field in the drift region is approximately homogeneous. Protrusions of the strong electric field from the GEM holes form a field line funnel towards the GEM holes like in a GEM detector (see Chapter 2.2). Depending on U_{GEM} the funnel is formed differently[1].
For properly chosen U_{GEM} and U_{ampl}, the electric fields within the GEM foil and the Micromegas amplification region are of the same order. Except at the copper corners of the GEM foil, the magnitude of the electric field is homogeneous. There and especially at the gaps between the GEM strips the electric field is stronger.

As it is shown in the detailed view of the voltage configuration inside a GEM hole (see Figure 5.3) the previously explained protruding field lines reduce the voltage difference inside the GEM holes. Especially in the center of the hole at the surface of the foil facing towards the drift region, the voltage is lower than the voltage of the surrounding copper, i.e. instead of the set -200 V only -170 V is observed in the center of the hole on the top side. This effect is also observed at the surface of the hole facing toward the amplification region. Depending on the ratio of the applied electric fields $|\vec{E}_{ampl}|/|\vec{E}_{GEM}|$, there is either a protrusion of the GEM voltage into the amplification region or a protrusion of the amplification voltage into the GEM holes. The voltage at the bottom surface of the GEM hole is either decreased or increased.
Since both electric fields, $|\vec{E}_{ampl}|$ and $|\vec{E}_{GEM}|$, are of the same order of magnitude, this effect is much weaker here than on the top side of the foil. The actual simulated voltage difference at the position of the holes for different U_{GEM} is shown in Figure 5.4.
Due to the protruding field lines the actual $|\vec{E}_{GEM}|$ is reduced inside the holes. Directly above the holes, the electric field in the drift region $|\vec{E}_{drift}|$ is increased. The protruding electric field is not sufficient to create Townsend avalanches in the drift region.
For higher U_{GEM} the effect of protruding electric fields is more pronounced.

[1] To be more precise, the extent of the funnel depends on the ratio $|\vec{E}_{GEM}|/|\vec{E}_{drift}|$. If this ratio becomes larger, the field line funnel is more pronounced.

This effect also occurs at Micromegas detectors. The influence of this effect is weaker here. Higher voltages are needed at a Micromegas detector to reach the same amplification field as inside the GEM foil. Assuming that for the same electric field strength, the voltage protrusions to the drift region are the same, the influence of the protrusions on the amplification fields of the Micromegas detector is less than that of the SGR detector[2].

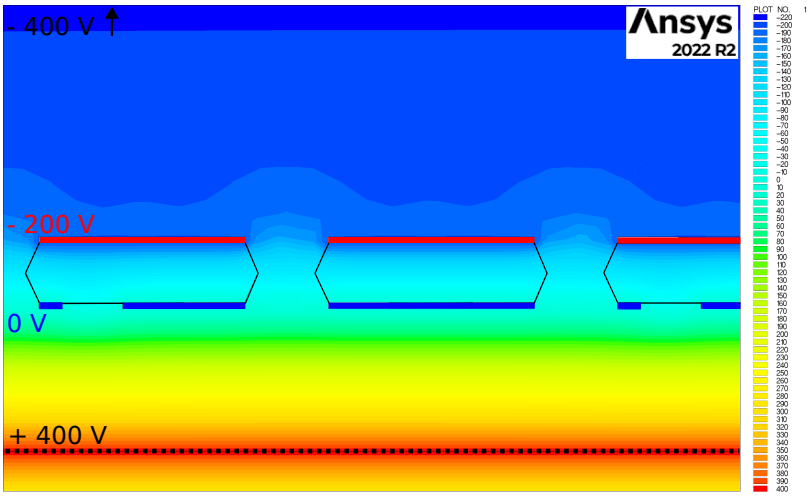

(a) Simulated voltage distribution.

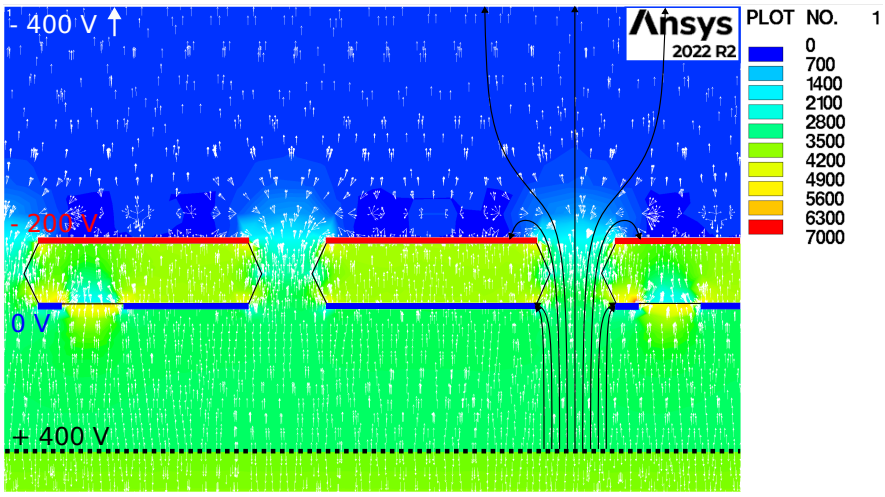

(b) Simulated distribution of the electric field.
The white arrows point in direction of the electric field. A sketch of some field lines is drawn inside the figure. The density of the arrows and sketched field lines is not proportional to the electric field. The field strength is shown by the color coding only.

Figure 5.2: Simulated electric potential end electric field in a SGR detector with the segmentation on the bottom side using ANSYS [ANS, 2022].
Whereas the electric field in the drift region is quite low ($\approx 600\,\mathrm{V/cm}$), it is much higher inside the holes and in the amplification region ($\approx$ few $\mathrm{kV/cm}$). The field lines are bent from the drift region through the holes of the GEM foil forming a funnel.
$U_{ampl} = 400\,\mathrm{V}$, $U_{GEM} = 200\,\mathrm{V}$, $U_{drift} = 420\,\mathrm{V}$

[2]To reach $|\vec{E}_{ampl}| = |\vec{E}_{GEM}| = 40\,\mathrm{kV/cm}$, a voltage $U_{ampl} = 480\,\mathrm{V}$ is required for a Micromegas detector. To reach this field with a SGR foil, $U_{GEM} = 200\,\mathrm{V}$ is required. A voltage reduction of 30 V (as shown in Figure 5.4) at the center of the GEM hole or opening of the micro-mesh reduces the electric field by 15% in the SGR foil (at $U_{GEM} = 200\,\mathrm{V}$) and by 6.25% at the Micromegas detector (at $U_{ampl} = 480\,\mathrm{V}$).

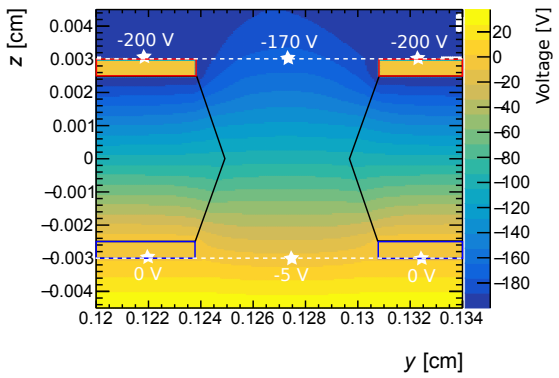

Figure 5.3: Voltage configuration inside the GEM foil.
At the position of the holes, the voltage created by the GEM foil expands to the amplification and drift region. The actual voltage difference between the top side and the bottom side of the GEM hole is less than the applied voltage difference.
U_{ampl} = 310 V, U_{GEM} = 200 V, U_{drift} = 420 V

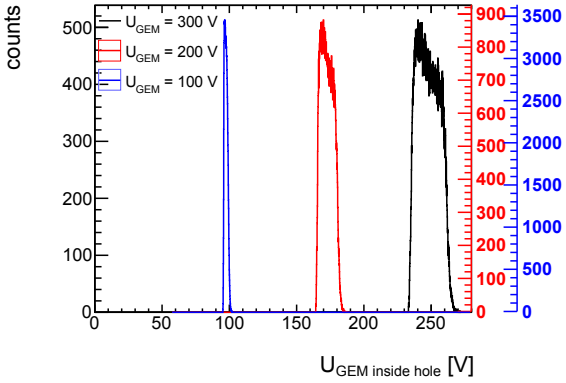

Figure 5.4: Actual voltage difference between the top and the bottom side of the GEM foil at the different X/Y positions of the hole. The actual electric field inside a GEM hole ($U_{GEM\ inside\ hole}$/d) is less than the set electric field $U_{GEM\ set}$/d, with d being the thickness of the foil.
With increasing U_{GEM} the actual voltage difference decreases.
U_{ampl} = 310 V, U_{drift} = 420 V

5.2 Simulation of the Charge Drift and Amplification Processes using Garfield++

The Electric field configuration (see Chapter 5.1) is loaded by Garfield++. The charge drift and electron avalanche process are simulated. Before the actual gas amplification is investigated (see Chapter 5.2.3), the transparency of the SGR foil for electrons (see Chapter 5.2.1) and for back-drifting ions (see Chapter 5.2.2) is investigated.

5.2.1 Simulation of the Transparency of the SGR Foil for Electrons

The optical transparency of the SGR foil is approximately 12 %. It is defined as the percentage of holes in the total area of the SGR foil[3]. Without an electric field applied to the SGR foil, only 12 % of the electrons created in the drift region pass through the foil.
Applying a voltage between the two surfaces of the SGR foil creates an electric field funnel that guides the primary electrons into and through the GEM holes (see Chapter 5.1). This increases the transparency of the SGR foil to electrons. The electron transparency of the SGR foil is defined as:

$$transparency = \frac{N_{transparent\ e^-\ drift}}{N_{all\ e^-\ drift}} \tag{5.1}$$

With $N_{transparent\ e^-\ drift}$ being the number of transparent electron drifts and $N_{all\ e^-\ drift}$ being the total number of primary electrons. An electron drift is considered transparent if at least one electron leaves the GEM hole for one primary electron.

With increasing U_{GEM} at constant U_{drift} the electric field funnel becomes more pronounced. The electron transparency increases (see Figure 5.5).

[3]The size of the holes is defined by the smallest diameter of the hole, which is 50 µm (see Chapter 2.2).

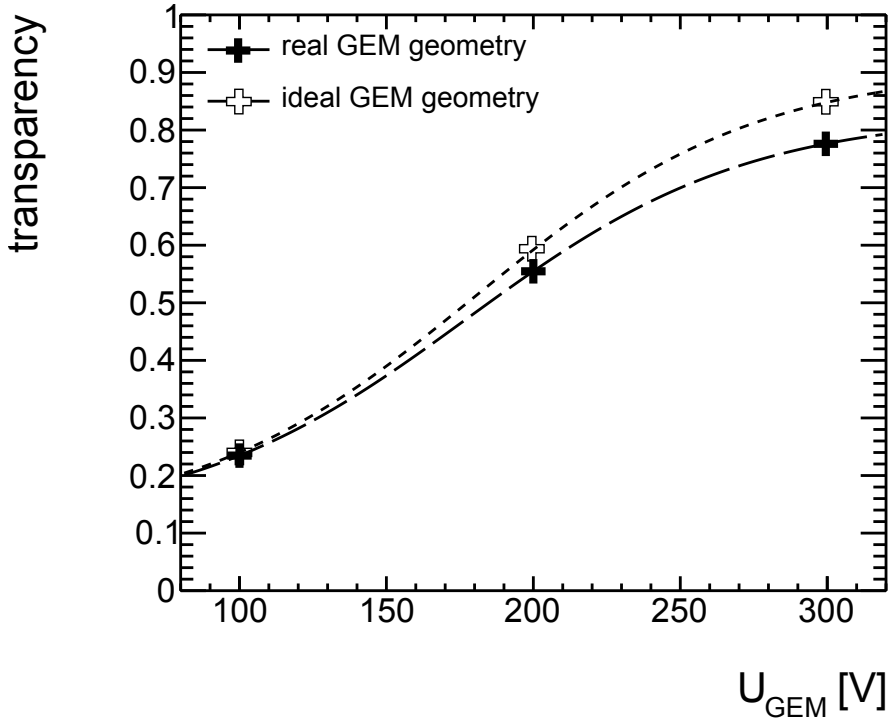

Figure 5.5: Simulated transparency for a SGR foil with the segmentation on the bottom side. The transparency increases with increasing U_{GEM}.
Ideal geometry refers to a SGR foil with: $r_{hole\ copper} = 35\,\mu m$ and $r_{middle} = 25\,\mu m$. Both radii have the same center.
The real geometry refers to the measured geometry: $r_{hole\ copper} = 35\,\mu m$ and $r_{middle} = 24\,\mu m$. The center of both radii are shifted by $3\,\mu m$ to each other (see Figure 5.6).
$U_{ampl} = 310\,V$, $U_{drift} = 420\,V$

In the ideal case, the hole in the copper surface has the same center as the hole in the middle between both copper surfaces. As it is observed with a microscope this is not the case (see Figure 5.6). The holes in the copper surface are shifted by $3\,\mu m$ to the hole in the middle of the foil. The displacement of the two copper surfaces to each other is in the opposite direction so that the centers of the holes on both copper surfaces are $6\,\mu m$ apart. This was adapted in the geometry simulated with ANSYS [ANS, 2022]. These asymmetric holes reduce the electron transparency of the foil. Furthermore, the shifting of the holes does not lead to any appreciable change in the electric field experienced by an electron along the drift path.
This correction is necessary to achieve a match of the pulse height when comparing the simulation with the measurement (see Figure 5.14). For instance, without these corrections, the simulated pulse heights in Figure 5.14e were about 1.5 times too high, while the simulated pulse heights in Figure 5.14a would agree with the measurement.

The transparency of the foil is not measured, but the pulse heights of the simulated signals, which depend among other things on the transparency, agree with measurements (see Figure 5.14).

(a) Segmented side of the SGR foil

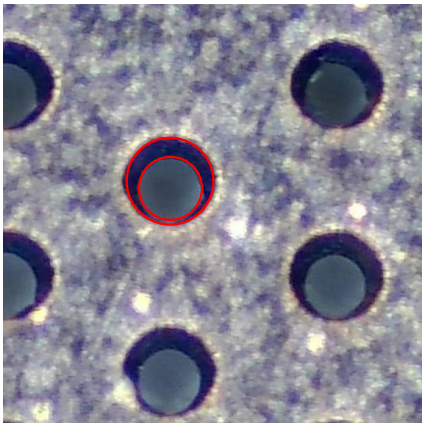

(b) Non segmented side of the SGR foil

Figure 5.6: Photo of GEM holes of the SGR foil taken with a Microscope. The investigated area of the foil is pressed planar onto a table.
The hole in the middle between the two surfaces of the SGR foil does not have the same center as the hole in the copper surface. Exemplarily both diameters are marked for the same hole. The center is shifted by 3 µm. On the other side of the SGR foil, it is shifted in opposite direction, such that the center of the holes at the surface is shifted by 6 µm with respect to each other.
This behavior is the same for various observed holes. The parallax as the origin of this effect is excluded.

5.2.2 Simulation of the Transparency of the SGR Foil for Back-Drifting Ions

The fraction of ions drifting through the GEM holes to the top side of the SGR foil increases with increasing U_{GEM} (see Figure 5.7). This works analogously to the transparency of the SGR foil for electrons (see Chapter 5.2.1).
The strength of the electric field funnel increases with increasing U_{GEM}. More precisely, the funnel strength increases with the increasing ratio of the two electric fields $|\vec{E}_{GEM}|/|\vec{E}_{ampl}|$. Therefore the influence of U_{GEM} is even stronger at constant pulse height than at constant U_{ampl}[4].
At a constant pulse height, the simulated fraction of back-drifted ions increases from 20 % (for U_{GEM} = 100 V, U_{ampl} = 490 V) to 50 % (for U_{GEM} = 300 V, U_{ampl} = 310 V) (see Figure 5.7).

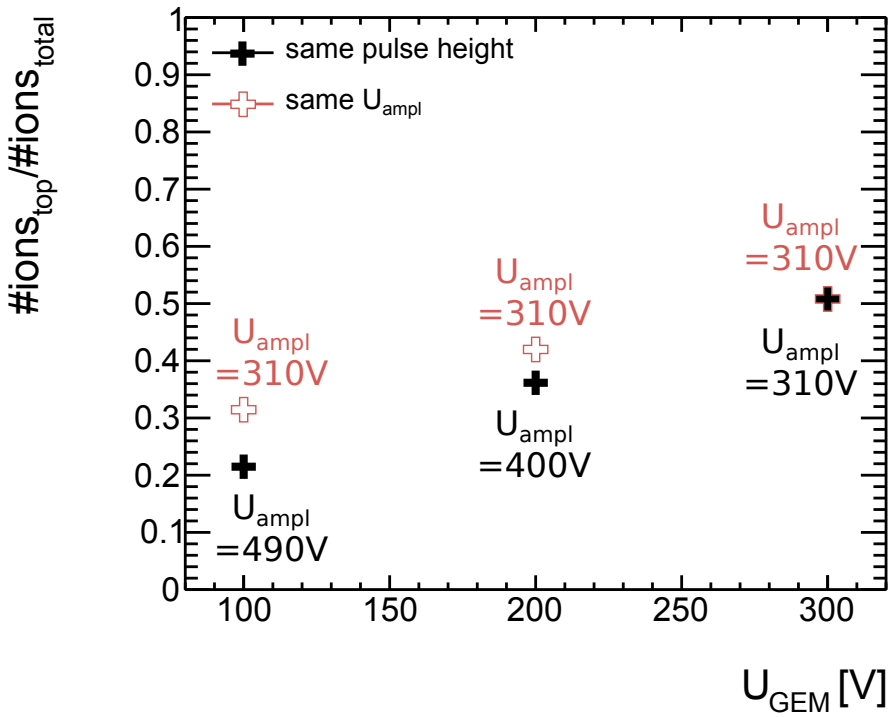

Figure 5.7: Simulated fraction of ions ending on the top side of the SGR foil, which is segmented on the bottom side.
The pairs of voltages for identical pulse height correspond to the values shown for the strip signals (in Figure 5.14).
For comparison, values for constant U_{ampl} = 310 V are given. The fraction increases if the ratio $|\vec{E}_{GEM}|/|\vec{E}_{ampl}|$ increases and thus with increasing U_{GEM}.
U_{drift} = 420 V.

[4] To reach a constant pulse height, U_{ampl} must decrease with increasing U_{GEM}.

5.2.3 Simulation of the Gas Amplification

The SGR detector has two amplification stages. One inside the SGR foil and one in the Micromegas amplification region. The gain is the multiplication factor due to the gas amplification. For following simulations, it is defined:

$$\begin{aligned} G_{GEM} &= \frac{N_{e^- \ created \ in \ GEM}}{N_{e^- \ primary}} \\ G_{ampl} &= \frac{N_{e^- \ collected \ on \ anode}}{N_{e^- \ exiting \ GEM}} \\ G_{total} &= \frac{N_{e^- \ collected \ on \ anode}}{N_{e^- \ primary}} \end{aligned} \tag{5.2}$$

The simulated gain G_{GEM} of the SGR foil is convoluted with the transparency of the SGR foil, which only reaches values smaller than 100 % (see Chapter 5.2.1).
Figure 5.8a shows as expected (see Equation 1.8), the gain inside the GEM holes increases exponentially with increasing $\mathrm{U_{GEM}}$. At $\mathrm{U_{GEM}} = 100\,\mathrm{V}$ on average 0.4 electrons are created per primary electron. This value increases up to 40 at $\mathrm{U_{GEM}} = 300\,\mathrm{V}$ (250 V if voltage correction is applied).
The measured data are compared with gain measurements done with a Micromegas detector [Lippert, 2012]. For Micromegas detectors, the influence of the voltage protrusions on the electric field is lower as for a SGR foil (see Chapter 5.1). To compare the gain simulated for an SGR detector with the gain measured with a Micromegas detector, $\mathrm{U_{GEM}}$ must be corrected for the electric field protrusions. For this comparison, the average values of reduced voltages shown in Figure 5.4 are used as the corrected voltages.
The simulated gain of the ideal SGR foil (see Figure 5.8a) is in good agreement with the gain measured by Lippert [2012] with a Micromegas detector.
In contradiction to a GEM foil, no charges are stopped in the Micromegas detectors during the amplification process. In GEM foils few charges end up on the Kapton surface inside the GEM holes (see Figure B.1). As a result, the gain simulated in the GEM foil is slightly lower than the gain predicted by measurements with a Micromegas detector. This is especially true when the asymmetry of the holes is taken into account (see Figure 5.6).
The gain in the Micromegas amplification region also increases exponentially with increasing $\mathrm{U_{ampl}}$ (see Figure 5.8b). For $\mathrm{U_{ampl}} \approx 300\,\mathrm{V}$ the gain in the amplification region is $\mathcal{O}\left(\mathrm{G_{ampl}}\right) = 40$. For $\mathrm{U_{ampl}} \approx 500\,\mathrm{V}$ the gain increases up to 5000. These values are slightly higher than the expected gain according to Lippert [2012].
Multiplying the gain in the SGR foil (see Figure 5.8a) by the gain in the Micromegas amplification region (see Figure 5.8b) gives the total gain of the SGR detector at a given voltage combination (see Figure 5.8c). For measurements and simulations of 5.9 keV photons the voltage combination is chosen such that the total gain is $\mathcal{O}\left(\mathrm{G_{total}}\right) \approx 1000$. This is fulfilled for the SGR detector with the segmentation on the bottom side for the following voltage combinations:

- $\mathrm{U_{drift}} = 420\,\mathrm{V}$, $\mathrm{U_{GEM}} = 300\,\mathrm{V}$, $\mathrm{U_{ampl}} = 310\,\mathrm{V}$
- $\mathrm{U_{drift}} = 420\,\mathrm{V}$, $\mathrm{U_{GEM}} = 200\,\mathrm{V}$, $\mathrm{U_{ampl}} = 400\,\mathrm{V}$
- $\mathrm{U_{drift}} = 420\,\mathrm{V}$, $\mathrm{U_{GEM}} = 100\,\mathrm{V}$, $\mathrm{U_{ampl}} = 490\,\mathrm{V}$

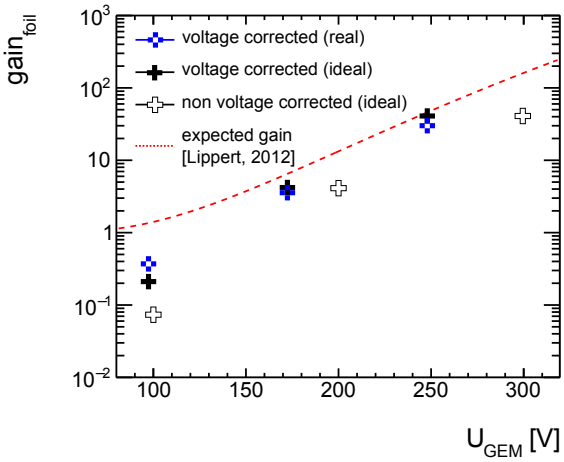

(a) Simulated gain in the GEM foil (G_{foil}) in dependence on U_{GEM}.
Ideal refers to the nominal SGR foil dimensions. Real refers to the SGR foil dimensions as observed in Figure 5.6.
The gain in the SGR foil is convoluted with the foil transparency (see Figure 5.5).
U_{drift} = 420 V, U_{ampl} = 310 V.

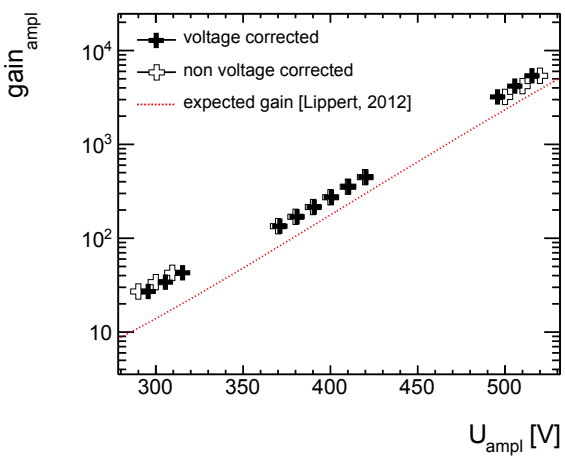

(b) Simulated gain in the Micromegas amplification region G_{ampl} in dependence on U_{ampl}.
Data points at $U_{ampl} \approx 300$ V correspond to experimental data with U_{GEM} = 300 V, points at $U_{ampl} \approx 400$ V to U_{GEM} = 200 V, and points at $U_{ampl} \approx 500$ V to U_{GEM} = 100 V.
U_{drift} = 420 V.

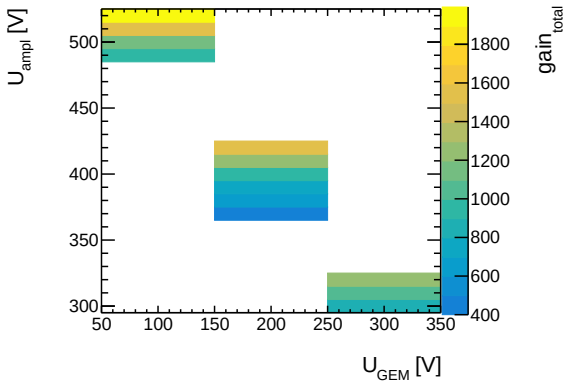

(c) Simulated total gain of the SGR detector G_{total} in dependence on U_{ampl} and U_{GEM}.
The values are simulated for the voltage combination used in the experiment.
U_{drift} = 420 V.

Figure 5.8: Simulated gains in the different detector regions. The red dashed line is the expected gain for a Micromegas detector according to Lippert [2012].
The corrected voltage values (see Chapter 5.1) take the difference in detector geometry between Micromegas and SGR detector into account.
The simulated values are in agreement with the measurements.
G_{total} is determined as the product of G_{foil} (Figure a) and G_{ampl} (Figure b).
80 - 100 events are simulated for each shown point, U_{drift} = 420 V.

5.3 Simulation of the Signal Induction

Charge movements in the detector induce a signal as described in Chapter 4.4.1. If not mentioned differently, the signal induction in a SGR detector is explained in this work as an example of the setup with the segmentation on the bottom side of the SGR-foil.
The weighting fields (see Chapter 4.4.1) are simulated for all readout strips using ANSYS [ANS, 2022] (see Chapter 4.1). The DLC anode is not treated as an electrode for the weighting field simulation. An infinitely large resistive layer[5] does not affect the signal induced directly by the avalanche on the readout strip [Riegler, 2002].
For one SGR strip and one strip of the top Micromegas readout strip layer, the resulting weighting field is shown in Figure 5.9[6]. The strength of the weighting field in the Micromegas amplification region is about the same for the GEM strips and the top Micromegas strips. The further away from the center of the strip the weaker the weighting field becomes. As shown in Figure 5.9, mostly the field lines do not cross the DLC layer vertically[7].
According to Equation 4.1 charge movements induce a signal if there is a parallel weighting field component to the direction of the charge movement[8].
Using these weighting field configurations, GARFIELD++ (see Chapter 4.4) computes the induced signal on the readout strips by Equation 4.1.
The polarity of the induced signal for charge movements in different directions is shown for the top GEM strips in Figure 5.10a and for the top Micromegas readout strips in Figure 5.10b.
In simple terms, a positive charge drifting along the weighting field lines induces a negative signal and a positive charge drifting against the weighting field lines induces a positive signal. For electrons, it is vice versa.

[5] For the investigated setup, the spatial expansion of the avalanche is much smaller than the size of the DLC layer.

[6] The weighting field of the bottom readout strip layer at the location of the amplification region is similar but weaker due to the shielding provided by the top readout strip layer.

[7] Only in the center of the strip do the field lines cross the DLC layer vertically.

[8] Only if the weighting field is perpendicular to the charge movement, no signal is induced.

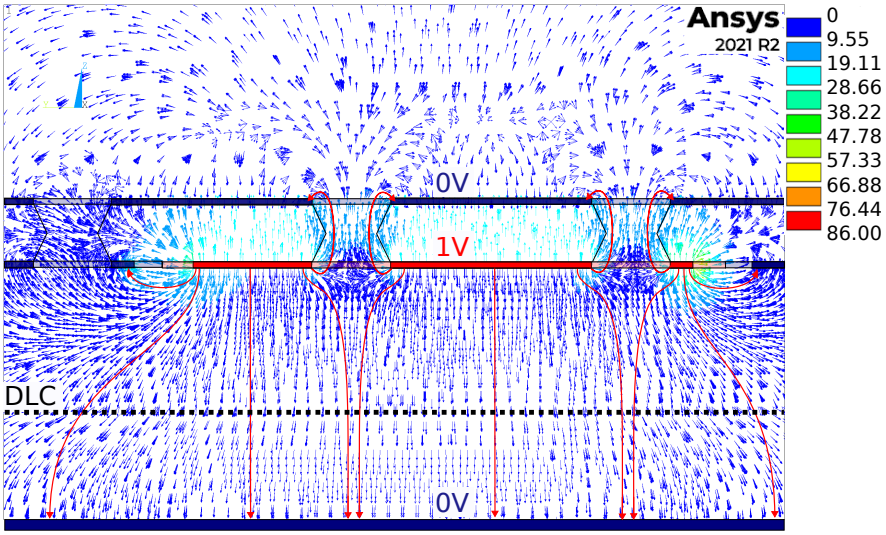

(a) Weighting field lines of the GEM strips in the Y – Z plane.
One of the GEM strips is set to 1 V (red). All other electrodes are set to 0 V.

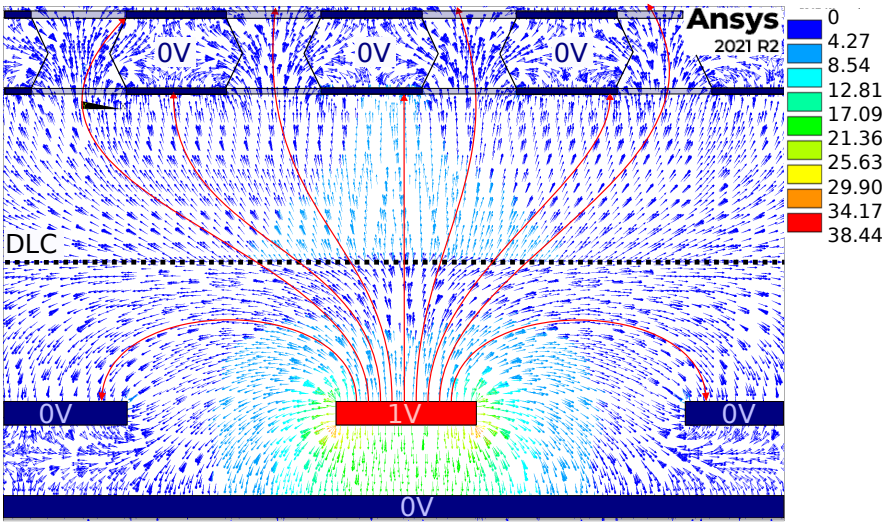

(b) Weighting field lines of the top Micromegas strips in the X – Z plane (bottom Micromegas strips are similar).
One of the top readout strips is set to 1 V (red). All other electrodes are set to 0 V.

Figure 5.9: Weighting field configuration for the different readout layers simulated with ANSYS [ANS, 2022].
A readout strip of interest is set to 1 V, all the other electrodes are set to 0 V. The resistive DLC anode is not considered as an electrode.
The magnitude of the weighting field is shown by the color of the small vectors.
The detector geometry as well as some exemplary field lines are sketched in the same figure.

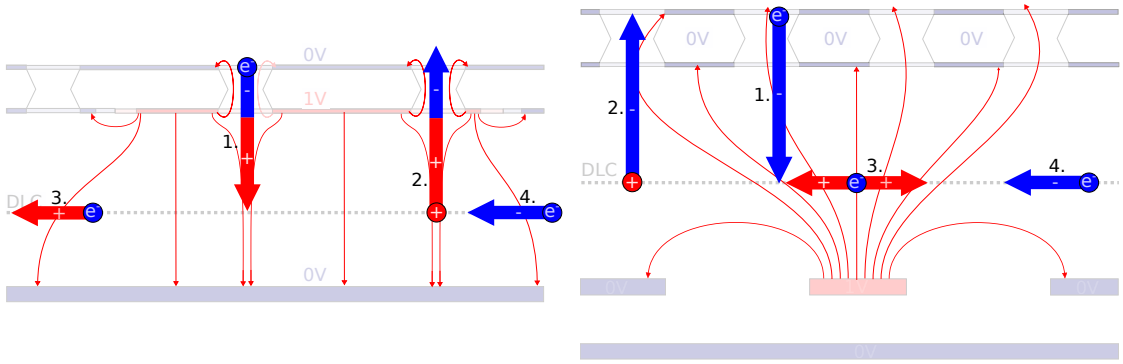

(a) Polarity of the induced signal for the bottom GEM strips.

(b) Polarity of the induced signal for the top Micromegas strips.

Figure 5.10: Polarity of the induced signal according to Equation 4.1 for the movement of different charges in different directions.
Some weighting field lines are drawn for a bottom GEM strip (left) and a top Micromegas strip (right) being the electrode under investigation. The density of the sketched field lines is not proportional to the field strength.
The color of the arrows indicating the direction of movement of the charges shows the polarity of the signal induced as a result of this movement (red: +; blue: -). The following charge movements are considered:

1. Electrons drifting from the GEM foil to the anode.
2. Ions drifting from the anode toward the GEM foil.
3. Electrons drifting on the DLC layer away from the investigated strip.
4. Electrons drifting on the DLC layer towards the investigated strip.

5.3.1 Signal Induced due to Charge Movement in the Amplification Regions

In this section, only the signal induced by the amplification processes in the SGR foil and Micromegas amplification region is considered.
The simulated signal of a SGR detector is shown in Figure 5.13. For the Micromegas readout strips it is negative, for the GEM strips it is positive.

The signal induced by the two avalanche processes is uni-polar on the Micromegas strips. The polarity of the induced signal on a Micromegas strip due to different charge movements is shown in Figure 5.10b. The signal shapes of the Micromegas strips are similar for both SGR detector types and thus independent of the position of the segmentation (see w/o electron spread Figures 5.13a-d).
The signal shape of the GEM strips is strongly dependent on the position of the segmentation (see Figures 5.13e and 5.13f).
The signals on all readout strip layers consist of a fast, peaked signal at the beginning and a longer, usually lower, continuous tail.
The mobility of electrons is several orders of magnitude greater than that of ions (see Chapter 1.1.3). The fast signal is the avalanche of electrons moving to the anode. For the Micromegas strips this signal is negative, for both GEM strip layers it is positive.
The longer-lasting tail is the ion movement towards the SGR foil. The ion signal starts approximately at the same time when the electron avalanche signal is collected[9].

[9]Strictly speaking, it starts at the time of ionization, which is shortly before.

On the Micromegas strips the ion signal ends shortly after the centroid of the ion cloud has either stopped on the SGR foil or entered the GEM holes (compare Figure 5.11 and Figures 5.13a-d (w/o electron spread))[10].

The signal of the GEM strips on the bottom side is bipolar (see Figure 5.13e).
The polarity of the induced signal on a bottom (non-segmented) GEM strip due to different charge movements is shown in Figure 5.10a. As long as the ions drift in the amplification region to the SGR foil a positive signal is induced on the bottom GEM strips. When ions enter the GEM holes and drift through the holes to the top of the foil, a negative signal is induced onto the bottom GEM readout strips (compare Figure 5.11 and Figure 5.13e). Since the drift through the holes happens after the drift in the Micromegas amplification region, this results in a negative component after the positive component of the signal is finished. The signal becomes bipolar.
With increasing U_{GEM} more ions drift through the GEM holes to the top side of the foil (see Chapter 5.2.2). The more ions drift through the holes, the more bipolar the signal becomes.

The signal of the GEM strips on the top side of the SGR foil is unipolar (see Figure 5.13f).
The capacitive coupling of the signal from the bottom side of the SGR foil to the GEM strips is negligible since the signal couples equally on all 212 GEM strips. Each strip receives only about 0.5 % of the coupled signal.
Only the signal induced directly by charge movement on this readout strip layer is relevant (see chapter 5.3). The weighting field lines of these strips are anti-parallel to the ion movement[11] in the Micromegas amplification region and through the GEM holes. A purely positive

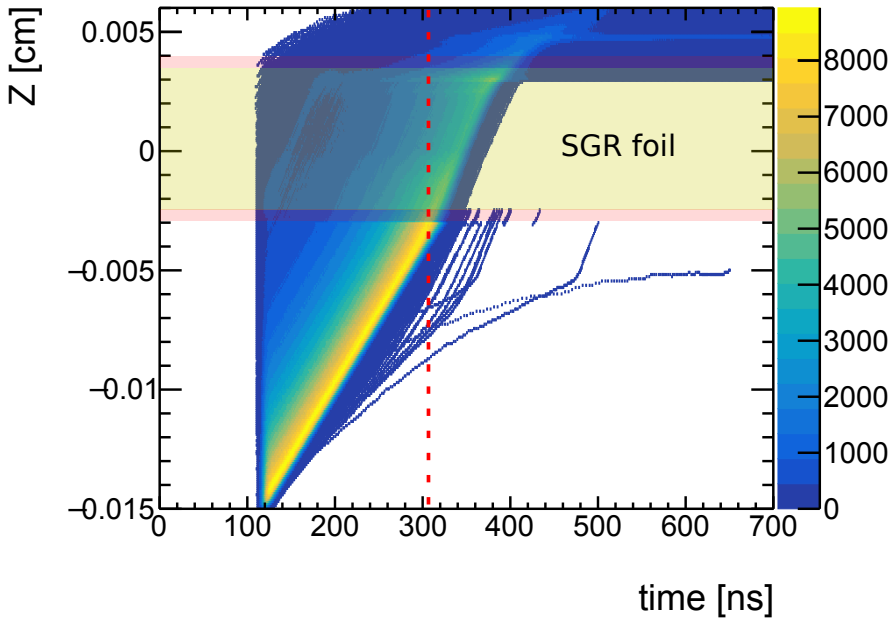

Figure 5.11: Position of the ions drifting towards and through the GEM holes in the SGR foil. The same event is shown as for the bottom segmented SGR detector in Figure 5.13.
Most ions start close to the anode (Z = −150 µm) at t ≈ 120 ns. The centroid of the ion cloud reaches the SGR foil t ≈ 305 ns. A fraction of the ions is drifting through the GEM holes. After that time the signal induced on the bottom GEM strips becomes negative (see Figure 5.13e).
U_{drift} = 420 V, U_{GEM} = 300 V, U_{ampl} = 310 V

[10] The charge movement inside the GEM holes is hardly resolved by the Micromegas readout strips. The bottom side of the SGR foil shields the signal induced by this movement from the Micromegas readout strips.
[11] The weighting field lines are also parallel to the electron movement.

signal is induced on the readout strips on the top side of the SGR foil (see Figure 5.13f). The bottom side of the SGR foil shields the signal induced by the charge movement in the Micromegas amplification region. The charge movement in the Micromegas amplification region has hardly any influence on the signal of the top GEM strips. The signal on the top GEM strips reaches its maximum after most ions entered the GEM holes (compare Figure 5.11 and Figure 5.13f). Since most of the electron avalanche takes place in the Micromegas amplification region, hardly any fast electron signal is observed on the top SGR strips. The signal on this readout strip layer is almost exclusively induced by ion motion inside the holes.
The number of ions ending on the top GEM strips increases with U_{GEM} (see Figure B.2 and Figure 5.7). The more ions drift to the top side of the SGR foil, the higher the signal gets on the top GEM strips.

Combining all the previous information, it is concluded that the signal of both Micromegas strip layers is mainly induced by the charge movement in the amplification region[12]. Therefore, the signals from these readout strip layers of a SGR detector (see Figures 5.13a-d) are assumed to look very similar to those of a standard Micromegas detector.

5.3.2 Signal Induced due to Charge Movement on the DLC Layer

The electron avalanche (see Chapter 5.2.3) is collected at the DLC layer anode. Due to its high resistivity, the electrons do not flow off instantaneously after the charge avalanche has arrived there. This leads to a local charge excess at the positions where the electron avalanche has arrived. A voltage difference with the rest of the anode is created. To compensate for this, the charges diffuse on the anode until they finally arrive at the HV-supply line and flow off. Depending on the detector layout the charges spread along one coordinate, as for a resistive strip anode, or radially as for a DLC layer anode (see Figure 5.12).
In the following, this movement of the electrons on the resistive anode is called electron spread.

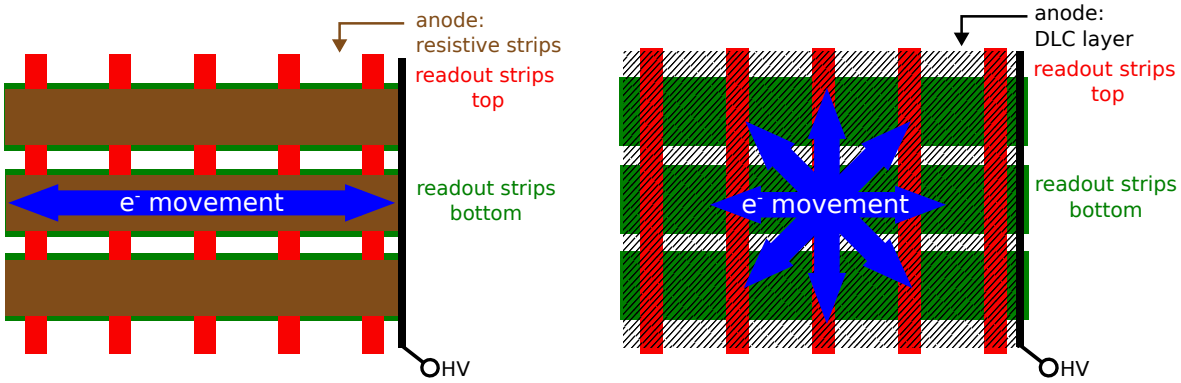

(a) Electron movement on the resistive strips.

(b) Electron movement on the DLC layer

Figure 5.12: Possible moving directions of the electrons after they arrived on the resistive anode.
On resistive strips (left) the electrons can only move along the strip coordinate.
On the DLC layer the electrons spread radially in all directions.
In both cases the electron spread toward the HV supply is slightly stronger.

[12]The signal induced by the charge movement in the GEM holes is shielded by the bottom surface of the SGR foil.

This electron spread influences the measurement (see Chapter 6.3). For the DLC layer anode, the average spread velocity is determined by measurements to be $\bar{v}_{\text{spread}} = 0.0045\,mm/ns$ (see Figure 6.8).
After the avalanche electrons arrived at the anode they remain in their position due to the electrical force of the positively charged ion cloud. This force continuously decreases as the ion cloud moves away from the anode toward the SGR foil. The electrons slowly begin to spread. When the ion cloud ends on an electrode, the charge of the ions is compensated instantaneously. The force that held the electrons in position disappears abruptly and the electrons are free to spread.

The measured drift velocity $\bar{v}_{\text{spread}}$ is the drift velocity averaged over all spreading electrons and all time steps of the spread. Depending on the position of the electron, the actual velocity of each electron differs from that value. To calculate the actual drift velocity for each electron, it is assumed that the charges on the anode propagate by diffusion.
Diffusion is described by Ficks's law [Fick, 1855]:

$$\vec{J} = -D\nabla c \tag{5.3}$$

with D being the diffusion coefficient, c being the concentration and $\vec{J}$ being the particle flux density. With the electric current on the anode $\vec{I}_{\text{spread}} \propto \vec{v}_{\text{e}^-}$ and the number of electrons $N_{e^-} \propto c$, according to Equation 5.3, for charge movement on a 2D layer, the following applies:

$$\vec{v}_e \propto \vec{I}_{spread} \propto \nabla N_{e^-} \tag{5.4}$$

In the simulation, for simplicity, each electron arriving at the anode is moved in time steps of $\Delta t = 1\,ns$ with $\vec{v}_{\text{e}^-}$ after the corresponding ion has stopped its drift.
For the simulation, $\vec{v}_{\text{spread}}$ is determined for each electron as a function of its position using Relation 5.4.
It is assumed that all charges on the anode are Gaussian distributed[13]. To determine $\vec{v}_{\text{e}^-}$ the hit distribution on the anode is fit with a 2D-Gaussian function. The derivative of the 2D Gaussian function is determined at the position of each electron. According to Equation 5.3 and Relation 5.4 this is proportional to $\vec{v}_{\text{e}^-}$.
The exact diffusion coefficient D has not yet been determined. The mean drift velocity determined via Relation 5.4 is normalized to the mean velocity $\bar{v}_{\text{spread}}$ determined via measurements (see Figure 6.8).
After each time-step Δt, $\vec{v}_{\text{e}^-}$ is determined anew for each electron. The normalization factor always remains the same.
If $\vec{v}_{\text{spread}}$ would be the same for all electrons, the influence of the electron spread on the signal shape would be too strong (see Figure B.4).

The charge spread on the DLC anode induces a signal as previously explained unless the charges move perpendicularly to the weighting field lines (see Figure 5.10).
On a resistive strip anode, the drift is only possible along the resistive strip coordinate. Whereas the weighting field lines of the readout strips parallel to the resistive strips show no parallel component to the charge movement, the weighting field lines of the other readout strip layer show a parallel component to the charge movement. The electron drift is only resolved in one direction.
On the DLC layer anode the electrons spread in all directions (see Figure 5.12). The weighting field lines of both readout strip layers show parallel components to the charge movement. The electron spread is resolved on both Micromegas readout strip layers.

[13] The periodic pattern of endpoints as shown in Figure 7.1b is ignored for simplicity.

In Figure 5.13 besides the pure avalanche signal also the signal is shown in which the electron spread on the DLC layer is considered.
Electrons drifting away from an investigated readout strip induce a positive signal on that strip. Electrons drifting towards that readout strip induce a negative signal (see Figure 5.10). Only the central strip in the signal cluster is investigated in Figure 5.13. Therefore, electrons mainly move away from the strip under consideration. On the central strip in the cluster, mostly a positive signal is induced. This holds for all readout strip layers in both SGR detector setups.

For simplicity, in the simulation, it is assumed that the spreading of electrons begins only when the ions stop at the electrodes. For the investigated voltages at least 50 % of the ions are stopped at the bottom of the SGR foil (see Figure 5.7). Therefore, the electron spread signal starts when the remaining ions drift through the GEM holes. A positive component is added to the prompt avalanche signal when the ion signal is almost terminated[14]
The positive component due to the electron spread makes the signal of the Micromegas strips bipolar (see Figures 5.13a-d).
A signal is also induced on the GEM strips on the bottom side. Due to the much smaller parallel component of the weighting field, the induced signal is smaller and hardly visible in Figure 5.13e. Since the positive component due to the electron spread starts at approximately the same time as the negative component of the prompt signal, the negative component of the GEM signal shrinks minimally.
The electron spread on the DLC layer is not resolved with the top GEM strips (see Figure 5.13f). As discussed in 5.3.1, charge movements in the amplification region are shielded from the top GEM strips. Capacitive coupling from the non-segmented side of the foil (bottom) to the segmented side (top) is negligible.

As for the signal induced due to the avalanche process (see Chapter 5.3.1) it is assumed that the signal of the DLC layer Micromegas detector influenced by the electron spread looks very similar to the signal of the Micromegas readout strips in the SGR detector.
As already mentioned, the electron spread signal is resolved on only one layer in resistive strip detectors. Due to the higher electron spread velocity in resistive strip detectors (see Figure 6.8), the signal induced by the electron spread is higher in the resistive strip detector than in the DLC layer detector. As it will be proven by the measurements in Chapter 6.3.2, the bipolarity is more pronounced in the resistive strip detectors than in the DLC layer detectors.

[14] Due to the spatial expansion of the ion cloud, this timing is slightly before the ion signal finishes.

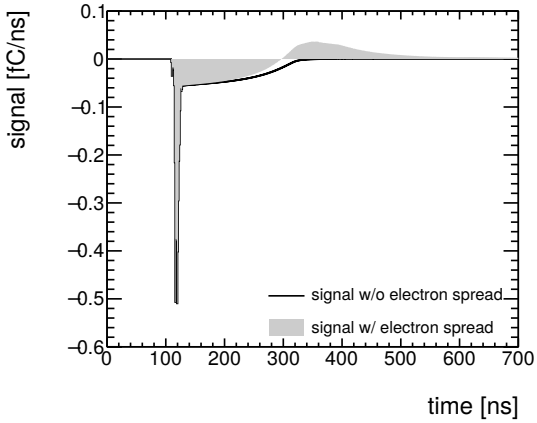

(a) Top Micromegas readout strip.
SGR foil segmented on the bottom side.

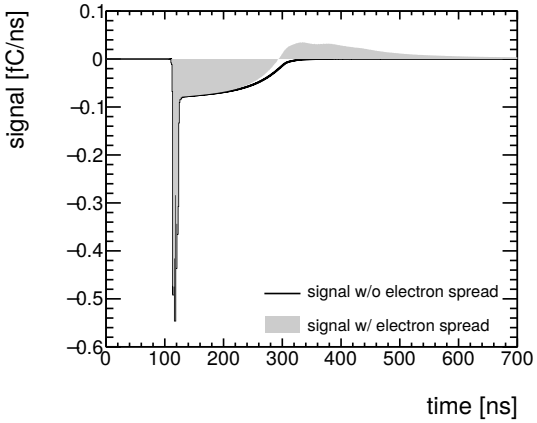

(b) Top Micromegas readout strip.
SGR foil segmented on the top side.

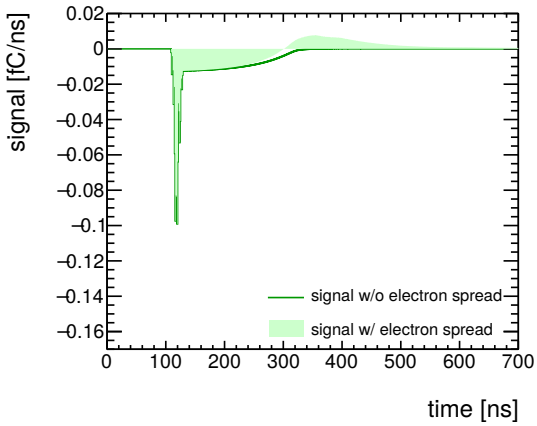

(c) Bottom Micromegas readout strip.
SGR foil segmented on the bottom side.

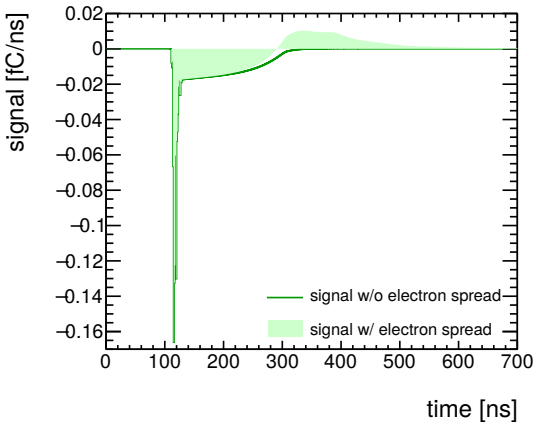

(d) Bottom Micromegas readout strip.
SGR foil segmented on the top side.

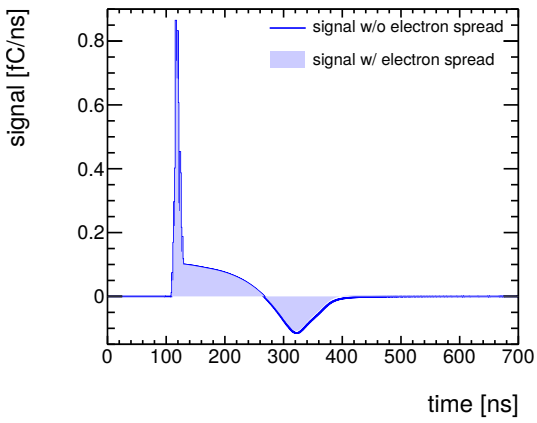

(e) GEM strip on the bottom side.
SGR foil segmented on the bottom side.

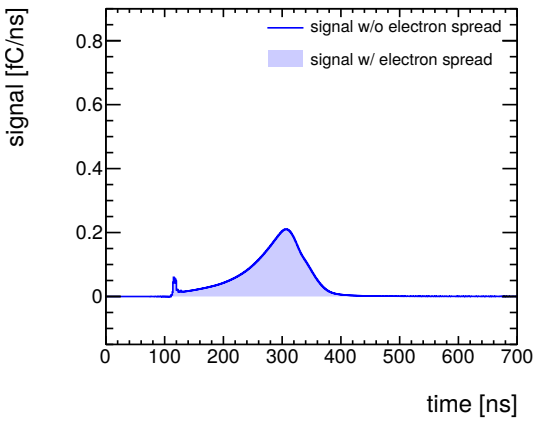

(f) GEM strip on the top side.
SGR foil segmented on the top side.

Figure 5.13: Simulated signal of a single 5.9 keV photon event for a SGR detector with the segmentation on the bottom (left) and on the top (right) side. The highest strip signal of the cluster is shown.
The signal of a SGR detector resolves the prompt signal induced by the electrons in the avalanche (peak at 100 ns) as well as the slower ion drift (tail).
The signal is plotted with (shade histograms) and without (open histograms) consideration of the electron spread on the DLC layer. While the signals of the Micromegas readout strips (green and black) become bipolar by the electron spread, the signals of the two GEM strip layers (blue) are hardly affected by the electron spread.
After the readout electronics is considered in the simulation, the simulated signal shapes are compared with measurements (see Figure 5.14).
U_{drift} = 420 V, U_{GEM} = 300 V, U_{ampl} = 310 V (SGR bottom), U_{ampl} = 340 V (SGR top)

5.3.3 Comparison of the Simulated Signal with the Measured Signal

At last, the influence of the readout electronics on the signal shape is simulated as described in Chapter 4.4.2. The required strip capacitances are listed in Table 5.1. These were determined by assuming the detector to be a plate capacitor for simplicity (see Chapter 3.3).
As measured in [Klitzner, 2019] the input resistance of the APV25 is R = 300 Ω.

electrode	capacitance
top Micromegas strips	30 pF
bottom Micromegas strips	25 pF
bottom GEM strips	40 pF
top GEM strips	30 pF

Table 5.1: Calculated capacitances of all readout electrodes.
The listed capacitances are the summed capacitances between the listed electrode and all other electrodes (incl. ground).
The capacitances are calculated assuming the detector can be approximated as a plate capacitor (see Equation 3.1).

For varieties of U_{GEM} and U_{ampl} the simulated signals of the highest signal strip of each layer in an event are shown in Figure 5.14. The simulated signals shown are averaged over 100 simulated events.
The simulated signal shapes match the measured signals for both SGR detectors. Deviations in the signal length are due to insufficiently known ion mobilities (see Chapter 4.4). The ion mobility is also affected by possible impurities in the gas, air pressure, and temperature. Unfortunately, these values are not available for the measurements. While the signals match well at high U_{ampl}, the deviation becomes slightly larger for decreasing U_{ampl}. The ion mobility at low voltages is likely lower than assumed.
Deviations in the bipolar component are due to the simplification of the electron spread. It was assumed that the electron distribution on the anode is Gaussian (see Chapter 5.3.2).
The pulse height of the measured signal and the simulated signal are approximately equal. Deviations are due to the detector structure, which is assumed to be ideal. Possible deformations of the foil and deviations from the nominal dimensions have been neglected except for those shown in Figure 5.6.
The ratio of the simulated pulse heights of the different readout strip layers to each other also agrees with the measurements.

Looking at the spatial propagation of the signal on the top Micromegas readout strip layer, a V-shape characteristic of the electron spread is visible (see Figure 5.15). Strips that barely resolve a prompt avalanche signal resolve only the electron spread. At first, the movement of the charges in the direction of these strips is resolved (negative signal as shown in Figure 5.10). After that, the movement away from these strips is resolved (positive signal as shown in Figure 5.10). Due to the finite speed of the electrons on the DLC layer, these signals are created at a later time. The simulated signal shown in Figure 5.15b is similar to the signal measured with a Micromegas detector (see Figure 6.6).

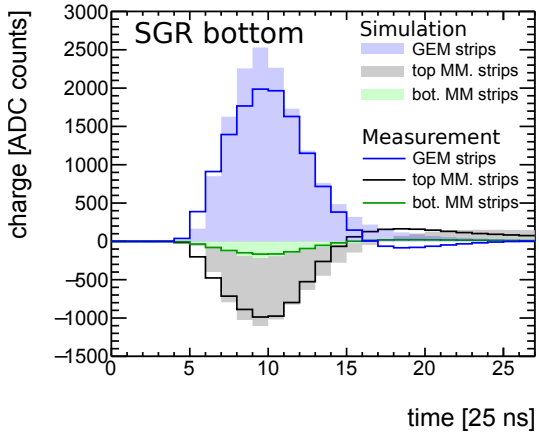

(a) U_{drift} = 420 V, U_{GEM} = 100 V, U_{ampl} = 490 V
Total gain: G_{total} = 979

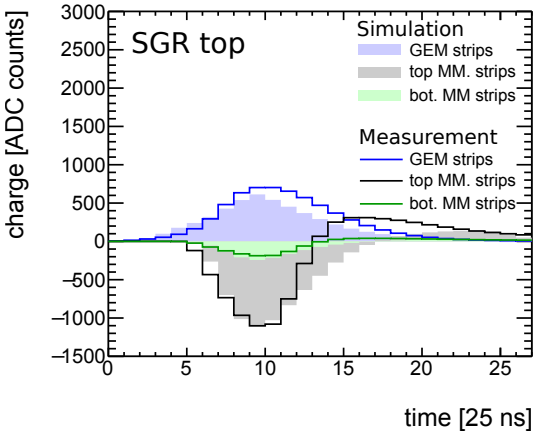

(b) U_{drift} = 420 V, U_{GEM} = 100 V, U_{ampl} = 510 V
Total gain: G_{total} = 1131

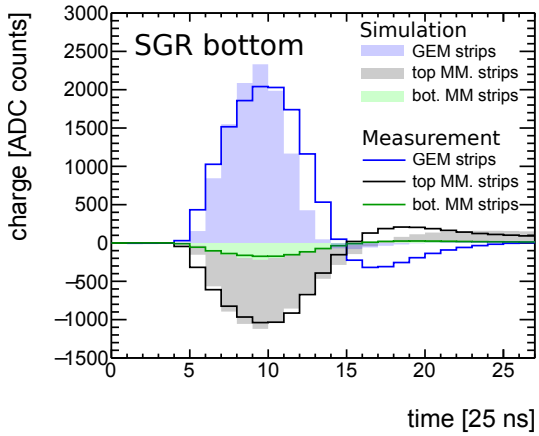

(c) U_{drift} = 420 V, U_{GEM} = 200 V, U_{ampl} = 400 V
Total gain: G_{total} = 973

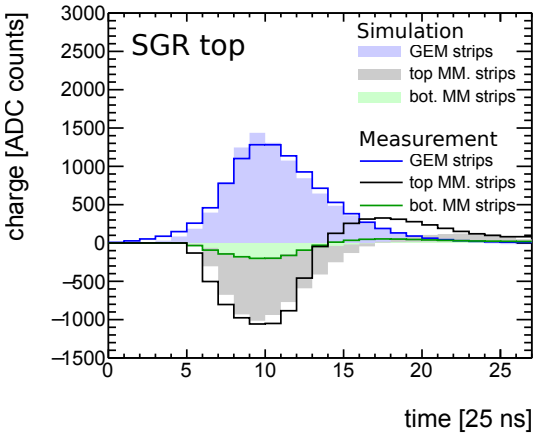

(d) U_{drift} = 420 V, U_{GEM} = 200 V, U_{ampl} = 430 V
Total gain: G_{total} = 1292

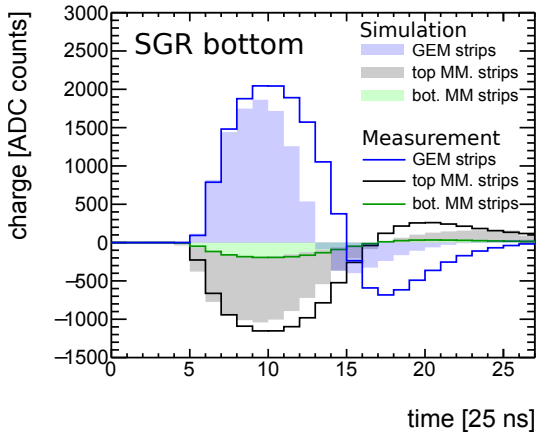

(e) U_{drift} = 420 V, U_{GEM} = 300 V, U_{ampl} = 310 V
Total gain: G_{total} = 1023

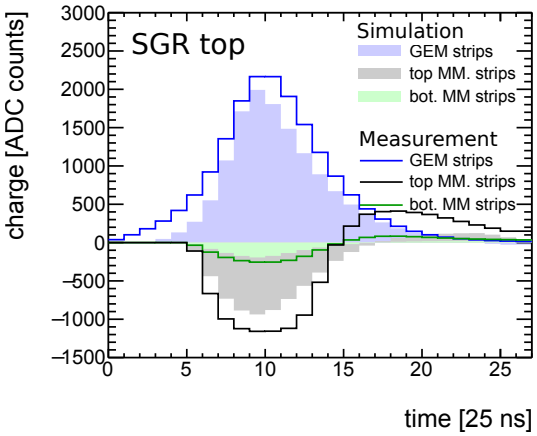

(f) U_{drift} = 420 V, U_{GEM} = 300 V, U_{ampl} = 350 V
Total gain: G_{total} = 1447

Figure 5.14: Simulated (filled) and measured (lines) signals of a SGR detector with the segmentation on the bottom side (left) and on the top side (right).
The highest signal strip in an event is shown. All signals are aligned to peak at the same time. The measured signal is averaged over a few thousand events. The simulated signal is averaged over 100 events.
The electron spread on the DLC layer is considered for this simulation (see Chapter 5.3.2). The readout electronics is simulated as described in Chapter 4.4.2.
The simulated data are normalized to the measured data. The normalization factor is the same for all signals shown.
The stated gain is calculated using Equation 5.2. The gain is convoluted with the transparency of the SGR foil. Therefore, the specified gain differs in the figures shown.
Signals are shown for approximately the same measured pulse height with the top Micromegas strips.

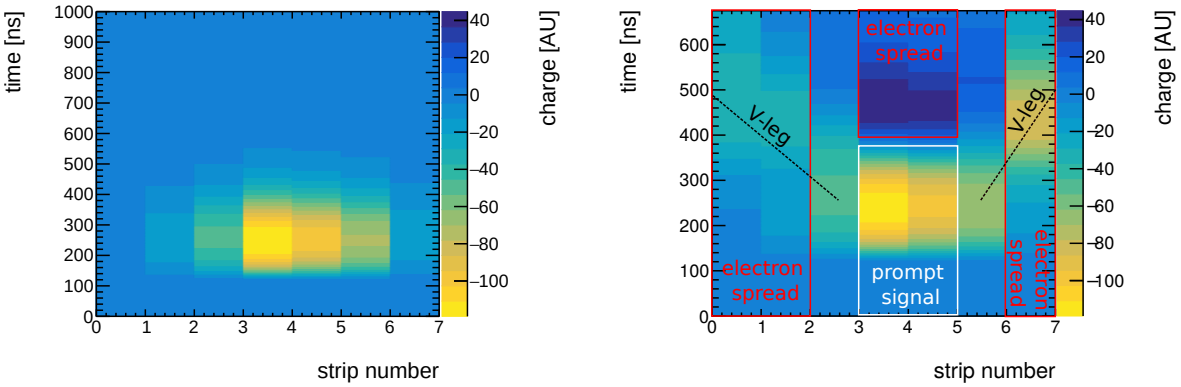

(a) Electron spread on the anode not included.

(b) Electron spread on the anode included.

Figure 5.15: Simulated time-dependent charge signal for all strips hit in a single event for the top Micromegas readout strip layer.
Strips, which hardly resolve prompt avalanche signal, resolve only electron spreading (strips 0,1, and 6).
At first, the movement of the electrons in the direction of these strips is resolved as a negative signal (see Figure 5.10). This is resolved for strips 0,1, and 6 (red box).
After that, the movement away from these strips is resolved as a positive signal (see Figure 5.10). The signal shape of strips 3 and 4 thus becomes bipolar (white box).
A V-shape characteristic for the resolved electron spread is resolved (indicated by the V-legs).
The electron spread is not properly resolved in this simulation on the outermost strips (strips 0 and 6). These strips only see the charge movement toward the strip, but not the charge movement away from the strip.
In this figure, the readout electronics is simulated as described in Chapter 4.4.2.
In measurements using a DLC anode, this characteristic V-shape is observed (see Figure 6.6a, note that the pulse height of the experimentally measured signal is inverted.).
U_{drift} = 420 V, U_{GEM} = 300 V, U_{ampl} = 310 V

5.4 Summary of the Simulated Signal Creation of an SGR Detector

The signal formation in a SGR detector using a DLC layer anode was simulated with ANSYS (see Chapter 4.1) and GARFIELD++ (see Chapter 4.4). The simulated gain matches the expectation (see Figure 5.8).
Like a typical Micromegas signal, the signal of the SGR detector consists of a fast signal due to the electron avalanche and a slower signal caused by the ion movement (see Chapter 5.3.1). The charge movement on the anode affects the signal shape of the Micromegas readout strips (see Chapter 5.3.2). The signal becomes bipolar. The simulated Micromegas signal matches the measured signal (see Figure 5.14). The V-shape of the signal characteristic for the electron spread is resolved in the simulation (see Figure 5.15). This is compatible to the measurements (see Figure 6.6).
The signal of the GEM strips on the bottom side of the SGR foil is bipolar. The bipolarity gets stronger with increasing U_{GEM} (see Figure 5.14). More ions are drifting through the hole towards the top side (see Figure 5.7). The simulated signal shapes and pulse heights agree with the measured signals (see Figure 5.14).

Chapter 6

Characterization of the 2D DLC layer Micromegas Detector using ^{55}Fe

The anode structure for the SGR detector is one of the first produced 2D readout structures using a DLC layer as an anode. Whereas 2D resistive strip type Micromegas detectors are used for multiple years the 2D DLC layer type detectors were not investigated yet. DLC layer Micromegas detectors need to be understood in order to understand the SGR detector. Measurements performed with a DLC layer Micromegas detector are compared to measurements made with resistive strip Micromegas detectors. The only differences between the two detectors are the anode structure and the height of the amplification region. Due to the different heights of the amplification regions, a higher U_{ampl} is needed for the DLC layer detector to reach the same gain.
Unless otherwise stated, the measurement results shown are for the DLC layer Micromegas detector.
Signals and pulse heights induced by electrons moving toward the readout strips and ions moving away are negative. For optical reasons, these signals are inverted in this chapter. When speaking of negative or positive signals, this refers to the signal shape shown in the following figures.

6.1 Measurement Setup

The setup of the detector is shown in Figure 6.1. The detector was continuously flushed with a gas mixture of Ar : CO_2 at a volume % ratio of 93 : 7. It was irradiated with an ^{55}Fe source.
The detector was read out using six APV25 front-end boards in a master-slave configuration. One FEC card and one ADC card were used (see Chapter 3.2). HV was applied to the anode and the cathode[1]. The error of the applied voltages is $U_{set} \pm 0.3\,\% \pm 0.5\,V$. This error is not further specified in the following work.
While the cathode voltage was kept constant at $U_{drift} = 300\,V$[2] the amplification voltage was varied. At least several thousand events were measured for each voltage configuration shown in the following chapters.

[1] CAEN Model A1821H(N) [CAEN, 2013]
[2] With a drift gap of 5 mm height, this corresponds to the voltage to reach the maximum drift velocity according to Figure 1.3.

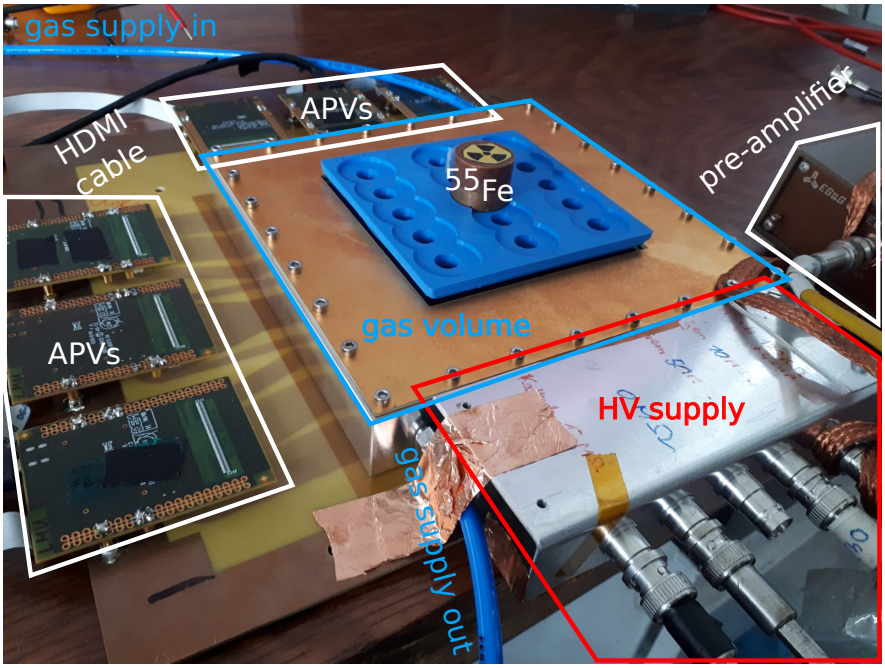

Figure 6.1: Measurement setup for the measurement with a Fe55 γ – source.
As a trigger, the amplified signal of the micro-mesh respectively the non-segmented side of the GEM foil is used. The detector is read out with six APV25 front-end boards in a master-slave configuration using a SRS.

The micro-mesh was grounded via a pre-amplifier[3]. The pre-amplified signal of the mesh was used to trigger. It was shaped by a spectroscopy amplifier[4] and converted to a Nuclear Instrumentation Standard (NIM) signal by a Constant Fraction Discriminator (CFD)[5]. A dual timer[6] extended the duration of the NIM signal until it was reset via a signal from the DAQ PC. The reset signal was sent when the event was fully processed by the DAQ PC[7]. The NIM signal from the dual timer was used to trigger the SRS. A sketch of the readout logic is shown in Figure 6.2.
This setup was used to analyze the signal shape as well as the pulse height and the dynamic range of the detector.

For these measurements, the ^{55}Fe isotope was well suited. As summarized in [Danger, 2014] the main decay products leaving the ^{55}Fe source are 5.9 keV photons. These photons interact via the photoelectric effect in the detector gas (see Figure 1.2). Depending on the atomic shell that is ionized, the ion may be in an excited state after ionization. Based on the deexcitation processes of the ion, either the total photon energy E_γ is released in the detector volume, or part of the initial energy leaves the detector in the form of another photon so that only $E_{\text{Ar escape}} = 3\,keV$ is deposited in the detector volume.
The ratio between both energies is:

$$\frac{E_\gamma}{E_{Ar\ escape}} = \frac{5.9\,keV}{3\,keV} = 1.97 \tag{6.1}$$

[3]Ortec Model 142PC [Ortec, 2002]
[4]Ortec Model 452 [Ortec, 1970]
[5]CAEN Model N843[CAEN, 2021]
[6]CAEN Model N93B [CAEN, 1991]
[7]Problems occur with the SRS if multiple triggers arrive while the data of the previous event are still being processed

The photoelectrons generated by the photoelectric effect ionize other gas atoms. The resulting electrons drift along $\vec{E}_{drift}$ into the amplification region. The energy of the photoelectron is proportional to the average number of electrons produced by it [Sauli, 1977].

When the energy spectra are considered in the following chapters, the Argon escape peak refers to the measured energy corresponding to 3 keV photoelectrons.

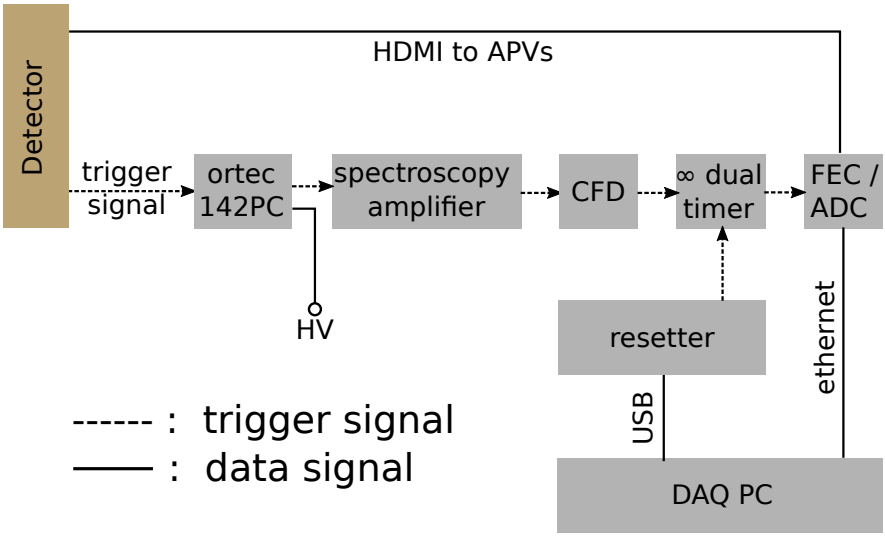

Figure 6.2: Schematic picture of the trigger and DAQ setup used for measurements with a ^{55}Fe γ – source.
The signal of the micro-mesh is used for triggering. The signal on the micro-mesh is pre-amplified (Ortec 142PC) and guided via LEMO cables (dashed lines) to the NIM modules. To ensure that no new trigger is accepted before the present signal is processed, the NIM pulse of the trigger signal is made infinitely long by a dual timer. After all data are processed by the SRS and the DAQ PC the dual timer is reset. New triggers can be accepted.
The APV25 front-end boards are connected via HDMI cables to the ADC card, which is directly connected to the FEC card (PCIe). The FEC itself is read out by the DAQ PC via an Ethernet cable. The FEC card receives the trigger signal from the dual timer.

6.2 Pulse Height Homogeneity for the DLC Layer Micromegas Detector

The backside of the readout structure is strengthened by a 10 mm aluminum plate to avoid deformations of the readout PCB (see Figure 6.3).
The micro-mesh of the DLC layer detector Micromegas lies on top of the pillars. The pillars define the height of the amplification region. It must be ensured that the micro-mesh touches the pillars everywhere to obtain a uniform amplification field and thus a uniform gain over the entire active area. The micro-mesh is pressed onto the coverlay outside of the active area[8] (see Figure 6.3). In Figure 6.4 approximately 30 % variation in the pulse height is observed in dependence of the position.
Comparing details between Figure 6.4a and Figure 6.4b the pulse height variation is stronger on the bottom readout strip layer than on the top readout strip layer. At lower pulse heights, readout strips are more likely discarded as noise. As a result, the total reconstructed cluster pulse height is lower than the actual cluster pulse height. This enlarges the pulse height inhomogeneity.
The pulse height is higher towards the edges of the active area along the Y-axis and smaller towards the edges of the active area along the X-axis. Apart from the possibility that the pillars may not have the same height, this is most likely because the micro-mesh does not lie on the pillars uniformly due to deformations of the micro-mesh or the anode.
It is expected that this does not strongly influence the spatial properties of the detector since the pulse height variation is continuous over the whole detector.
Areas of reduced pulse height are observed with the top readout strips (X-coordinate) at the X-positions of the pillars[9] and with the bottom readout strips (Y-coordinate) at the Y-position of the pillars[10]. The reason for this is still under investigation. Apart from these inefficient regions, no variations in pulse height are observed in the spatial expansion of a signal cluster[11].

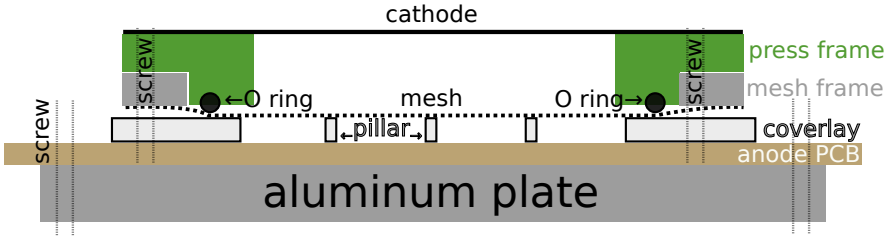

Figure 6.3: Schematic of the mounting of the DLC layer Micromegas detector.
The backside of the readout structure is strengthened by an aluminum plate, which is screwed to the readout PCB.
To ensure the micro-mesh touches the pillars everywhere, it is pressed via a press frame to the coverlay. A flexible O-ring is used between the press frame and micro-mesh to compensate for irregularities. The press frame slightly extends into the active area. This leads to inefficient areas at the edge of the active area (see white areas in Figure 6.4).

[8] The height of the coverlay is the same as the height of the pillars.
[9] This is best visible at X=210 or X=265 in Figure 6.4a.
[10] This is best visible at Y=95 or Y=150 in Figure 6.4b.
[11] The spatial expansion of a cluster are a few strips.

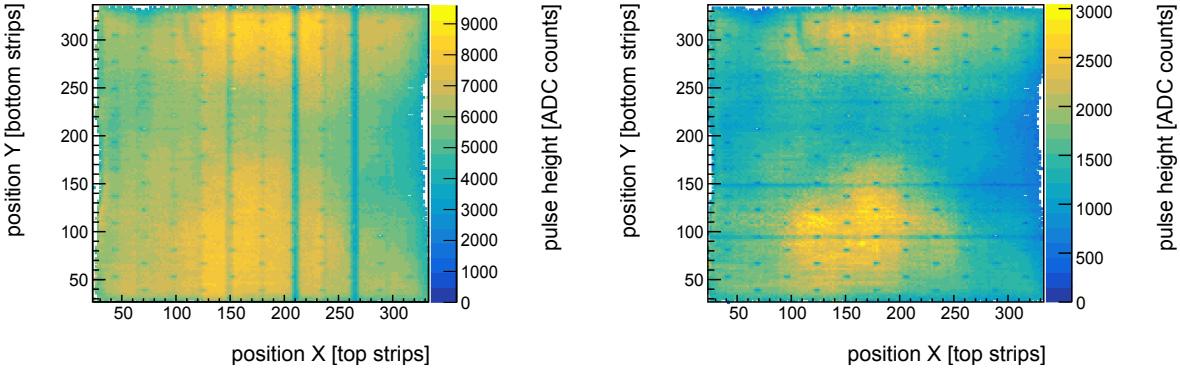

(a) Pulse height of the top Micromegas strips in dependency of the 2D hit position.
At the X-position of the pillars (best visible at X=210 or X=265) the pulse height is reduced.

(b) Pulse height of the bottom Micromegas strips in dependency of the 2D hit position.
At the Y-position of the pillars (best visible at Y=95 or X=150) the pulse height is reduced.

Figure 6.4: Mean cluster pulse height in dependency of the 2D hit position.
The position dependence of the pulse height is visible at the same positions for both readout strip layers. Small deformations of the anode plane, respectively unequal pillar heights result in an unequal height of the amplification gap. The amplification field is not the same everywhere.
The pulse height reconstructed with the top readout strip layer is higher than that of the bottom readout strip layer.
Different from Chapter 6.4, the electron spread as well as saturated events are included in the shown data.
The white areas at the border of the active area are inefficient areas due to the mounting of the press frame.
U_{drift} = 300 V, U_{ampl} = 570 V.

6.3 Electron Spread Analysis

In Figure 6.5 and Figure 6.6 the time-depended charge signals are shown for all strips in one signal cluster. The V-shape observed in Figures 6.5a, 6.6a, and 6.6b is typical for the resolution of electron motion on the anode. After the electron avalanche reaches the anode, the electrons diffuse with a finite velocity (see Figure 6.8) on the resistive layer until they reach the HV supply line (see Chapter 5.3.2). Strips that do not see the prompt signal of the avalanche observe only the signal of the electron spread at a later time. The greater the distance of a strip from the center of the signal cluster, the later the signal arrives and the lower it is.
This charge movement on the resistive anode and the induction of the signal by this movement is explained in Chapter 5.3.2. It is resolved with both the resistive strip Micromegas detector (see Figure 6.5a) [12] and less pronounced with the DLC layer Micromegas detector (see Figure 6.6). The electron spread on the anode is characterized in the following chapter.

[12] The V-shape is only resolved on the readout strips perpendicular to the resistive strips

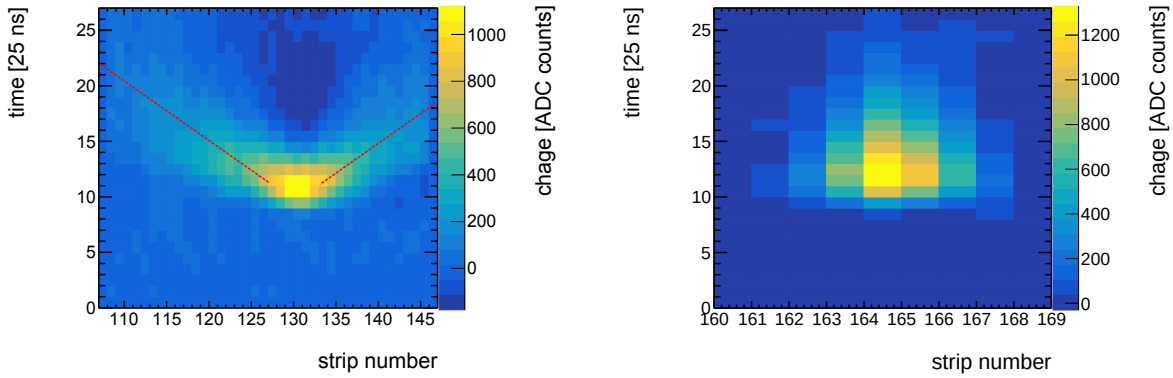

(a) Top readout strip layer.
Approximately 25 strips detect a signal.

(b) Bottom readout strip layer.
Approximately 7 strips detect a signal.

Figure 6.5: Time-dependent charge signal for all strips hit in an event for a resistive strip Micromegas detector.
Since charges can only spread along one coordinate, the V-shape characteristic of the charge movement on the anode (indicated by the red dashed line) is resolved only by the top readout strip layer. On the bottom readout strip layer, only the prompt avalanche signal is resolved.
U_{ampl} = 530 V, U_{drift} = 300 V.

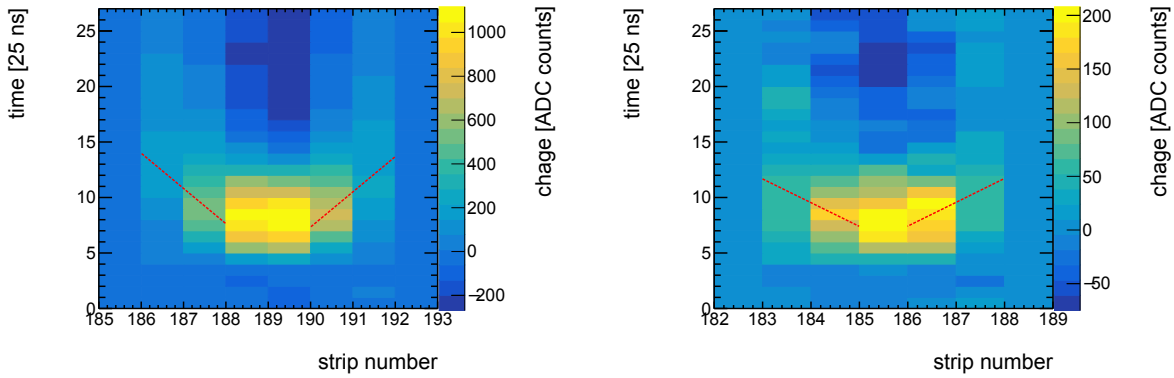

(a) Top readout strip layer.
Approximately 6 strips detect a signal.

(b) Bottom readout strip layer.
Approximately 5 strips detect a signal.

Figure 6.6: Time-dependent charge signal for all strips hit in an event for a DLC layer Micromegas detector (single event).
Since the charges spread in all directions on the anode layer, the V-shape characteristic of the charge movement on the anode (indicated by the red dashed lines) is resolved on both readout strip layers. Due to the low pulse height of the bottom readout strip layer (the signal on the bottom readout strips is about five times lower), the pulse height of the V-legs is too low to be properly resolved with the readout electronics used. The V-shape is only indicated on this layer.
U_{ampl} = 560 V, U_{drift} = 300 V.

6.3.1 V-shape Analysis

The size of the cluster depends on how pronounced the electron spread is (see Figure 6.7)[13]. On the resistive strip detector, the spread is resolved on the top readout strip layer only, where the readout strips are perpendicular to the resistive strips. On average up to 28 readout strips show a signal on that layer per event. On the layer which does not resolve the electron spread up to six strips are hit. Assuming that the size of the prompt avalanche signal is the same on both readout strip layers, it can be concluded, that six of the 28 readout strips hit on the top layer originate from the prompt avalanche signal. The other 22 readout strips see only the electron spread.
On the DLC layer detector only up to eight strips are hit in total on the top and up to six strips on the bottom readout strip layer. The electron spread is resolved on fewer strips than on the resistive strip Micromegas detector.
To understand this, the signal induction by the electron movement on the anode, as described in Chapter 5.3.2, is considered again. The pulse height of the induced signal is proportional to the number of moving electrons (see Equation 4.1). Simplified, this relationship can be represented as follows: The fewer charges cross a strip, the lower the signal induced on this strip. Charge movement parallel to the readout strip is not resolved by a strip.
While in a resistive strip anode, the charge movement is forced to the direction along the resistive strips, on the DLC layer anode the electrons can propagate in all directions. The charge density and thus the number of charges simultaneously crossing a strip decreases with $1/r^2$ for the DLC layer detector and with $1/r$ for the resistive strip Micromegas detector. The pulse height of the signal induced due to charge movement on the anode is lower for the DLC layer detector than for the resistive strip Micromegas detector. The farther a strip is from the centroid of the cluster, the fewer charges are crossing a strip at the same time. The strip pulse height gets lower and the duration of a strip signal gets longer (see Figure 6.5 and Figure 6.6). This effect is stronger on the DLC layer detector than on a resistive strip detector and thus the electron spread is less visible on the DLC layer detector than on the resistive strip detector.
In principle, it is possible to resolve the electron spread on both readout strip layers with the DLC layer detector. But due to the lower pulse height on the bottom readout strip layer, it is not possible to resolve it at the same voltages as it is resolved with the top readout strips (see Chapter 6.6.2). Only at high U_{ampl}, when the top readout strip layer is already saturated[14] a clear V-shape is observed by the bottom readout strip layer.
In addition, the pulse height of the spreading signal is proportional to the velocity of the diverging charges (see Equation 4.1). This is lower for the DLC layer detector (see Figure 6.8). The velocity is determined by the slope of the V-legs (see Figure 3.12).

All these considerations ignored the fact that the resistive anode is connected to a high voltage line on one side[15]. Thus, in the direction of the high-voltage line, the force that initiates the electron drift is stronger. This is visible in the electron spread velocity in Figure 6.8. Towards the HV supply, the drift velocity is slightly higher.
In summary, due to the electron spread in two directions in the DLC layer detector, the pulse height of the diverging signal is lower than in the resistive strip detector. Therefore, it is resolved on fewer strips (see Figure 6.7). In the case of superposition with the prompt avalanche signal, the influence of the electron spread signal is also significantly lower in the DLC layer detector than in the resistive strip detector.

[13] This does not apply to particles that pass through the detector at an angle and ionize the gas along their trajectory.
[14] The APV25 ASICs saturate at 1500-1800 ADC counts. This will be discussed in detail in Chapter 6.5.
[15] The HV supply line extends along one entire anode side.

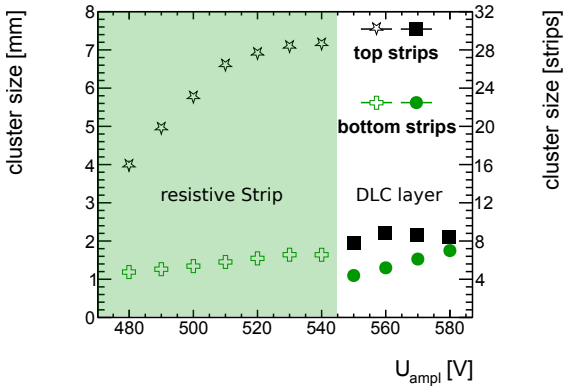

Figure 6.7: Mean cluster size for the resistive strip and the DLC layer Micromegas detector for different U_{ampl}.
Due to the geometry of the resistive strip detector, the electron spread is observed only on the top readout strip layer.
On the DLC layer Micromegas detector the electron spread is resolved on both readout layers. Due to the low pulse height on the bottom readout layer, the electron spread is only well resolved on the top readout strip layer.
Since the electrons spread in all directions on the resistive layer, the electron spread is weaker than if the spread is restricted to the axis of the resistive strips.
U_{drift} = 300 V

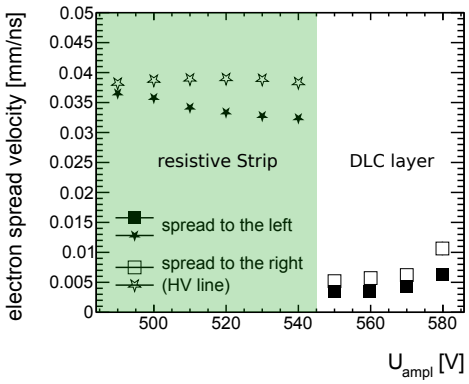

Figure 6.8: Mean electron spread velocity on the anode for a resistive strip and the DLC layer Micromegas detector.
Since the electron spread is forced in one direction, the electron velocity is higher for the resistive strip detector than for the DLC layer detector.
The HV supply for the anode is on the right side of the signal. Therefore the velocity in this direction is higher in both cases.
The shown values correspond to the top readout strip layer. Only velocities for well-resolved V-shapes are shown.
U_{drift} = 300 V

6.3.2 Signal Shape Analysis

As explained in Chapter 5.3.2 the electron spread is also observed in the signal shape. In the following the signal shapes of the highest signal strip are compared for resistive strip and DLC layer detectors. The knowledge gained through simulations (see Chapter 5) is used to understand the measured signal shapes.
Once again as a reminder: The signals shown in this chapter are displayed inverted. A positive signal shown corresponds to a negative signal induced on a strip and vice versa.

For resistive strip detectors, the readout strip layer which is influenced by the electron spread observes a bipolar signal. The other readout strip layer shows a unipolar signal (see Figure 6.9a). Bipolar signals are typical for signals induced due to charge movement on a resistive anode. The duration of the unipolar signal is longer than the duration of the positive component of the bipolar signal. After some time the signal of the electron spread starts to dominate. A negative signal due to the electron spread is already induced while the signal of the bottom readout strip layer is still positive. The full bipolar signal of the top readout strip and the unipolar signal of the bottom readout strip show the same length.
For the DLC layer anode both readout strip layers are influenced by the electron spread (see Chapter 6.3.1). A bipolar signal is observed on both readout strip layers (see Figure 6.9b). The duration of the positive component of the bipolar signal is longer than that of the bipolar signal of the resistive strip detector and shorter than that of the unipolar signal of the resistive strip detector. The negative component begins to dominate at a later time in these detectors than in the resistance strip detector. As already observed in the analysis of the V-shape of the signal (see Chapter 6.3) the signal induced due to the electron spread is pronounced weaker at the DLC layer detector as for the resistive strip detector. This is reflected in the less dominant negative component of the signal. Even if the electron spread can only be observed weakly in the V-shape of the signal, especially in the bottom readout strip layer, the negative component is clearly visible on both readout strip layers. The signal observed is bipolar.

If the height of the signals is now considered, it is noticeable, that it differs for both readout strip layers.
On the DLC layer Micromegas detector the observed strip pulse height of the top readout strips is five times higher than that of the bottom readout strips. A lower pulse height on the bottom strips than on the top strips is expected due to the simulations presented in Chapter 5.3.3 (see Figure 5.14)[16]. The negative component of the signal starts to dominate at a later time. Therefore, this superimposes less with the promptly induced signal of the ion drift. The maximum strip pulse height is less reduced by the electron drift. Since the electron spread is resolved on both layers, its influence on the total strip pulse height is the same on both readout strip layers.
In contrast to the DLC layer Micromegas detector, in the resistive strip Micromegas detector the strip signal on the bottom readout strip layer is 1.2 times higher than on the top readout strip layer (see Figure 6.9a). This is inconsistent with the expectation. The bottom readout layer is further away from the amplification region. In addition, the signal induced on this layer is shielded by the top readout strip layer. Since it is assumed that the readout structure is identical to that of the DLC layer detector, this can only be explained by a large influence of the electron spread on the pulse height. When the charges drift away from a strip they induce negative signals on the strip (see Figure 5.10b[17]). If the negative component starts to dominate early, during positive signals being induced by ions still drifting to the mesh,

[16] The simulations are performed for a SGR detector. As it will be shown in Chapter 7.3, the signal shapes of a Micromegas detector are the same as those of a SGR detector.
[17] In this figure the signals are not inverted.

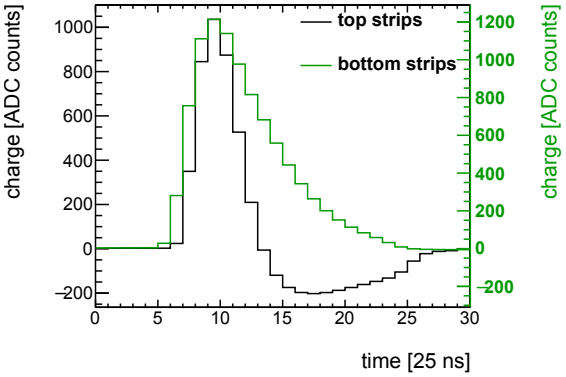

(a) Signal of a 2D resistive strip Micromegas detector.
Since only the top readout strips are perpendicular to the resistive strips, the charge movement is resolved by this readout strip layer only. This is reflected in the bipolar signal shape. The negative component of the signal due to the charge movement reduces the pulse height of the signal. Therefore the signal is higher on the bottom strips and the duration of the positive component is much shorter.
A different scaling for both readout strip layers is used.
U_{ampl} = 530 V, U_{drift} = 300 V.

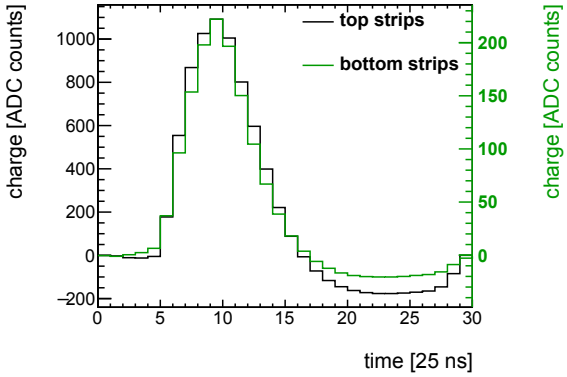

(b) Signal of a 2D resistive DLC layer Micromegas detector.
Due to the radial charge movement on the DLC layer, the electron spread is resolved by both readout strip layers. This is reflected in the bipolar signal shape. The bipolar component is weaker compared to a spread along one direction (see Figure 6.9a).
Due to the shielding of the signal by the top readout strips, the pulse height on the bottom layer is a factor of 5 times smaller than on the top readout strips.
A different scaling for both readout strip layers is used.
U_{ampl} = 550 V, U_{drift} = 300 V.

Figure 6.9: Signal shapes for the different investigated Micromegas detectors, averaged over at least 30.000 events.
The leading strip in the cluster is shown. All signals are shifted such that the maximum charge is reached at the same time.

the pulse height is reduced. Whether this is sufficient to reduce the pulse height of the top readout strip layer to such an extent remains to be investigated.
In summary, the signal shape of both readout strips of the DLC layer detector is influenced by the electron spread on the anode. This is expressed in the bipolar strip signal shape. This is much less pronounced than for a resistive strip detector.

6.4 Data Preparation - Cut off V-Shape

As shown in Chapter 5.3.2, the V-shape of the electron spread is not observed on one layer of the resistive strip detector. At low U_{ampl} the V-shape is also not resolved by the APV25 ASICs on the bottom readout strip layer of the DLC layer. By resolving the V-shape the cluster pulse height is increased by the strips which only resolve signals due to the electron spread. To minimize the effects of electron spread, an attempt is made to discard signals that are created only by the charge movement on the anode.

Another possible measure besides the number of hit strips, which is used to characterize how pronounced the electron spread is, is the difference between the timings of the first strip ($t_{\text{first strip}}$) and the last strip ($t_{\text{last strip}}$) in the cluster (see Figure 6.10)[18]. If no electron spread

[18] This does not apply to particles that pass through the detector at an angle and ionize the gas along their trajectory.

is resolved, as on the bottom readout strip layer of the resistive strip detector, this value is close to zero for ^{55}Fe signals. Signals that only resolve electron spread arrive at a much later time. This increases the time difference. Since the diffusion velocity of electrons is lower on the DLC layer anode than in the resistive strip anode (see Figure 6.8), the time difference is larger in the DLC-layer detector, even though the spread is observed on fewer strips. By applying a cut on that time difference signals created only by electron spread are discarded. From the bottom readout strip layer of the resistive strip Micromegas detector[19] the spread of the signal time (t_0 in Equation 3.6) due to uncertainties in the time reconstruction can be extracted (see Figure 6.11). Almost all strips are hit within Δt = 37.5 ns. Assuming that the time reconstruction works equally well, it is assumed that for all readout strip layers on both detectors, strip signals within that time window are mainly influenced by the prompt avalanche signal. Strips with Δt > 37.5 ns are assumed to be only created due to charge movement on the DLC layer. These strips are neglected for further analysis (see Figure 6.12). Thus, the influence of electron movement on the measurement data is minimized. The influence of electron spread on strips resolving both the electron diffusion signal and the direct avalanche signal cannot be reduced by this method.
If not otherwise stated, all strips with Δt > 37.5 ns are neglected.

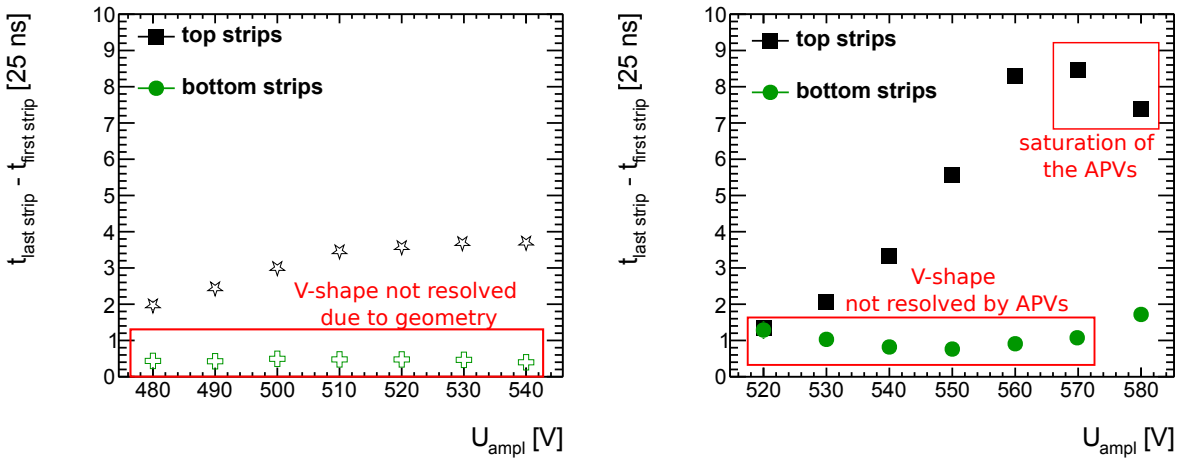

(a) Resistive strip Micromegas detector. **(b)** DLC layer Micromegas detector.

Figure 6.10: Mean event duration ($t_{last} - t_{first}$) for a resistive strip Micromegas detector and for a DLC layer Micromegas detector in dependency of the amplification voltage U_{ampl}. The event duration is taken as a measure of the electron spread.
Due to the geometry of the readout structure, the V-shape of the signal is only resolved by the top strips with the resistive strip detector.
With the DLC layer detector the V-shape of the signal can be resolved with both readout strip layers. Due to the lower pulse height of the bottom layer only for U_{ampl} > 570 V, the V-shape of the signal is resolved with the bottom strips. For this voltages saturation of the APV25 ASICs on the top readout strip layer starts to dominate.
Due to the higher electron spread velocity (see Figure 6.8) the time difference is shorter for the resistive strip detector, even if the spread is observed on more strips (see Figure 6.7).

[19] This layer does not resolve the electron spread.

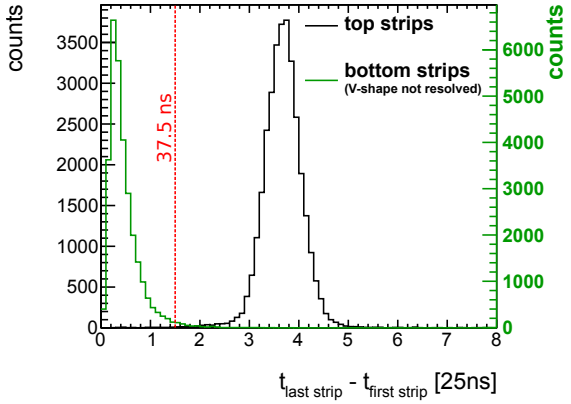

Figure 6.11: Event duration ($t_{last} - t_{first}$) for a resistive strip detector (^{55}Fe signals). Multiple thousand events are shown.
Since the electron spread is only resolved on the top readout strip layer the event duration on the bottom strips represents the directly induced signal only. Due to uncertainties at the time reconstruction, it is spread up to approximately 37.5 ns. This value is taken for the cut on the event duration on all other readout strip layers to neglect the signal induced by the electron spread (see Figure 6.12).
U_{ampl} = 530 V U_{drift} = 300 V

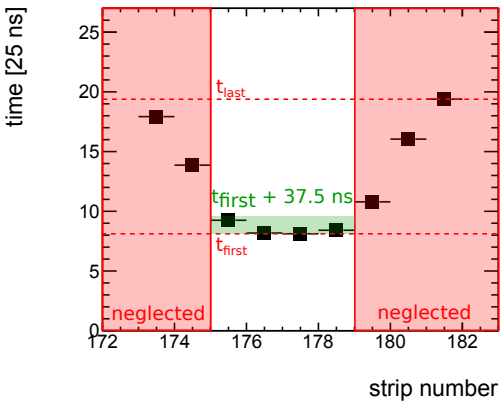

Figure 6.12: V-shape of one signal cluster using a DLC layer Micromegas detector (top Micromegas strips).
For comparison of detector properties, only the immediate signal is used. Strips with a timing outside the range t_{first} + 37.5 ns are discarded. This value is the time spread due to uncertainties in the time reconstruction obtained from the readout strip layer of the resistive strip detector which does not resolve the electron spread (see Figure 6.11).
U_{drift} = 300 V, U_{ampl} = 560 V

6.5 Saturation Analysis

The APV25 readout ASICs saturate at 1500-1800 ADC counts. If the signal detected by a readout strip is above this value, it will be truncated at 1500-1800 ADC counts (see Figure C.1). This results in a peak between 1500-1800 ADC counts in the strip pulse height distribution (see Figure 6.13). For saturated strips, the exact strip pulse height is not known. The reconstructed pulse height is lower than the actual pulse height detected by the strip. Truncating the signal at a certain level shortens the reconstructed duration of the signal rise compared to the same signal that would not be saturated. Both, the strip signal time t_0 and the strip pulse height q_0 reconstructed with the signal fit (see Chapter 3.4) are influenced by saturation. Thus saturated strips result in poorer position, energy, and time resolution.
One tries to operate the detector with as high U_{ampl} as possible so that almost no saturation is observed. At U_{ampl} = 560 V already 10 % of all hit strips are saturated on the top readout strip layer whereas no saturation is observed on the bottom readout strip layer (see Figure 6.14). This already indicates the problems of this readout structure. The bottom readout strip layer resolves much lower signals.
For the subsequent characterization of the DLC layer Micromegas detector, the saturation of the top readout strip layer has a major influence. To minimize the influence of saturated strips, events with more than one saturated strip are discarded unless otherwise specified.

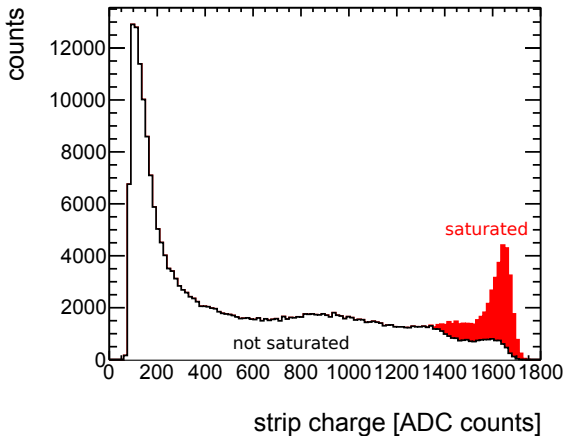

Figure 6.13: Distribution of the strip charge q_0 from Equation 3.6 for multiple thousand events.
The red-filled area originates from APV25 readout channels which are saturated.
U_{ampl} = 560 V, U_{drift} = 300 V.

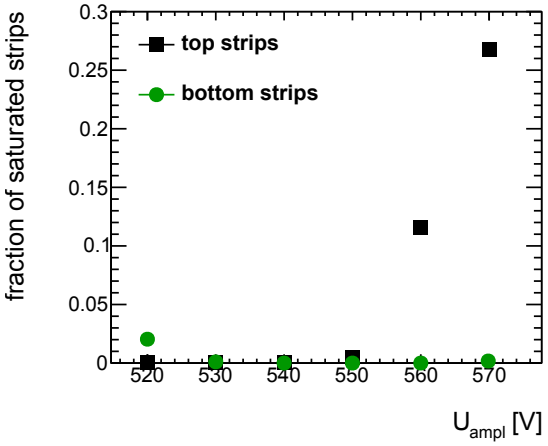

Figure 6.14: Fraction of the saturated number of strips.
Whereas the top readout strips start saturating at U_{ampl} = 560 V, no saturation is observed at the bottom readout strips up to U_{ampl} = 570 V.
U_{drift} = 300 V.

6.6 Pulse Height Analysis

After the electron spread is cut off and saturated events are neglected the cluster pulse height of the signal is analyzed. Before the pulse height of the different readout strip layers is compared (see Chapter 6.6.2), the energy resolution of the detector is investigated (see Chapter 6.6.1). In this section, pulse height refers to the summed-up charges of all hit strips in a cluster (see Equation 3.7).

6.6.1 Energy Resolution of the DLC Layer Micromegas Detector

The observed cluster pulse height is proportional to the energy of the photoelectrons created by ^{55}Fe. The energy of the photoelectrons is either 5.9 keV or 3 keV (see Chapter 6.1). This leads to two peaks in the pulse height spectrum. One peak corresponds to 5.9 keV (γ-peak) and one peak corresponds to 3 keV (Ar-escape peak). The ability to separate both peaks is a measure of the energy resolution of the detector. The position and width of both peaks are reconstructed via a double Gaussian fit as shown in Figure C.2.
In Figure 6.15 the pulse height spectrum for the DLC layer Micromegas detector is shown for three values of U_{ampl} where at least two indicated peaks are resolved on both readout strip layers.
For $U_{ampl} < 550$ V no double peak spectrum is observed on the bottom readout strip layer. The signals created by the 3 keV photoelectron are too small to be separated from background noise (see Chapter 3.5).
For $U_{ampl} \geq 560$ V the double peak spectrum is nicely resolved by the bottom readout strip layer, but the signal on the top readout strip layer is already influenced by saturation (see Chapter 6.5). The peak created by the 5.9 keV photoelectron is not resolved correctly. Its actual pulse height is larger than the resolved one. With increasing saturation, both peaks merge. Since saturated events are discarded for this work the 5.9 keV peak disappears.
How well the photon peak can be reconstructed is illustrated in Figure 6.16. There the ratio between the pulse height of both peaks is plotted. It is expected to be 1.97 (see Equation 6.1).

Only for a few U_{ampl}, this ratio is reconstructed on both readout strip layers simultaneously[20] with the DLC layer detector. At $U_{ampl} < 550\,V$ the stated ratio is nicely resolved by the top readout strips, but not by the bottom readout strips. For $U_{ampl} > 570V$, the double-peak spectrum is well resolved with the bottom readout strips, but not with the top readout strips due to saturation.
With the resistive strip detector, a double peak spectrum is reconstructed with both readout strip layers for multiple voltages.
This already indicates the problem of the limited dynamic range for a 2D particle reconstruction when the resistive strips are replaced by a resistive DLC layer.

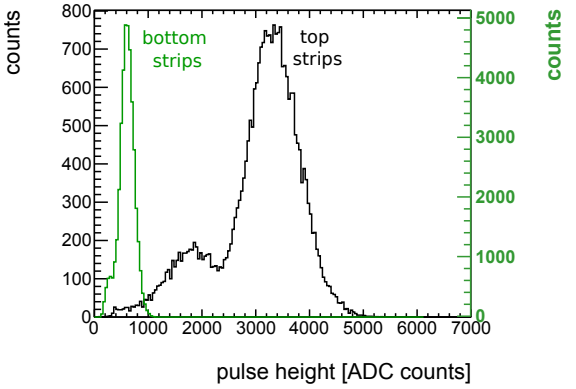

(a) $U_{ampl} = 550\,V$, $U_{drift} = 300\,V$.
30.000 events are shown for both readout strip layers.

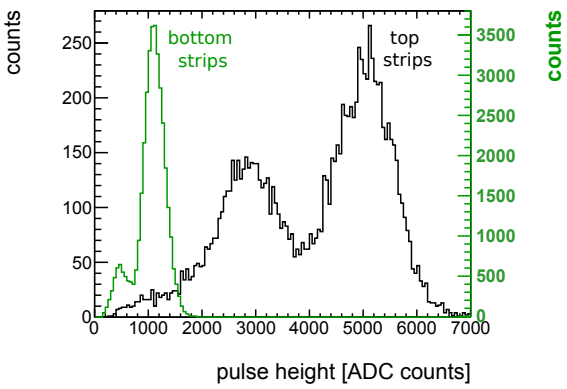

(b) $U_{ampl} = 560\,V$, $U_{drift} = 300\,V$.
14.000 events for the top strips and 30.000 events for the bottom strips are shown.

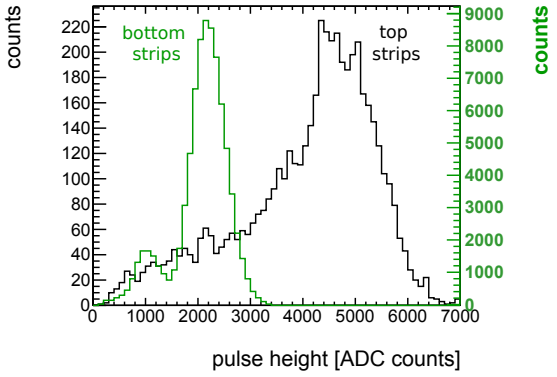

(c) $U_{ampl} = 570\,V$, $U_{drift} = 300\,V$.
5.000 events for the top strips and 71.000 events for the bottom strips are shown.

Figure 6.15: Argon spectrum measured with a ^{55}Fe 5.9 keV γ – source.
The spectrum is measured with the DLC layer Micromegas detector. Saturated events are neglected.
Only for the three shown voltages, the double peak spectrum is reconstructed on both readout strip layers simultaneously. For higher voltages too many events are lost due to saturation, for lower voltages, the Ar-escape peak is not resolved by the bottom Micromegas strips.

[20] Only for $U_{ampl} = 550\,V$ a double peak spectrum is indicated on both readout strip layers and no saturation is observed at the top readout strips.

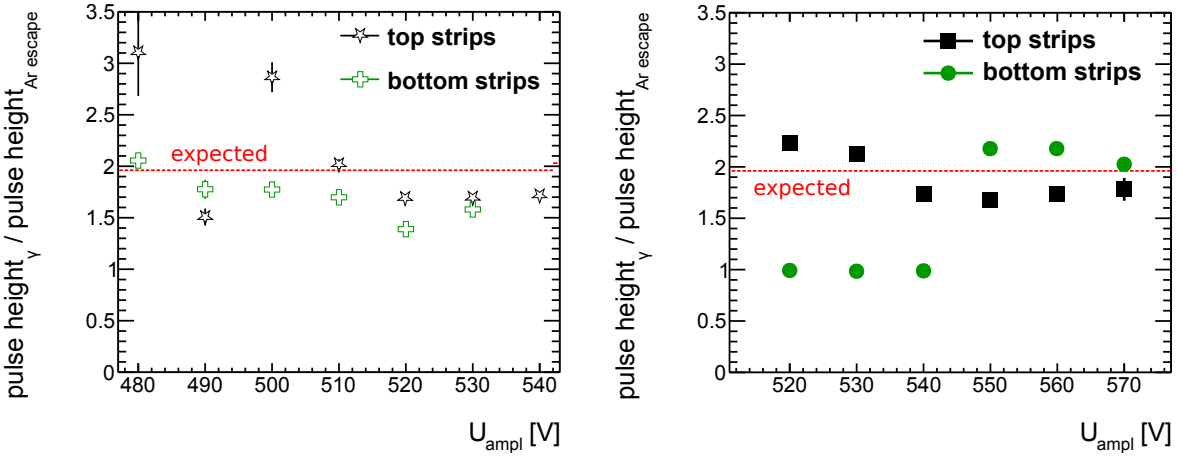

(a) Resistive strip Micromegas detector.

(b) DLC layer Micromegas detector.

Figure 6.16: Ratio between the 5.9 keV γ – peak and the Ar-escape peak. A ratio of 1.97 is expected.
With the DLC layer detector (right) only for the spectra shown in Figure 6.15 this ratio is reconstructed on both readout strip layers simultaneously. For lower pulse heights the Ar-escape peak is not reconstructed by the bottom readout strips. For $U_{ampl} > 570$ V too many events are lost due to saturation.
With the resistive strip Micromegas detector (left) the double peak spectrum is reconstructed on both readout strip layers simultaneously for multiple different U_{ampl}. The reconstruction works better with the bottom readout strip layer which does not resolve the electron spread.
Only data are shown where less than 30 % of all strips were saturated.
$U_{drift} = 300$ V.

Another measure for the energy resolution res_E is the width σ of the 5.9 keV γ-peak normalized by the reconstructed pulse height of the 5.9 keV peak Q_{tot} (see Figure C.2):

$$res_E = \frac{\sigma}{Q_{tot}} \tag{6.2}$$

σ is obtained via a Gaussian fit to the 5.9 keV γ-peak. For the DLC detector res_E is smaller than 25 % (see Figure 6.17b).
The energy resolution of both readout strip layers of the resistive strip Micromegas detector is constant for all tested U_{ampl}. It is approximately 10 % (see Figure 6.17a).
With the DLC layer detector, an energy resolution comparable to that of a resistive strip detector is hardly reached. Inhomogeneities in the pulse height depending on the position (see Figure 6.4) reduce the energy resolution. In the resistive strip detector, the micro-mesh is laminated into the pillars (see Chapter 3.1). The height of the amplification region is fixed. The DLC layer detector uses a floating mesh, it is not insured that the micro-mesh touches all the pillars. The height of the amplification region is not fixed. Little deviations in the height of the amplification gap lead to deviations in the pulse height[21]. Thus the energy resolution gets worse. Due to electrical forces which increase with U_{ampl}, the micro-mesh gets pulled down towards the anode until it touches the pillars. The height of the amplification region gets more homogeneous. Thus, with increasing U_{ampl} the energy resolution improves for both readout strip layers.

[21] As shown in [Herrmann, 2019] a change in the pillar height by 1 µm results in a change of the mean cluster pulse height by 113 ADC counts

When saturation effects begin to dominate at the top readout strip layer for $U_{ampl} > 550\,V$ the reconstructed energy resolution is no longer reliable because saturated events that would broaden the peak are discarded.
The resolution of the top readout strips is better than that of the bottom readout strips. The bottom readout strip layer reaches the same energy resolution as the top readout strip layer if U_{ampl} is increased by 20 V - 30 V. Since both readout strip layers obtain the signal from the same amplification region it is not possible that both readout strip layers show the same energy resolution.

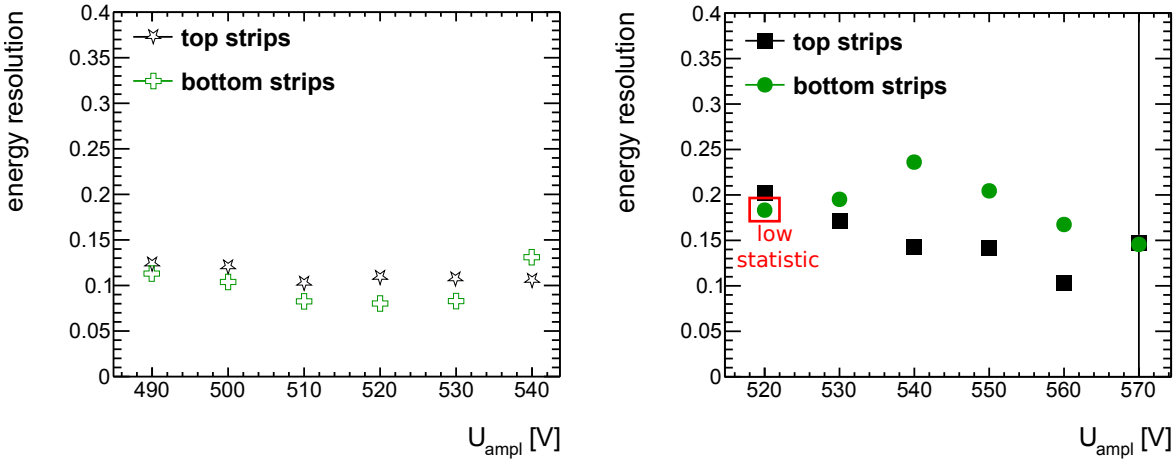

(a) Resistive strip Micromegas detector.

(b) DLC layer Micromegas detector.
At $U_{ampl} = 530\,V$ the pulse height of the bottom readout strips is strongly influenced by falsely discarded strips due to low strip pulse heights.

Figure 6.17: Energy resolution according to Equation 6.2.
At the DLC layer detector the energy resolution of the top Micromegas strips is better than for the bottom Micromegas strips, until saturated events start to dominate at $U_{ampl} \approx 570\,V$.
At the resistive strip Micromegas detector, the energy resolution is approximately constant for both readout strip layers. The energy resolution for the resistive strip Micromegas detector is better than for the DLC layer detector.
$U_{drift} = 300\,V$.

6.6.2 Pulse Height Analysis of Both Readout Strip Layers

As expected (see Chapter 1.1.2) the pulse height of the DLC layer Micromegas detector increases exponentially on both readout strip layers with increasing U_{ampl} (see Figure 6.18). This shows that each readout strip layer is working individually as expected. Comparing the pulse heights of both readout strip layers one observes that the pulse height on the top readout strip layer is on average six times higher than the pulse height on the bottom readout strip layer (see Figure 6.19b). This is approximately the same ratio as for the pulse height of the highest strip in the cluster (see Figure 6.9b). The top readout strip layer is shielding the signal from the bottom readout strip layer. This leads to problems in the dynamic range of the detector for a 2D reconstruction.

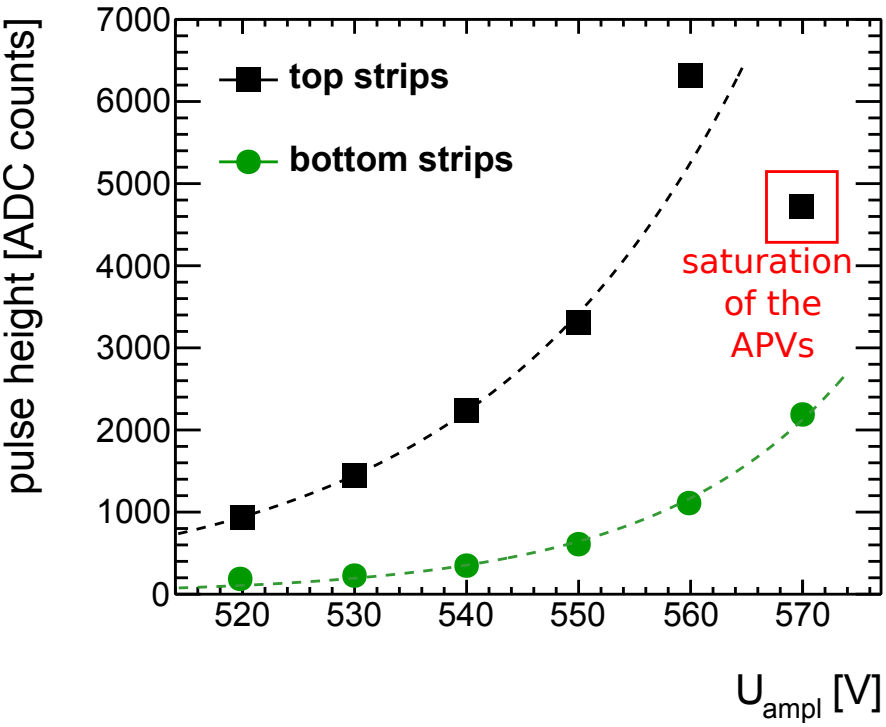

Figure 6.18: Cluster pulse height of the DLC layer Micromegas detector in dependency of U_{ampl}.
As cluster pulse height the MPV of the 5.9 keV photon peak is taken (see Figure C.2). On both readout strip layers, the pulse height increases exponentially with increasing U_{ampl}. At 570 V the influence of saturation of the APV25 chips is visible.
U_{drift} = 300 V.

For the resistive strip detector where the layout is the same besides the resistive anode, the ratio between the cluster pulse heights is two (see Figure 6.19a). However, the strip pulse height of the highest strip in the cluster on the bottom readout strip layer is about 1.2 times higher (see Figure 6.9a). Presumably, not all the electron spread signal is cut away.
The different ratios for both detectors can have several reasons:

- The inhomogeneity of the electric field close to the resistive strip edges guides the electrons onto the resistive strip. More electrons are collected on the resistive strip than in the gap between the strips. By aligning the resistive strips with the bottom readout strips it is ensured that most charges end up on top of the bottom readout strips and not on top of the gap between the bottom readout strips. This effect does not apply to the DLC layer detector. There the electrons arrive homogeneously distributed.

- The electron spread has a much larger impact on the pulse height as expected. The electron spread is clearly more pronounced at the resistive strip detector (see Chapter 6.3.2 and 6.3). While the electron spread has the same relative influence on both readout strip layers at the DLC layer detector, it only influences the top strips at the resistive strip detector. By superimposing the directly induced signal with the signal induced by the electron spread the pulse height can be reduced.

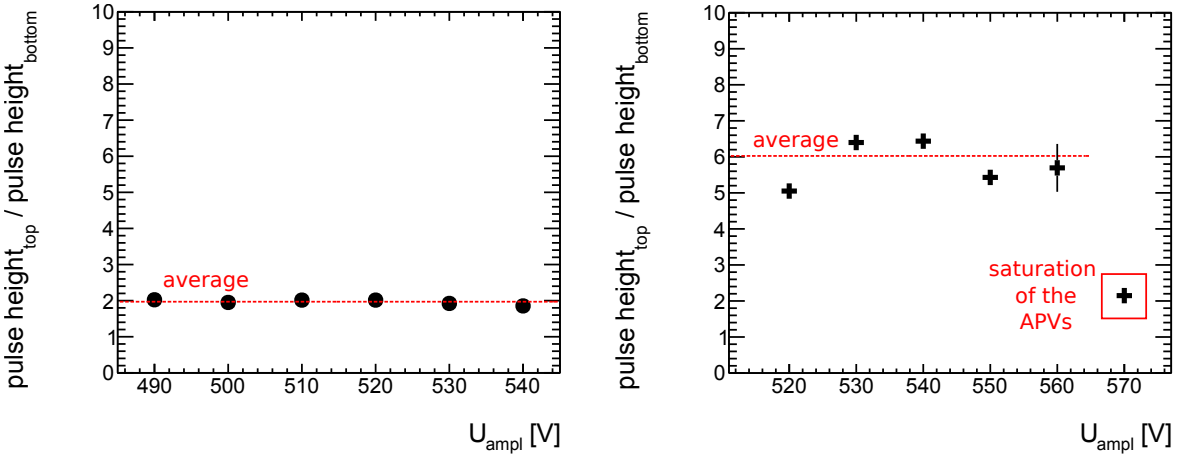

(a) Resistive strip Micromegas detector. **(b)** DLC layer detector.

Figure 6.19: Ratio between the cluster pulse heights of both readout strip layers.
As cluster pulse height for each readout layer the MPV of the 5.9 keV photon peak is taken (see Figure C.2).
For the resistive strip detector (left) the pulse height of the top readout strip layer is two times higher than that of the bottom readout strip layer. This is in contradiction to the strip pulse height in Figure 6.9a. This is because it was apparently not possible to cut off the entire electron spread signal as described in Chapter 6.4.
For the DLC layer detector (right) the pulse height of the top readout strip layer is five to six times higher than that of the bottom readout strip layer. At 570 V the influence of saturation of the APV25 chips is visible.
U_{drift} = 300 V.

6.7 Summary of the Characterization of the DLC Layer Detector

The DLC layer detector was investigated with a ^{55}Fe 5.9 keV γ source. In the following, the presented measurement results with the DLC layer detector are summarized. Suggestions on how to improve the detector are given.

6.7.1 Summary of the Measurement Results

The DLC layer Micromegas detector works. At the working point of each detector layer an energy resolution similar, but slightly worse than the energy resolution of a resistive strip Micromegas detector was reached (see Figure 6.17). The characteristic Argon spectrum was reconstructed with each readout strip layer individually (see Figure 6.16). As expected the pulse height of each readout strip layer increased exponentially with increasing U_{ampl} (see Figure 6.18.
The comparison of the measurements with a DLC layer anode with the measurements of a resistive strip anode showed that the choice of the anode has a large influence on the detector properties.
After the electron avalanche arrived at the anode, the diffusion of charges on the anode was resolved with both readout strip layers in the case of the DLC layer anode (see Figure 6.6) and with only one readout strip layer in the case of the resistive strip anode for geometrical reasons (see Figure 6.5). The impact of the electron spread was suppressed at the DLC layer detector (see Chapter 6.3). Therefore also the timing of the signal was less affected by the electron spread. This allowed a position determination using the µTPC method as it will be shown in Chapter 9.4.2.

However, the dynamic range of the detector deteriorated. The pulse height was on average six times higher on the top readout strip layer compared to the bottom readout strip layer (see Figure 6.19b). For the resistive strip detector, this ratio was two (see Figure 6.19a). The problem of the dynamic range of the detector is reflected in the fraction of reconstructed 2D events (see Figure 6.20). Only for $U_{ampl} \geq 540\,V$ the bottom readout strip layer detects an event when the top readout strip layer detects an event. The saturation strongly influences the signal at $U_{ampl} \geq 560\,V$. Combining these values with those from the Argon escape peak analysis (see Chapter 6.6.1), one finds that the 2D readout worked well only for $U_{ampl} = 550\,V$. Nevertheless, each readout strip layer separately worked fine for multiple values of U_{ampl}. The layout of the readout structure using a DLC layer as anode needs to be improved for a 2D reconstruction.

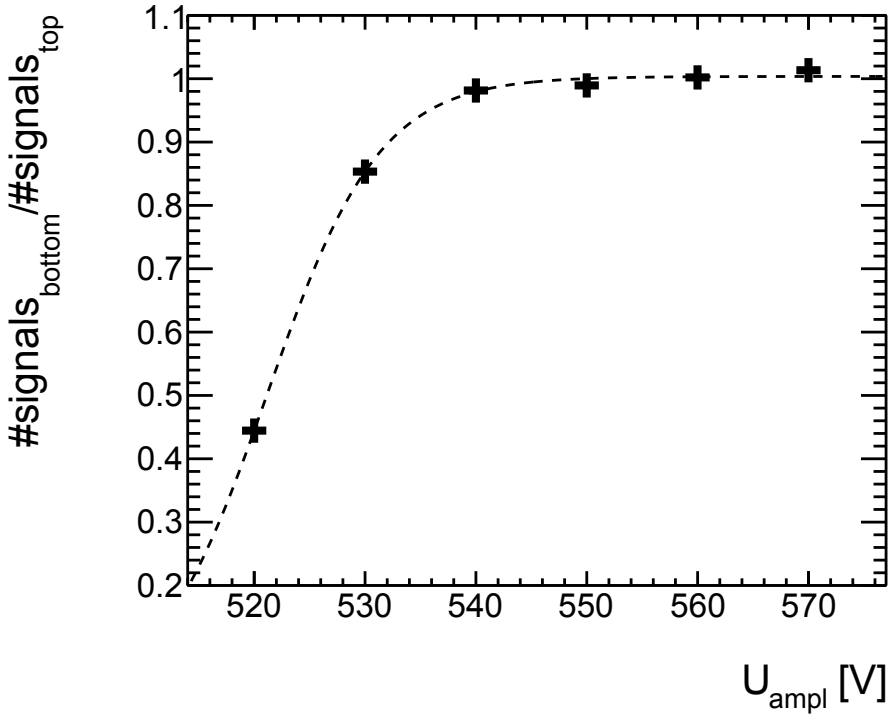

Figure 6.20: DLC detector, efficiency of the bottom readout strip layer in dependence of U_{ampl}. An event is considered efficient if a hit is detected in the bottom readout strip layer when the top layer is hit.
$U_{drift} = 300\,V$

6.7.2 Proposals for the Improvement of the Dynamic Range

To improve the dynamic range of the detector there are multiple different possibilities:

- An adapter board as described in Chapter 3.3 can be used to reduce the pulse height of the top readout strip layer. This allows the detector to be operated at a higher gain so that the pulse height on the bottom readout strip layer is high enough to be read out and the top readout strip layer is not saturated.
- The layout of the readout structure can be optimized. Enlarging the gap between the top readout strips and enlarging the width of the bottom readout strips minimizes the shielding by the top readout strips. The pulse height of both readout strip layers becomes similar.
- Changing the detector gas to a gas with a higher ion mobility might decouple the signal induced by the electron spread from the signal directly induced by the avalanche[22].
- Determine the second coordinate at the position of the mesh. The pulse height at the micro-mesh is approximately the same as the pulse height at the anode. The pulse height should be similar to the pulse height of the top readout strip layer. This leads to the development of the SGR detector.
- Apply a software extrapolation of the chipped pulse using a template of averaged unsaturated pulses.

[22] The use of a mixture $Ne : CF_4$ with a volume ratio of 80:20 helped to reconstruct bipolar signals in [Klitzner, 2019].

Chapter 7

Characterization of the SGR Detector using ^{55}Fe

The DLC layer Micromegas readout structure investigated in chapter 6 is used as the readout structure for the SGR detector. The measurements executed with the Micromegas detector are repeated with the SGR detector. Thus, the influence of replacing the micro-mesh by a SGR foil is investigated.
When speaking about standard DLC layer Micromegas detector it refers to the DLC layer Micromegas detector analyzed in chapter 6.
As done in chapter 6 saturated events are rejected and the electron spread signal on the Micromegas readout strip layers is cut off.
For optical reasons, the signals of the Micromegas readout strips are inverted in this chapter. When speaking of negative or positive signals, this refers to the signal shape as shown in the referred figures.

7.1 Measurement Setup

The measurement setup is the same as described in Chapter 6.1. The SGR detector is irradiated by ^{55}Fe. The only difference is that instead of the Micromegas detector a SGR detector is used. The investigated SGR detector has three readout strip layers:

- **Top Micromegas strips**: This is the same readout strip layer as the top strip layer in the standard DLC layer Micromegas detector.
- **Bottom Micromegas strips**: This is the same readout strip layer as the bottom strip layer in the standard DLC layer Micromegas detector.
- **GEM strips**: These are the readout strips located on the segmented GEM foil (SGR foil). Depending on the detector setup, the GEM strips are located either on the top or the bottom side of the SGR foil.

The signal of the non-segmented side of the SGR foil is used to trigger. All readout strips are read out using APV25 hybrid boards in a master-slave configuration. In total eight APV25 front-end boards are used. The strips on the GEM foil are read out using the adapter board described in chapter 3.3. This is needed to prevent noise coupling from the APV25 to the trigger signal. If an external trigger signal is used or the readout electronics is self-triggering, no adapter board is required.

By the adapter board, the strip pulse height and thus the cluster pulse height of the GEM strips are reduced by a factor of 4.48 (see figure 3.6). If not stated differently the measured pulse heights of the GEM strips are corrected for this factor.
Two different types of SGR detectors are investigated. One SGR detector is segmented on the bottom side (SGR bottom), the other on the top side (SGR top) of the SGR foil. Starting from Chapter 7.3, the measurement results for SGR bottom are displayed on the left side of the page and the measurement results for SGR top are displayed on the right side of the page.

7.2 Pulse Height Homogeneity

According to the simulation done as described in Chapter 5 the electron avalanche is built up inside and directly below the GEM holes. The pattern of the holes is observed on the anode (see Figure 7.1a). The same applies to the ions on the GEM foil. There most ions end up on the edge of the metal around the holes of the SGR foil (see Figure 7.1b).
Measurements cannot resolve the pattern of the holes. Besides the fact that the electron movement on the DLC layer blurs the pattern on the anode, this pattern cannot be resolved by the readout structure. The pattern is much finer than the periodicity of the readout strips. The measured data are not influenced by the clusters of the electron avalanche endpoints. This proves the 2D pulse height distribution for a completely irradiated detector (see Figure 7.2). No GEM hole-induced inhomogeneities are observed on the scale of the simulated pattern.
The pulse height in dependency of the position is more inhomogeneous as for the DLC Micromegas detector (for the Micromegas detector see Figure 6.4). While in the case of the Micromegas detector, only a pulse height dependency from the edge of the active area to the center was seen, the pulse height fluctuations in the SGR detector are more frequent. Irregular patterns can be seen in the pulse height. The same pulse height variation pattern is observed with the top Micromegas strips and GEM strips. Little deformations of the SGR foil cause this effect.
The micro-mesh of the Micromegas detector is more stretched than the SGR foil and thus more resistant to small bucklings. When the SGR foil is slightly deformed, the deformation persists and is only weakly compensated by the tension of the SGR foil. In addition to unintentional mechanical deformations of the foil, deformations of the foil also occur on the frame to which the foil is glued (foil frame in Figure 2.9). Different thicknesses of the glue cause deformations of the foil or prevent the foil from lying everywhere on the coverlay. On the spots where the foil is deformed, the foil does not touch the pillars. Therefore a fixed equal distance between the foil and the anode is not given everywhere.
To compensate for deformations of the foil caused by variations in the thickness of the glue and to ensure (as good as it is possible) that the foil lies everywhere on the pillars, the foil is pressed onto the coverlay with an extra press frame[1] (see Chapter 2.3.3). The voltage difference U_{ampl} between the anode and the SGR foil applies a force to the SGR foil pulling the foil towards the anode. The influence of this force to equal out the deformations is minimal. The pulse height inhomogeneity does not reduce with an increasing U_{ampl} (see Figure 7.3).
Gluing the foil to the pillars might reduce this problem. This was not applied in this thesis since it was planned to switch between different foils. Increasing the tension with which the SGR foil is stretched compensates for slight deformations of the foil. Since the existing SGR foils were already stretched and glued on a frame, this option was also not possible.

[1] Coverlay and pillars are made out of the same material in the same production step. They have the same height.

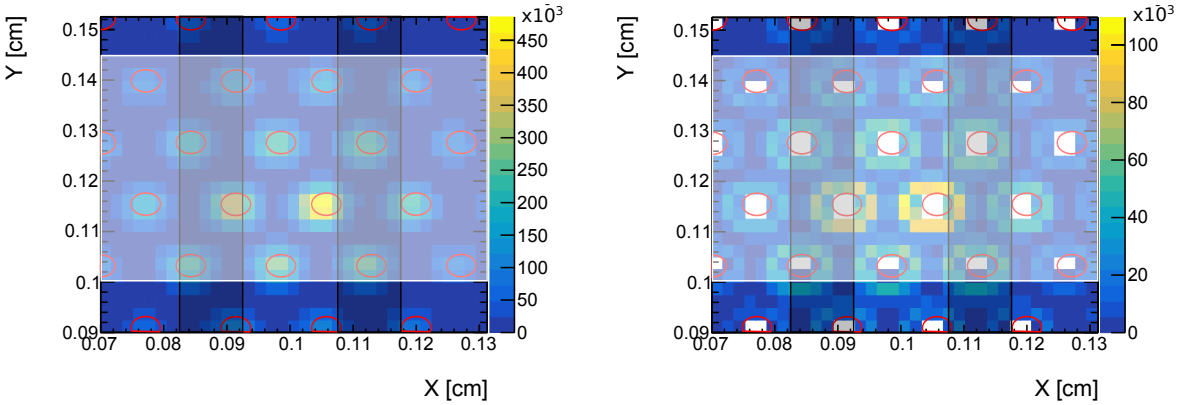

(a) Hit position of the electrons on the anode.

(b) Hit position of the ions on the bottom side of the GEM foil.

Figure 7.1: Simulated hit position of the electrons/ions.
The GEM foil is segmented on the bottom side. The positions of the top Micromegas strips (light black box), GEM strips (light white box), and holes (red circles) are indicated. A cluster of electrons below the GEM holes is observed. Ions are mostly collected by the GEM strips on the copper edge around the hole. The electron/ion pattern is smaller than the pitch of the readout strips. Therefore it is not resolved.
U_{ampl} = 420 V, U_{GEM} = 200 V, U_{drift} = 420 V.

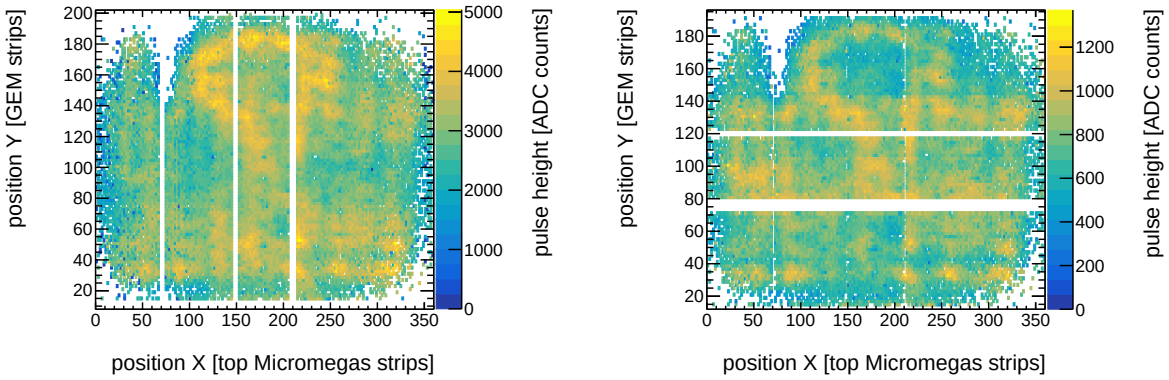

(a) Pulse height of the top Micromegas strips in dependency of the 2D hit position.

(b) Pulse height of the GEM strips in dependency of the 2D hit position.

Figure 7.2: Measured mean cluster pulse height in dependency of the 2D hit position for multiple thousand events.
Almost the full active area is irradiated using ^{55}Fe.
A position dependency of the pulse height is visible at the same positions for both readout strip layers. A reason for that are deformations of the GEM foil, which lead to variations in the height of the amplification region.
The segmentation is on the bottom side of the foil. U_{ampl} = 400 V, U_{GEM} = 200 V, U_{drift} = 420 V.

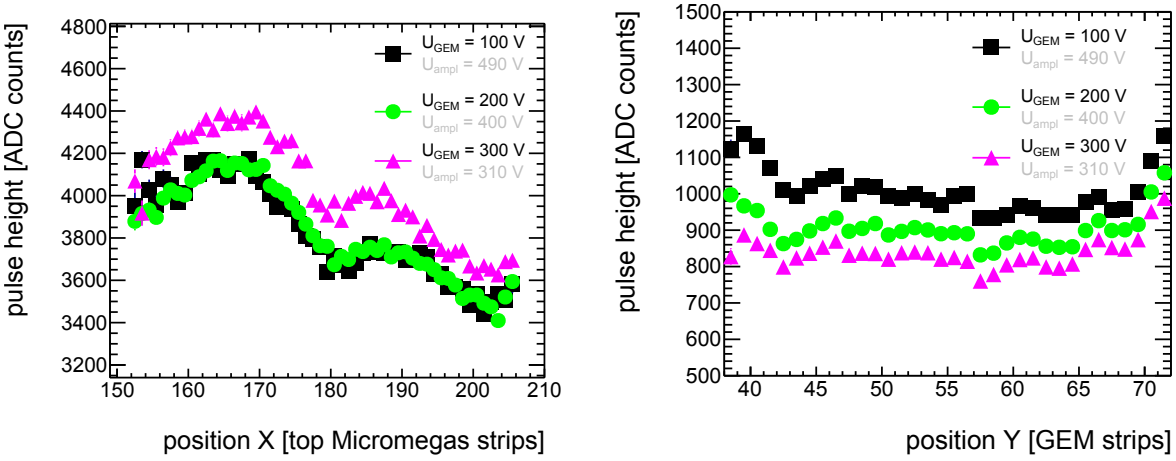

(a) Mean pulse height of the top Micromegas strips in dependency of the 1D hit position.

(b) Mean pulse height of the GEM strips in dependency of the 1D hit position.
The adapter board is not corrected.

Figure 7.3: Mean pulse height in dependency of the 1D hit position.
The position dependency is not changing with U_{GEM} or U_{ampl} respectivelly. The pulse height of the GEM strips decreases with increasing U_{GEM}. The pulse height of the top Micromegas strips remains at approximately the same values.
The segmentation is on the bottom side. Values are shown for the Voltages of figure 7.7.

7.3 Signal Shape Analysis

The signal shapes of the Micromegas readout strip layers of the SGR detector (see Figure 7.4) are the same as for the standard DLC layer Micromegas detector (see Figure 6.9b). The ratio of the strip pulse heights of the two Micromegas readout strip layers to each other is the same as for the standard DLC layer Micromegas detector. Even though the maximum drift distance of the ions is longer for the SGR detector than for the Micromegas detector[2] and even though the electric fields are lower for the SGR detector, replacing the micro-mesh with a SGR or GEM foil does not affect the signal shape of the Micromegas readout strips. The duration of the signal and the expression of the bipolarity are the same as for a Micromegas detector. This is because the signal induced by the charge movement through the holes of the SGR foil is shielded from the Micromegas readout strips by the bottom side of the SGR foil. As found by simulations (see Chapter 5.3), the only signals observed by the Micromegas readout strips are charges moving in the Micromegas amplification region.
The signal detected by the GEM readout strip in the center of the cluster is approximately twice that of the top Micromegas strips. This ratio originates from the geometry of the detector. The periodicity of the GEM strips is approximately two times larger than for the Micromegas readout strips[3].
The signal of the GEM strips on the bottom side is bipolar. As explained in Chapter 5.3.1, ions drifting from the anode in the direction of SGR foil induce a positive signal on the GEM strip. After the ions arrived at the SGR foil they are either stopped on the foil or drift through a GEM hole toward the top side of the foil. When the ions drift through a GEM hole they drift away from the GEM strip and thus induce a negative signal to the GEM strip. Even though most ions are formed in the last amplification step near the anode, some ions are formed earlier. The number of ions created decreases exponentially the closer they are to the SGR foil. This leads to the fact that not all ions arrive at the SGR foil at the same time due to the different lengths of the drift paths. Ions arriving early at the GEM foil

[2] For the SGR detector it is $d = d_{\text{amp gap}} + d_{\text{foil}}$. For the Micromegas detector, it is $d = d_{\text{amp gap}}$.
[3] The periodicities are: $p_{\text{GEM}} = 484\,\mu m$ and $p_{\text{Micromegas}} = 250\,\mu m$

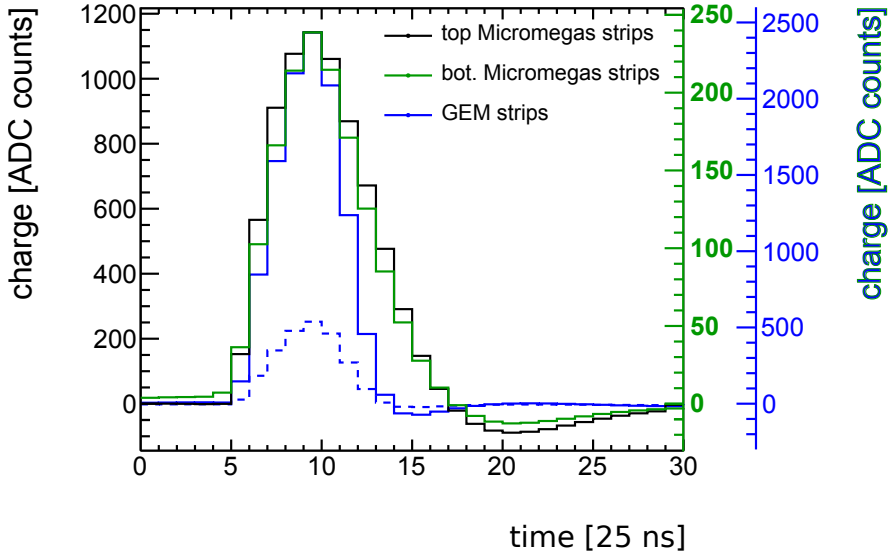

Figure 7.4: Signal of a SGR detector (segmentation on the bottom side of the foil) using a DLC layer as an anode (different scaling is used for each readout strip layer).
The highest strip in the cluster is shown. The signal shown is averaged over approximately 22.000 events. All 22.000 signals are shifted such that the maximum charge is reached at the same time. To read out the GEM strips an adapter board is used (see Chapter 3.3). Thereby the pulse height is reduced by a factor of 4.48 (see figure 3.6). The blue continuous line is the signal as it is expected to be without the adapter board. The dashed blue line is the measured values with the adapter board.
The corrected strip pulse height of the GEM strips is approximately two times higher than the pulse height of the top Micromegas readout strips. This is because the periodicity of GEM strips is 1.9 times higher than the periodicity of Micromegas strips.
U_{ampl} = 400 V, U_{GEM} = 200 V, U_{drift} = 420 V.

and drifting through the GEM holes generate a negative signal while ions arriving later still induce a positive signal. Therefore, the duration of the positive component of the GEM strip signal decreases compared to the Micromegas strips.

The signal shape of the GEM strips strongly depends on the location of the segmentation[4] and the voltage U_{GEM} applied between the top and bottom side of the SGR foil (see Figure 7.5). Choosing U_{ampl} such that the pulse height of the top Micromegas readout strip layer is the same for different U_{GEM}, it is observed that for detectors with the segmentation on the bottom side, the negative component of the signal becomes more dominant as U_{GEM} increases (see Figure 7.5a). The electric field funnel pulling the ions inside the GEM holes gets stronger with increasing U_{GEM}. As shown in simulations (see Chapter 5.2.2), with increasing U_{GEM}, more ions drift through the holes to the top side of the GEM foil and fewer ions end up on the GEM strips on the bottom side. The height of the GEM strip signal decreases a little with increasing U_{GEM}. Besides the fact that fewer ions end on the strips, it is also due to the negative component of the signal becoming more pronounced as U_{GEM} increases. A superposition with the positive signal, as described before, leads to a stronger reduction of the positive signal.
For the detector with the segmentation on the top side, only unipolar signals are detected. At properly chosen U_{drift}, no ions drift away from the GEM strips toward the cathode. Only ion movements toward the GEM strips are resolved. The amplitude of the signal on the GEM strips is strongly dependent on U_{GEM} (see Figure 7.5b). Mostly charge movements inside the GEM holes are resolved by the readout strips on the top side of the SGR foil. All other

[4]The segmentation is either on the top or on the bottom side of the SGR foil.

charge movements are shielded by the bottom side of the SGR foil. Therefore, the strip pulse height of GEM strips on the top side behaves like the negative component of the signal of GEM strips on the bottom side. Both reflect the number of ions drifting through the GEM holes to the top side of the SGR foil. As U_{GEM} increases, the strip pulse height of the top GEM strips decreases.

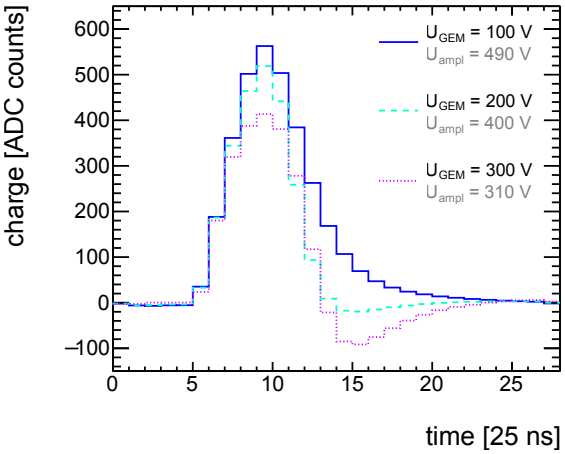

(a) Segmentation on the bottom side of the GEM foil.
With increasing U_{GEM} the GEM foil gets more transparent for back-drifting ions and the bipolar component of the signal increases (see Chapter 5.2.2). The drift through the holes away from the GEM strips causes the negative component.
The strip pulse height decreases slightly with increasing U_{GEM}.

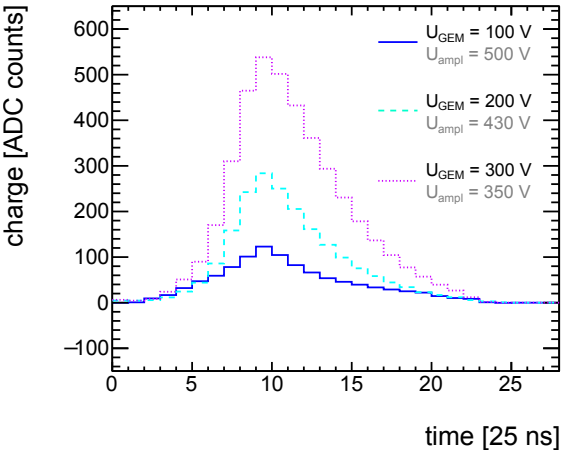

(b) Segmentation on the top side of the GEM foil.
With increasing U_{GEM} the GEM foil gets more transparent for back drifting ions (see Chapter 5.2.2). More ions are ending on the GEM strips. Mostly the charge movement inside the GEM holes is observed by the GEM strips. Therefore the signal becomes larger.
The strip pulse height is strongly depending on U_{GEM}.

Figure 7.5: Signal shape of the GEM strips for different U_{GEM}, at the same pulse height on the top Micromegas readout strip layer.
The highest strip in the cluster is shown. The signal shown is averaged over at least 15.000 events. All 15.000 signals are shifted such that the maximum charge is reached at the same time. The influence of U_{GEM} on the readout strips on the top side (right) of the SGR foil is larger than for the readout strips on the bottom side (left) of the SGR foil.
U_{drift} = 420 V.

7.4 Cluster Size

The spatial extent of the cluster (cluster size) is approximately the same on the top Micromegas readout strips and GEM readout strips. For both the signal is distributed on up to 2 mm. For the top Micromegas readout strips slightly more strips are hit (see Figure 7.6). As already observed with the DLC layer Micromegas detector, this is due to the spreading of electrons on the DLC layer anode. This propagation is mainly resolved with the Micromegas readout strips (see Chapter 6.3.1). To obtain comparable data on the different readout strip layers, the V-shape of the signal on the readout strips is cut off in the following measurements as explained in Chapter 6.4.
The reconstructed cluster size is in good agreement with the expectation. At least for the setup with the segmentation on the bottom side, both readout strip layers are expected to resolve a similar signal. No electrodes shield the signals from these layers, which are created by the electron avalanches in the amplification region.

Only if the transparency of the SGR foil for back-drifting ions is high enough ($U_{GEM} \geq 200\,V$) the cluster size on the top GEM strips is the same as for the top Micromegas strips.

The signal in the SGR detector is distributed on approximately the same area as in the standard DLC layer Micromegas detector (compare Figure 7.6 with Figure 6.7). As for the DLC layer Micromegas detector, the cluster size of the bottom Micromegas readout strips is lower than that of the top Micromegas readout strips.
Replacing the micro-mesh with a GEM foil has no impact on the cluster size.

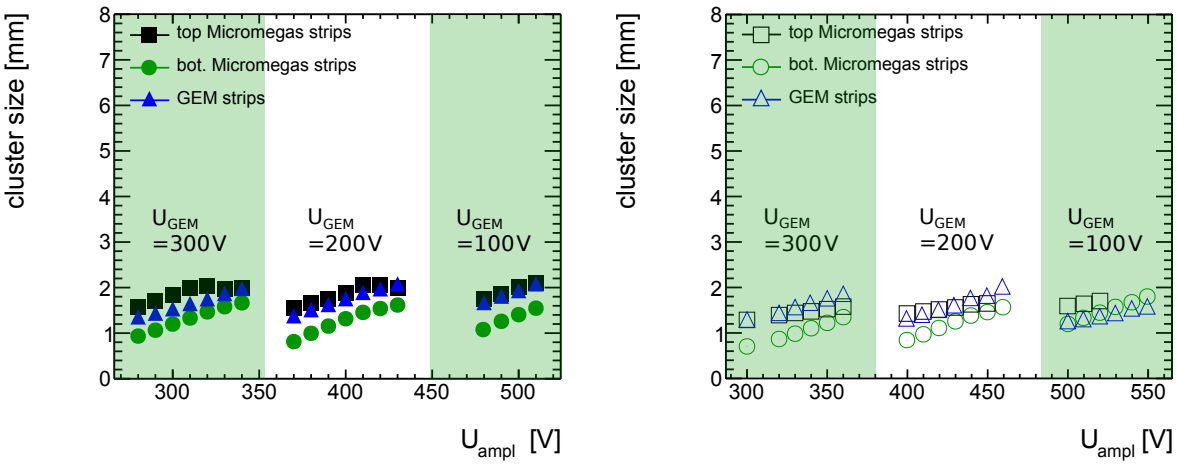

(a) Segmentation on the bottom side of the GEM foil.

(b) Segmentation on the top side of the GEM foil.

Figure 7.6: Mean cluster size in mm on all readout strip layers for different U_{GEM} (columns) and U_{ampl} (X-axis).
The cluster size of the GEM and top Micromegas readout strip layer is approximately identical. As with the DLC layer Micromegas detector, on the bottom Micromegas readout strip layer, the signal is resolved on slightly fewer readout strips. This holds for both detector setups, except for $U_{GEM} = 100\,V$ for the setup with the segmentation on the top side.
The electron spread is not cut off for these figures.
$U_{drift} = 420\,V$.

7.5 Pulse Height Analysis

After the electron spread is cut off and saturated events are neglected the cluster pulse height of the signal is analyzed. Before the pulse height of the different readout strip layers is compared (see Chapter 7.5.2), the energy resolution of the detector is investigated (see Chapter 7.5.1).
Some measured values are compared with simulated values according to the simulation from Chapter 5.
In this section pulse height refers to the summed-up charges of all hit strips in a cluster (see Equation 3.7).

7.5.1 Ar Escape Peak Analysis as a Measure of the Energy Resolution

As explained in Chapter 6.6.1, before the energy resolution is determined according to Equation 6.2, it is investigated how accurately the characteristic Argon spectrum can be reconstructed.
The spectrum is compared for different U_{GEM}. U_{ampl} is chosen such that the reconstructed pulse height of the 5.9 keV peak is the same for different U_{GEM} for both SGR detector setups.

For the SGR detector with the segmentation on the bottom side the spectrum is nicely reconstructed with the GEM strips and with the top Micromegas readout strips (see the left column in Figure 7.7). The two peaks are better separated with increasing U_{GEM} and thus decreasing U_{ampl}. For higher U_{GEM} the field line funnel pulling the electrons from the drift region into the GEM holes is stronger. More primary electrons reach the amplification regions and are thus detected. This has a stronger effect on the Ar-escape peak, where fewer electrons are produced in the drift region due to the lower energy of the photoelectrons.
For the SGR detector with the segmentation on the top side, the double peak spectrum is less pronounced[5] as for the detector with the segmentation on the bottom side (see the right column in Figure 7.7). This holds for the GEM readout strips and the Micromegas readout strips. With increasing U_{GEM} the double peak structure becomes more visible, but not as good as for the detector with the segmentation on the bottom side. The segmentation facing toward the drift region may influence the transparency of the GEM foil.
To detect charges with the GEM readout strips on the top side charges need to pass through the GEM holes two times:

1. The electrons from the drift region need to enter the holes to be amplified. This step is the same for both detector setups. Therefore for both SGR setups, the double peak spectrum becomes more visible at the Micromegas strips with increasing U_{GEM}.

2. The ions need to drift back through the hole to be detected by the top GEM strips. This step mostly influences the signal of the GEM strips on the top side. The more ions drift to the top of the SGR foil, the higher the pulse height of the GEM strips gets and the better the two peaks are separated. Therefore the pulse height of the GEM strips is strongly depending on U_{GEM}.

As for the DLC layer Micromegas detector (see Figure 6.15) it is difficult to reconstruct the characteristic pulse height spectrum with the bottom Micromegas readout strip layer at the same voltages. The ratio of 1.97 (see Equation 6.1) between the two peaks in the pulse height spectrum is reconstructed for multiple voltage combinations with both SGR detector types (see Figure 7.8).
For the detector with the segmentation on the bottom side, this ratio is constant on all readout strip layers for multiple voltage combinations if $U_{GEM} \geq 200\,V$.
For the detector with the segmentation on the top side, the values are more widely scattered around 1.97. This is in agreement with the impression noted from Figure 7.7. The segmentation on the top side of the SGR foil slightly distorts the energy resolution and thus degrades the reconstruction of the characteristic Argon spectrum. In addition, small deformations of the SGR foil can also lead to this.

[5] The spectra are compared at the same pulse heights for the top Micromegas strips.

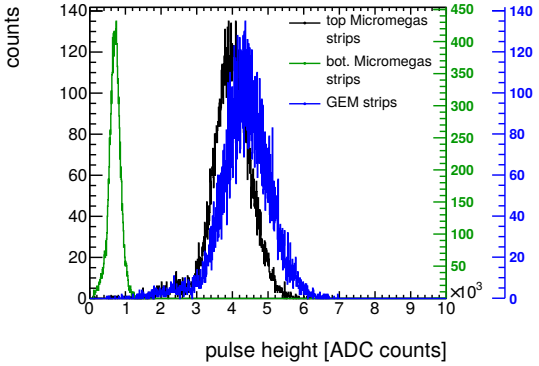

(a) Segmentation on the bottom side of the GEM foil. At least 15.000 events are shown. U_{ampl} = 490 V, U_{GEM} = 100 V, U_{drift} = 420 V.

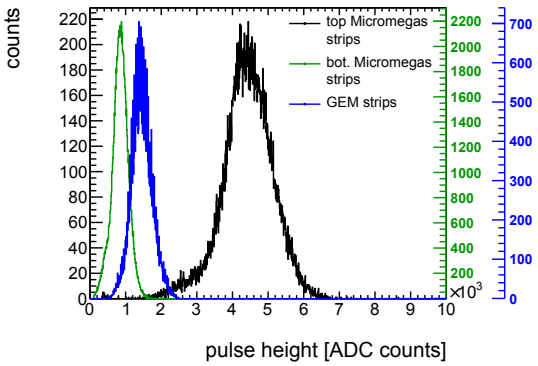

(b) Segmentation on the top side of the GEM foil. At least 25.000 events are shown. U_{ampl} = 510 V, U_{GEM} = 100 V, U_{drift} = 420 V.

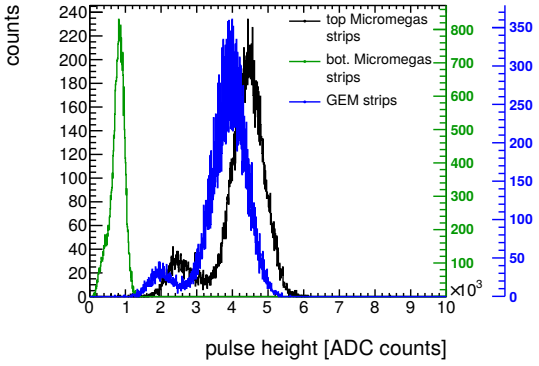

(c) Segmentation on the bottom side of the GEM foil. At least 22.000 events are shown. U_{ampl} = 400 V, U_{GEM} = 200 V, U_{drift} = 420 V.

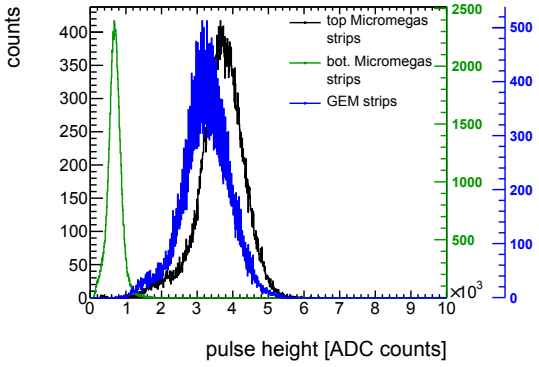

(d) Segmentation on the top side of the GEM foil. At least 42.000 events are shown. U_{ampl} = 440 V, U_{GEM} = 200 V, U_{drift} = 420 V.

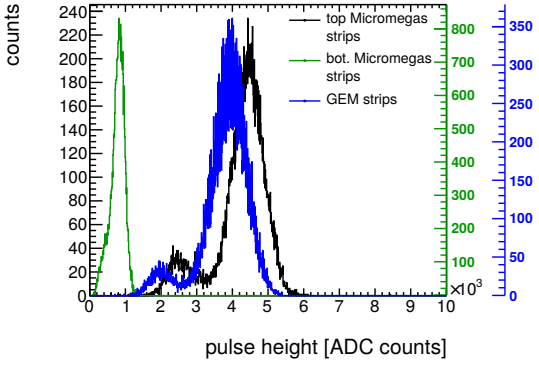

(e) Segmentation on the bottom side of the GEM foil. At least 19.000 events are shown. U_{ampl} = 310 V, U_{GEM} = 300 V, U_{drift} = 420 V.

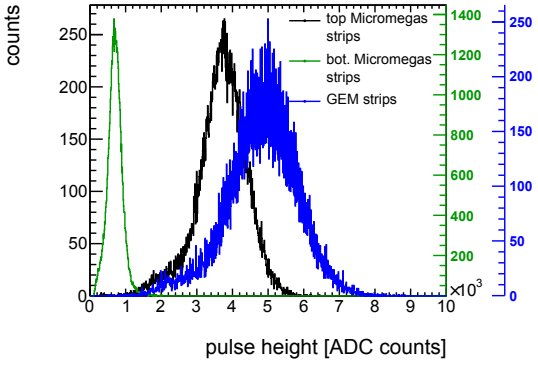

(f) Segmentation on the top side of the GEM foil. At least 6.000 events are shown. U_{ampl} = 360 V, U_{GEM} = 300 V, U_{drift} = 420 V.

Figure 7.7: Argon spectrum (cluster pulse height) measured with a ^{55}Fe 5.9 keV γ – source at approximately the same pulse height for the top Micromegas strips.
For the SGR detector with the segmentation on the bottom side (left), it is possible to reconstruct the spectrum for different voltage combinations with the GEM and top Micromegas strips equally well. For the detector with the segmentation on the top side (right), the escape peak is weaker visible. The pulse height of the top GEM strips is strongly dependent on U_{GEM}. This is not observed for the detector with the segmentation on the bottom side.
For both detector setups, the Ar-escape peak becomes more prominent with increasing U_{GEM}.
As for the DLC layer Micromegas detector (see Figure 6.15) it is difficult to reconstruct the spectrum with the bottom Micromegas strips at the same voltages.
The signal of the GEM strips is multiplied by a factor of 4.48 to compensate for the effects of the adapter board (see Chapter 3.3). Saturated events are rejected for these spectra.

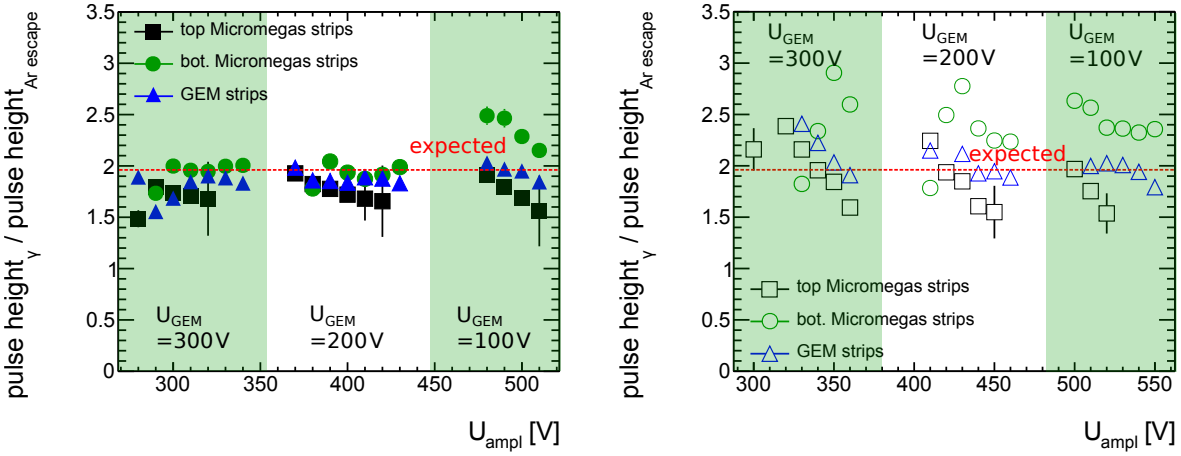

(a) Segmentation on the bottom side of the GEM foil.

(b) Segmentation on the top side of the GEM foil.

Figure 7.8: Ratio between the 5.9 keV γ – peak and the Ar-escape peak for different U_{GEM} (columns) and U_{ampl} (X-axis).
A ratio of 1.97 is expected. For $U_{GEM} \geq 200$ V a constant ratio of approximately two is reconstructed with all readout strip layers. For $U_{GEM} = 100$ V a dependency on U_{ampl} is observed.
For the detector with the segmentation on the top side, the values are spread broader around 2.
Only values with less than 30 % of the strips being saturated are shown. Values with only one peak respectively with no hint of a second peak are discarded.
$U_{drift} = 420$ V

Another measure of energy resolution is the width σ of the 5.9 keV γ-peak σ normalized to its mean reconstructed pulse height (see Equation 6.2 and Figure C.2).
For the detector with the segmentation on the bottom side, it is between 0.1 and 0.15 for the top Micromegas and GEM strips. No strong dependency on U_{GEM} is observed (see Figure 7.9a).
For the setup with the segmentation on the top side, the energy resolution is between 0.12 and 0.2 for the top Micromegas and GEM strips (see Figure 7.9a). The energy resolution of the GEM strips improves with increasing U_{GEM}. Especially at $U_{GEM} = 100$ V the energy resolution of the GEM strips deteriorates, since less ions drift through the GEM holes to the top of the foil (see Figure B.3).
As for the standard DLC Micromegas detector, the values for the bottom Micromegas readout strip layer are worse. Overall a similar energy resolution as for the standard DLC Micromegas detector (see Figure 6.17) is reached with the Micromegas readout strips.
All these measurements prove that replacing the micro-mesh in a Micromegas detector with a SGR foil has no significant effect on the energy resolution of the Micromegas readout strips. Only a dependence between the measurement accuracies and the location of the segmentation of the GEM foil is recognizable. The detector properties are slightly worse if the segmentation is on the top side. This will be investigated in Chapter 7.6.

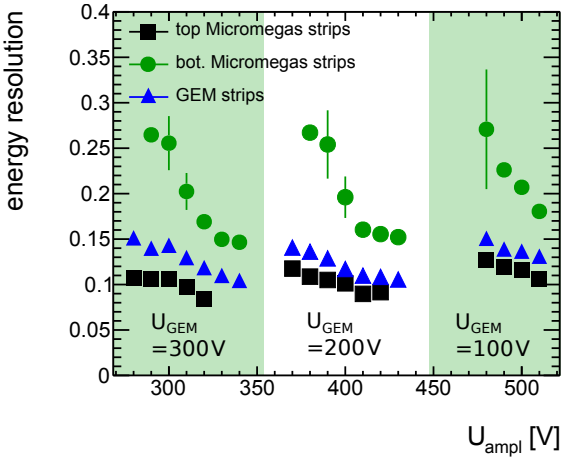

(a) Segmentation on the bottom side of the GEM foil.

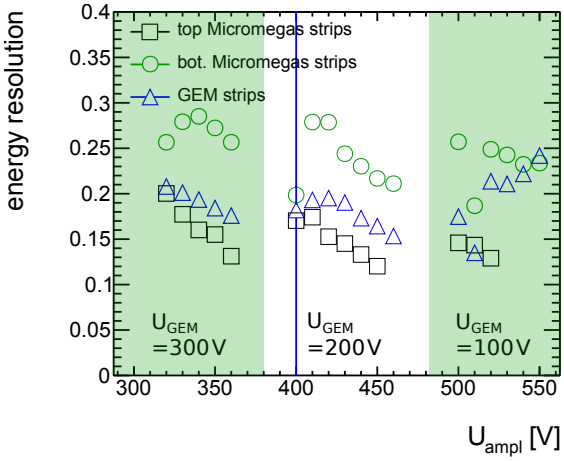

(b) Segmentation on the top side of the GEM foil.

Figure 7.9: Energy resolution of the SGR detector layers for different U_{GEM} (columns) and U_{ampl} (X-axis).
The energy resolution is defined according to Equation 6.2. The energy resolution of the top Micromegas strips is slightly better than that of the GEM strips. If the segmentation is on the bottom side of the GEM foil values of around 10 % are reached for the GEM and top Micromegas strips. For the segmentation on the top side of the GEM foil, the energy resolution is slightly worse. This will be further investigated in Chapter 7.6.
Only values are shown with less than 30% of the strips being saturated.
U_{drift} = 420 V

7.5.2 Pulse Height Analysis of Both Readout Strip Layers

As expected (see Chapter 1.1.2) and already observed for the DLC layer Micromegas detector (see Chapter 6.6.2) the pulse height of all readout strip layers increases exponentially with increasing U_{ampl} for all measured U_{GEM} (see Figure 7.10). The pulse height of the GEM strips is multiplied by 4.48 to correct for the used adapter board (see Chapter 3.3).
A linear correlation between the pulse height on the top Micromegas readout strips and the GEM strip is clearly visible (see Figure 7.11).
For the detector with the segmentation on the bottom side the corrected pulse height of the GEM strips is similar to that of the top Micromegas strips (see Figure 7.12a).
For the detector with the segmentation on the top side, the pulse height of the GEM strips is similar to the pulse height of top Micromegas readout strips for $U_{GEM} \geq 200$ V (see Figure 7.12b)[6]. For lower U_{GEM} fewer ions are drifting through the holes to the top side of the SGR foil, where the signal is detected. According to the simulations explained in Chapter 5, 2.5 times fewer ions are drifting back to the top side of the SGR foil for U_{GEM} = 100 V as for U_{GEM} = 300 V (see Figure B.3). The ratio shown in Figure 7.12b differs by a factor of 3.5 for U_{GEM} = 100 V from that for U_{GEM} = 300 V.
For both detector setups, the pulse height on the bottom Micromegas readout strips is lower by a factor of approximately five to seven (see Figure 7.12).

[6] More precisely, the signal of the GEM strips at U_{GEM} = 300 V is a factor 1.3 higher than on the Micromegas strips and at U_{GEM} = 200 V a factor 0.88 lower. This, together with the fact that the pulse heights of the top Micromegas strips for signal shown in Figure 7.5b are not the same, explains the apparent contradiction to Figure 7.5b.

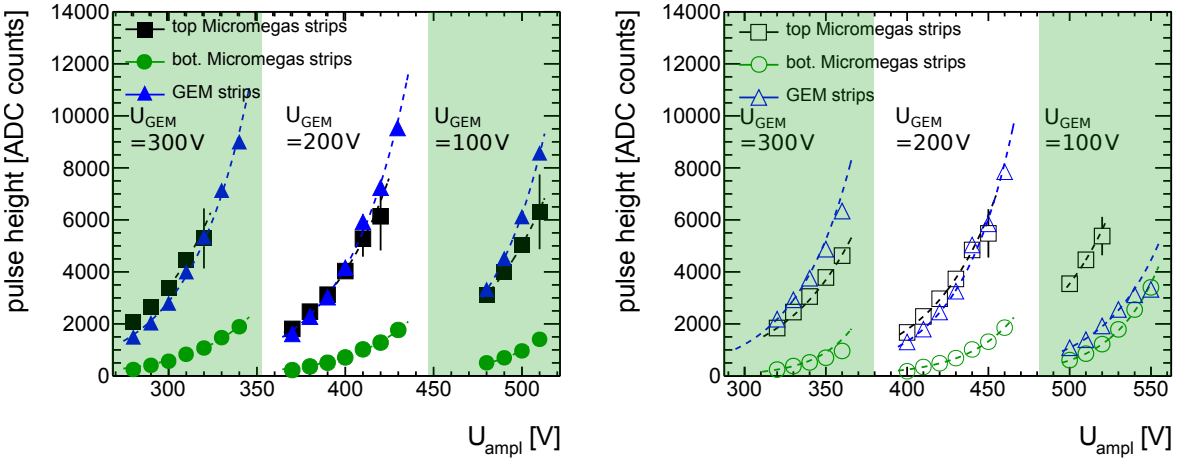

(a) Segmentation on the bottom side of the GEM foil.

(b) Segmentation on the top side of the GEM foil. No data are simulated for $U_{GEM} = 200\,V$.

Figure 7.10: Pulse height for different U_{GEM} (columns) and U_{ampl} (X-axis).
As pulse height the MPV of the 5.9 keV photon peak is taken (see Figure C.2).
On all readout strip layers, the pulse height increases exponentially with increasing U_{ampl}. For the detector with the segmentation on the top side the pulse height of the GEM strips is strongly dependent on U_{GEM}. This is not the case for the inverse layout.
The signal of the GEM strips is multiplied by a factor of 4.48 to compensate for the effects of the adapter board (see Chapter 3.3).
Only values are shown with less than 30% of the strips being saturated.
$U_{drift} = 420\,V$

The ratios shown in Figure 7.12 are in good agreement with the simulation as described in Chapter 5. For the simulation, only the electron avalanche in the given geometry is simulated. The electron spread on the DLC layer anode is neglected for this simulation. Since the simulated (without electron spread taken into account) pulse height values agree with the measured (influenced by electron spread) ones, it can be assumed that the amplitude of the signals is hardly affected by the charge movement on the resistive layer. Since the electron spread does hardly induce a signal on the GEM strips (in simulation and measurements), it can be excluded that the pulse heights are reduced equally on all readout strips due to the electron drift. In this case, the factor for the GEM strips would not match. Based on the simulation, it can be concluded that the problematic dynamic range of the Micromegas readout structure is solely due to the detector geometry. Discrepancies between measurements and simulation for the bottom Micromegas strips are due to the lower sensitivity of the APV25 readout chips at low pulse heights. Incorrectly discarded strip signals reduce the cluster pulse height and thus increase the shown factor.

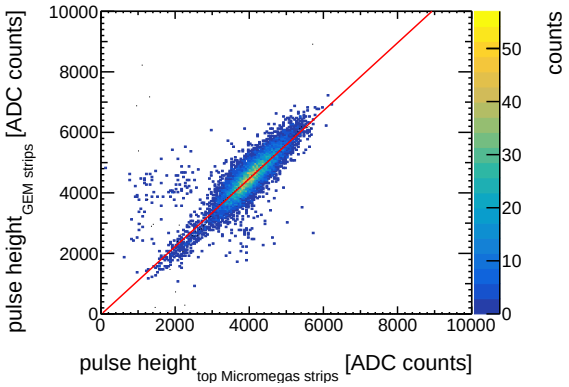

(a) Segmentation on the bottom side of the GEM foil.
Slope of the linear fit: 1.12
U_{ampl} = 490 V, U_{GEM} = 100 V, U_{drift} = 420 V.

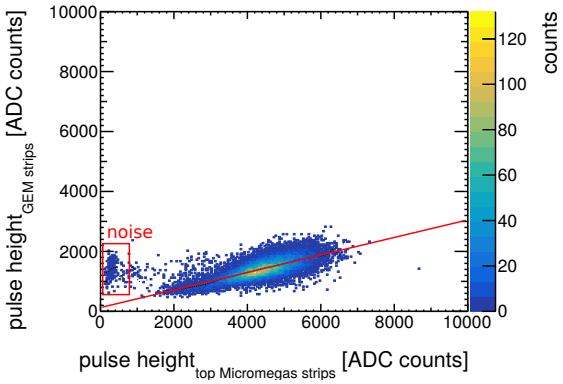

(b) Segmentation on the top side of the GEM foil.
Slope of the linear fit: 0.29
U_{ampl} = 510 V, U_{GEM} = 100 V, U_{drift} = 420 V.

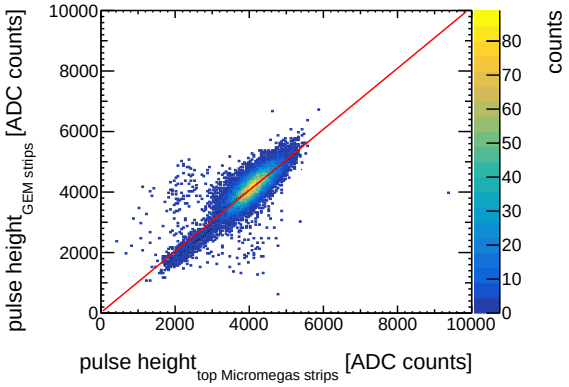

(c) Segmentation on the bottom side of the GEM foil.
Slope of the linear fit: 1.01
U_{ampl} = 400 V, U_{GEM} = 200 V, U_{drift} = 420 V.

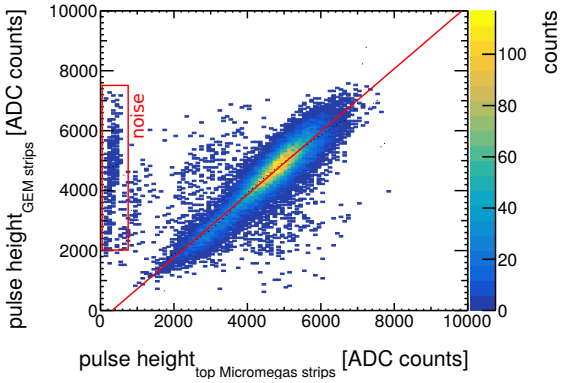

(d) Segmentation on the top side of the GEM foil.
Slope of the linear fit: 1.05
U_{ampl} = 440 V, U_{GEM} = 200 V, U_{drift} = 420 V.

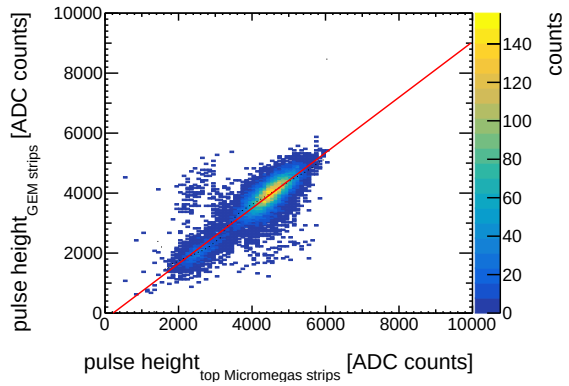

(e) Segmentation on the bottom side of the GEM foil.
Slope of the linear fit: 0.95
U_{ampl} = 310 V, U_{GEM} = 200 V, U_{drift} = 420 V.

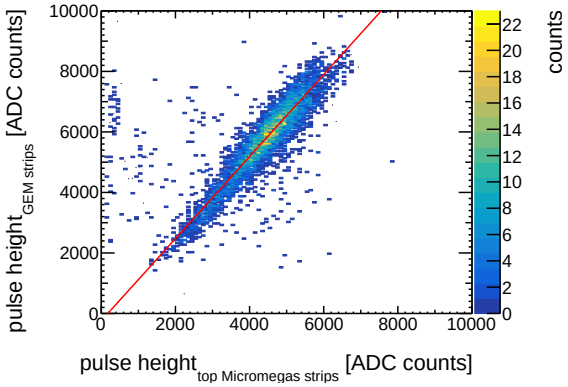

(f) Segmentation on the top side of the GEM foil.
Slope of the linear fit: 1.25
U_{ampl} = 360 V, U_{GEM} = 300 V, U_{drift} = 420 V.

Figure 7.11: Correlation between the pulse height reconstructed with the GEM strips (Y-axis) and the top Micromegas strips (X-axis).
A linear correlation between both pulse heights is observed for all voltage configurations shown. Except for the detector with the GEM strips on the top side at U_{GEM} = 100 V (see Figure b), the pulse heights of the GEM strips and top Micromegas strips are similar (slope of the fit ≈ 1). The inverse of the slope is in agreement with the values shown in Figure 7.12.
The pulse height of the GEM strips is corrected for the adapter board.
The same data are shown as in Figure 7.7.

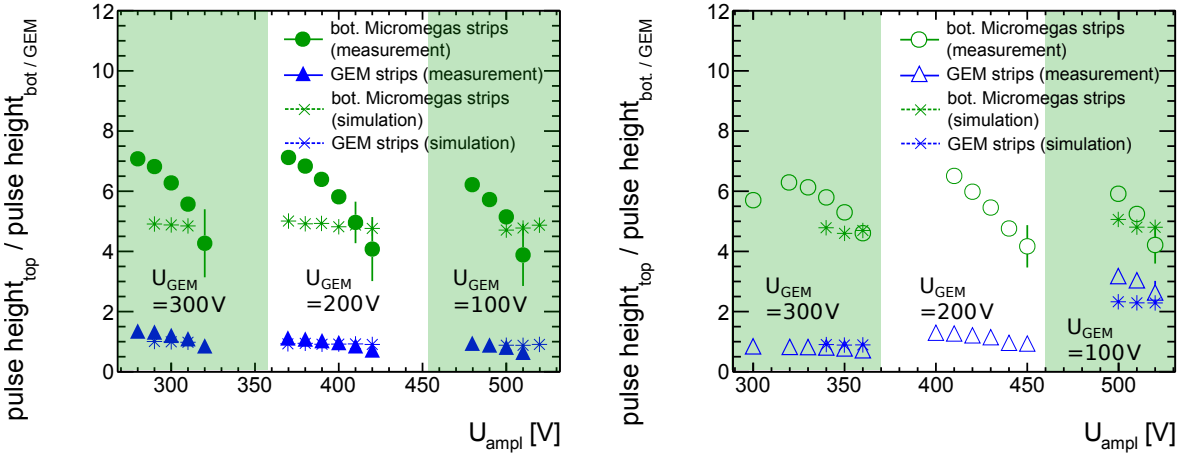

(a) Segmentation on the bottom side of the GEM foil.

(b) Segmentation on the top side of the GEM foil.

Figure 7.12: Ratio between the cluster pulse heights of the top Micromegas and the other two readout strip layers for different U_{GEM} (columns) and U_{ampl} (X-axis).
As pulse height for each readout layer the MPV of the 5.9 keV photon peak is taken (see Figure C.2).
For most voltages, the pulse height of the GEM strips is approximately the same as for the top Micromegas strips, whereas the signal on the bottom Micromegas readout strips is five to seven times smaller. This is in agreement with the DLC Micromegas data (see Figure 6.19b).
At lower U_{GEM}, the ratio shown increases for the GEM strips on the top of the foil (blue data points at U_{GEM} = 100 V in Figure b). Fewer electrons are drifting through the holes to the readout strips (see figure B.2).
The measured values are in agreement with the simulations from Chapter 5.
The measured signal of the GEM strips is multiplied by a factor of 4.48 to compensate for the effects of the adapter board (see Chapter 3.3).
Only measurement values are shown with less than 30% of the strips being saturated.
U_{drift} = 420 V

7.6 Comparison of both SGR Detector Setups Segmentation on the Top vs Segmentation on the Bottom

Considering Figure 7.10 again, it is noticeable that for all U_{GEM} higher U_{ampl} are needed for the detector configuration with the segmentation on the top side to reach the same pulse height. This also applies to the pulse height of the Micromegas readout strips which are expected to be independent of the transparency for back drifting ions. For both SGR detectors the Micromegas readout strips behave similarly as if the readout structure is used for a typical Micromegas detector (see Chapter 6).
As simulations have shown, the segmentation of the SGR foil has a big impact on the transparency of the SGR foil[7]. When the segmentation is on the bottom side almost all charges are drifting through the GEM holes (see Figure 7.13a). The top side is a continuous surface interrupted only by the GEM holes. Since the electric field is highest on the edges of the copper most charges are pulled into and through the hole (see Figure 5.2).
When the segmentation is on the top side many electric field lines in the drift region are also ending on the edge of the GEM strips. Therefore also the drifting charges might end there (see Figure 7.13b). The transparency of the foil is reduced by GEM strips on the top side.

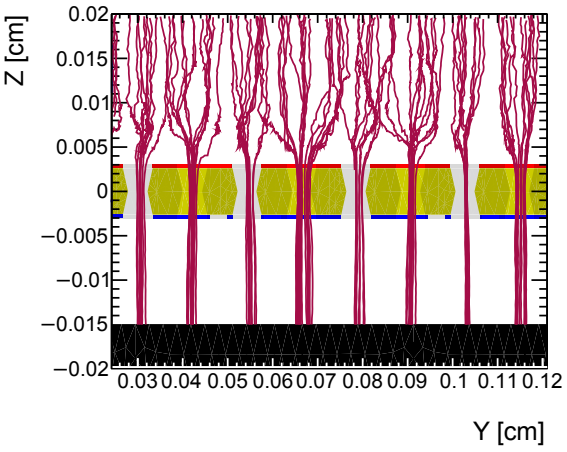

(a) Segmentation on the bottom side of the GEM foil.

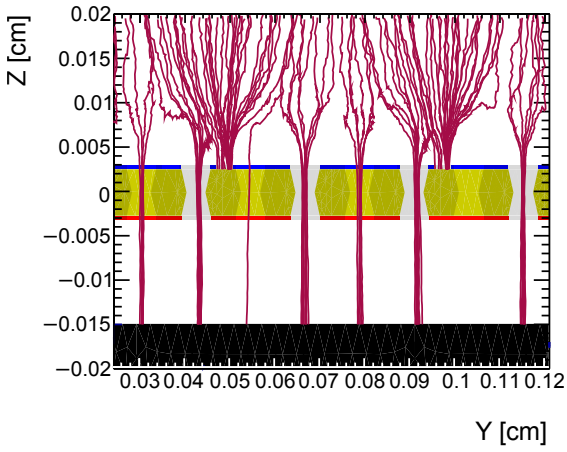

(b) Segmentation on the top side of the GEM foil.

Figure 7.13: Simulation of the particle path of negatively charged particles starting at the cathode (Y/Y plane).
The path of all charges is projected onto the Y/Z plane. For visualization reasons, negative ions are simulated instead of electrons due to the reduced lateral diffusion of the ions. The simulation is done with Garfield++ [Alsamak et al., 2022].
For the design with the segmentation on the bottom side (Figure a), the transparency of the GEM foil is not influenced by the segmentation.
For the design with the segmentation on the top side (Figure b), many particles are ending in the gap between the strips (Y≈ 0.05 cm, and Y≈ 0.95 cm). The transparency decreases compared to the design with the segmentation on the bottom side.
U_{ampl} = 300 V, U_{GEM} = 300 V, U_{drift} = 420 V

[7]The simulation shown is similar to the one shown in Chapter 5. The only difference is that only the drift of 800 electrons is simulated and not the avalanche process.

In Figure 7.14 the measured pulse height ratio between both SGR setups for the top Micromegas strips is shown[8]

$$\frac{pulse\,height_{\,seg.\,bot.}}{pulse\,height_{\,seg.\,top}} \tag{7.1}$$

This ratio is compared with the corresponding simulated ratio of the transparencies:

$$\frac{transparency_{\,seg.\,bot.}}{transparency_{\,seg.\,top}} \tag{7.2}$$

The transparency is given by Equation 5.1. With increasing U_{GEM} this fraction increases for simulation and measurement similarly. For the SGR detector with the segmentation on the top side, more electrons are ending at the Kapton at the border rim of the GEM strips.
This also explains why the Ar pulse height spectrum (see Chapter 7.5.1) is worse if the segmentation is on the top side.
The simulated ratio is slightly lower than the measured ratio. The discrepancy between simulation and measurement is due to an optimized geometry for the simulation. Only the drift and not the full avalanche of the electrons is simulated. The processes in the Micromegas amplification region and inside the GEM hole are neglected. Furthermore, data were taken with both detectors at different times (weeks). The environmental conditions and thus the detector responses were different.

[8] As shown previously, the pulse height of the Micromegas strips is not affected by the back drift of the ions as is the case for the GEM strips.

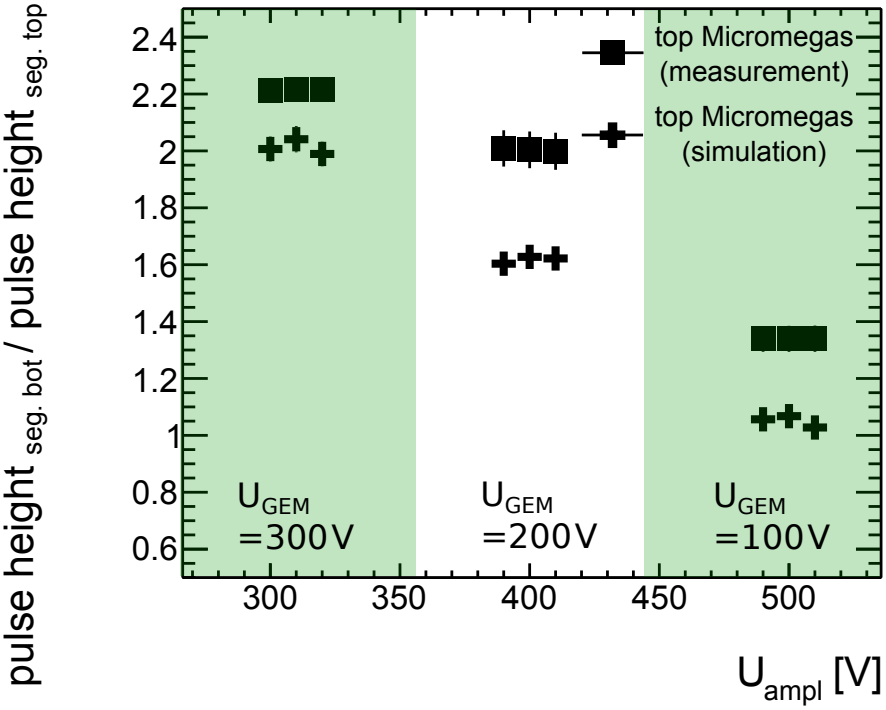

Figure 7.14: Comparison of the measured top Micromegas readout strip pulse height for the SGR detector with the segmentation on the top or the bottom side.
Measured data are compared with the simulated ratio of the corresponding transparencies.
To minimize the influence of the cluster size, the charge of the maximum strip is taken as pulse height. The measured pulse height data are extrapolated to the U_{ampl} shown to have data for the same voltage for both detectors that are not affected by saturation.
The drift of the electrons is simulated. An event is considered transparent when the electron is entering the GEM hole.
Both detectors are identical except for the position of the segmentation, therefore the increase of the pulse height with U_{ampl} is expected to be the same for both detectors.
No dependency on U_{ampl} is observed for the measurement and the simulation.
With increasing U_{GEM} more electrons are ending in the gap between the GEM strips for the detector with the segmentation on the top side. For the detector with the segmentation on the bottom side, the GEM strips have much less influence on the transparency and thereby on the pulse height (see figure 7.13). The ratio increases with increasing U_{GEM}.
U_{drift} = 420 V.

7.7 Absorption Spectroscopy of a 3D-Printed Picture of "The Scream"

To obtain a first impression of the spatial resolution of the detector, a 3D printed picture of "The Scream" by Edvard Munch is irradiated using a ^{55}Fe source. The positions of the photons are measured with the SGR detector. The Y-coordinate is obtained by the GEM strips on the bottom side, and the X-coordinate by the top Micromegas readout strips.
The contrast of the painting is reflected in the thickness of the 3D print (see Figure 7.15a). The thickness ranges from 0.5 mm in light areas to 2.9 mm in dark areas. The material of the 3D print is a PLA filament [Innofil3D].
In the areas where the 3D print is thicker, more photons are absorbed by the PLA than in the thinner areas. Almost all photons are absorbed in the thicker areas. This is reflected in the hit position distribution (see Figure 7.15b). Dimensions of the picture larger than 1-2 mm, are resolved. The resolution is limited by the angle of inclination of the photons. The ^{55}Fe source is positioned such that the entire detector is irradiated. While the photons traverse

the 3D print approximately vertically in the center, the angle of inclination increases steadily toward the edges of the 3D print. The distance between the 3D print and the conversion point of the photon in the detector volume is approximately 2 cm. This lever arm shifts the measured position of the photon relative to the position at which the photon crossed the 3D print when the photon enters the detector at an angle.
Furthermore the shape and position of the pillars[9] are resolved as inefficient spots in the hit distribution (X ≈ 180 in Figure 7.15b). At the position of the pillars, no gas amplification in the Micromegas amplification gap takes place. The spatial resolution of the detector is better than the dimension of a pillar.

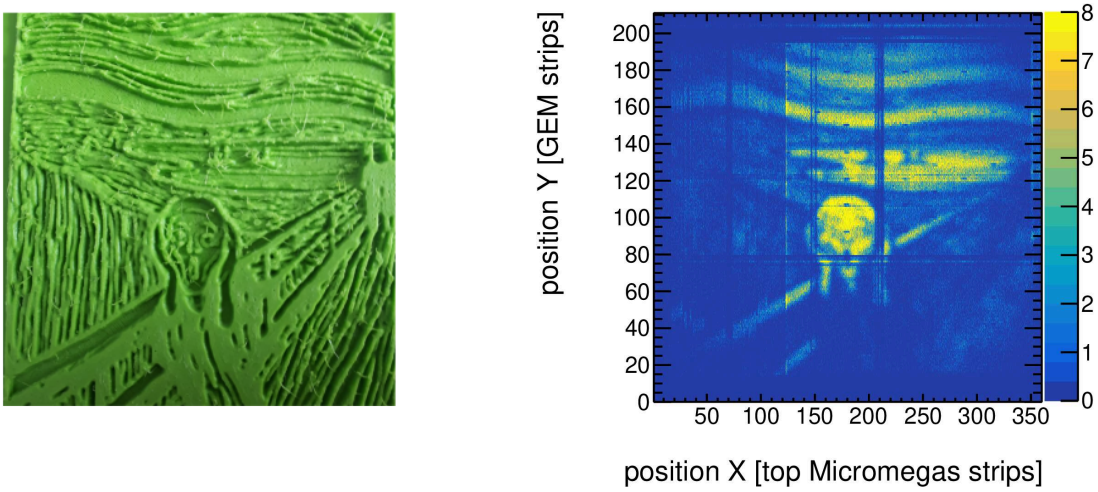

(a) 3D printed picture of "The Scream".

(b) Absorption spectroscopy image of the 3D printed picture of "The Scream"

Figure 7.15: The 3D printed picture of "The Scream" is irradiated with ^{55}Fe.
More photons are absorbed in thicker regions. The picture is reproduced using the SGR detector. A problematic readout chip on the left of the X-coordinate causes lower contrast for 0 < X < 120. Observed inefficient lines are caused by problematic readout strips of the Micromegas readout structure (This was observed as well with the standard DLC layer Micromegas detector as shown in Chapter 6.2).
Also, the shape of the pillars is resolved as inefficient spots (best visible as dark blue spots along the Y coordinate for X ≈ 180). The width of the pillars is 200 µm. Therefore the spatial resolution is considerably better than that.
The X-coordinate is obtained with the top Micromegas strips and the Y-coordinate with the GEM strips.
U_{ampl} = 440 V, U_{GEM} = 200 V, U_{drift} = 420 V

7.8 Summary of the Characterization of the SGR Detector

Two SGR detectors were investigated. One had a segmentation on the bottom side, the other on the top side of the SGR foil. Both detector setups showed good results.
Replacing the micro micro-mesh by a SGR foil did not influence the signal shape of the Micromegas readout strips (compare Figure 7.4 with Figure 6.9b). Whereas the pulse height of the GEM strips on the bottom side was almost not affected by U_{GEM} a strong dependency was observed for the GEM strips on the top side (see Figure 7.12). This has also been true for energy resolution (see Figure 7.9).
With both detector setups, it was possible to reconstruct the characteristic Ar-spectrum simultaneously with the GEM and top Micromegas readout strips (see Figure 7.7). The

[9] $A_{pillar} = 1.2 \times 0.2\,mm^2$, $d_{pillar} = 7\,mm$

reconstruction worked better for the setup with the segmentation on the bottom side since a segmentation on the top side strongly influences the transparency of the SGR foil (see Figure 7.14).
The pulse height of the GEM strips was similar to the pulse height of the top Micromegas readout strips (see Figure 7.12). A good 2D-position reconstruction was possible with a SGR detector obtaining one coordinate from the GEM strips and the other one from the top Micromegas readout strips. This was reflected in an absorption spectroscopy picture of a 3D print of "The Scream" (see figure Figure 7.15).
For best measurement results, a minimum GEM voltage of $U_{GEM} = 200\,V$ must be applied.

Chapter 8

Outlook: Characterization of a Double-Sided SGR Detector

Since both SGR detectors worked well (see Chapter 7), a third version of an SGR detector is built and tested. The difference to the previously described SGR detectors is, that the SGR foil is segmented on both sides. At the investigated detector the segmentation of the SGR foil is parallel on both sides. The GEM strips on the top side are shifted by half a pitch to the bottom side.
The purpose of this chapter is to briefly demonstrate that this type of detector works similarly well as the previously characterized SGR detectors.
As in the previous chapters, saturated events are rejected in the analysis. The signal on the Micromegas readout strip induced only by the electron spread on the anode is truncated.

8.1 Measurement Setup

The setup is similar to the setup described in Chapter 7.1. The SGR detector is irradiated by ^{55}Fe.
The investigated SGR detector has four readout strip layers:

- **Top Micromegas strips**: This is the same readout strip layer as the top strip layer in the standard DLC layer Micromegas and single-sided SGR detector.
- **Bottom Micromegas strips**: This is the same readout strip layer as the bottom strip layer in the standard DLC layer Micromegas and single-sided SGR detector.
- **Bottom GEM strips**: These are the readout strips located on the bottom side of the SGR foil. As for a single-sided SGR detector the GEM strips are at ground potential. As for the detectors analyzed in Chapter 7, the adapter board must be used for this side only if the coupling of noise to the trigger signal needs to be prevented (see Chapter 3.3).
- **Top GEM strips**: These are the readout strips located on the top side of the SGR foil. To this readout strip layer a high voltage U_{GEM} is applied. This layer can only be read out if the adapter board as described in Chapter 3.3 is used. Each GEM strip is set on HV separately via the adapter board. Only the fast signal is decoupled via the high pass filter on the adapter board. This allows the readout ASICs to be grounded, while the GEM strips are set to high voltage.

A double-sided SGR detector, in which all readout strips are equipped with readout electronics, can only be read out if an external trigger, e.g. a scintillator signal, is used or if the readout electronics is capable to trigger internally.
In the following measurements, one side of the SGR foil is not read out with APV25 ASICs and is instead used to trigger[1]. The setup is similar as described in Chapter 7.1. The measurements are performed separately for the bottom and top readout of the SGR foil. The data are combined afterward.

The detector is only investigated at $U_{GEM} = 200\,V$.
To prevent coupling of noise from the APV25 readout chips to the trigger signal, the GEM strips are read out using the adapter board.

8.2 Pulse Height Analysis

In this section, the pulse height of all readout strip layers is considered and compared with each other. As in the previous chapters, the energy resolution of the detector is also investigated.
In this section, pulse height refers to the summed-up charges of all hit strips in a cluster (see Equation 3.7).
The pulse height of the GEM strips is corrected for the adapter board (see Chapter 3.3) if not stated differently.

8.2.1 Ar Escape Peak Analysis as a Measure of the Energy Resolution

As described in Chapter 6.6.1 the ratio of the 5.9 keV γ-peak to the 3 keV Ar-escape peak is a measure of the energy resolution of the detector (see Figure 8.1).
With the double-sided SGR detector, a double peak-like structure is reconstructed for multiple different U_{ampl}. Even though for $U_{ampl} < 440\,V$ the double peak shape of the spectrum is only indicated the ratio is reconstructed with the bottom Micromegas readout strip layer. At $U_{ampl} = 440\,V$ the Ar spectrum is reconstructed nicely on all readout strip layers. For higher U_{ampl} saturated strips on the top Micromegas readout strip layer start to dominate.
The reconstruction of the Argon spectrum with the double-sided SGR detector works similarly well as with the SGR detector with the segmentation on the bottom side. The amplification voltages to resolve the Ar spectrum are in the same range as for the SGR detector with the segmentation on the top side (see Figure 7.8b). This underlines that a segmentation on the top side of the SGR foil influences the detector properties as described in Chapter 7.6.
The reason why this detector behaves slightly better than the SGR detector with the segmentation on the top side is still under investigation. Fewer deformations of the foil or a more precise production of the foil can be a reason for that.

Another measure for the energy resolution is the width of the 5.9 keV photoelectron peak normalized by the reconstructed pulse height (see Equation 6.2).
The energy resolution is between 10 %, and 20 % for all readout strip layers (see Figure 8.2). This value is approximately the same for the bottom GEM strip and the top Micromegas readout strips. Both readout strips observe the non-shielded signal of the charge movement in the Micromegas amplification region.
The other two readout strip layers are shielded from the Micromegas amplification region by

[1] For the trigger signal, all strips are galvanically coupled.

one layer of readout strips[2]. This explains the slightly worse energy resolution for the top GEM and the bottom Micromegas strips.
The energy resolution of the double-sided SGR detector is similar to the energy resolution of the SGR detector with the segmentation on the bottom side. The reason why the energy resolution of the lower Micromegas strips for the double-sided SGR detector is better than for the two single-sided SGR detectors (see Figure 7.9) and than for the DLC layer Micromegas detector (see Figure 6.17) is still under investigation.

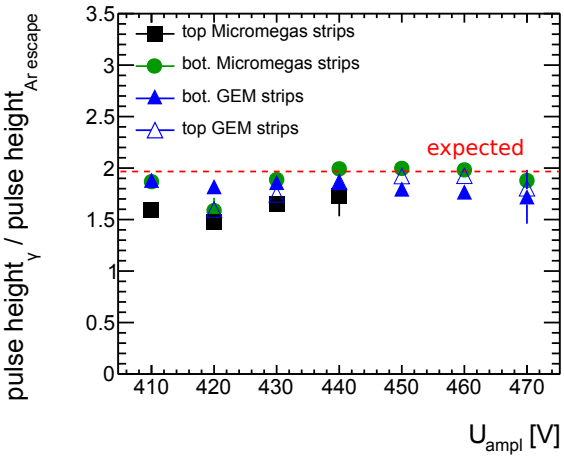

Figure 8.1: Ratio between the 5.9 keV γ – peak and the Ar-escape peak in dependence of U_{ampl}.
A ratio of 1.97 is expected. A constant ratio close to the expected one is reconstructed with all readout strip layers. The reconstructed ratio is similar to that of the SGR detector with the segmentation on the bottom side (see Figure 7.8b).
Only values are shown with less than 30 % of the strips being saturated. For $U_{ampl} > 440$ V more than 30 % of all top Micromegas readout strips are saturated.
$U_{GEM} = 200$ V, $U_{drift} = 420$ V.

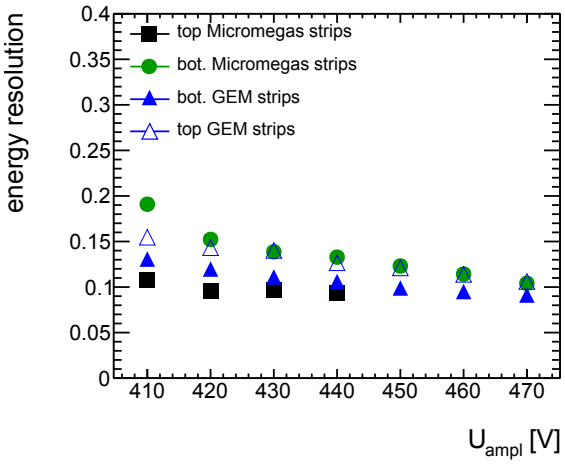

Figure 8.2: Energy resolution of the SGR detector layers in dependence of U_{ampl}.
The energy resolution is determined according to Equation 6.2. An energy resolution of approximately 10 % is reached with all readout strip layers.
The energy resolution of the bottom GEM (blue filled triangles) and top Micromegas readout strips (black squares) is similar to that of the SGR detector with the segmentation on the bottom side (see Figure 7.9a). The resolution of the other two readout strip layers is better than that of the single-sided SGR detector (see Figure 7.9b).
Only values are shown with less than 30 % of the strips being saturated. For $U_{ampl} > 440$ V more than 30 % of all top Micromegas readout strips are saturated.
$U_{GEM} = 200$ V, $U_{drift} = 420$ V.

[2]The bottom Micromegas readout strips are shielded by the top Micromegas readout strips. The top GEM strips are shielded by the bottom GEM strips.

8.2.2 Pulse Height Analysis of All Readout Strip Layers

As expected (see Chapter 1.1.2) and observed for the DLC layer Micromegas detector (see Chapter 6.6.2) and the single-sided SGR detector (see Chapter 7.5.2) the pulse height increases exponentially with increasing U_{ampl} (see Figure 8.3). To reach the pulse heights shown, similar U_{ampl} are needed as in the SGR detector with the segmentation on the top side (see Figure 7.10). Differences can be explained by different environmental conditions[3]. This underlines as well that a segmentation on the top side of the SGR foil influences the detector properties as described in Chapter 7.6.

The ratio of the pulse height between the different readout strip layers (see Figure 8.4) is independent of U_{ampl}. As expected and observed in the single-sided SGR detector (see Figure 7.12a), the pulse height of the bottom GEM strips is the same as for the top Micromegas strips.
The pulse height of the bottom Micromegas strips is as for the single-sided SGR detector (see Figure 7.12) approximately five times smaller than for the top Micromegas strips. The only difference is that this value is not depending on U_{ampl} as it is observed for the single-sided SGR detector. Possibly the detector was better grounded than the single-sided SGR detector, which resulted in low signals being better resolved and not discarded as noise.
The pulse height of the top GEM strips is 1.5 times smaller than for the top Micromegas strips. For the single-sided SGR detector, this ratio is approximately 1.2 (see Figure 7.12b). The explanation is analogous to the electron transparency of the SGR foil as described in Chapter 7.6. As the transparency of the SGR foil for electrons in the drift region is reduced by the segmentation facing towards the drift region, the transparency of the SGR foil for ions is reduced by the segmentation facing towards the Micromegas amplification region. Fewer ions are drifting through the holes to the top GEM strips. Since this is the main part of the signal induced on the top GEM strips, the pulse height of these strips is reduced.

[3]The room temperature differed by up to 15 °C. The air pressure differed by up to 20 mbar.

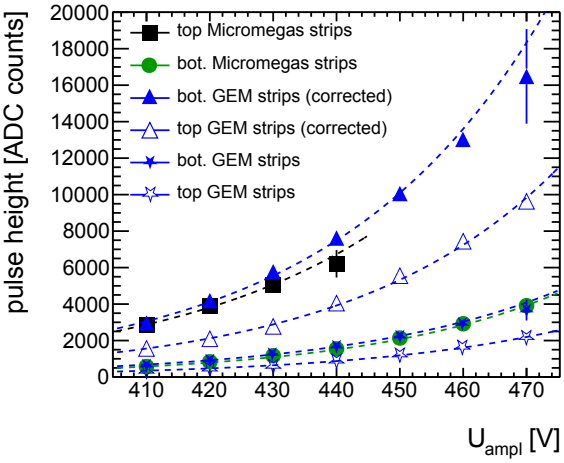

Figure 8.3: Pulse height in dependence of U_{ampl}.
On all readout strip layers, the pulse height increases exponentially with increasing U_{ampl}. The pulse height of the top Micromegas readout strips is approximately the same as for the bottom GEM strips after the pulse height is corrected for the adapter board (see Chapter 3.3).
Mainly the ions drifting through the GEM hole induce a signal on the top GEM strips (see simulations in Chapter 5.3.1). Since not all ions are drifting back the pulse height on the top GEM strips is smaller.
Only values with less than 30% of the strips being saturated are shown.
U_{GEM} = 200 V, U_{drift} = 420 V.

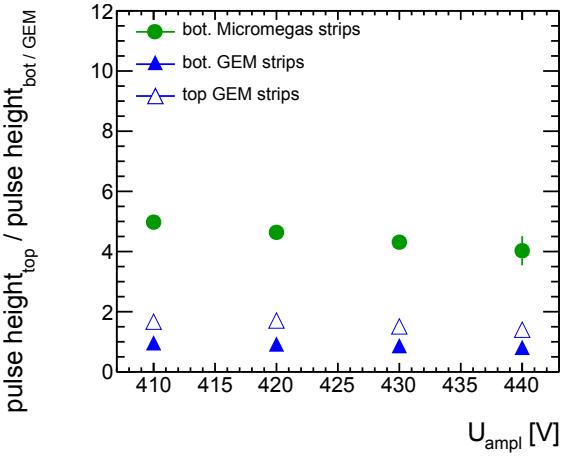

Figure 8.4: Ratio between the pulse height of the top Micromegas and the other three readout strip layers in dependence of U_{ampl}. The values are similar to the values reconstructed with a single-sided SGR detector (see Figure 7.12). A difference is the less pronounced pulse height dependency for the bottom Micromegas readout strips.
The pulse height of the top Micromegas readout strips is the same as that of the bottom GEM strips. The ratio of the top GEM strips is larger in the double-sided SGR detector (approximately 1.5) than in the single-sided SGR detector (approximately 1.2 in Figure 7.12b).
Only values with less than 30 % of the strips being saturated are shown.
U_{GEM} = 200 V, U_{drift} = 420 V.

8.3 Summary of the Characterization of the Double-Sided SGR Detector

A SGR detector with the segmentation on both sides was investigated. The segmentation was parallel on both sides but shifted by half a pitch to each other. The detector showed similar good results as the single-sided SGR detector (see Chapter 7).
As for the single-sided SGR detector, the pulse height of the bottom GEM strips was similar to the pulse height of the top Micromegas readout strips (see Figure 8.4). Compared to the single-sided SGR detector the ratio between the pulse height of the top GEM strips and top Micromegas increased by a factor of 1.5 for the top GEM strips. As the segmentation on the top side of the SGR foil influences the electron transparency of the SGR foil (see Chapter 7.6) the transparency of the SGR foil for back drifting ions decreases by the segmentation on the bottom side.
All readout strip layers of the double-sided SGR detector showed a good energy resolution (see Figure 8.2).
The detector was operated at similar U_{ampl} as the single-sided SGR detector with the segmentation on the top side.

Chapter 9

Determination of the Spatial and Angular Properties of the SGR Detector at the H4 Beam-Line (SPS / CERN)

As a final check, the spatial and angular properties of the SGR detector are determined. An experiment was carried out at the H4 beam line at CERN's Super Proton Synchrotron (SPS) [Charitonidis and Efthymiopoulos, 2017]. 120 GeV muons were used to investigate the performance of the detector. By varying the values of U_{GEM} and U_{ampl}, the properties of the detector were precisely determined, and the results, including spatial resolution and efficiency for both perpendicular and inclined tracks, are presented in this chapter.
This experiment focuses on the investigation of the GEM strips and the top Micromegas readout strips. Therefore the SGR detector is investigated close to the working point of the GEM strips and the top Micromegas readout strips. As mentioned in Chapter 6.7.1, the bottom Micromegas strip layer is not at the working point in this case[1].
In this chapter, the X-coordinate is defined as the coordinate measured by the top Micromegas readout strip layer, while the Y-coordinate is defined as the coordinate measured by both the GEM strips and the bottom Micromegas readout strip layer.
The pulse height in this chapter refers to the summed-up charges of all hit strips in a cluster (see Equation 3.7).
In this chapter the V-legs of the signal which are created due to the electron spread on the anode (see Chapter 6.3) are not cut off.

9.1 Measurement Setup

Two SGR detectors were investigated using a precise reference track defined by four reference detectors (see Figure 9.1). The two SGR detectors are identical in construction to those studied in Chapter 7. One SGR detector is segmented on the top side and the other on the bottom side of the SGR foil.
Both detectors were mounted rotatable in the center of a Micromegas hodoscope. The hodoscope consists of three $9 \times 9\,\mathrm{cm}^2$ 2D resistive strip Micromegas detectors, as explained in

[1] Due to the design of the readout structure no common working point is found for the top and bottom Micromegas strips (see Chapter 6.7.1)

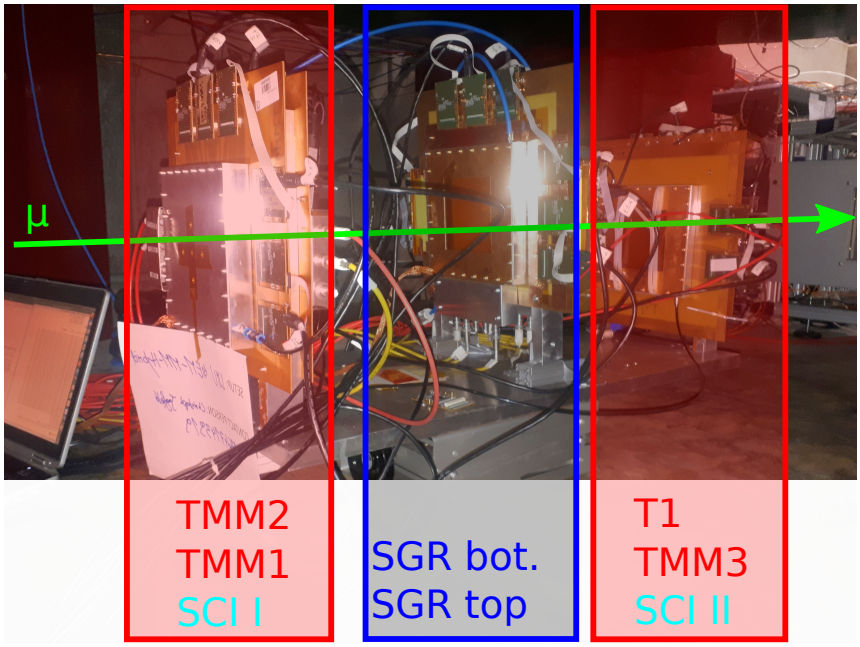

Figure 9.1: Measurement setup at the SPS H4 beam line.
Four reference detectors determining a precise reference track were used to investigate two SGR detectors.
The two SGR detectors (SGR bot. and SGR top) are mounted rotatably in the middle between the reference detectors (TMM1-3 and T1). The scintillators (SCI I and SCI II) which are not visible in the photo are used to provide a trigger signal.
The setup was located inside the Goliath magnet, which was switched off the whole time [Gol, 2023].

Chapter 3.1 and one $10 \times 10\,\mathrm{cm}^2$ 1D resistive strip Micromegas detector[2]. The reference detectors were mounted in pairs of two. The distance between both pairs of reference detectors was approximately 80 cm. All detectors were mounted in the same rack (see Figure 9.1)
The detector hodoscope was placed in the Goliath magnet [Gol, 2023] which was switched off during the measurements.
All Micromegas and SGR detectors were read out with APV25 readout chips in a SRS (see Chapter 3.2). 36 APV25 hybrid boards in a master-slave configuration and three FEC and ADC cards were used. Each FEC card was connected via Ethernet to the DAQ PC. To synchronize the FEC cards a SRU was used which is also connected via Ethernet to the DAQ PC.
The trigger signal was provided by two scintillators read out with photomultiplier tubes[3]. On each pair of reference detectors, a scintillator was mounted at the position of the active area. The signal of each photomultiplier was converted into a NIM signal using a leading edge discriminator[4]. A coincidence of both signals was required[5]. The further trigger logic was the same as for the measurement with ^{55}Fe (see Chapter 6.1).
A sketch of the used SRS and the trigger logic is shown in Figure 9.2.
The APV25 hybrid boards were mounted directly onto the connectors on the SGR foil. No adapter boards were needed in between since the trigger was provided externally.
Due to the design of the rotatable rack for the SGR detectors, the SGR detectors had to be

[2]This detector has 256 readout strips with a pitch of 400 μm. The resistive strips are parallel to the readout strips.
[3]Hamamatsu R4124 [Hamamatsu, 1988]
[4]CAEN Model N840 [CAEN, 2005]
[5]CAEN Model N405 [CAEN, 1993]

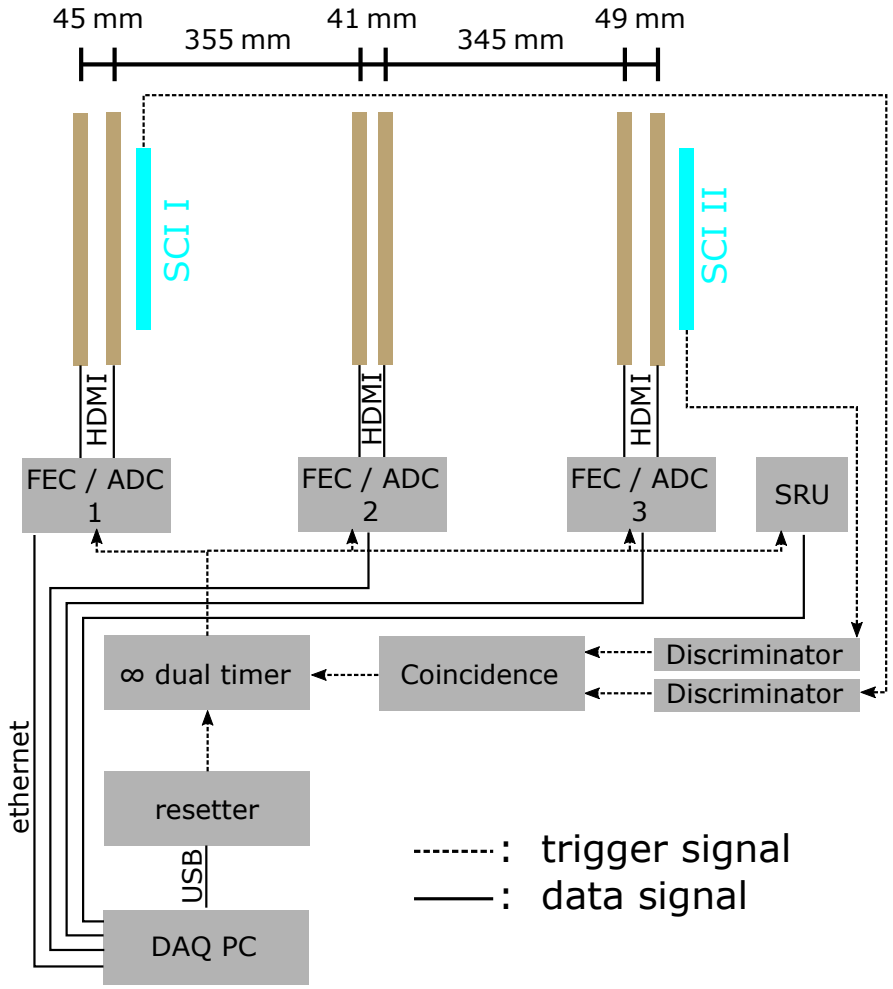

Figure 9.2: Schematic picture of the trigger and DAQ setup.
For triggering, the coincident signal of two scintillators separated by about 80 cm and read out by photo multipliers was used. The signal was guided via LEMO cables to the NIM modules. To ensure that no new trigger was accepted before the present signal was processed, a dual timer made the NIM pulse of the trigger signal infinitely long. After all the data were processed the dual timer was reset. New triggers could be accepted.
The APV25 front-end boards were connected via HDMI cables to three different ADC cards, which were directly connected to the FEC cards. Each FEC card was read out by the DAQ PC via an Ethernet cable (see Chapter 3.2). The FEC cards and the SRU received the trigger from the dual timer. The SRU was used to synchronize the FEC cards using a common trigger counter.

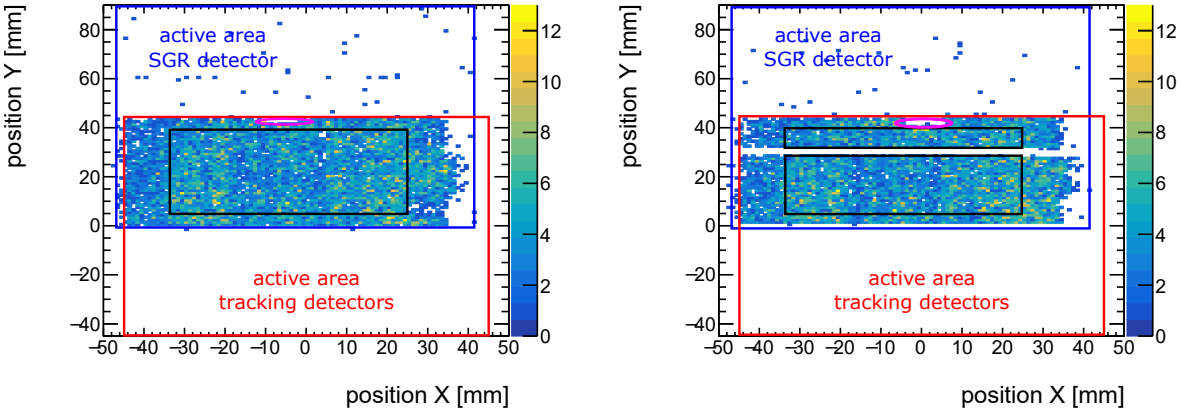

(a) Segmentation on the bottom side of the GEM foil.
U_{drift} = 420 V, U_{GEM} = 200 V, U_{ampl} = 440 V.

(b) Segmentation on the top side of the GEM foil. The inefficiency at Y ≈ 30 mm is caused by broken APV25 channels.
U_{drift} = 420 V, U_{GEM} = 200 V, U_{ampl} = 450 V.

Figure 9.3: Hit distribution in the SGR detector using 120 GeV muons.
The active area of the tracking detectors (red) and of the SGR detectors (blue) are marked.
The setup was read out when both scintillators were hit. These were located at the position of the tracking detectors.
The area marked in black is used in the following for the analysis.
The inefficiency at the pink ellipse is due to a stamp in the drift region, pressing the SGR foil to the pillars.
The beam profile is much larger than the active area of the detectors. The oddly shaped edge of the beam profile can be seen to the right of the hit distribution.

mounted higher in the Y-position than the tracking detectors. Only half of the active area of the SGR detectors overlapped with the active area of the tracking detectors (see Figure 9.3). Due to the position of the trigger scintillators, which were in the position of the active area of the reference detectors, only events hitting the lower half of the SGR detectors were recorded. The size of the muon beam profile was larger than the active area of the detectors.
The muons were delivered in bunches with a length of approximately 5 s. Two bunches arrived within an interval of 30 - 60 s. Within a bunch, approximately 10000 muons traversed the active area. Approximately one thousand particles per bunch were read using the SRS as described above. The processing time of the data on the PC limits the measurement rate to about 500 Hz.
For each detector configuration, about 50000 events were recorded.
In the following of this chapter figures on the left side refer to the SGR detector with the segmentation on the bottom side of the SGR foil and figures on the right side refer to the SGR detector with the segmentation on the top side of the SGR foil.

9.2 Track Reconstruction

Unlike 5.9 keV photons, as used in the previous chapters, 120 GeV muons are not stopped when interacting within the detector volume. Their energy loss is given by the rising part in Figure 1.1. While passing through all detectors of the hodoscope and leaving a signal in them they are hardly deflected. The position in the reference detectors is always reconstructed for the perpendicular muon beam using the centroid method (see Chapter 3.6.1). It is used to determine a reference track. The track is reconstructed using the χ^2 minimization method (see Chapter 3.7). Four reference detectors are used. An exemplary event for a track reconstruction along the Y coordinate is shown in Figure 9.4. Whereas along the precision

coordinate of the SGR foil (Y-coordinate), all reference detectors are resolving, only three detectors are resolving along the other coordinate (X-coordinate)[6].
To obtain an accurate reference track, all detectors must be aligned with each other. The alignment procedure is described in Chapter 3.8.
The track resolution is determined with Equation 3.12. For the X-coordinate, which is determined using three reference detectors, it is approximately 60 µm. Meanwhile, for the Y-coordinate, which is determined using four reference detectors, it is approximately 25 µm at the position of the SGR detectors (see Figure 9.5). The resolutions of the reference detectors determined with the geometric mean method (see Equation 3.14) are listed in Table 9.1. To determine the resolution of the reference detectors along the X-coordinate, one of the SGR detectors is included in the track fitting. The interpolation error of the track would otherwise have been too large due to the large lever arm. Regardless of the asymmetry of the setup for the determination of the X-reference track[7], the geometric mean method determines approximately the same resolution (res ≈ 100 µm) for all X-reference detectors.
In Table 9.1 it is obvious that the resolution of the Y layers of the reference detectors is significantly better than that of the X-layers. As described in Chapter 6.3.1, resistive strip detectors observe signals on up to 22 strips which are only induced by the electron spread on the resistive strips. This decreases the resolution of the X-readout strip layer. Using optimized reconstruction methods, which give less weight to signals influenced by electron spread (e.g. Equation 3.9), improves the resolution of the X-reference detectors (see Table 9.3). Since this method is a subject of investigation in this thesis (see Chapter 9.4.3), it

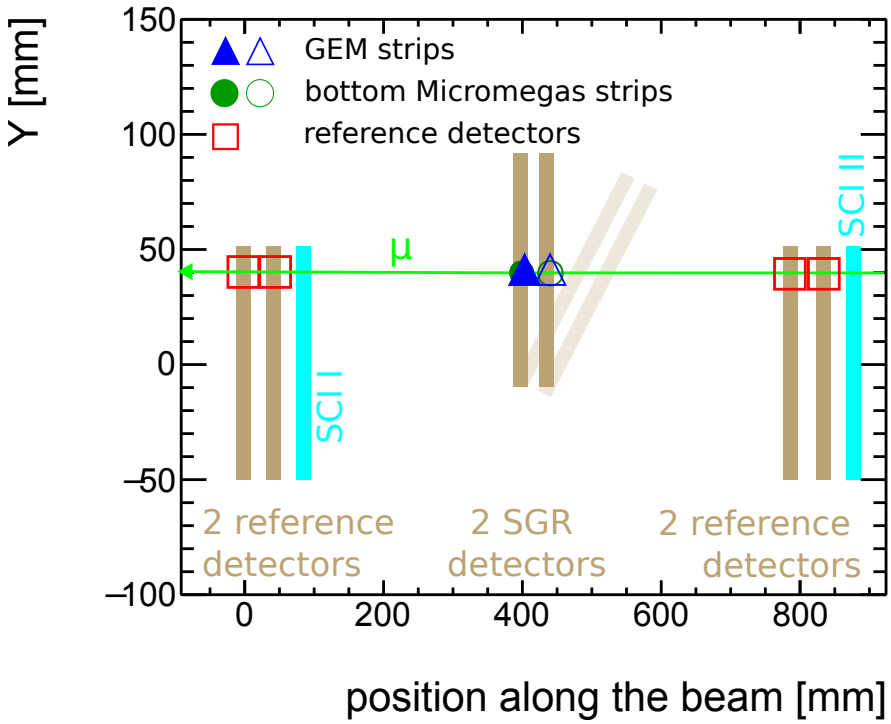

Figure 9.4: Reference track reconstruction using four resistive strip Micromegas detectors as reference.
A linear function is fit to the measured positions in the reference detectors (red non-filled squares). To investigate the detectors under investigation (2 SGR detectors, in the middle, that also can be tilted), the track is interpolated to its position.
The positions of the active areas of all detectors along the Y-coordinates are roughly indicated.

[6] The detector at 780 mm in Figure 9.4 is a 1D detector.
[7] Two reference detectors are located with a distance of 45 mm to each other at z ≈ 0 and the other one is located at z ≈ 800 mm.

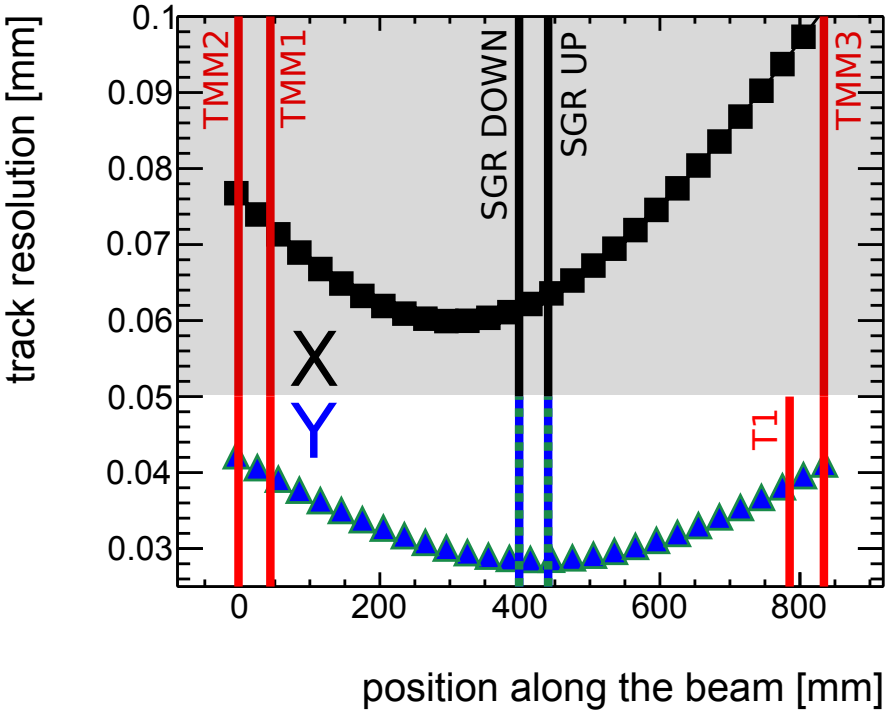

Figure 9.5: Resolution of the reference tracks determined using Equation 3.12 [Horvat, 2005].
black squares: X-coordinate (top Micromegas strips)
blue triangles: Y-coordinate (bottom Micromegas strips / GEM strips)
The positions of the detectors are marked. A track resolution of 25 µm in the Y-direction and 60 µm in the X-direction is reached. The detectors under investigation are placed at the position of the best track resolution along the Y-coordinate (resolution coordinate of the GEM-strips).

is not used for reference position reconstruction. For the analysis of the SGR detectors, only events are used where a signal was detected on both readout strip layers in each reference detector. Only reference tracks whose interpolated position intersects the active area of the SGR detectors are used. More precisely, to avoid effects at the border of the active area of the SGR detectors or the reference detectors, the allowed fiducial area for reconstructed tracks is chosen slightly smaller than the overlap of the active areas (see the black box in Figure 9.3). If a detector reconstructs more than one hit position, the whole event is discarded, because the exact assignment of the reconstructed X-position to the reconstructed Y-position is not clear. The timing information and the pulse heights of the signals could be used to distinguish between several particles and ensure a unique reconstruction, but for safety reasons, this was not used in this work.
In total, a usable track was reconstructed in approx. 14 % of all events. The event selection is considered in more detail in Appendix D.4.

	Y			X		
	included	excluded	geometric mean	included	excluded	geometric mean
TMM1	40.1 ± 0.2	85 ± 1	58 ± 1	73.8 ± 0.9	141 ± 2	102 ± 2
TMM2	37.3 ± 0.2	91 ± 4	58 ± 4	70.7 ± 0.9	145 ± 2	101 ± 2
TMM3	37.2 ± 0.2	88 ± 1	57 ± 1	42.5 ± 0.5	244.8 ± 3	102 ± 5
T1	39.9 ± 0.2	80 ± 1	56 ± 1	-	-	-

Table 9.1: Resolution of the reference detectors determined with the geometric mean method (see Equation 3.14).
All values are shown in µm

9.3 Pulse Height Analysis of Both Readout Strip Layers

As expected and also observed by irradiating the detector with 5.9 keV photons (see Chapter 7.5.2) the pulse height increases exponentially with increasing U_{ampl} (see Figure 9.6).
As with the measurements with ^{55}Fe, the detector with the segmentation on the top of the SGR foil requires U_{ampl} being higher by 20-30 V to achieve the same pulse height as with the detector with the segmentation on the bottom side.
Since the V-legs of the signal which are created due to the electron spread (see Chapter 6.3) are not truncated for the analysis of the 120 GeV muon data, the pulse height of the top Micromegas readout strips is always slightly higher than that of the GEM strips[8]. The pulse heights of the GEM and top Micromegas strips are similar in the setup with the segmentation on the bottom side. In the setup with the segmentation on the top side, a strong dependence of the pulse height on the GEM strips by U_{GEM} is observed. This is in agreement with the measurements using 5.9 keV photons (see Figure 7.10).
For measurements at U_{GEM} = 300 V, the same pulse heights cannot be achieved as for measurements with lower U_{GEM}. The Raether limit is already exceeded at the U_{ampl} required (U_{ampl} > 320 V), discharges occur.

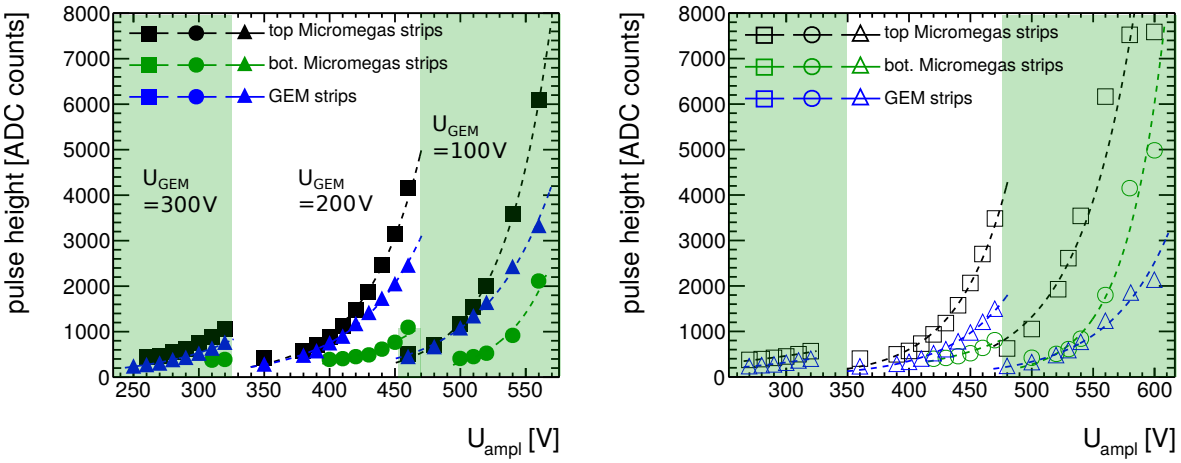

(a) Segmentation on the bottom side of the SGR foil.

(b) Segmentation on the top side of the SGR foil.

Figure 9.6: Mean pulse height for different U_{GEM} (columns) and U_{ampl} (X-axis).
On all readout strip layers, the pulse height increases exponentially with increasing U_{ampl}. For the detector with the segmentation on the top side the pulse height of the GEM strips is strongly dependent on U_{GEM}. For the inverse setup, the pulse height of the GEM strips is approximately the same as for the top Micromegas strips.
For U_{GEM} = 300 V, the Raether limit is reached at U_{ampl} > 320 V, so the maximum pulse height reached is lower than for the other values of U_{GEM}.
Only values are shown with less than 30% of the strips being saturated.
U_{drift} = 420 V.

[8] In Chapter 7.5.2 the V-legs of the spatial signal expansion are truncated for a better comparison of the different readout strip layers. This is not applied in this chapter, since the focus is on the determination of the resolution of the SGR detectors. The influence of the V-legs on the resolution is also part of the investigation (see Chapter 9.4.3).

9.4 Spatial Resolution Determination

Using the reference track the spatial resolution of the two SGR detectors is determined as described in Chapter 3.9.1.
The centroid method (see Chapter 3.6.1) was always used to determine the position of the reference detectors. For the perpendicularly incident muons, this method was also used to determine the position in the SGR detectors.

9.4.1 Spatial Resolution for Perpendicular Tracks

The reconstructed position is homogeneously distributed on the bottom half of the SGR detectors (see Figure 9.3). A spatial resolution better than 80 µm is achieved with the top Micromegas readout strips and with the GEM strips (see Figure 9.7).
Due to limitations of the dynamic range (see Chapter 6.7.1) the bottom Micromegas readout strip layer is not operated at the working point. At the tested voltages the spatial resolution reaches values up to 100 µm. The resolution of both SGR setups is in the same range.
As found in the study with the ^{55}Fe source (see Chapter 7.6), a 20 V higher U_{ampl} is needed for the SGR detector with the segmentation on the top side.
The resolution is better for the GEM strips than for the top Micromegas readout strips at almost all voltage combinations. Even at the same pulse height the resolution of the GEM strips is better than that of the top Micromegas readout strips (see Figure 9.8). The electron spread on the resistive layer may influence the spatial resolution of the Micromegas readout strips. If it is not resolved symmetrically around the centroid of the directly induced avalanche signal it shifts the reconstructed centroid and thereby influences the spatial resolution. Since the V-shape of the signal due to electron spread is not influencing the GEM strip readout the resolution of the GEM strips is better. This holds for both SGR setups.
As it will be shown in Chapter 9.4.3, the influence of the electron spread on the position resolution can be reduced.
To compare the influence of U_{GEM} on the detector resolution, the resolution is considered as a function of pulse height. Comparison of the resolution at the same pulse height for different U_{GEM} shows that the resolution improves with higher U_{GEM} on all readout strip layers (see Figure 9.9). As for the energy resolution (see Chapter 7.5) the funnel of the electric field pulling the electrons into the GEM holes increases with increasing U_{GEM}. More primary electrons reach the amplification region. The spatial resolution improves.
Unfortunately one can not operate the SGR foil at arbitrary high voltages. With increasing U_{GEM} the discharge probability inside the GEM foil increases. Therefore, because of the high gain inside the foil at $U_{GEM} = 300,\mathrm{V}$, the Micromegas amplification voltage U_{ampl} cannot be set high enough without exceeding the rather limit (see Chapter 1.1.2) to achieve better resolution than at $U_{GEM} = 200,\mathrm{V}$.

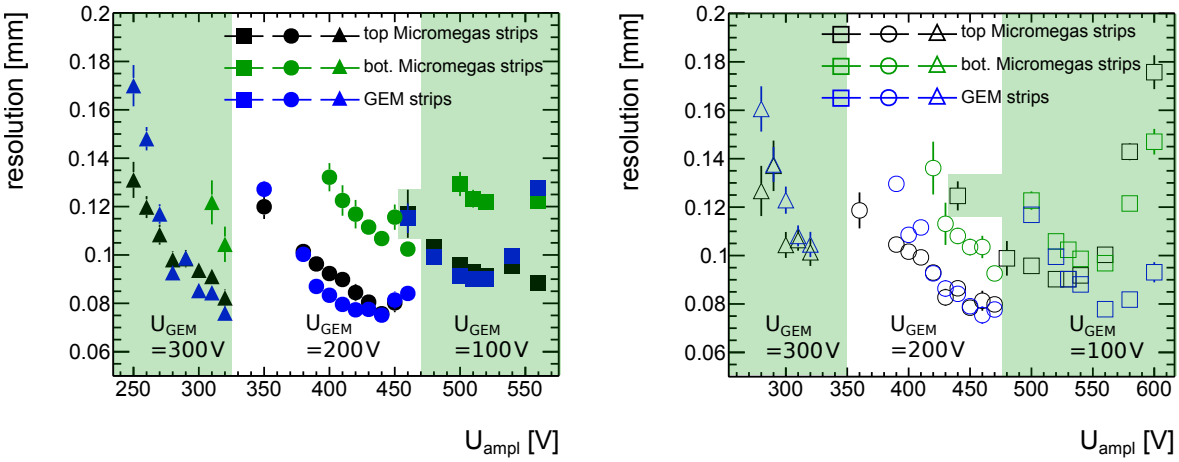

(a) Segmentation on the bottom side of the SGR foil.

(b) Segmentation on the top side of the SGR foil.

Figure 9.7: Spatial resolution for different U_{GEM} (columns) and U_{ampl} (X-axis) for perpendicularly incident muons.
The resolution is determined as described in Chapter 3.9.1. A resolution better than 80 µm is reached for both detectors. As for the pulse height (see Chapter 7.6) U_{ampl} needs to be increased by 20-30 V for the SGR detector with the segmentation on the top side to reach same values as for the detector with strips on the bottom side.
Only values are shown with less than 10% of all hit readout strips being saturated.
U_{drift} = 420 V.

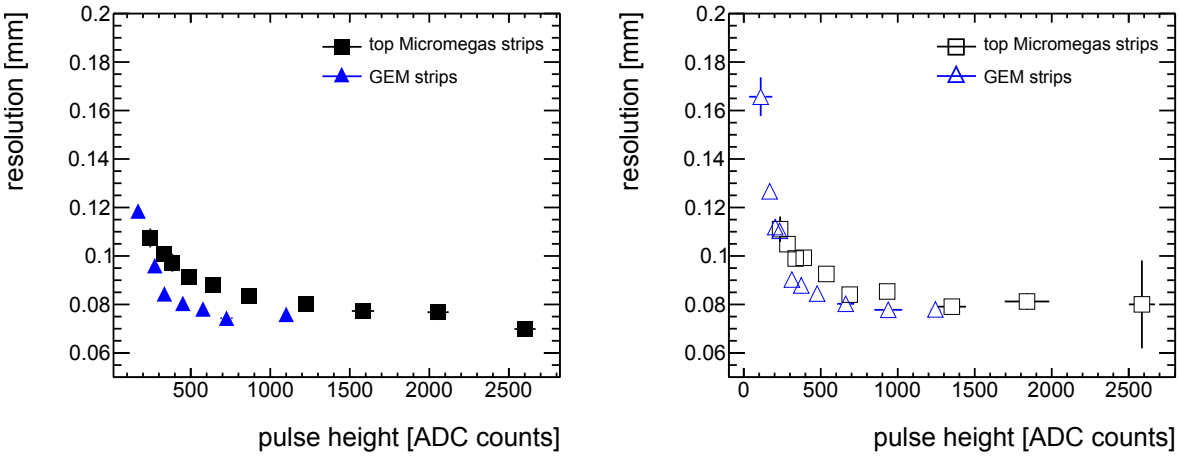

(a) Segmentation on the bottom side of the SGR foil.

(b) Segmentation on the top side of the SGR foil.

Figure 9.8: Spatial resolution of the GEM strips in dependence of the mean cluster pulse height. For all pulse heights, the resolution is better for the GEM strips than for the Micromegas strips until they saturate. Due to the approximately two times larger strip width the GEM strips saturated earlier than the Micromegas strips.
Only values with less than 10 % of all readout strips being saturated are shown.
U_{GEM} = 200 V, U_{drift} = 420 V.

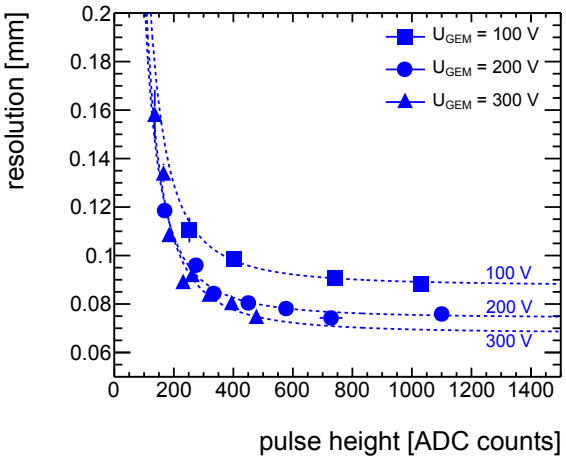

(a) GEM strips, segmentation on the bottom side of the SGR foil.

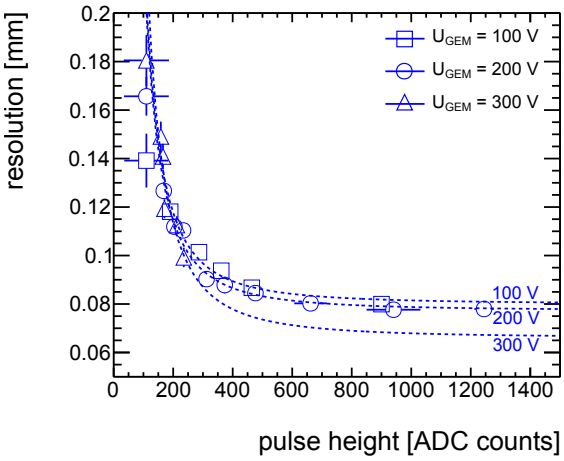

(b) GEM strips, segmentation on the top side of the SGR foil.

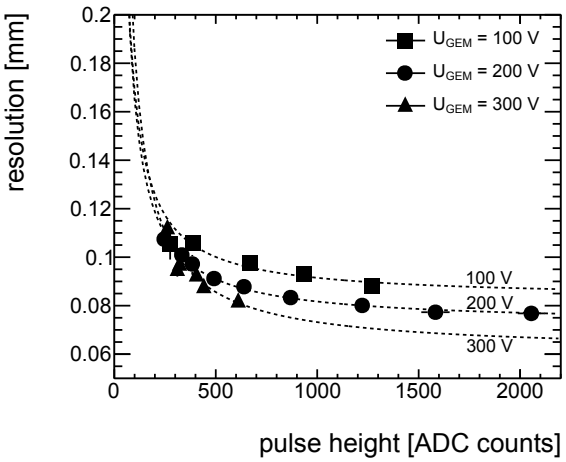

(c) Top Micromegas strips, segmentation on the bottom side of the SGR foil.

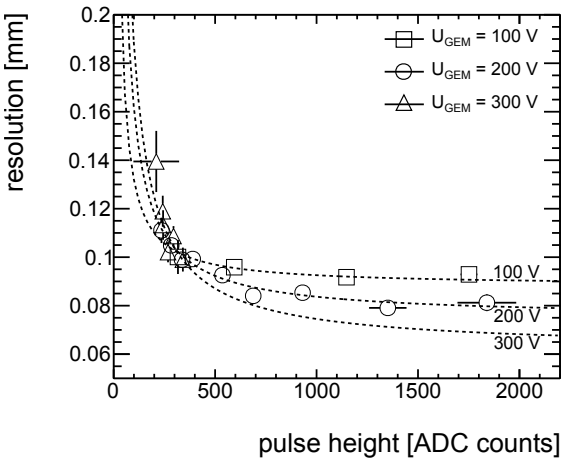

(d) Top Micromegas strips, segmentation on the top side of the SGR foil.

Figure 9.9: Spatial resolution in dependence of the mean cluster pulse height for different U_{GEM} (markers).
For visual reasons, the distributions are fitted with a hyperbolic function.
At both detectors and readout strip layers a better resolution is reached at the same pulse height for a higher U_{GEM}. When U_{GEM} increases more primary electrons are guided into the amplification regions. The position reconstruction gets more precise.
U_{drift} = 420 V.

9.4.2 Spatial Resolution for Inclined Tracks

The two SGR detectors are rotatably mounted in the setup. In addition to perpendicularly incident muons, the detectors were also investigated with muons passing through the detector at an angle of incidence of $\Theta = 20 \pm 1°$ and $\Theta = 26.5 \pm 1°$. The position of the inclined tracks is determined with the µTPC method (see Chapter 3.6.2) and with the centroid method (see Chapter 3.6.1). The SGR detectors were rotated around the X-axis only, such that the rotation is resolved by the GEM strips and bottom Micromegas readout strips. Since the bottom Micromegas strips are not operated at the working point, the main focus is on the GEM strips in this section.
The reference detectors remained perpendicular to the muon beam.

With the GEM strips on the bottom side a spatial resolution of approximately 200 µm at $\Theta = 20°$ and 250 µm at $\Theta = 26.5°$ is reached using the µTPC method (see Figure 9.10a). These spatial resolutions are significantly better than the corresponding centroid resolutions, which are 300 µm at $\Theta = 20°$ and 400 µm at $\Theta = 26.5°$.
Also for the detector with the segmentation on the top side, the µTPC resolution is better than the resolution determined with the centroid method (see Figure 9.10b). Especially for the setup with the GEM strips on the top side of the foil, the spatial resolution improves with increasing U_{GEM} (see Figure 9.9).
For all tested voltages, the resolutions determined with both methods are better for the detector with the segmentation on the bottom side. It can be excluded that this is due to different pulse heights on both detectors. This behavior is still visible when the resolution is plotted against the pulse height (see Figure D.1). Likely, the reduced electron transparency of the SGR foil with segmentation on the top side (see Chapter 7.6) influences the spatial resolution, as it does for all other measured values. The fewer primary electrons are amplified and detected, the worse the spatial resolution.

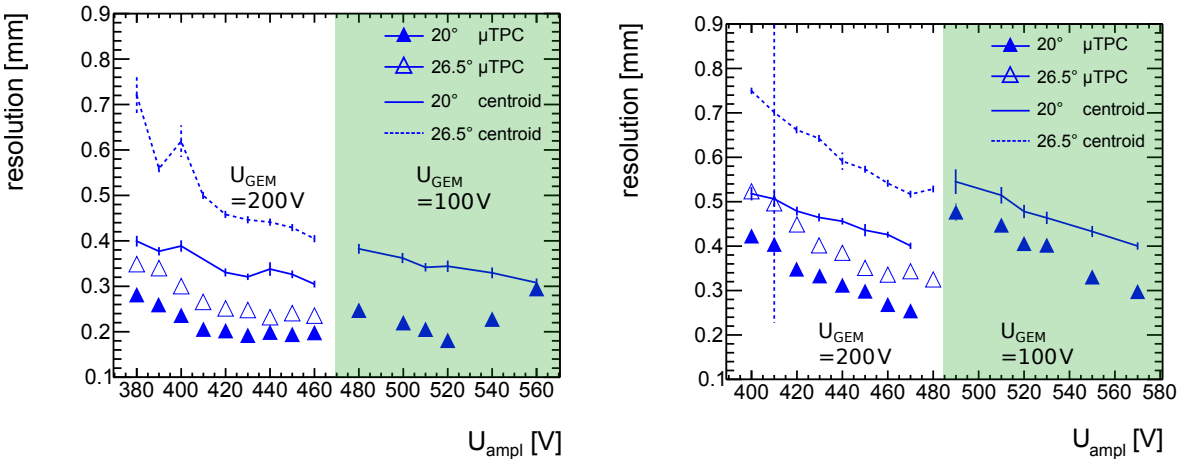

(a) GEM strips, segmentation on the bottom side of the SGR foil.

(b) GEM strips, segmentation on the top side of the SGR foil.

Figure 9.10: Spatial resolution for different U_{GEM} (columns), different U_{ampl} (X-axis) and different incident angles.
The spatial resolution using the µTPC method (triangles) is better than the centroid position (lines) for inclined tracks.
Since the fraction of ions traversing the holes to the readout strips on the top side is depending on U_{GEM}, the resolution of the top GEM strips improves with increasing U_{GEM}.
$U_{drift} = 420\,V$.

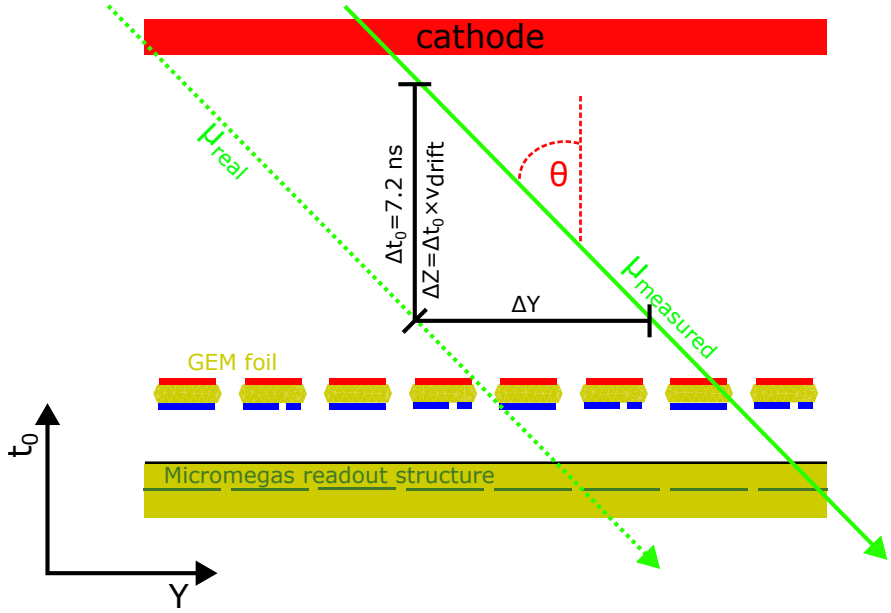

Figure 9.11: Schematic of the spread Δy due to non synchronized triggers.
Due to non-synchronized triggers the absolute timing information of each strip has a spread of up to $\Delta t_0 = 7.2\,\text{ns}$. Δt_0 is the same for all readout strips in an event. The reconstructed track is shifted by Δz and thus the reconstructed Y-position is shifted by Δy.
The sketch is not to scale.

The APV25 is sampling in 25 ns steps (see Chapter 3.2). At non-synchronized triggers, the absolute timing information of each strip has a spread of up to $\Delta t_0 = 25/\sqrt{12}\,ns = 7.2\,ns$. Since this time shift is the same for all readout strips in an event this leads to a shift of the track along the Z-axis by maximum $\Delta Z = \Delta t_0 * v_{\text{drift}}$. Thereby the resolved position is shifted at $\Theta = 20°$ by $\Delta Y = \Delta Z * \tan(\Theta) \approx 126\mu m$.
This timing offset can be measured using an external TDC. Thereby the μTPC resolution improves. This was not applied to the shown data. Therefore it can be assumed that better spatial resolutions can be achieved with the μTPC method than shown in Figure 9.10.

With res_{measured} being the μTPC resolution shown in Figure 9.10 the achievable resolution calculates as:

$$res = \sqrt{res^2_{measured} - \Delta y^2} \tag{9.1}$$

The best reached μTPC resolution for both detector types and both investigated angles is presented in Table 9.2.

	res_{measured} (20°)	res (20°)	res_{measured} (26.5°)	res (26.5°)
GEM strips bottom	200 ± 10 μm	155 ± 25 μm	250 ± 10 μm	220 ± 20 μm
GEM strips top	240 ± 10 μm	200 ± 25 μm	320 ± 10 μm	290 ± 20 μm

Table 9.2: Spatial resolution using the μTPC method (best values achieved).
res_{measured} is the best resolution reached in Figure 9.10 for each readout strip layer and each angle. res is calculated using Equation 9.1.
The error of res is calculated using gaussian error propagation wit the assumption: $\Delta(\Delta y) = 0$

9.4.3 Improvement of the Spatial Resolution for the Resistive Layer Detector for Perpendicular Tracks

As it is shown in Figure 9.7 and Figure 9.8 the spatial resolution for the GEM strips is better than for the top Micromegas readout strips, even though the pitch of the GEM strips is almost two times higher as for the Micromegas readout strips.
The electron spread on the DLC layer (see Chapter 6.3.1) influences the spatial resolution of the Micromegas strips[9]. Attempts are done to disentangle the electron spread signal from the prompt avalanche signal for the position reconstruction. A cut, as explained in Chapter 6.4, cannot be applied easily, because especially near the strips on which the prompt avalanche signal is detected, both signals are not well distinguishable. If the electron spread signal is not cut off equally well on both sides of the centroid the spatial resolution degrades.
The different reconstruction methods described in Chapter 3.6.1 are tested.
The first technique only uses the V-shape of the signal. The prompt avalanche signal is cut off. Only the V-legs of the signal are used. The timing information instead of the strip pulse height is used for this method. A linear fit is applied on each V-leg of the signal (see Figure 3.12). The intersection of both functions is used as a hit position. The spatial resolution of this method is worse than the standard centroid resolution (see Figure 9.12). This method is affected by the low pulse heights of the electron spread signal, as the timing accuracy degrades at low pulse heights. This method is only applicable when the electron spread is resolved on multiple strips. It might be well suited for resistive strip detectors, where the electron spread is stronger resolved and on approximately 20 strips (see Figure 6.7).
The second reconstruction method is an improvement of the centroid method. Instead of applying a fixed cut to the timing information to eliminate the V-legs, this method minimizes the influence of electron spread by weighting each strip with the inverse squared strip time t^{-2} in addition to the charge weight (see Equation 3.9). Thereby later signals like the electron spread signal are weighted less than the prompt avalanche signal. Using this method the spatial resolution improves by up to 20 µm (see Figure 9.12). A spatial resolution of 60 µm is reached on the top Micromegas readout strip layer using this method. This way, a better resolution is achieved with the Micromegas strips than with the GEM readout strips.

The resolution of the reference detectors improves if the position in the reference detectors is determined with Equation 3.14 (compare Table 9.3 and Table 9.1). Since this method is investigated in the presented measurements, it is not further used to determine the position of the hits in the reference detectors.

	included	excluded	geometric mean
TMM1X	68.6 ± 0.7 µm	97 ± 1 µm	82 ± 1 µm
TMM2X	69.1 ± 0.8 µm	109 ± 5 µm	86.84 ± 2 µm
TMM3X	31.7 ± 0.4 µm	177 ± 2 µm	74.8 ± 1 µm

Table 9.3: Resolution of the reference detectors (in µm) for the readout layer which is influenced by the electron spread on the anode, when Equation 3.9 is used to determine the hit position in each detector.
The spatial resolution is determined using the geometric mean method (see Equation 3.14).

[9]The GEM strips are hardly resolving the electron spread.

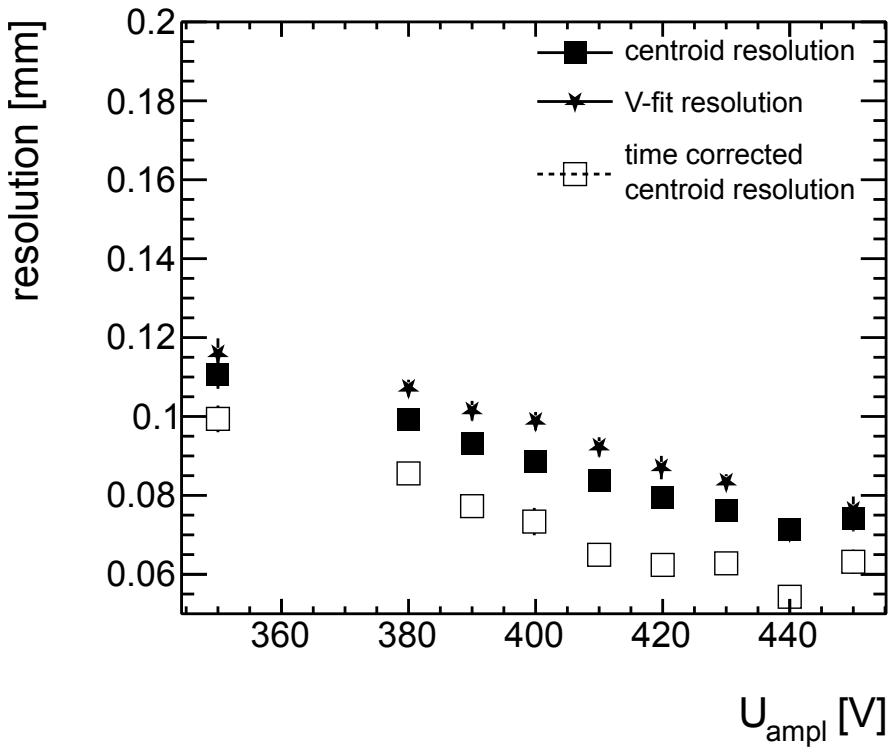

Figure 9.12: Spatial resolution for perpendicularly traversing particles in dependence of U_{ampl} for different position reconstruction methods (see Figure 3.12).
The resolution of the top Micromegas strips for the SGR detector with the segmentation on the bottom side is shown.
centroid resolution: Position determined with Equation 3.8.
V-fit resolution: Position determined with V-shape time fit as shown in Figure 3.12.
time corrected centroid resolution: Position determined by the t^{-2} weight in addition to the centroid method. (see Equation 3.9).
Using the time correction, the influence of the electron spread on the DLC layer anode decreases. The position is mostly influenced by the prompt avalanche signal.
U_{GEM} = 200 V, U_{drift} = 420 V.

9.5 Efficiency Determination

The efficiency is determined using Equation 3.29. An event is considered efficient if the residual is smaller than 1 mm ($|\Delta x| < 1\,mm$). The efficiency is shown in Figure 9.13. For both detector setups, a spatial efficiency better than 90 % is reached with the GEM and top Micromegas strips. As with the spatial resolution (see Chapter 9.4.1), U_{ampl} must be increased by 20 V for the SGR detector with the segmentation on the top side to achieve the same efficiencies as for the inverse detector setup.
The efficiency for the top Micromegas strips is 4 % higher than for the GEM strips for both detector setups. Since this effect is observed with both setups, it cannot be attributed to the reduced electron transparency with the SGR detector with the segmentation on the top side (see Chapter 7.6). The difference can only result from events that were not detected at all, and not from poorly reconstructed events that show a large residual $|\Delta x|$. This would have been noticed when determining the spatial resolution. The resolution of the GEM strips is of the same order of magnitude as that of the top Micromegas strips. With 80 µm, it is significantly better than the 1 mm limit for efficiency determination.
The gap between GEM strips may have an impact on the detection efficiency. According to Marques et al. [2020], the gain decreases by segmenting the GEM foil. However, Marques et al. [2020] examined segmentations that deviate from the present design. The GEM holes were not completely surrounded by copper in any of their designs[10]. According to ANSYS simulations (see Figure 5.2) the electric field inside and below the GEM holes near the segmentation does not seem to be affected by the segmentation. It is rather improbable that the lower efficiency is due to segmentation only.

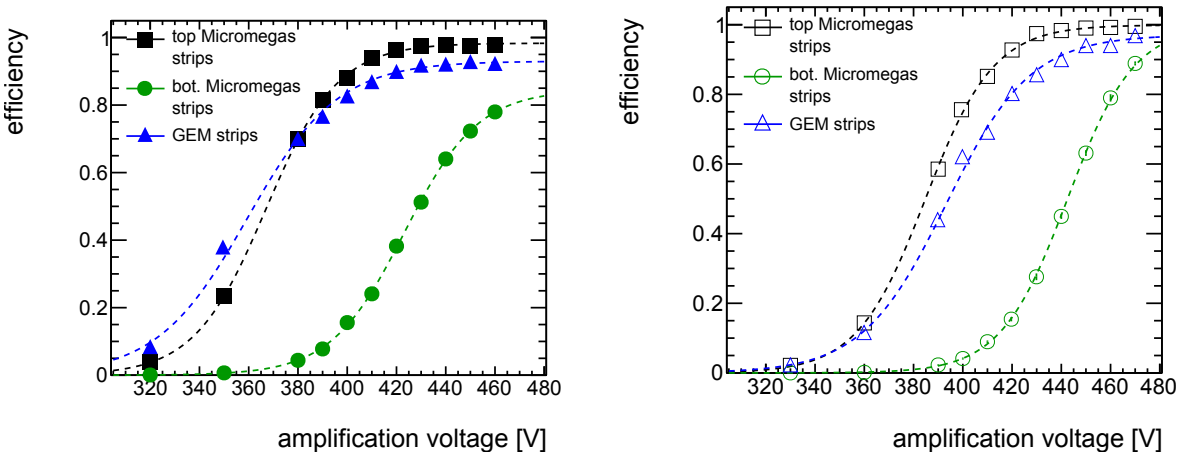

(a) Segmentation on the bottom side of the SGR foil.

(b) Segmentation on the top side of the SGR foil.

Figure 9.13: Efficiency for different U_{ampl}.
An event is considered as efficient if the residual from the reference track is smaller than 1 mm (see Equation 3.29).
The GEM and top Micromegas strips reach values well above 90 %. Since the bottom Micromegas strips were not operated at the working point the efficiency is lower. As for the pulse height (see Chapter 7.6) U_{ampl} needs to be increased by 20-30 V for the SGR detector with the segmentation on the top side to reach same values as for the detector with the segmentation on the bottom.
For visual reasons data are only shown for U_{GEM} = 200 V. The data for all U_{GEM} are shown in Figure D.2.
U_{drift} = 420 V.

[10] At the SGR foils used for this thesis the segmentation is such that all holes are surrounded by copper (see Figure 2.8b)

Since the bottom Micromegas readout strip layer is not operated at the working point, the spatial efficiency is lower but reaches similar values like the other readout strip layers at higher voltages.

9.6 Angular Resolution

Using the μTPC method the incident angle of the traversing particle can be reconstructed using a single readout strip layer (see Chapter 3.6.2). For $\Theta = 20°$ and $\Theta = 26.5°$ the incident angle and the angular resolution is determined as described in Chapter 3.9.2.
Both incident angles are nicely reconstructed using the GEM strips (see Figure 9.14). Also here, the angular resolution is better at $U_{GEM} = 200\,V$ than for $U_{GEM} = 100\,V$ (compare with Chapter 9.4.2). This effect is more pronounced for the detector with the segmentation on the top side. This is in agreement with all previously presented measurements.
The angular resolution is in the order of a few degrees. The best reached angular resolution for $\Theta = 20°$ at $U_{GEM} = 200\,V$ is: $\sigma_< = 2.25°$ and $\sigma_> = 2.45°$. At $\Theta = 26.5°$ the best resolution at $U_{GEM} = 200\,V$ is: $\sigma_< = 2.75°$ and $\sigma_> = 3°$. For the setup with the segmentation on the bottom side, the angular resolution is slightly better than for the setup with the segmentation on the top side. This is in agreement with the reconstructed position using the μTPC method (see Chapter 9.4.2).

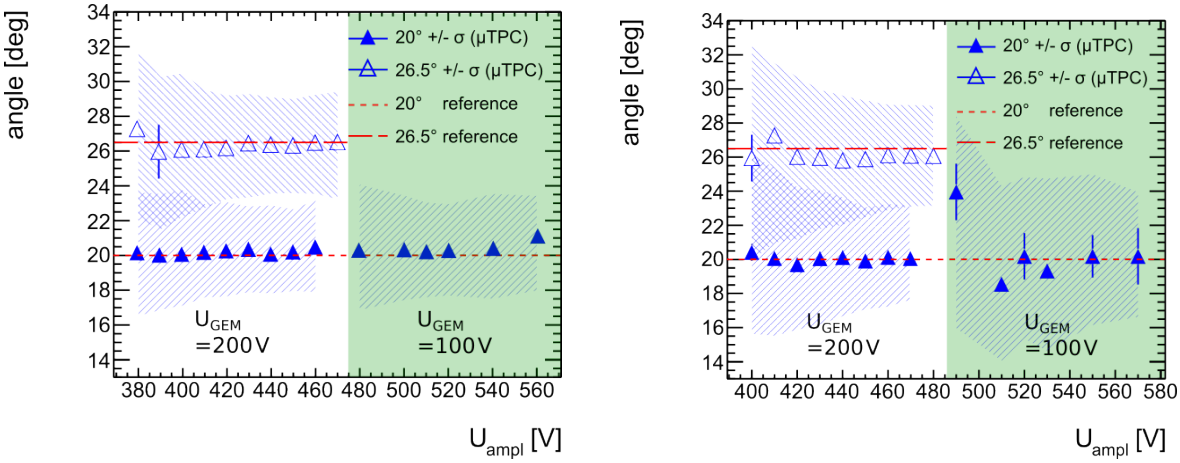

(a) Segmentation on the bottom side of the SGR foil.

(b) Segmentation on the top side of the SGR foil.

Figure 9.14: Reconstructed angle (points) and angular resolution (shaded area) for different U_{GEM} (columns) and U_{ampl} (X-axis).
The reconstructed angle is determined using the μTPC method (see Chapter 3.6.2). The angular resolution is determined as described in Chapter 3.9.2.
With both detector setups, the incident angles are well reconstructed. For both setups the best reached angular resolutions are between $\sigma_\Theta = 2.2°$ and $\sigma_\Theta = 2.9°$ for $\Theta = 20°$ and between $\sigma_\Theta = 2.75°$ and $\sigma_\Theta = 3°$ for $\Theta = 26.5°$.
The angle reconstruction works better for $U_{GEM} = 200\,V$ than for $U_{GEM} = 100\,V$.
Only values with less than 10 % of all readout strips in a cluster being saturated are shown.
$U_{drift} = 420\,V$.

It is also possible to reconstruct the incident angle using the bottom Micromegas readout strips (see Figure D.3). Since this layer is not operated at the working point the angular properties are worse than for the GEM readout strips. Nevertheless, Figure D.3 shows that the μTPC method is applicable to resistive layer detectors. The influence of the electron spread on the signal timing is low.

9.7 Summary of the Spatial and Angular Properties of the SGR detector

As a final check two SGR detectors were investigated at the SPS at CERN using 120 GeV muons.
For both SGR detector setups a position reconstruction efficiency well above 90 % is reached with the GEM strips and top Micromegas readout strips (see Figure 9.13).
With both detector setups, a spatial resolution of 80 μm is achieved for perpendicularly incident muons using the GEM or the upper Micromegas strips (see Figure 9.7). The spatial resolution of the top Micromegas strips is slightly worse due to the influence of the electron spread on the anode. This can be corrected by adjusting the reconstruction algorithms (see Figure 9.12).
Using the strip timing information and the μTPC method a position for inclined tracks is reconstructed with an accuracy of 155 μm for $\Theta = 20°$ and 250 μm for $\Theta = 26.5°$ (see Figure 9.10).
The incident angle is reconstructed with an accuracy of approximately 2-3° (see Figure 9.14).
Furthermore, it is shown that the μTPC method is also applicable to the Micromegas readout strips despite the electron spread on the DLC resistive layer (see Figure D.3).
As in all previous measurements, the spatial and angular resolution improves with increasing U_{GEM}.
In summary, both SGR detectors show excellent spatial and angular properties.
Combining the position information of the GEM and top Micromegas strips, a 2D position is determined very well. Both coordinates are determined equally well.

Outlook:
With an optimized Micromegas readout structure, a detector with three different readout strip layers (X, Y, U) can be built with a SGR foil whose readout strips are turned by 45° as proposed in Chapter 2.3.4. This allows a 2D reconstruction of multiple particle hits, where all particles are detected at the same time, like in a Cerenkov Ring Imaging Detector (see Chapter 2.3.4).

Chapter 10

Summary

In this thesis, a Segmented GEM Readout (SGR) detector was developed and investigated. The SGR detector is a hybrid of a Micromegas and a GEM detector.
Both differ mainly in the structure of the amplification region. In the amplification region the number of electrons gets multiplied by electron avalanches (see chapter 1.1.2).
In a Micromegas detector, the amplification takes place in a high electric field ($\mathcal{O}\left(|\vec{E}_{\mathrm{ampl}}|\right)$ = 50 kV/cm) between a micro micro-mesh and the anode in a distance of about 120 µm from each other (see chapter 2.1.1).
In GEM detectors, the amplification takes place inside the holes of a GEM foil. A GEM foil is a 50 µm thick insulating Kapton foil coated with 5 µm copper on each side. The foil has holes with a radius of r ≈ 25 µm arranged in a triangular pattern with a distance d ≈ 140 µm. A high electric field is applied between both foil surfaces (see Chapter 2.2).
The SGR detector is based on a Micromegas detector, which uses a DLC layer as the anode. A SGR foil is used instead of the micro-mesh (see Chapter 2.3). The SGR foil is a GEM foil, whose copper surface on one or both sides is segmented into strips (see Figure 2.8). These strips act as an additional layer of readout strips. The SGR detector features a position-sensitive readout on the Micromegas readout structure (Micromegas strips) and on the SGR foil (GEM strips).

The SGR detector has three regions of different electric fields.
In a several-millimeter thick region of a low electric field the gas is ionized by incoming radiation and the charges are separated (see Chapter 1.1.3).
In the two regions of the high electric fields, the number of electrons gets multiplied by electron avalanches (see Chapter 1.1.2).
In the pre-amplification step inside the SGR foil the number of electrons is multiplied by a factor up to 30 (see Chapter 5.2.3).
In the main amplification step (Micromegas amplification region), the number of electrons is multiplied to such an extent that a total of about 200.000-300.000 electrons arrive at the anode (see Chapter 5.2.3).
The avalanche process induces a signal on a micro-structured anode or separate readout strip layers below it. Depending on the readout structure, a 2D readout is possible. Usually, two layers of readout strips perpendicular to each other are used for 2D position reconstruction. As shown in this thesis one coordinate, usually the coordinate of the top readout strip layer is reconstructed more accurately than the other. The pulse height of the two readout strip layers can be very different (see Chapter 6), which significantly hinders a 2D particle reconstruction with highest spatial resolution and efficiency. The SGR detector solves that problem.

The signal formation process of a SGR detector was investigated and successfully simulated using the ANSYS and Garfield++ software (see Chapter 5).
As in a typical Micromegas detector the signal consists of a fast peak-shaped electron signal and a longer-lasting signal due to the ion movement in the amplification region (see Chapter 5.3.1). After the electron avalanche is collected on the anode the electrons remain at their position on the DLC layer until the ion drift has finished. After this, the electrons begin to drift radially in all directions on the anode. The Micromegas readout strips are sensitive to the electron spread (see Chapter 5.3.2). It is observed in the spatial expansion of the signal and the signal shape. The signal shape of the Micromegas readout strip layers below the anode becomes bipolar. The electron spread has hardly any influence on the signal shape of the GEM strips.
The signal of the GEM strips differs strongly between the segmentation on the top and the bottom side of the SGR foil. The signal of the readout strips on the bottom side of the SGR foil changes polarity at the moment the ion cloud enters the GEM holes. The signal of the readout strips on the top side of the SGR foil only resolves the drift of the ions through the hole. Therefore, this is solely positive. The charge movement in the Micromegas amplification region is shielded by the bottom surface of the SGR foil.
The number of ions drifting through the GEM holes increases with increasing voltage applied to the GEM foil (U_{GEM}). With increasing U_{GEM} the signal of the bottom GEM strips becomes more bipolar and the signal of the top GEM strips becomes higher.
The simulated signals agree with measurements performed using 5.9 keV photons (see Chapter 5.3.3).

As simulations and measurements have shown, the electron transparency of the SGR foil decreases for the foil with the segmentation on the top side (see Chapter 7.6). Electrons are guided to the gap between the strips. This is compensated by applying higher amplification fields for the detector with the segmentation on the top side. Independent of the position of the segmentation the energy resolution of the SGR detector, which was determined by irradiating the detector with 5.9 keV photons is good. Slightly better values are achieved with the detector with the segmentation on the bottom side of the SGR foil.
It is also possible to construct a well-working SGR detector with segmentation on both sides (see Chapter 8). A common working point for both GEM strip layers and the top Micromegas layer is found.
Replacing the micro-mesh with a SGR foil has no influence on the detector properties of the Micromegas readout strips compared to the standard DLC layer Micromegas detector.

To determine the spatial and angular properties of the SGR detector, measurements were performed using 120 GeV muons provided by the SPS at CERN (see Chapter 9). When the GEM strips are perpendicular to the top Micromegas strips it is possible to reconstruct the 2D-position of perpendicular traversing particles with efficiencies well above 90 % and with a resolution of better than 80 µm in both coordinates (see Chapter 9.4). The X-coordinate is obtained by the top Micromegas strips and the Y-coordinate by the GEM strips. This applies to both SGR detector types.
Reconstruction of inclined traversing particles is well possible with a resolution of approximately 200 µm at $\Theta = 20°$ and 250 µm at $\Theta = 26°$, respectively.
Due to a pulse height difference by a factor of six between the Micromegas readout strip layers, it is not possible to reconstruct a position on both coordinates equally well with a standalone DLC layer Micromegas detector. The SGR detector solves that problem.

For a further improved Micromegas readout structure which is well resolving a 2D-position by itself, it will be possible to build a SGR detector with four different readout coordinates.

X and Y coordinates are resolved by the Micromegas strips.
U and V are resolved by the GEM strips on a SGR foil which is turned by 45° to the Micromegas strips.
This allows a 2D reconstruction also for experiments where multiple particles are traversing the detector simultaneously (see Chapter 2.3.4).

In summary, the SGR detector built is a hybrid of the Micromegas and GEM detector. It reconstructs particles very well in two coordinates. On the one hand, it is read out like a usual Micromegas detector at the anode and on the other hand, the position is also determined by readout strips on a GEM foil which replaces the micro-mesh.

List of Abbreviations

ADC Analog to Digital Converter

ANSYS ANalysis SYStem

ASIC Application Specific Integrated Circuit

ATLAS A Toroidal LHC ApparatuS

CFD Constant Fraction Discriminator

CMS Compact Muon Solenoid

DAQ Data AcQuisition

DLC Diamond Like Carbon

FEC Front End Concentrator

GEM Gas Electron Multiplier

Micromegas MICRO MEsh GAseous Structure

MPGD Micro Pattern Gasseous Detectors

NIM Nuclear Instrumentation Standard

PCB Printed Circuit Board

SGR Segmented Gem Readout

SPS Super Proton Synchrotron

SRS Scalable Readout System

SRU Scalable Readout Unit

TPC Time Projection Chamber

Bibliography

[ANS(2022)] ANSYS MAPDL 2022 R2. 2022. URL https://www.ansys.com/.

[Gol(2023)] Goliath. 2023. URL https://sy-dep-epc-hpc.web.cern.ch/spectrometers/Goliath/general.stm.

[Kap(2023)] Kapton® polyimide films. 2023. URL https://www.dupont.com/electronic-materials/kapton-polyimide-film.html.

[Alexopoulos et al.(2011)] Alexopoulos, T., Burnens, J., de Oliveira, R., et al. A spark-resistant bulk-micromegas chamber for high-rate applications. *Nuclear Instruments and Methods in Physics Research Section A: Accelerators, Spectrometers, Detectors and Associated Equipment*, 640(1):110–118, 2011. ISSN 01689002. doi:10.1016/j.nima.2011.03.025. URL https://linkinghub.elsevier.com/retrieve/pii/S0168900211005869.

[Alsamak et al.(2022)] Alsamak, Ibrahim, Baraka, Kim, Caiazza, Stefano, et al. Garfield++. 2022. URL https://garfieldpp.web.cern.ch/garfieldpp/.

[Baek et al.(2012)] Baek, C.-H, Lee, S.-J, Cho, I.-H, et al. Development of the scalable readout system for micro-pattern gas detectors and other applications. *Journal of Instrumentation*, 2012:17–21, 2012. doi:10.1088/1748-0221/8/03/C03015.

[Biagi(2021)] Biagi, Stephen. MAGBOLTZ - Transport of electrons in gas mixtures. 2021. URL https://magboltz.web.cern.ch/magboltz/.

[Bortfeldt et al.(2017)] Bortfeldt, J., Biebel, O., Flierl, B., et al. Low material budget floating strip Micromegas for ion transmission radiography. *Nuclear Instruments and Methods in Physics Research Section A: Accelerators, Spectrometers, Detectors and Associated Equipment*, 845:210–214, 2017. ISSN 0168-9002. doi:10.1016/J.NIMA.2016.05.003.

[Bortfeldt(2014)] Bortfeldt, Jonathan. *Development of Floating Strip Micromegas Detectors*. Ph.D. thesis, Ludwig-Maximilians Universität München, München, 2014. doi:10.5282/edoc.16972. URL https://edoc.ub.uni-muenchen.de/16972/.

[CAEN(1991)] CAEN. Technical Information Manual, Mod. N93B, Dual Timer. 1991. URL https://www.caen.it/?downloadfile=3941.

[CAEN(1993)] CAEN. Technical Information Manual, Revision n. 0, Mod. N405. 1993. URL https://www.caen.it/?downloadfile=3932.

[CAEN(2005)] CAEN. Technical Information Manual, Revision n. 5, Mod. N840-N841. 2005. URL https://www.caen.it/?downloadfile=3945.

[CAEN(2013)] CAEN. Technical Information Manual, Revision n.3, Mod. A1821 series. 2013. URL https://www.caen.it/?downloadfile=3925.

[CAEN(2021)] CAEN. Technical Information Manual, Revision n. 7, Mod. N842-N843. 2021. URL https://www.caen.it/download/?filter=N843.

[Carnegie et al.(2005)] Carnegie, R. K., Dixit, M. S., Dubeau, J., et al. Resolution studies of cosmic-ray tracks in a TPC with GEM readout. *Nuclear Instruments and Methods in Physics Research, Section A: Accelerators, Spectrometers, Detectors and Associated Equipment*, 538(1-3):372–383, 2005. ISSN 01689002. doi:10.1016/J.NIMA.2004.08.132.

[Charitonidis and Efthymiopoulos(2017)] Charitonidis, N. and Efthymiopoulos, I. Low energy tertiary beam line design for the CERN neutrino platform project. *Physical Review Accelerators and Beams*, 20(11), 2017. ISSN 24699888. doi:10.1103/PHYSREVACCELBEAMS.20.111001.

[Colaleo et al.(2015)] Colaleo, A, Safonov, A, Sharma, A, et al. CMS Technical Design Report for the Muon Endcap GEM Upgrade. 2015. URL https://cds.cern.ch/record/2021453.

[Danger(2014)] Danger, Helge. *Untersuchung von Aufladeeffekten und Alterungsstudie an einem Micromegas Detektor mit resistiver Streifenanode*. Ph.D. thesis, Ludwig-Maximilians Universität München, München, 2014. URL https://www.etp.physik.uni-muenchen.de/publications/theses/download/dipl{_}hdanger.pdf.

[Deisting et al.(2018)] Deisting, Alexander, Garabatos, Chilo, and Szabo, Alexander. Ion mobility measurements in Ar-CO2, Ne-CO2, and Ne-CO2-N2 mixtures, and the effect of water contents. *Nuclear Instruments and Methods in Physics Research Section A: Accelerators, Spectrometers, Detectors and Associated Equipment*, 904:1–8, 2018. ISSN 0168-9002. doi:10.1016/J.NIMA.2018.07.008.

[Einstein(1905)] Einstein, Albert. Über einen die Erzeugung und Verwandlung des Lichtes betreffenden heuristischen Gesichtspunkt. *Annalen der Physik*, 322(6):132–148, 1905. ISSN 15213889. doi:10.1002/ANDP.19053220607.

[Fick(1855)] Fick, Adolf. Ueber Diffusion. *Annalen der Physik*, 170(1):59–86, 1855. ISSN 15213889. doi:10.1002/ANDP.18551700105.

[Flierl(2018)] Flierl, Bernhard. *Particle tracking with micro-pattern gaseous detectors*. Ph.D. thesis, Ludwig-Maximilians Universität München, München, 2018. doi:10.5282/edoc.22198. URL https://edoc.ub.uni-muenchen.de/22198/.

[Frauenfelder and Henley(1979)] Frauenfelder, Hans 1922 and Henley, Ernest M. 1924-2017. *Teilchen und Kerne*. Oldenbourg, München [u.a.], 1979. ISBN 3486205919.

[Giomataris et al.(2006)] Giomataris, I., De Oliveira, R., Andriamonje, S., et al. Micromegas in a bulk. *Nuclear Instruments and Methods in Physics Research, Section A: Accelerators, Spectrometers, Detectors and Associated Equipment*, 560(2):405–408, 2006. ISSN 01689002. doi:10.1016/J.NIMA.2005.12.222.

[Giomataris et al.(1996)] Giomataris, Y., Rebourgeard, Ph, Robert, J. P., et al. MICROMEGAS: A high-granularity position-sensitive gaseous detector for high particle-flux environments. *Nuclear Instruments and Methods in Physics Research, Section A: Accelerators, Spectrometers, Detectors and Associated Equipment*, 376(1):29–35, 1996. ISSN 01689002. doi:10.1016/0168-9002(96)00175-1.

[Hamamatsu(1988)] Hamamatsu, Photonics K K. PHOTOMULTIPLIER TUBE R4124 . 1988.

[Herrmann(2019)] Herrmann, Maximilian Georg. *Series calibration of segmented and multi-layered micromegas modules for ATLAS*. Ph.D. thesis, Ludwig-Maximilians Universität München,

München, 2019. doi:10.5282/edoc.25055. URL https://edoc.ub.uni-muenchen.de/25055/.

[Horvat(2005)] Horvat, Sandra. *Study of the Higgs Discovery Potential in the Process pp -> H -> 4μ*. Ph.D. thesis, 2005. URL http://cds.cern.ch/record/858509.

[Hough(1962)] Hough, Paul V C. METHOD AND MEANS FOR RECOGNIZING COMPLEX PATTERNS. 1962. URL https://www.osti.gov/biblio/4746348.

[Iakovidis(2014)] Iakovidis, Georgios. Research and Development in Micromegas Detector for the ATLAS Upgrade. 2014. URL https://cds.cern.ch/record/1955475.

[Innofil3D()] Innofil3D. Technical Data Sheet Innofil3d PLA. URL https://asset.conrad.com/media10/add/160267/c1/-/en/001417263DS01/.

[Jagfeld et al.(2023)] Jagfeld, Christoph, Biebel, Otmar, Hertenberger, Ralf, et al. Development of a Segmented GEM Readout detector. *Nuclear Instruments and Methods in Physics Research Section A: Accelerators, Spectrometers, Detectors and Associated Equipment*, 1046:167654, 2023. ISSN 01689002. doi:10.1016/J.NIMA.2022.167654.

[Jones et al.(1999)] Jones, L L, French, M J, Moreira, P, et al. The APV25 deep submicron readont chip for CMS detectors. 1999. doi:10.5170/CERN-1999-009.162. URL https://cds.cern.ch/record/432224.

[Kawamoto et al.(2013)] Kawamoto, T, Vlachos, S, Pontecorvo, L, et al. New Small Wheel Technical Design Report. Technical report, 2013. URL https://cds.cern.ch/record/1552862.

[Kleinknecht(2005)] Kleinknecht, Konrad. *Detektoren für Teilchenstrahlung*. Vieweg+Teubner Verlag, Wiesbaden, 2005. ISBN 978-3-8351-0058-9. doi:10.1007/978-3-322-82205-5.

[Klitzner(2019)] Klitzner, Felix. *Development of novel two-dimensional floating strip micromegas detectors with an in-depth insight into the strip signal formation*. Ph.D. thesis, Ludwig-Maximilians Universität München, München, 2019. doi:10.5282/edoc.24286. URL https://edoc.ub.uni-muenchen.de/24286/.

[Korff(1946)] Korff, Serge Alexander. *Electron and nuclear counters*. Van Nostrand, Toronto, 1946.

[Lippert(2012)] Lippert, Benedikt. Studien zur Signalentstehung und Parametrisierung der Gasverstärkung in einem Micromegas-Detektor. 2012. URL https://www.etp.physik.uni-muenchen.de/publications/bachelor/download{_}auth{_}etp/bac12{_}blippert.pdf.

[Lösel(2017)] Lösel, Philipp. *Precision calibration of large area micro pattern gaseous detectors*. Ph.D. thesis, Ludwig-Maximilians Universität München, München, 2017. doi:10.5282/edoc.21251. URL https://edoc.ub.uni-muenchen.de/21251/.

[Marques et al.(2020)] Marques, A. P., Brunbauer, F. M., Müller, H., et al. Minimizing distortions with sectored GEM electrodes. *Nuclear Instruments and Methods in Physics Research, Section A: Accelerators, Spectrometers, Detectors and Associated Equipment*, 961, 2020. ISSN 01689002. doi:10.1016/J.NIMA.2020.163673.

[Morishima et al.(2017)] Morishima, Kunihiro, Kuno, Mitsuaki, Nishio, Akira, et al. Discovery of a big void in Khufu's Pyramid by observation of cosmic-ray muons. *Nature 2017 552:7685*, 552(7685):386–390, 2017. ISSN 1476-4687. doi:10.1038/nature24647. URL https://www.nature.com/articles/nature24647.

[Ortec(1970)] Ortec. Instruction Manual 452 Spectroscopy Amplifier. 1970.

[Ortec(2002)] Ortec. Model 142PC Preamplifier Operating and Service Manual. 2002. URL https://www.ortec-online.com/-/media/ametekortec/manuals/1/142pc-mnl.pdf?la=en{&}revision=db2675d3-d2e4-4253-8b0e-9ab8cb04d8fb.

[Pinto(2010)] Pinto, Serge Duarte. Micropattern gas detector technologies and applications, the work of the RD51 collaboration. 2010. doi:10.1109/NSSMIC.2010.5873870.

[Raether(1964)] Raether, Heinz. *Electron avalanches and breakdown in gases*. Washington (D.C.) : Butterworths, 1964., 1964. ISBN 9780598450210.

[Ramo(1939)] Ramo, Simon. Currents Induced by Electron Motion* INTRODUCTION N designing vacuum tubes in which electron. 1939. doi:10.1109/JRPROC.1939.228757.

[Riegler(2002)] Riegler, Werner. Induced signals in resistive plate chambers. *Nuclear Instruments and Methods in Physics Research, Section A: Accelerators, Spectrometers, Detectors and Associated Equipment*, 491(1-2):258–271, 2002. ISSN 01689002. doi:10.1016/S0168-9002(02)01169-5.

[Rinnagel(2022)] Rinnagel, Maximilian. *Development of an Inverted Ring Imaging Cherenkov Micromegas (in preperation)*. Not published, Ludwig-Maximilians Universität München, München, 2022.

[Rolandi et al.(2008)] Rolandi, Luigi, Riegler, Werner, and Blum, Walter. *Particle Detection with Drift Chambers*. Particle Acceleration and Detection. Springer Berlin Heidelberg, Berlin, Heidelberg, 2 edition, 2008. ISBN 978-3-540-76683-4. doi:10.1007/978-3-540-76684-1. URL http://link.springer.com/10.1007/978-3-540-76684-1.

[Sauli(1997)] Sauli, F. GEM: A new concept for electron amplification in gas detectors. *Nuclear Instruments and Methods in Physics Research Section A: Accelerators, Spectrometers, Detectors and Associated Equipment*, 386(2-3):531–534, 1997. ISSN 01689002. doi:10.1016/S0168-9002(96)01172-2. URL https://linkinghub.elsevier.com/retrieve/pii/S0168900296011722.

[Sauli(1977)] Sauli, Fabio. Principles of operation of multiwire proportional and drift chambers. 1977. doi:10.5170/CERN-1977-009. URL https://cds.cern.ch/record/117989.

[Sauli(2016)] Sauli, Fabio. The gas electron multiplier (GEM): Operating principles and applications. *Nuclear Instruments and Methods in Physics Research, Section A: Accelerators, Spectrometers, Detectors and Associated Equipment*, 805:2–24, 2016. ISSN 01689002. doi:10.1016/J.NIMA.2015.07.060.

[Schindler(2022)] Schindler, H. Garfield++ User Guide. 2022. URL https://garfieldpp.web.cern.ch/garfieldpp/documentation/UserGuide.pdf.

[Shockley(1938)] Shockley, W. Currents to Conductors Induced by a Moving Point Charge ARTICLES YOU MAY BE INTERESTED IN. *Journal of Applied Physics*, 9:635, 1938. doi:10.1063/1.1710367.

[Smirnov(2007)] Smirnov, Igor. HEED. 2007. URL http://ismirnov.web.cern.ch/ismirnov/heed.

[The National Institute of Standards and Technology()] The National Institute of Standards and Technology. The National Institute of Standards and Technology (NIST). URL https://www.nist.gov/pml/xcom-photon-cross-sections-database.

[Townsend(1910)] Townsend, John. *The Theory of Ionization of Gases by Collision*. Constable Company LTD, London, 1910.

[Workman and Others(2022)] Workman, R L and Others. Review of Particle Physics. *PTEP*, 2022:083C01, 2022. doi:10.1093/ptep/ptac097.

Appendix A

Tools and Methods for the Measurement of the Detector

Capacities between the GEM strip and all Other Electrodes

name	electrodes	capacity
$C_{\text{strip–top}}$	GEM strip - top side of the SGR foil	28.3 pF
$C_{\text{strip–strip (active area)}}$	GEM strip - GEM strip (active area)	2×2.72 pF
$C_{\text{strip–strip (guiding)}}$	GEM strip - GEM strip (non active area)	2×1.23 pF
$C_{\text{strip–Micromegs ro top}}$	GEM strip - top Micromegas readout strips	2.5 pF
C_{strip}	sum of all capacities	38.7 pF

Table A.1: Capacities between a GEM strip and the other detector electrodes.
Only the most important capacities are shown.
The detector is approximated as a plate capacitor (see Equation 3.1). Due to the GEM holes the area of the capacitor is reduced. The calculated capacities are multiplied by $(1 - \textit{optical transparency}) \approx 25\,\%$.
C_{strip} is the capacity of one GEM strip. It is the sum of all capacities between the GEM strip and all other electrodes. Since smaller capacities (e.g. between the cathode and the GEM strips) are not considered in this calculation the actual C_{strip} is slightly larger. In the following it is approximated $C_{\text{strip}} \approx 40\,\text{pF}$.

Hough Transformation

The Hough transformation is a method to identify straight lines [Hough, 1962].
A set of lines going through the point $\vec{P} = (X, Y)$ can be described by the parameters α, which is the angle between the normal of the line and the X-axis, and d which is the shortest distance to the origin. The point $\vec{P} = (X, Y)$ is given in the Hough space by the parameterization:

$$d(\alpha) = X \times cos(\alpha) + Y \times sin(\alpha) \tag{A.1}$$

All points in the X/Y-space that lie on a line are defined by the same α and d. Therefore, a line in X/Y-space is given by a point in Hough space. This point lies at the intersection of the lines $d(\alpha)$.
The Hough transform of an μ-track passing through the detector at an angle of $\Theta = 20°$ is shown in Figure A.1. Using the distance between $\vec{P}$ transformed into Hough space and the intersection of all lines in Hough space, the error for the point in the μ-TPC method is adjusted.

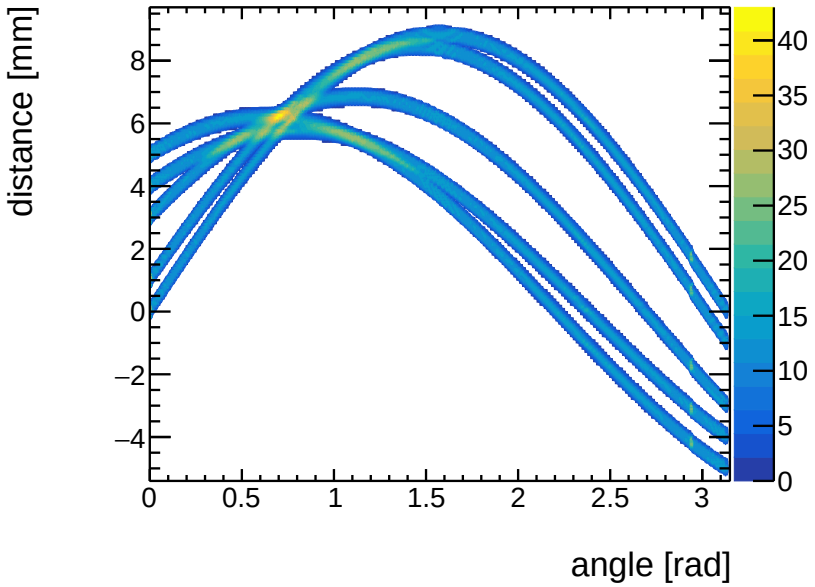

Figure A.1: Hough transformation for the track shown in Figure 3.13. Using the distance between the point $\vec{P}$ transformed into Hough space and the intersection of all lines in Hough space, the error for the point in the μTPC method is adjusted.
$\Theta = 20°$, $U_{GEM} = 200\,V$, $U_{ampl} = 440\,V$.

Appendix B

Signal Creation in the SGR Detector

B.1 Electron End Point Inside the SGR Foil

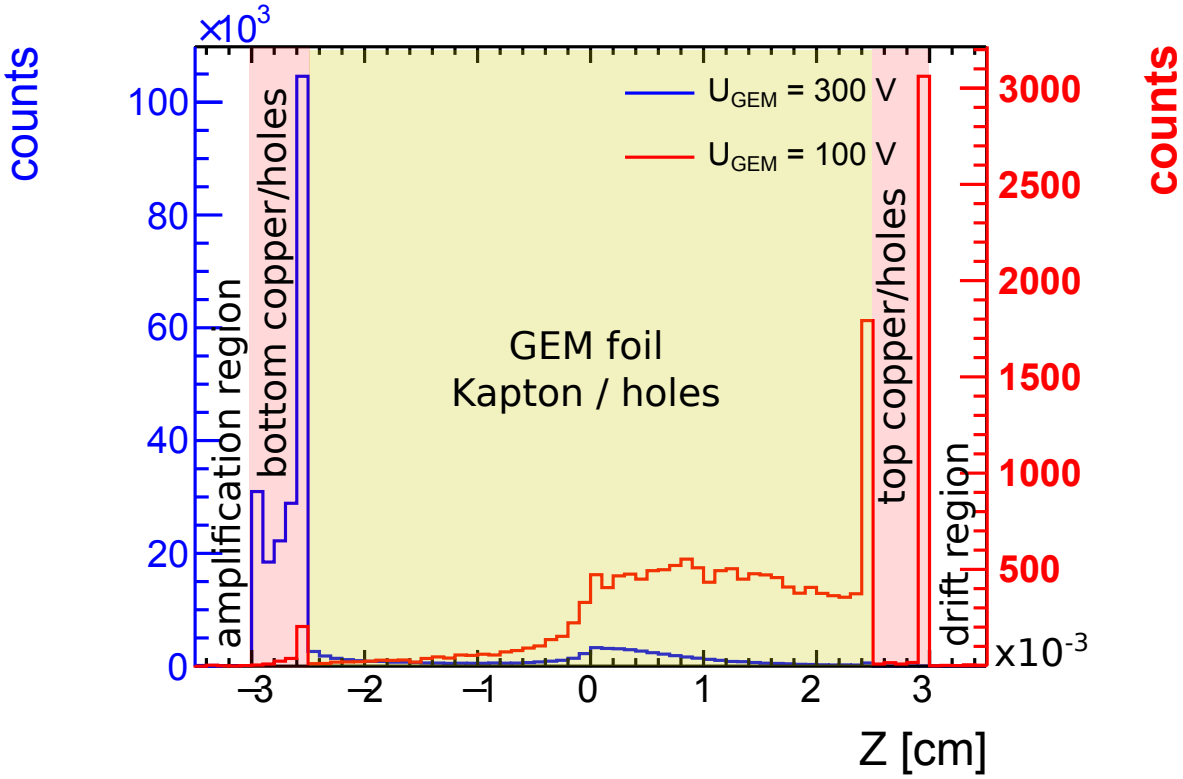

Figure B.1: Simulated electron end position along the Z-axis inside the SGR foil with the segmentation on the bottom side.
In this figure the electron endpoints of 100 5.9 keV photon events are shown.
The position of the SGR foil and its copper coating are marked. The segmentation is on the bottom side of the SGR foil.
For higher U_{GEM} more electrons end up on the Kapton inside the GEM holes, but also more electrons are generated inside the GEM holes.
Most of the electrons are stopped in the upper half of the GEM foil since the diameter of the hole decreases from 70 µm on the surface to 50 µm.
U_{drift} = 420 V, U_{GEM} = 300 V, U_{ampl} = 310 V;
U_{drift} = 420 V, U_{GEM} = 100 V, U_{ampl} = 490 V

B.2 Ion End Point Inside the SGR Foil

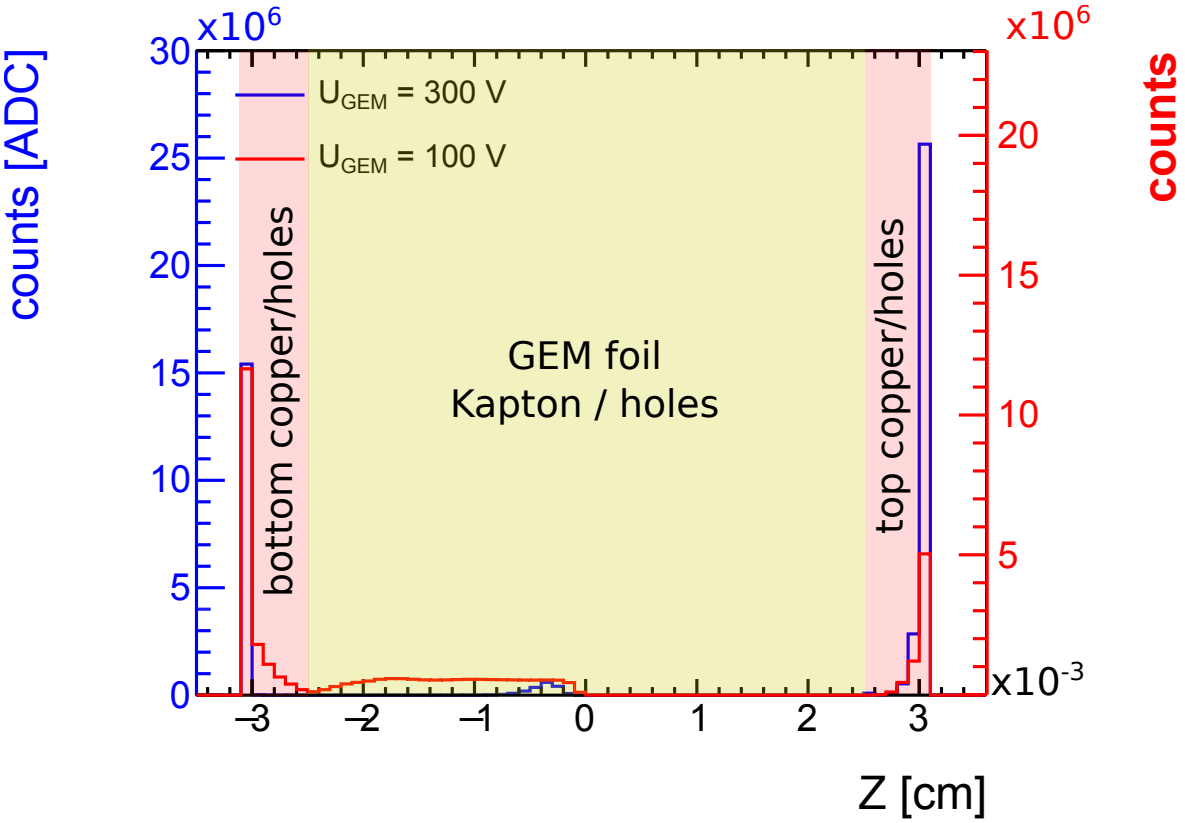

Figure B.2: Simulated ion end position along the Z axis.
In this figure the ion endpoints (inside the SGR foil) of 100 5.9 keV photon events are shown.
The position of the SGR foil and its copper coating are marked. The segmentation is on the bottom side of the SGR foil.
For higher U_{GEM} more electrons are drifting through the hole to the top side of the GEM foil.
Ions are stopped inside the hole on the Kapton.
U_{drift} = 420 V, U_{GEM} = 300 V, U_{ampl} = 340 V
U_{drift} = 420 V, U_{GEM} = 100 V, U_{ampl} = 520 V.

B.3 Simulated Fraction of Back Drifting Ions for an SGR Detector with the Segmentation on the Top Side

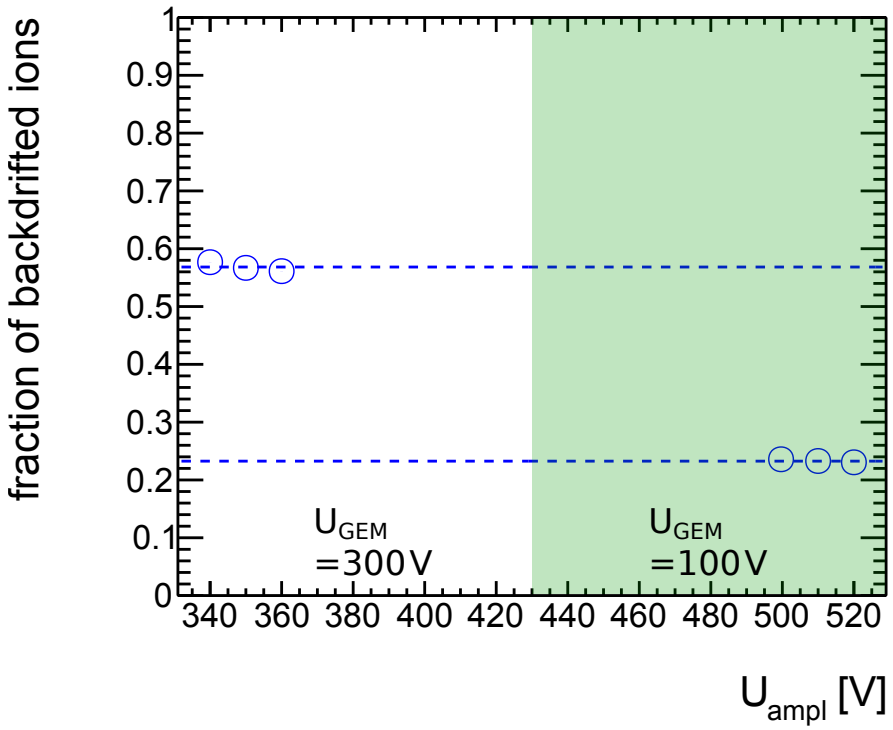

Figure B.3: Simulated fraction of ions drifting to the top side of the SGR foil if the segmentation is on the top side.
2.5 times more ions are drifting to the top side of the SGR foil for U_{GEM} = 300 V as for U_{GEM} = 100 V. U_{drift} = 420 V.

B.4 Simulated Electron Diffusion on the Resistive Anode

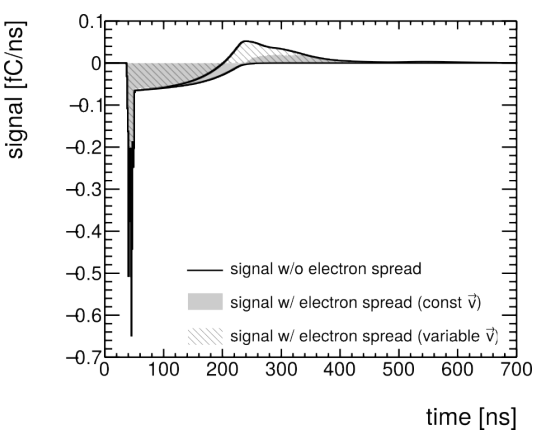

(a) Simulated signal of a single 5.9 keV photon event (readout electronics not simulated).

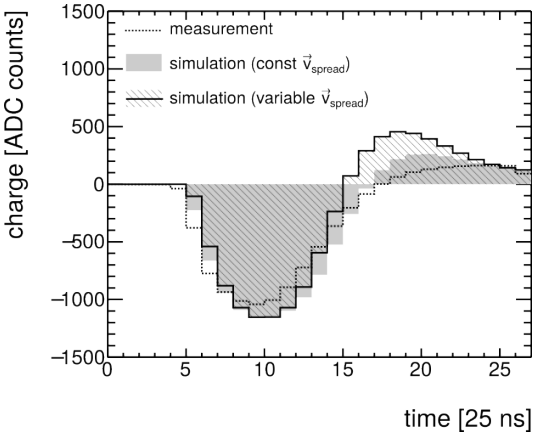

(b) Simulated signal of 5.9 keV averaged over 100 photon events (readout electronics simulated).
The simulated signal is compared with the measured signal averaged over a few thousand events.

Figure B.4: Simulated signal of 5.9 keV photons for the top Micromegas readout layer of a SGR detector. The highest strip signal of the cluster is shown.
In Figure a, a single event is shown without the readout electronics being simulated.
In Figure b, 100 events were simulated, including the readout electronics. The simulated signals are compared to measured signals. The simulated signal is shown without the electron spread included in the Simulation (open histograms in Figure a).
The hatched histograms are the simulated signal when a constant spread velocity of $\vec{v}_{\text{spread}} = 0.0045\,\text{mm/ns}$ is used for the simulation.
The shade histogram shows the simulated signal when a different spread velocity is used for each electron as described in chapter 5.3.2. This signal fits best to the measured data.

Appendix C

Characterization of the 2D DLC Layer Micromegas Detector Using ^{55}Fe

C.1 Saturated Strip Signal

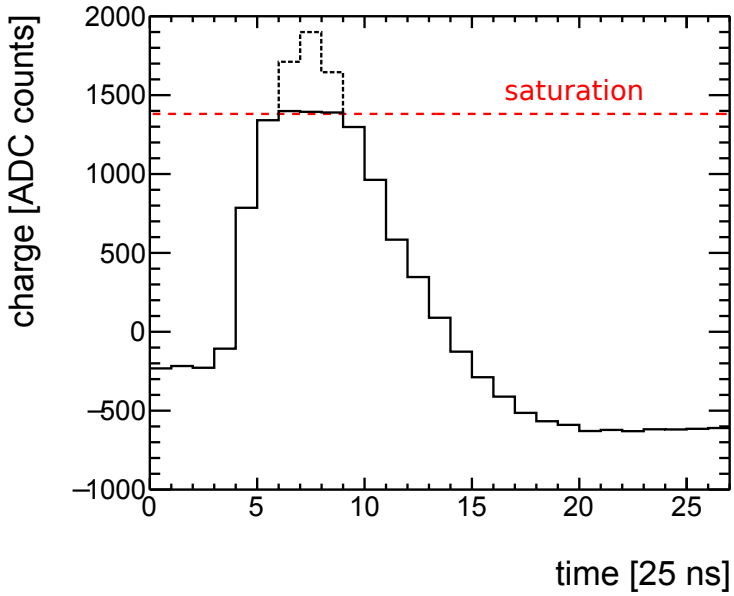

Figure C.1: Saturated strip signal of the top readout strip layer.
The signal is cut off due to saturation of the APV25 readout ASICs. No information for the signal higher as the saturation value is available. The reconstructed signal height is lower than the actual one (dashed lines). The signal that is higher than the saturation value (dashed line) is drawn with arbitrary values only for visualization reasons.
U_{drift} = 420 V, U_{GEM} = 200 V, U_{drift} = 430 V.

C.2 Energy Resolution

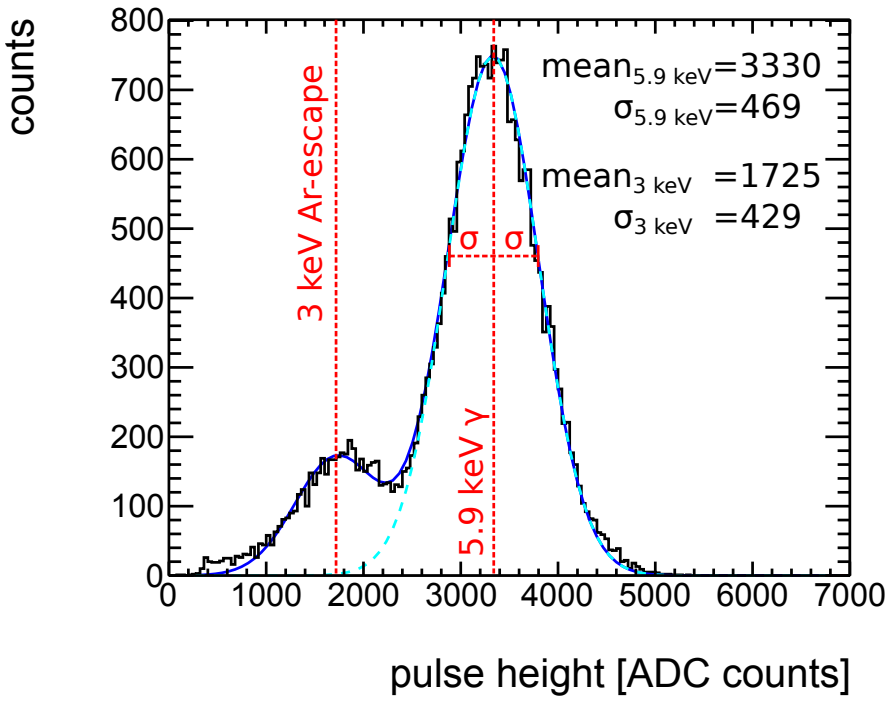

Figure C.2: Characteristic Argon spectrum reconstructed with the top readout strip layer of a standard DLC layer Micromegas detector.
To obtain the width σ and position of both peaks a double Gaussian fit (similar to Equation 3.26) is applied.
$\sigma_{5.9\,\mathrm{keV}}$ is taken as the width of the 5.9 keV γ-peak and $\mathrm{mean}_{5.9\,\mathrm{keV}}$ is used as pulse height.
U_{drift} = 300 V, U_{ampl} = 550 V.

Appendix D

Spatial and Angular Properties of the SGR Detector

D.1 Spatial Resolution

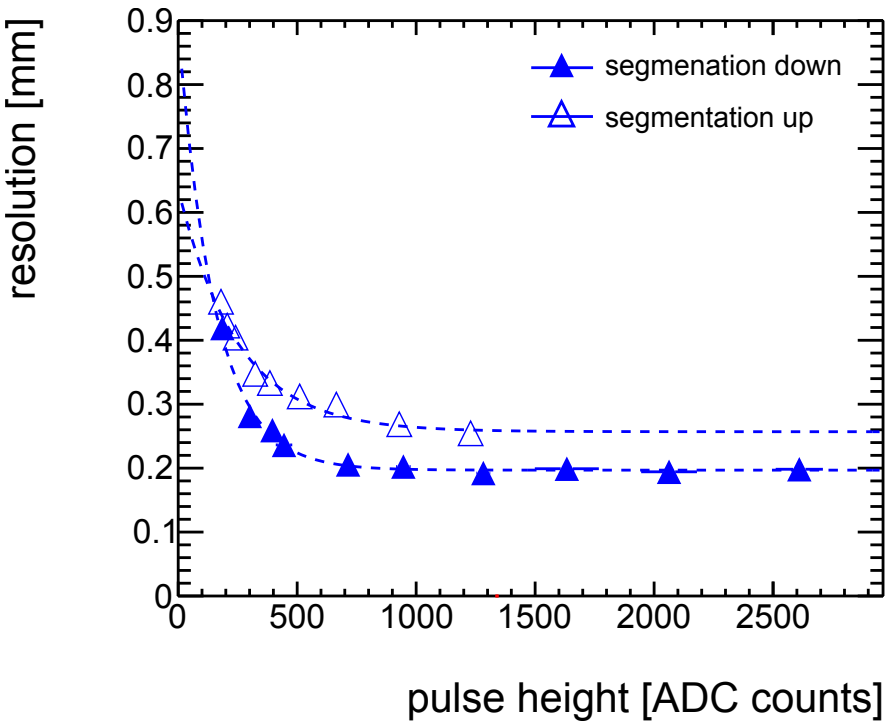

Figure D.1: Resolution for 120 GeV muons traversing the detector with an angle of inclination of $\Theta = 20°$ plotted against the mean cluster pulse height.
The position is determined using the μTPC method (see chapter 3.6.2).
At the same pulse height the resolution for the SGR detector with the segmentation on the bottom side is better.
U_{drift} = 420 V, U_{GEM} = 200 V.

D.2 Spatial Efficiency

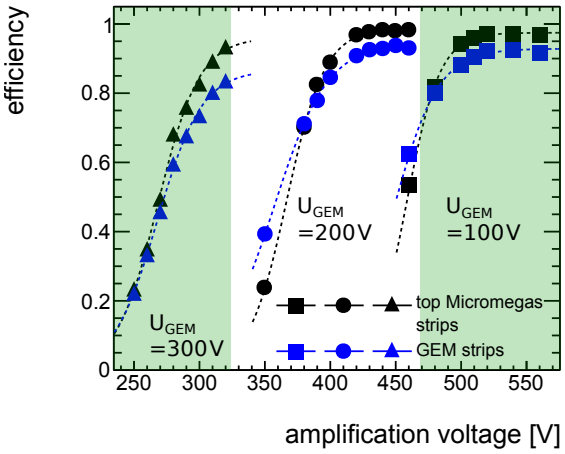

(a) Segmentation on the bottom side of the SGR foil.

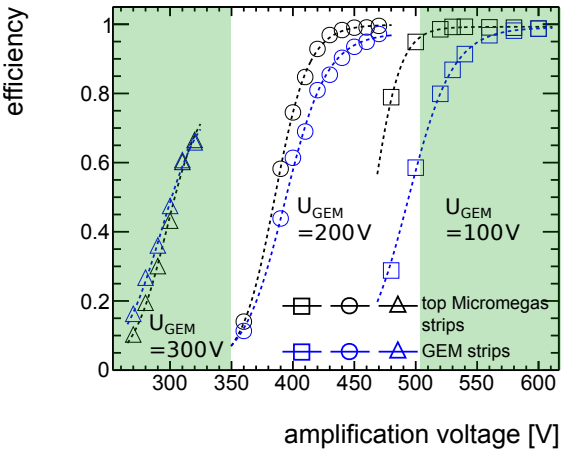

(b) Segmentation on the top side of the SGR foil.

Figure D.2: Spatial efficiency for different U_{GEM} (columns), different U_{ampl}.
An event is considered as efficient if the distance to the reference track is less than 1 mm.
The GEM and top Micromegas strips reach values higher than 90 %. Since the bottom Micromegas strips are not operated at the working point the efficiency is lower and not shown here. As for the pulse height (see chapter 9.3), U_{ampl} needs to be increased by 20-30 V for the SGR detector with the segmentation on the top side to reach equal efficiencies as the inverse detector.
U_{drift} = 420 V.

D.3 Angular Resolution

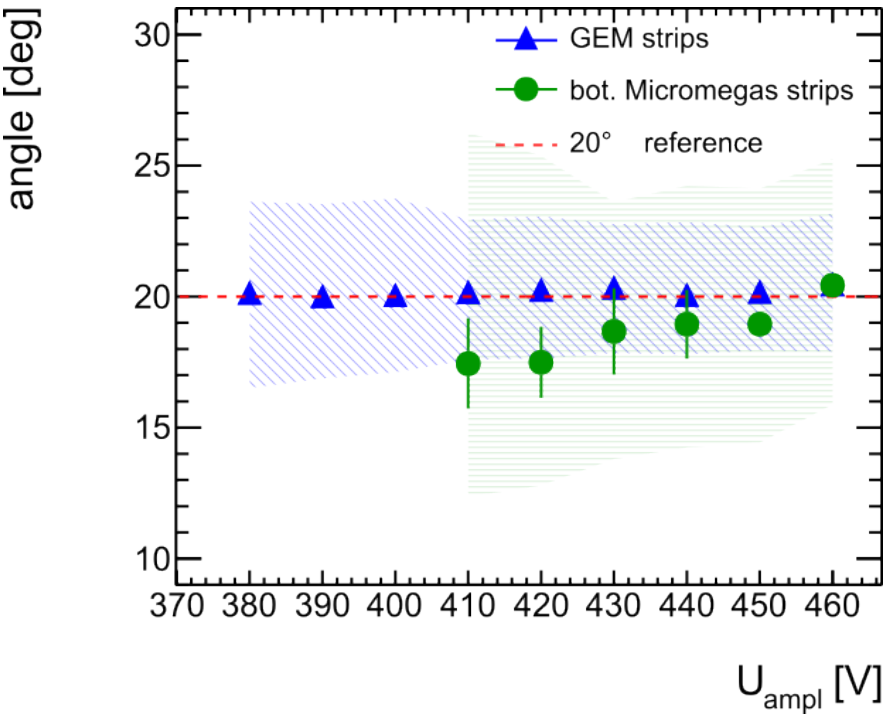

Figure D.3: Reconstructed angle using the μTPC method.
The angle is reconstructed with the bottom Micromegas strip layer and with the GEM strips. Since the bottom Micromegas readout strip layer is not operated at the working point the angular properties are worse than that for the GEM strips.
Nevertheless, even though the signal on the bottom Micromegas readout strips is influenced by the electron spread on the DLC layer the angle reconstruction using the μTPC method is possible. U_{GEM} = 200 V, U_{drift} = 420 V.

D.4 Event Selection

The reconstructed tracks are required to meet the event selection criteria specified in Figure D.4. If these criteria are not met, the entire event is discarded for further analysis. Figure D.4 shows how many events are left after each selection criteria is applied. About 14 % of all recorded events are used for the analysis of the SGR detectors.

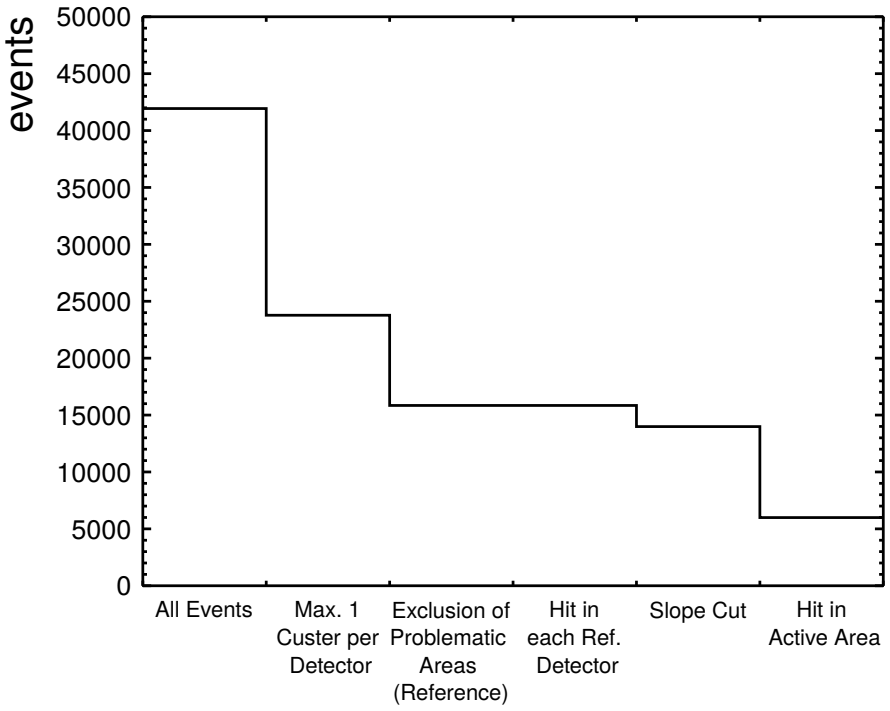

Figure D.4: Number of reconstructed tracks that meet the selection criteria used.
Values are exemplary shown for the top GEM strips and U_{drift} = 420 V, U_{GEM} = 200 V, U_{ampl} = 440 V.
Following selection criteria are applied:

- All Events: Total number of recorded events in the dataset used.

- Max. 1 Cluster per Event: It is required that no detector reconstructs more than one cluster. This is necessary to ensure that the reference track is reconstructed correctly.

- Exclusion of Problematic Areas: In all X layers, problematic regions were observed at the edges of the APVs (at strips $X \approx 122 \pm 18$ and $X \approx 236 \pm 18$), which lead to increased tracking inaccuracy. Only hits in the reference detectors outside these ranges are used. This behavior was not observed on the Y-readout layers.

- Hit in each Ref. Detector: To obtain a high track accuracy, it is required that all reference detectors reconstruct a track.

- Slope Cut: It is required that the track slope reconstructed with only the first two reference detectors (TMM1 and TMM2 in Figure 9.1) is approximately equal to the track slope reconstructed with only the last two reference detectors (TMM3 and T1 in Figure 9.1). This excludes multiple scattering and incorrectly reconstructed tracks.

- Hit in Active Area: It is required that the extrapolated reference track intersects with the fiducial active area of the SGR detectors. Due to the mounting of the detectors, only the top half of the active area of the reference detectors overlaps with the active area of the SGR detectors (see Figure 9.3).

Danksagung

An dieser Stelle möchte ich an all diejenigen meinen großen Dank aussprechen, die mich beim Anfertigen meiner Dissertation unterstützt und motiviert haben. Besonders hervorheben möchte ich:

- Meinem Doktorvater Professor Otmar Biebel, der mein Interesse an der Teilchenphysik, insbesondere der Detektorentwicklung, geweckt hat und mir die Möglichkeit geboten hat, in seiner Arbeitsgruppe diese Thesis zu verfassen. Für seine hilfreichen Anregungen und lehrreichen Unterhaltungen an der Kaffeemaschine möchte ich mich herzlich bedanken.
- Auch möchte ich Professor Wolfgang Dünnweber danken, dass er sich bereit erklärt hat, das Zweitgutachten für diese Arbeit zu verfassen.
- Dr. Ralf Hertenberger danke ich für all seine Unterstützungen und Ratschläge. Besonders aber danke ich ihm für die hilfreichen Korrekturen gegen Ende meiner Arbeit.
- Dr. Eraldo Oliveri und Professor Yorgos Tsipolitis danke ich, dass sie mir ermöglicht haben, die Testmessungen am CERN durchzuführen.
- Fabian Vogel danke ich besonders für seine Unterstützung während der Testmessungen am CERN und für das Korrekturlesen meiner Arbeit. Nicht zu vergessen ist sein Einsatz, den Arbeitstag jeden Morgen mit den anderen Doktoranden und mir bei mehreren Tassen Kaffee zu beginnen.
- Natürlich danke ich auch allen anderen (ehemaligen) Mitgliedern unserer Arbeitsgruppe, Dr. Valerio D'Amico, Dr. Bernhard Flierl, Stefanie Götz, Dr. Maximilian Herrmann, Dr. Felix Klitzner, Dr. Alexander Lory, Katrin Penski, Maximilian Rinnagel und Dr. Chrysostomos Valderanis, für ihre Hilfe und den Spaßbei der Arbeit.
- Zu guter Letzt gilt mein Dank meiner Familie und meinen Freunden, besonders meinen Eltern Mathilde Kienlein-Jagfeld und Matthias Jagfeld sowie meinem Bruder Sebastian Jagfeld, für ihre Geduld und den Zuspruch. Vor allem danke ich meiner Freundin Carolin Mirlach, die mir besonders in den letzten Monaten den Rücken freigehalten hat und für die ich in letzter Zeit zu wenig Zeit hatte.